Micromechanics of particle-coated bubbles: deformation from quasistatic to millisecond timescales

Saikat Saha

Supervisors: Dr. Valeria Garbin & Prof. Paul F. Luckham

Department of Chemical Engineering
Imperial College London

Thesis submitted in accordance with the requirements of Imperial College London for the degree of Doctor of Philosophy

September 2020

Declaration

The work presented in this dissertation is the result of my own original research. All else is appropriately referenced.

This thesis is part of the ExtreFlow Project funded by the European Union's Horizon 2020 Excellent Research program, ERC StG project number 639221.

The copyright of this thesis rests with the author. Unless otherwise indicated, its contents are licensed under a Creative Commons Attribution-NonCommercial 4.0 International Licence (CC BY-NC 4.0). Under this licence, you may copy and redistribute the material in any medium or format. You may also create and distribute modified versions of the work. This is on the condition that: you credit the author and do not use it, or any derivative works, for a commercial purpose. When reusing or sharing this work, ensure you make the licence terms clear to others by naming the licence and linking to the licence text. Where a work has been adapted, you should indicate that the work has been changed and describe those changes. Please seek permission from the copyright holder for uses of this work that are not included in this licence or permitted under UK Copyright Law.

Saikat Saha

September 2020

This thesis is dedicated to my Mother, who has been my constant source of strength and inspiration. Thank you for everything Mom.

Acknowledgements

I am grateful to Dr. Valeria Garbin for giving me this valuable opportunity to pursue my passion for scientific research, and providing me a vivid glimpse of it from a global perspective. I have been strongly encouraged to pursue and develop upon my own instincts and ideas, unconstrained, to be a free thinker. At the same time, she has taught me to stay focused, be rigorous and consistent, with constant advice and feedback. She has pushed me to take up teaching activities and attend summer schools, conferences for my own betterment. Overall, she has been very supportive and I consider myself fortunate to have her as my supervisor.

I am grateful to Prof. Paul F. Luckham for his guidance as both my mentor, and subsequently, as my co-supervisor. I have enjoyed our pleasant coffee sessions. He is kind, caring and, in my opinion, has a free-spirited outlook towards research which has made our discussions all the more memorable for me.

In my years at Imperial College, I have had wonderful times, thanks to the members in the group of Flow and Dynamics of Soft Matter, of which I have been a part of. Akaki, Axel, Marco, Diego, Nerine, Christiana and Brice have been both friends and sources of constructive criticism in my work. I am glad that I was given the opportunity to co-supervise both undergraduate and master's students Sarah, Hoon, Vaughn, Ailsa, James and Francis. The hands-on working with the students in helping them setting up and doing the experiments, planing of projects and working as a team in general was an enjoyable experience. Throughout, there have been several people who have kept me motivated and made me happy. A few names, among many, are Matt, Marine and Ilya. Thanks to Dilip, I have been able to journey, and appreciate the natural beauty and the culture of The United Kingdom, as a whole.

Outside the university circle, I have found a good friend in Alice. During my stay in England, I have made fond memories thanks to her parents, Sue and John, and family.

One is a sum of their experiences and the imprints left upon by those around. My family and friends, back home, in India, have had a vital role in shaping me to be who I am. My mother is one of the strongest people I know. She has pushed me to be the best version of myself. She taught me the meaning of the translated verse “Do your duty, do not worry about the outcome”. At times when things feel uncertain and beyond my control, that verse from The Bhagavad Gita, has helped me to stay focused on my priorities. Raju mama, the first to get me into the habit of reading, taught me the importance of maintaining a childlike wonder about the world, motivated and guided me to pursue the field of Science. My Grandfather taught me to solve quadratic equations, Newton’s Laws of Motion and their applications. Every question, philosophical or otherwise, I would direct to him, and he always had the answers. Nidhu meso has selflessly helped me in so many ways. Balaka masi, Dalu masi, Piku masi, Manu masi, Anu mama, Bithi masi, Abhi mama, and so many more, played unique roles in influencing my life. And of course, my friends, to name a few among many, Anindya, Ankit, Pankaj, Chitra, Arijit, Deblina, Annie, Indrajit, Sudeep, Dibakar, Dorje..., have each taught me specific values.

Saikat Saha

London

September 2020

List of publications

1. S. Saha, B. Saint-Michel, V. Leynes, B.P. Binks & V. Garbin. Stability of bubbles in wax-based oleofoams: decoupling the effects of bulk oleogel rheology and interfacial rheology. Rheologica Acta 2020, 59: 255-266.

Abstract

Particles adsorbed at fluid-fluid interfaces confer stability to dispersed systems such as foams and emulsions. The emergent properties associated with the interfacial microstructure underpins the creation of functional materials. In the design, synthesis and application of such materials, it is essential to understand the dynamic behaviour of structured interfaces at deformation timescales that are relevant in practical scenarios.

In this experiment-driven study, a bubble is used as a probe to understand the stability mechanisms and dynamics of fluid-fluid interfaces coated with particles. First, in a model wax-based oil foam, or oleofoam, bubble dissolution time, under controlled conditions, is used as a parameter to assess the bulk and interfacial rheological contributions responsible for the remarkable stability observed. Focus is then drawn to interfacial phenomena, by removing bulk effects, through microscopic observations of crystal-coated bubbles undergoing deformation due to either bubble dissolution or ultrasound-driven volumetric oscillations. In this way phenomena at two extreme timescales, 10^4 s and 10^{-4} s, are observed and interpreted. Finally, the effect of unsteady, fast deformation on a complex interface is systematically studied using a well characterised model interface, comprising of bubbles coated with optically resolvable, monodisperse latex microspheres. The bubbles are subjected to acoustic forcing, leading to the rapid cyclic compression and expansion of the colloidal monolayer. Effects of pressure amplitude, particle size and surface coverage on bubble excursions are studied.

The results signify the importance of local mesoscopic phenomena in explaining the stability of oleofoams, where invoking macroscopic rheological reasoning alone is somewhat inadequate. Experimental timescales strongly influence the nature, integrity and response of complex interfaces to imposed stresses. Further, a bubble driven by ultrasound has potential in studying time-dependent interfacial mechanics.

Table of contents

List of figures **19**

List of tables **25**

1 Introduction **27**

2 Background and theory **31**

2.1 Fluid-fluid interfaces 31

2.1.1 Thermodynamics of fluid interfaces 31

2.1.2 Surface-active agents 33

2.1.3 Colloids 34

2.1.4 Surface stress tensor 34

2.1.5 Emulsions and foams 35

2.1.6 Interfacial rheology 35

2.2 Interfaces stabilised by particles 36

2.2.1 Free energy of particle detachment from a planar interface . . . 36

2.2.2 Interactions between colloids at interfaces 39

2.2.3 Curvature of monolayers 44

2.2.4 Pickering bubbles 44

2.3 Buckling behaviour of particle-coated microbubbles 44

2.4 Interfacial rheometry using pendant drops 49

2.4.1 Pendant drop tensiometry 49

2.4.2 Drop shape fitting elastometry 51

2.4.3 Gibbs elasticity 53

2.5 Theory of bubble dissolution 54

2.5.1 Effect of varying temperature on bubble dissolution 55

2.5.2 Effect of bulk and interfacial rheology on bubble dissolution . . 56

2.6 Bubbles as rheological probes 60

2.6.1 Bubble dynamics in an oscillating pressure field 60

2.6.2 Oscillating bubble as an interfacial rheological probe 61

3 Experimental methodology 67

3.1 Materials 67

3.2 Preparation of observation cells for optical microscopy 68

3.3 Oleofoam preparation and microscopic visualisation 68

3.4 Sample preparation for use with temperature-controlled stage 70

3.4.1 Introduction of sample and purging 70

3.4.2 Calibration of the temperature-controlled stage 70

3.5 Image analysis algorithms for measuring bubble size 71

3.6 Bulk rheological characterisation of samples 73

3.7 Drop shape analysis 74

3.7.1 Setup for pendant drop tensiometry and contact angle measurement 74

3.7.2 Drop shape fitting elastometry 75

3.8 Measurement of surface energy 77

3.9 Design of an enclosure made of agarose gel to excite bubbles using ultrasound 78

3.9.1 Preparation of hydrogel 79

3.9.2 Dimensions of the enclosure 80

3.10 Preparation of colloid-coated bubbles 82
3.11 Placement of a single bubble into the enclosure 82
3.12 Glass plate with transducer 85
3.13 Generation of acoustic waves and observation of bubble oscillations . . 86

4 Stability of bubbles in wax-based oleofoams: decoupling the effects of bulk oleogel rheology and interfacial rheology 89

4.1 Introduction 89
4.2 Methods 91
  4.2.1 Characterisation of wax properties 91
  4.2.2 Foam preparation 92
  4.2.3 Video microscopy with temperature control 92
  4.2.4 Image analysis 93
  4.2.5 Bulk rheology 93
  4.2.6 Dilational interfacial rheology 94
4.3 Results 96
  4.3.1 Effect of preparation temperature and wax concentration on bubble formation 96
  4.3.2 Microscopic imaging of single bubble dissolution during heating 98
  4.3.3 Rheological measurements 104
4.4 Discussion and Conclusions 111
  4.4.1 Effect of temperature on bubble formation 111
  4.4.2 Effect of bulk rheology on bubble stability 112
  4.4.3 Local effects versus bulk rheology 113
  4.4.4 Effect of interfacial rheology on bubble stability 113
  4.4.5 Effect of heating on oleofoam stability 115
  4.4.6 Summary 115

5 Formation and dynamics of crystal-coated air-oil interfaces 117

5.1 Introduction 117

5.2 Methods 118

5.2.1 Preparation of oleogels and oleofoams 118

5.2.2 Microscopic imaging of samples 121

5.2.3 Surface free energy measurements 121

5.2.4 Ultrasound-induced bubble oscillations 122

5.3 Results 123

5.3.1 Morphology of crystals 123

5.3.2 Oscillatory rheology of oleogels 126

5.3.3 Wax-coated bubbles in oleofoams 128

5.3.4 Crystal growth in oleogels 129

5.3.5 Crystallisation at interfaces 130

5.3.6 Determination of adsorption energy of an adsorbed crystal layer 136

5.3.7 Behaviour of crystal-coated bubbles under varying deformation timescales 142

5.4 Discussion 148

5.4.1 Effect of shear and tempering history on bulk oleogel network . 148

5.4.2 Formation of a crystal-coated interface 148

5.4.3 Qualitative comparison of crystals in bulk and interface 149

5.4.4 Deformation of crystal-coated interfaces at varying timescales . 150

5.5 Conclusion 152

6 Dynamics of colloid-coated bubbles in ultrasound 153

6.1 Introduction 153

6.2 Methods 154

6.2.1 Pressure amplitude sweep experiments 155

6.2.2 Radius sweep experiments . . . 156

6.3 Results . . . 157

6.3.1 Radius-sweep experiments on bare bubble . . . 157

6.3.2 Pressure-sweep experiments on bare bubbles . . . 160

6.3.3 Surface microstructure of colloid-coated bubbles . . . 162

6.3.4 Oscillations of colloid-coated bubbles . . . 162

6.3.5 Pressure-sweep experiments on colloid-coated bubbles: $a = 2.5\ \mu$m colloids . . . 166

6.3.6 Effect of particle size . . . 170

6.3.7 Coated bubbles radius-sweep experiments . . . 170

6.4 Discussion . . . 172

6.4.1 Summary of experimental results . . . 173

6.4.2 Expansion-only behaviour of colloid-coated bubbles . . . 173

6.4.3 Limitations of the model . . . 177

6.4.4 Link to interfacial rheology . . . 178

6.4.5 Conclusions . . . 181

7 Conclusions **183**

References **189**

Appendix A Supporting content for Chapter 4 **201**

Appendix B Supporting content for Chapter 5 **211**

Appendix C Supporting content for Chapter 6 **221**

List of figures

2.1 Schematic of a particle adsorbed at an interface. 37

2.2 Schematic of the interactions between a pair of colloids at an interface. 41

2.3 Illustration of model describing the deformations of a colloidal armour on a bubble using a 1D particle-fibre. 45

2.4 Illustration of sinusoidal bending modes of a 1D particle-fibre. 48

2.5 Sampling the contour of a water pendant drop. 50

2.6 Schematic of an area element on the pendant drop with a complex interface. 52

2.7 Combined effects of interfacial elastic modulus and the bulk modulus on bubble dissolution. 59

2.8 Numerical solution of modified Rayleigh-Plesset equation to obtain radius-time curves for lipid coated bubbles. 64

3.1 Steps of image analysis for a bare bubble. 71

3.2 Steps of image analysis for a coated bubble 73

3.3 The various elements of the pendant drop setup. 75

3.4 Shape sampling of a pendant drop using Chebyshev transform for filtering. 76

3.5 Design of agarose gel enclosure 80

3.6 Isolating a bubble 83

3.7 Glass plate with transducer. 84

3.8 Langevin transducer used to strongly oscillate bubbles. 85

3.9 Sine-enveloped sine voltage signal used to insonify bubbles. 86

3.10 Schematic of the various acoustic and video microscopy elements used to oscillate and observe a bubble simultaneously. 87

4.1 Contact angle measurements of oil on wax and DSC measurements of paraffin wax. 92

4.2 Effect of preparation temperature on formation of bubbles in oleogels of Hydropel QB wax in sunflower oil. 97

4.3 Optical micrographs of oleofoam samples prepared using different wax concentrations. 98

4.4 Optical micrographs of oleofoam samples prepared at temperatures for different mixing times. 99

4.5 Dissolution behaviour of bubbles for set temperature profiles. 101

4.6 Image sequences of a bare bubble dissolving in oil; a wax-coated bubble dissolving in oil; and a bubble in an oleofoam. 103

4.7 Image sequences of evolution of bubbles in oleofoam as temperature varies 103

4.8 Flow rheology of sunflower oil, suspension of wax in oil, oleofoam and oleogel. 105

4.9 Oscillatory rheology of oleogel for amplitude sweep and temperature sweep. 107

4.10 Variation of effective surface tension of a wax-coated sunflower oil drop as it underwent compression and expansion cycles. 109

4.11 Interfacial rheology of oleogel layer at the air/oil interface. 110

5.1 Tempering profiles used to prepare oleofoams and oleogels. 120

5.2 Micrographs of crystals, with original samples and respective diluted samples. 123

5.3 Ellipse-fitting to determine size and shape distribution of crystals. . . . 124

5.4 Micrographs of rheometer-prepared oleogels. 126

5.5 Oscillatory frequency-sweep of different oleogels and oleofoam. 127

5.6 Polarised light optical microscopy of wax-coated bubbles resuspended in oil. 128

5.7 Crystal size distribution during cooling. 129

5.8 Unagitated crystallisation in presence of an air bubble. 131

5.9 Image sequence of crystallisation occurring in presence of an air bubble in the wax-oil suspension. 133

5.10 Crystallisation at oleogel interface. 134

5.11 Bubbles flattened between glass plates. 135

5.12 Estimation of adhesion energy of wax-crystal layer at bubble interface between two thermal equilibrium states. 137

5.13 Sessile drops of DMSO on a borosilicate glass slide and an U-oleogel. . 140

5.14 OW-fit to determine solid SFE. 141

5.15 Time sequence of a wax-coated microbubble undergoing slow dissolution, observed using polarised light microscopy. 143

5.16 Bubble-shape change and crystal expulsion at high-frequency volumetric oscillations. 144

5.17 Wax-coated bubble dissolution following crystal expulsion mediated by acoustic driven bubble oscillations at $f = 25$ kHz. 146

5.18 Effect of bubble deformation history on remnant interfacial layer. . . . 147

6.1 Image sequences of an oscillating bare bubble. 157

6.2 Radius-time curves for a bubble at different radii as it dissolved. 158

6.3 Bubble excursion amplitude x_0 against varying bubble radius R_0. . . . 159

6.4 Resonance curves for increasing pressure amplitude and linear interpolation of data. 160

6.5 Variation of excursion amplitude (x_0) with acoustic pressure in terms of amplification A (%) for bare bubbles. 161

6.6 Optical micrographs of colloid-coated microbubbles. 163

6.7 Radius-time curves of colloid-coated bubbles. 164

6.8 Comparing bubble excursions during expansion (x_e) and compression (x_c). 165

6.9 Image sequence of coated-bubble oscillations exhibiting buckling behaviour. 165

6.10 Excursions of bubbles coated by colloids with $a = 2.5$ μm. 167

6.11 Hysteresis in the response of a coated bubble with reduced coverage. . . 169

6.12 Bubbles coated with other particle sizes. 171

6.13 Radius-sweep experiments for coated bubbles, with particle size $a = 1.2$ μm. 172

6.14 Polar plot of bending modes with $n = 10, 20$ and 33. 175

6.15 Numerical solution of model presenting the radius-time curve for a bubble illustrating expansion-only behaviour. 176

6.16 Numerical analysis of the effect of interfacial viscoelasticity on radius-sweep on lipid-coated bubbles. 178

6.17 Radius-sweep curves for bare bubbles: experiment and theory. 180

A.1 Micrograph of oleogel with negligible number of bubbles. 203

A.2 Bubble population in oleofoams versus temperature of gel prior to agitation. 203

A.3 Optical micrographs of oleofoam samples on the day of preparation; 1 week after preparation; and 4 months after preparation. 204

A.4 Triplicate measurements of viscosity with varying temperature for sunflower oil, wax-oil suspension, oleofoam and oleogel. 205

A.5 Side-by-side comparison of oleogel rheology with sand paper. 205

A.6 Frequency sweep of oleogel at 70°C from $f = 0.1 - 50$ Hz at constant $\gamma = 0.05$ %. 206

A.7 Oscillatory rheology of oleogel with varying temperature during heating and cooling. 206

A.8 Magnified images of pendant drop of oil coated by wax crystals. 207

A.9 Curvature profiles of wax-coated sunflower oil drop for different states, given in terms of area fractions. 208

A.10 Variation of effective surface tension of a wax-coated oil drop suspended from a stainless-steel needle. 209

A.11 Estimates of interfacial rheological parameters from wax-coated oil drop, suspended from stainless-steel needle. 209

A.12 Determination of interfacial compression and shear moduli for wax-coated drop suspended from a PTFE needle. 210

B.1 Micrographs of different oleogels prepared without application of shear during crystallisation. 212

B.2 Oscillatory frequency and amplitude sweeps for U-oleogel, oleogel750 and oleofoam. 213

B.3 Oscillatory frequency sweeps for rheometer-prepared oleogels. 214

B.4 Oscillatory amplitude sweeps for rheometer-prepared oleogels. 215

B.5 Distinguishing between bare and wax-coated bubbles without and with cross-polarisers. 215

B.6 Micrographs showcasing crystal growth during cooling. 216

B.7 A close up of a wax-coated bubble resuspended in oil, viewed with cross-polarisers. 217

B.8 Image processing to determine geometrical variables to determine adsorption energy of wax-layer. 218

B.9 Micrographs of delaminated wax-layers left behind from dissolved wax-coated bubbles. 219

C.1 Radius-sweep experiments using two different gels. 222

C.2 Radius-sweep experiments illustrate that the same gel can be used for several days if stored properly. 223

C.3 Map of excursions of different bubbles, oscillated within the same gel, at different amplifier gain values and on different days. 224

C.4 Excursion versus increasing amplification for a bare bubble. 225

C.5 Colloidal armour resisting bubble coalescence. 226

C.6 Effect of surface coverage on interfacial structure. 227

C.7 Radius-time curve of a colloid-coated bubble oscillated with a 20 cycle acoustic pulse. 227

C.8 Shape change of colloid-coated bubble during oscillations. 228

C.9 Effect of reduced surface coverage on coated bubble radius-time curves. 228

C.10 Bubbles coated with colloids of size $a = 0.25$ μm. 229

C.11 Radius-sweep experiments for coated bubbles, with particle size $a = 1.2$ μm at $A = 60\%$. 230

List of tables

5.1 Surface tension components of liquids for determining surface energies of solid substrates. 122

5.2 Contact angles of various liquids on borosilicate glass and U-oleogel. . . 140

A.1 Dissolution times for bare, wax-coated and bubbles in oleofoam. 202

B.1 The various geometrical elements, for the bubble states $i = 1$ and 2, calculated using image analysis, to estimate adhesion energy of a crystal-layer with the air-oil interface. 211

Chapter 1

Introduction

Within the purview of fluid-fluid interfaces lie intricate cells comprised of liquid films sandwiched between air as in foams [1], or the globules of a liquid dispersed in another immiscible liquid forming an emulsion. From the realm of biological phenomena to industrial processes, encountering multi-phase systems and the interfaces between them is inevitable [2]. At the demarcating boundary, the molecules have higher free energy than those in the bulk and due to this the systems are prone to evolve into configurations with minimum surface to volume ratios [3]. This is the reason why foams and emulsions destabilise quickly.

Solid particles have high affinity to adsorb at interfaces, causing a reduction in surface free energy that is several orders of magnitude larger than that for molecular surfactants [4–6]. Depending on the interfacial concentration, there is ordering mediated through the mutual interactions among the particles, spanning across different length scales. This confers emergent properties to the 2D domains [7], which is the basis of advanced materials, having attributes such as specific optical properties, catalytic activity, wettability or viscoelasticity. The latter is responsible for resisting dynamic deformation of such systems and owes its origins to the nature of the interactions and their characteristic equilibration timescales [8–11]. Conversely, therefore, it is expected that such interfaces will exhibit diverse phenomena depending on the timescales of applied deformations [12]. This forms the subject matter of this thesis, where the dynamic behaviour of complex interfaces are explored at two extreme timescales, from the quasi-static to the highly unsteady and rapid setting. The observations are interpreted using both continuum approaches based on viscoelasticity, and a micromechanical approach. Such an understanding will aid in the formulation of novel approaches that are needed to probe the fine details of self-assembly, and eventually establish directed assembly protocols through finite controlled perturbance to artificially select a particular relaxation pathway.

In this thesis, with an experiment-based approach, bubbles are used as probes to study dynamic interfacial phenomena. A bubble, which harmoniously combines the advantages of having a large interfacial area while enclosing a highly compressible gas volume, that can be tuned through pressure changes, becomes a perfect candidate to observe interfacial phenomena. Through visual observation of particle-coated bubbles undergoing either *slow*, diffusion-limited dissolution or *fast*, ultrasound-driven volumetric oscillations, dynamic interfacial phenomena at two extreme timescales, specifically, $t \sim 10^4$ s and $t \sim 10^{-4}$ s are explored.

In this study, first, for a particle-coated bubble, embedded within a particulate gel network, the bubble dissolution time is measured, under controlled circumstances, and it is used as a parameter to compare the contributions of bulk and interfacial rheology in inhibiting bubble dissolution. The model system chosen is a wax-based oil foam, or oleofoam, of which a bubble coated with a crystal layer and embedded within a waxy oleogel, forms a representative subunit. This is illustrative of a practical system, whereby oleofoams hold great potential in the formulation of food or cosmetic products [13]. The lack of non-aqueous foaming agents makes the use of particles as a preferred feasible route to stabilising such oleofoams.

Second, it is investigated how the wax crystals are integrated into air-oil interfaces, leading to the formation of crystal-coated bubbles in the oleofoams. The dynamic behaviour of such interfaces are then observed, after removing the surrounding bulk crystal network, as the wax-coated bubbles either undergo dissolution or ultrasound-mediated volumetric oscillations. This way phenomena associated with the dynamics of crystal-coated interfaces, under two extreme deformation timescales, are studied and linked to the evolution of the interfacial microstructure.

Third, using a different model system, comprised of a bubble armoured by monodisperse, latex microspheres, suspended in an aqueous solution, the effects of unsteady, rapid, small-amplitude deformations of a complex interface are systematically studied. Both the micrometric colloids and the microstructures of the monolayers they constitute, can be resolved by optical microscopy. The coated bubbles are subjected to ultrasound-mediated volumetric oscillations and the dynamics are resolved using high-speed video microscopy and then analysed using image analysis. The effect of acoustic pressure, particle size and surface coverage on the bubble dynamics are studied. A framework is described to extract viscoelastic properties of the monolayer, with the notion being extendable to other complex interfaces subjected to such rapid deformations.

In summary, the main objectives of this thesis are:

1. to assess the contributions of bulk and interfacial rheology in inhibiting bubble dissolution in a crystal-based oleofoam;
2. to compare the dynamic behaviour of crystal-coated interfaces when deformed at quasi-static (10^4 s) and sub-millisecond timescales (10^{-4} s).
3. To study the oscillatory dynamics of colloid-coated bubbles, driven by ultrasound, and link the macroscopic response to the interfacial microstructure through continuum and micromechanical models.

The thesis is structured as follows. The basic theories and current understanding of interfacial phenomena, bubble dissolution, monolayer compression and ultrasound-induced bubble oscillations are reviewed in Chapter 2. The experimental methods used in preparing microscope samples, particle-stabilised foams, isolating bubbles from foams, determination of surface energy of substrates, details of the video-microscopy setup, ultrasound insonation, image analysis, and rheological characterisation are described in Chapter 3. In Chapter 4, the link between interfacial and bulk stability imparted by crystals, in the model wax-based oleofoam, are investigated. The formation; and the link between microstructure and dynamics of crystal-coated interfaces, using wax-coated bubbles, are the subject matter of Chapter 5. In Chapter 6, the oscillatory dynamics of colloid-coated bubbles, driven using ultrasound waves, are studied. Finally, in conclusion, in Chapter 7, the observations and interpretations in all the studies, formed through the preceding chapters, are collated to form an understanding of phenomena associated with the dynamics of complex interfaces. The significance in both immediate and broader scopes are discussed.

Chapter 2

Background and theory

2.1 Fluid-fluid interfaces

2.1.1 Thermodynamics of fluid interfaces

The boundary region between two bulk phases is known as an *interface*. If one of the phases is a gas or a vapour, the term *surface* is commonly used. The surface molecules having fewer nearest neighbours, have fewer intermolecular interactions than bulk molecules, and therefore are at a state of higher free energy than those in the bulk. Hence, there is a free energy change associated with the isothermal, reversible formation of a surface and this is termed as the *excess surface free energy* or *surface free energy*. These terms are usually expressed as specific surface free energy, that is, defined per unit area, with the units being mJ/m^2. An equivalent view, of the surface molecules experiencing an inward attraction normal to the surface, is to consider that the surface is in a state of lateral tension. For a plane surface, the force acting parallel to the surface and at right angles to a line of unit length, anywhere in the surface, is defined as the *surface tension*, which has units of mN/m. For a curved surface, the surface tension is independent of curvature as long as the radius of curvature is sufficiently greater than molecular dimensions. Both surface tension and specific excess surface free energy have units that are dimensionally equivalent, and both the quantities are numerically equal only for a pure liquid in equilibrium with its vapour.

For a pure liquid, the explicit thermodynamic definition of surface tension is [3]

$$\sigma = \left(\frac{\partial \mathfrak{A}}{\partial A}\right)_{T,V} \tag{2.1}$$

where $\mathfrak{A}$ is the Helmholtz free energy of the system and A is the area of the surface at constant system volume V and temperature T.

For an open system, comprised of more than one component, with infinitesimal changes being reversible, the differential expression for the internal energy U of the whole system is

$$\mathrm{d}U = T\mathrm{d}S - p\mathrm{d}V + \sigma \mathrm{d}A + \sum_i \mu_i \mathrm{d}n_i, \tag{2.2}$$

with the assumption that work done is entirely associated with change in volume of the bulk phases, having total volume V and pressure p, and change in area of the interface in between. The entropy and temperature of the system are S and T respectively. At equilibrium, the chemical potential for the i-th species remains the same throughout and n_i is the number of moles of the species in the system, with $\sum\limits_i$ denoting the summation over all species $1, ..., i$. The Helmholtz free energy of the system can be written as

$$\mathrm{d}\mathfrak{A} = -S\mathrm{d}T - p\mathrm{d}V + \sigma \mathrm{d}A + \sum_i \mu_i \mathrm{d}n_i \tag{2.3}$$

and hence, the surface tension for the multicomponent system is

$$\sigma = \left(\frac{\partial \mathfrak{A}}{\partial A}\right)_{T,V,n_i}. \tag{2.4}$$

Alternatively, this can also be defined with respect to the Gibbs free energy, with the Gibbs function given as $G = \mathfrak{A} + pV$, so that,

$$\sigma = \left(\frac{\partial G}{\partial A}\right)_{T,p,n_i}. \tag{2.5}$$

In particular, for the surface, the Helmholtz free energy is

$$\mathrm{d}\mathfrak{A}^{\mathrm{s}} = -S^{\mathrm{s}}\mathrm{d}T - p\mathrm{d}V^{\mathrm{s}} + \sigma \mathrm{d}A + \sum_i \mu_i \mathrm{d}n_i^{\mathrm{s}}, \tag{2.6}$$

where the superscript s denotes that the quantities refer to the surface alone. Integrating this equation, by holding the intensive properties T, p, μ_i and σ constant and noting that $V^{\mathrm{s}} \approx 0$, gives

$$\mathfrak{A}^{\mathrm{s}} = \sigma A + \sum_i \mu_i n_i^{\mathrm{s}} \tag{2.7}$$

which upon division by A yields

$$\sigma = \frac{\mathfrak{A}^{\mathrm{s}}}{A} - \sum_i \mu_i \Gamma_i^{\mathrm{s}}, \tag{2.8}$$

where Γ_i^{s} are the surface excess or total surface concentrations of the respective components. This demonstrates that in presence of many components, the surface tension does not equal the specific excess surface free energy. If σ_0 denotes the surface tension when no components other than the solvent are present at the surface, and σ be the value when adsorption has occurred, then the *surface pressure* or *spreading pressure* may be defined as

$$\pi = \sigma_0 - \sigma. \tag{2.9}$$

The altered surface tension, due to the presence of adsorbed species is called the *effective surface tension* σ_{eff}. In general, the surface tension may be regarded as a two-dimensional negative pressure, whereas, π may be considered as a 2D positive pressure exerted by the adsorbed molecules in the plane of the surface.

Work of adhesion and cohesion in a vacuum The free energy changes, or reversible work done, to separate unit areas of two surfaces, or media, from contact to infinity in a vacuum is known as the *work of adhesion* w_{12}, when the two media are different, or the work of cohesion, w_{11}, when the two media are the same [14].

2.1.2 Surface-active agents

Surface-active substances (or surfactants) consist of molecules containing both polar and non-polar parts, making them amphiphilic. Substances such as short-chain fatty acids and alcohols are soluble both in polar and non-polar solvents. The hydrocarbon part of the molecule is responsible for its solubility in the non-polar phase, while the polar -COOH or -OH groups have sufficient affinity towards the polar solvent. If these molecules become located at the interface between a polar and a non-polar phase, they tend to attain a configuration whereby the polar and non-polar parts are present in the respective phases for which they have the affinity for. This is energetically more favourable than complete solution in either phase. The strong adsorption of such substances at surfaces or interfaces in the form of an oriented monomolecular layer (or monolayer) is termed surface activity [2].

2.1.3 Colloids

A colloidal particle refers to a finely divided unit of matter that has a size between 1 nm to several micrometres. They may be solids with high elasticity, resistant to deformation, or may be soft particles such as microgels or bacteria. Here we will consider only rigid solid particles of a given size whenever we use the term 'colloid'. Some colloids may have the affinity to adsorb at the interface between two immiscible fluids, thereby can be considered to be 'surface active' [5, 15, 16, 4, 17–19]. The surface activity of these colloids is generally not due to their amphiphilic nature, as is otherwise the case for surfactant molecules. The particles can have homogeneous surface chemical composition and properties, and yet still adsorb at interfaces. This is described in section (2.2.1). There is a special class of particles, called Janus particles which are amphiphilic due to the presence of two surface regions with different chemical composition and wetting properties, making them both amphiphilic and surface active. Janus particles will not be considered here.

2.1.4 Surface stress tensor

The surface tension is an isotropic, thermodynamic property of the interface, which is dependent on the surface and bulk compositions of the adjacent phases at a given temperature, as described in section(2.1.1). When surface-adsorbed species form a microstructure, owing to the lateral interactions among the surface-active agents, deformations of the interface can lead to additional stresses, which may be considered as a mechanical response, originating from these interactions [20]. These elastic extra stresses consist of both isotropic and deviatoric components. The *surface stress* is related to the excess work needed to stretch or shear the interface at a constant number of particles and is influenced by the distortion of the interfacial microstructure, with respect to a reference state [21–23]. Thus, a single scalar value $\sigma_{\text{eff}}(\Gamma) = \sigma_0 - \pi(\Gamma)$ [see section(2.1.1); equation(2.9)], is then, no longer sufficient to describe the stress at the complex interface. Instead, a more generalised description requires the use of the surface stress tensor $\boldsymbol{\sigma} = \sigma_{\text{eff}}(\Gamma)\boldsymbol{I} + \boldsymbol{\sigma_e}$. The first term on the right, in addition to being a thermodynamic quantity, can also depend on the kinematics associated with transport exchanges of the surface agents between bulk and interface. This scalar quantity is multiplied with the second order unit surface dyadic tensor $\boldsymbol{I}$. $\boldsymbol{\sigma_e}$ is the elastic extra stress component, comprised of both isotropic and deviatoric extra stresses. Here, the bold letters are used to denote the second order tensors, subscript 'e' for elastic-extra stress components, superscripts 'iso' and 'd' for isotropic and deviatoric components, respectively. The isotropic component is given by the trace of the second order elastic extra stress tensor, $\sigma_e^{\text{iso}} = \text{tr}(\boldsymbol{\sigma_e})/2$, while the deviatoric stresses are given as $\boldsymbol{\sigma_e^{\text{d}}} = \boldsymbol{\sigma_e} - \frac{1}{2}\text{tr}(\boldsymbol{\sigma_e})\boldsymbol{I}$. Therefore, in tensorial notation, the total stress on a complex interface may be written as

$$\boldsymbol{\sigma} = \begin{pmatrix} \sigma^1 & 0 \\ 0 & \sigma^2 \end{pmatrix} = [\sigma_0 - \pi(\Gamma) + \sigma_e^{\text{iso}}]\boldsymbol{I} + \begin{pmatrix} \sigma_e^1 - \sigma_e^{\text{iso}} & 0 \\ 0 & \sigma_e^2 - \sigma_e^{\text{iso}}. \end{pmatrix} \tag{2.10}$$

The indices 1 and 2 denote two orthogonal coordinate directions on the surface.

2.1.5 Emulsions and foams

An emulsion is a dispersed system in which the phases are immiscible or partially miscible liquids [2]. The globules of the dispersed liquid in a typical emulsion are between $1 - 100$ μm in diameter. A foam is a coarse dispersion of gas in liquid [1]. Dispersed systems such as foams or emulsions are thermodynamically unstable, as the specific area arising from the creation of so many divided entities has a higher free energy compared to the flat interface between the constituent bulk phases [18]. The primary processes for instability of these systems, leading them towards complete phase separation, include creaming (for oil-in-water or O/W) or sedimentation (for W/O) in emulsions, which are analogous to drainage in foams.

2.1.6 Interfacial rheology

Interfaces can be subjected to deformation modes which involve curvature changes, shear and dilation [24, 25, 20]. When considering deformations only in the plane of the surface, it is necessary that the stress tensor component normal to a flat interface remains continuous for mechanical equilibrium. Under this condition, the deformation modes available are shear and dilation. In the former, the shape of the surface changes at constant area, whereas in the latter, the area changes at constant shape. The analogous treatment of deformation between interfacial (2D) and bulk (3D) systems is limited [24, 26]. One of the major differences arise due to the interface not being an autonomous system as it is only defined as the boundary between two immiscible bulk phases. Its motion is therefore always coupled to the adjoining bulk phases, making it difficult to define 'intrinsic' surface properties. The definition is only possible for a system in thermodynamic equilibrium, by the introduction of excess quantities and a dividing surface to which these quantities must be assigned. This is not possible in any rheological experiment as equilibrium is necessarily disturbed, leading to the dependence of the results on the methods used.

Another difference is that 3D liquids can be considered incompressible and their molecular volumes as constant. For interfaces with adsorbed surface active species, the area available to individual entities is not constant. In dilational deformation, a new surface can easily be made to appear somewhere, while an older one can disappear somewhere else. Hence, the 2D analogue of the continuity equation cannot be valid for the surface alone.

In presence of adsorbed surface-active agents conferring a microstructure at the interface, there are stresses arising from in-plane relaxation mechanisms and frictional effects between the constituents, whenever such 'complex' interfaces are subjected to deformation. Interfacial rheology defines the functional relationship between stress, deformation and rate of deformation, in terms of coefficients of elasticity and viscosity, by considering the discontinuous system in terms of continuum theory [26, 24].

A clean surface of a pure Newtonian liquid has no surface rheology as the surface tension is not affected by motion within, or outside, the surface. This is because the molecular relaxation processes are so fast that the surface structure and properties remain identical to those for liquids at rest.

2.2 Interfaces stabilised by particles

2.2.1 Free energy of particle detachment from a planar interface

A solid colloidal particle with homogeneous surface properties and composition, when adsorbed at an interface, under equilibrium positions itself according to its wetting

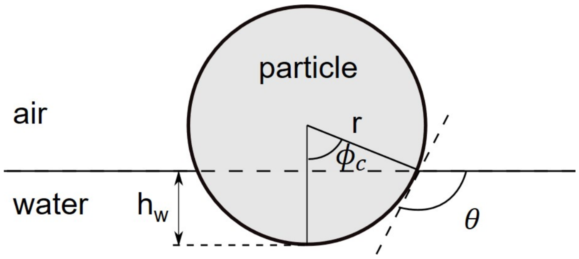

Fig. 2.1 A small spherical colloidal particle with radius r and contact angle θ attached to a planar air-water interface in its equilibrium state.

properties, which is characterised by the contact angle θ. This is the angle between the tangents to the solid surface and the fluid-fluid interface, measured through one of the liquids in each point of the three-phase contact line where the solid and the two fluids meet. The general convention is to measure the contact angle through the more polar liquid [4, 5]. This is illustrated in Figure 2.1 for a particle adsorbed at an air-water interface. The contact angle depends on the surface-free energies, or interfacial tensions at the particle-water, σ_{pw}, particle-air, σ_{pa}, and air-water, σ_{aw}, according to Young's equation [27]

$$\cos\theta = \frac{\sigma_{\mathrm{pa}} - \sigma_{\mathrm{pw}}}{\sigma_{\mathrm{aw}}}. \tag{2.11}$$

In case of aqueous solutions, θ for hydrophilic particles, e.g. metal oxides or any charged particles, is normally $< 90°$ leading to a larger fraction of the particles being submerged in water. For hydrophobic particles, e.g., suitably treated silica, generally $\theta > 90°$.

Hydrophilic or hydrophobic particles, with homogenous surface properties, strongly adsorb to the fluid(α)-fluid(β) interfaces. For instance, consider a spherical particle (s) of radius a, initially in phase α, is adsorbed at the $\alpha\beta$ interface. The new interfaces sα, sβ and $\alpha\beta$ have their respective interfacial tensions associated with them. Ignoring the line tension acting at the three-phase contact line $\alpha\beta$s, adsorption of the particle leads to an area of sα being lost and being replaced by an area sβ interface. More importantly, an area of the planar $\alpha\beta$ interface, normally having high tension, is lost due to the presence of the particle [4]. This lost area depends on θ.

The approach to estimate the energy required to remove a particle from a flat interface, once it is adsorbed at the interface, is described here, having been adapted from [5]. A particle, of arbitrary geometry, attached at a planar air-water interface, as shown in Figure 2.1, may be taken to be an equilibrium state 1. The surface free energy of this system at state 1, $G^{(1)}$, will be the sum of the products of the areas of the particle exposed to the air and water with the respective interfacial tensions between the solid and the bulk phases. Added to this will be the contribution from the area of the air-water interface times its surface tension. That is,

$$G^{(1)} = \sigma_{\text{aw}} A_{\text{aw}}^{(1)} + \sigma_{\text{pw}} A_{\text{pw}}^{(1)} + \sigma_{\text{pa}} A_{\text{pa}}^{(1)}, \tag{2.12}$$

where $A_{\text{aw}}^{(1)}$ is the area of the air-water interface, $A_{\text{pw}}^{(1)}$ and $A_{\text{pa}}^{(1)}$ are the areas of the particle-water and particle-air interfaces respectively, all at state 1. Similarly, when the particle is completely desorbed from the interface, and pushed into either phase, the free energy of the system at this equilibrium state 2 can be defined as $G^{(2)}$. The minimum energy associated with the detachment of the particle is then the difference $\Delta G_{\text{d}} = G^{(2)} - G^{(1)}$, which is called the free energy of particle detachment, and is given as

$$\Delta G_{\text{d}} = \begin{cases} \Delta G_{\text{dw}} = \sigma_{\text{aw}}(A_{\text{c}} - A_{\text{pa}}^{(1)} \cos\theta) & \text{for} \quad 0 \leq \theta \leq 90^\circ \\ \Delta G_{\text{da}} = \sigma_{\text{aw}}(A_{\text{c}} + A_{\text{pw}}^{(1)} \cos\theta) & \text{for} \quad 90^\circ < \theta \leq 180^\circ. \end{cases} \tag{2.13}$$

with $A_{\text{c}} = A_{\text{aw}}^{(2)} - A_{\text{aw}}^{(1)}$ being the area occupied by the particle when it was attached at the air-water interface, and the subscripts 'dw' or 'da' denote that the particle is either desorbed into the bulk water or air phases, respectively.

For a spherical particle, of radius a, the three-phase contact line becomes a circle of radius $r_c = a\sin\theta$. The depth of immersion of the particle in water is h_{w} and the height of the particle exposed to air is $h_{\text{a}} = 2a - h_{\text{w}}$. These quantities are related to the contact angle as

$$h_{\text{w}} = a(1 + \cos\theta). \tag{2.14}$$

The required particle areas, in the above equations become: $A_{\text{p}} = 4\pi a^2$, the total surface area of the particle; and $A_{\text{c}} = \pi(a\sin\theta)^2$ and $A_{\text{pw}}^{(1)} = 2\pi a^2(1 + \cos\theta)$. Thus, equation (2.13) becomes

$$\Delta G_{\text{d}} = \begin{cases} \Delta G_{\text{dw}} = \pi a^2 \sigma_{\text{aw}}(1 - \cos\theta)^2 & \text{for} \quad 0 \leq \theta \leq 90^\circ \\ \Delta G_{\text{da}} = \pi a^2 \sigma_{\text{aw}}(1 + \cos\theta)^2 & \text{for} \quad 90^\circ < \theta \leq 180^\circ. \end{cases} \tag{2.15}$$

Or in a more compact form,

$$\Delta G_{\text{d}} = \pi a^2 \sigma_{\text{aw}}(1 - |\cos\theta|)^2. \tag{2.16}$$

The above derivation assumes the case of a flat interface in the vicinity of the particle. This holds as long as the Bond number for the particle at the interface,

$$Bo = (\rho_\mathrm{w} - \rho_\mathrm{a}) a^2 g / \sigma_\mathrm{aw} \tag{2.17}$$

is much smaller than unity. ρ_w and ρ_a are the densities of water and air respectively, g is the acceleration due to gravity. Also, the particle must be perfectly smooth.

Hence, the minimum energy needed to detach a spherical particle from a flat interface is proportional to the square of the particle radius. For a particle of radius $a = 1$ μm, $\theta = 90°$, the minimum energy needed to desorb the particle into water from the air-water interface with $\sigma_\mathrm{aw} = 72$ mN/m, is $\Delta G_\mathrm{d} = 5.5 \times 10^7$ $k_\mathrm{B}T$. This means particles that are adsorbed at interfaces may be thought of as irreversibly adsorbed. This contrasts with the exchange of soluble surfactants between bulk and interface, over a fast timescale, which occurs as the detachment energies of soluble surfactants is typically $\sim k_\mathrm{B}T$ [4].

2.2.2 Interactions between colloids at interfaces

The adsorption of many colloidal particles at a fluid-liquid interface can lead to the formation of monolayers. Examples include polystyrene or silica particles at air-water interfaces [28, 29, 19] or silica particles at oil-water interfaces [30–32, 4, 5].

The aggregation of colloids in forming an interfacial microstructure is dictated by the interactions among the particles. Analogous to the self-assembly of particles observed in the bulk, interfacial particle networks too range from loose aggregates, with interparticle separation spanning a few particle diameters, to dense close-packed aggregates of touching particles[5]. The interaction energies being much larger than $k_\mathrm{B}T$, cause the system to be kinetically trapped in non-equilibrium states, which are dependent on the history of the sample [33]. In contrast to the interactions among the particles in the bulk, the interactions between particles trapped at the interface are further complicated due to the discontinuity in fluid properties across the interface, and hence, the asymmetry of the environment around the particles. The various interactions between colloids at interfaces consist of van der Waals, electrostatic, hydrophobic and capillary interactions [5, 34, 33], and these are considered below. For simplicity the bulk phases are considered to be polar or non-polar media with physical average properties such as mass density and dielectric constant. For perfectly smooth particles, with size range within a few nanometres to some micrometres, the interface may be considered approximately flat. This approximation helps in simplifying the computation of the interactions between the immersed parts of the particles. The following assumptions are made:

1. The different terms of the interaction energy are additive.
2. Some interactions are estimated using the approximation of a flat interface between two particles, while the interface deformation is accounted for in the analysis of capillary interactions.
3. Interactions occur only between the respective emergent parts and immersed parts of the particles. The interaction between the emergent part of one particle and the immersed part of the other particle has been neglected. This applies for the van der Waals and electrostatic interactions.
4. The interaction potential between spheres $U_{\mathrm{sph-sph}}(h_0)$, with a surface-surface separation h_0, is carried out using the Derjaguin approximation [35, 14, 36, 37]

   $$U_{\mathrm{sph-sph}}(h_0) = \int U_{\mathrm{flat}}(h) dS(h) \tag{2.18}$$

   which makes use of the corresponding interaction potential per unit area between infinite half-spaces, U_{flat}. The integration is to be done over the particle surface, with h_0 as the minimum distance between the colloids, and h is the local distance between a pair of flat surface elements. This approximation is useful for interactions with small range compared to the radius of curvature of the particles.

van der Waals interactions This interaction originates from the fluctuations of electron clouds around atomic nuclei, leading to the formation of temporary or permanent dipoles in neighbouring atoms or molecules, and the resultant attraction between them [14, 5]. For a pair of particles, of radii a, that are partially submerged in both fluids, air (fluid 1) and water (fluid 2), the magnitude of the van der Waals interaction energy depends on the properties of both fluids. Considering an air-liquid interface, an approximate estimate on this interaction between two spheres, at close surface-to-surface separation $r - 2a \ll a$, at the interface, is given as [33]

$$U_{\mathrm{vdW}}(r) \approx -\frac{A_{\mathrm{interface}}}{12} \frac{a}{r-2a}, \tag{2.19}$$

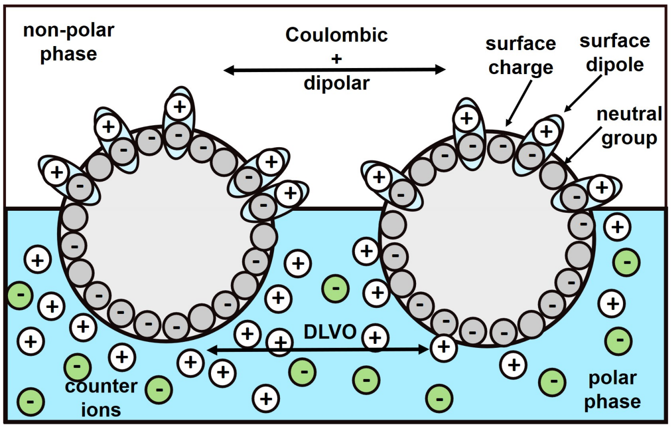

Fig. 2.2 The various interactions between colloids, other than capillary interactions, are assumed to occur through a flat interface. Also, the emergent and immersed parts of one particle are assumed to interact with the respective parts of another particle. This holds true for electrostatic interactions as the surface charges are screened in the polar phase.

where r is the centre-to-centre distance between the particles, and $A_{\text{interface}}$ is the effective Hamaker constant, estimated as

$$A_{\text{interface}} = A_{\text{P1P}} + f^2(3-2f)(A_{\text{P2P}} - A_{\text{P1P}}) \tag{2.20}$$

with A_{P1P} being the Hamaker constant between two particles, across water, while A_{P2P} is that across air. The fractional height of emergence of a particle in air is $f = (2a - h_{\text{w}})/a$, with h_{w} defined in equation (2.14).

Electrostatic interactions Chemical surface groups, on colloidal particles, can dissociate in polar media to form monopoles, or dipoles with counter-ions from the bulk. When preparing a monolayer of such particles, the formation process involves either agitation or a volatile spreading agent. On a microscale, the process is quite turbulent which can result in the particles rotating as well as trapping traces of polar liquid at the surfaces, around the hydrophilic surface charged groups [5]. Thus, a pair of particles trapped at an interface, experience a screened repulsive interaction through their double layers in the polar phase, while Coulombic and dipole-dipole repulsion interactions occur through the non-polar phase [5]. This is schematically presented in Figure 2.2. The charge-charge Coulombic interaction, through the non-polar phase, varies as $U_{\text{cc}} \propto 1/r$, whereas, the dipole-dipole interaction varies as $U_{\text{dd}} \propto 1/r^3$. The former is strongly influenced by the electrolyte concentration in the polar phase, as described below. Hence, for an air-water interface, with sufficient salt concentration in water, the screened Coulomb interaction energy through the aqueous phase and the dipole-dipole contribution through air, can be calculated in the limit where the surface potential ψ is small, such that $e\psi \ll k_{\mathrm{B}}T$, by solving the linearised Poisson-Boltzmann equation [33, 38], to give the electrostatic interaction potential as

$$U_{\text{electrostatic}}(r) = \frac{a_1 k_{\mathrm{B}} T}{3r} e^{-\kappa r} + \frac{a_2 k_{\mathrm{B}} T}{r^3}. \tag{2.21}$$

Here κ is the inverse Debye screening length; and the prefactors a_1 and a_2 determine the strengths of the interactions through the double layer and dipole-dipole interactions, respectively.

Effect of salt addition

Coagulation of particles at the interface is possible for high concentrations of salt [5]. Experimentally, for polystyrene particles trapped at air-water interfaces, the electrolyte concentration in the aqueous phase significantly affects the aggregation of the particles. The critical coagulation concentration (CCC) at interfaces, at which the initial aggregation rate reaches the maximum value, is usually found to be two orders of magnitude above the one in bulk dispersions [5]. The reason for aggregation is believed to be due to the dissociated monopolar charges, in the non-polar phase, being neutralised by high counter ion concentration inside the hydration water layer. Hence, at high salt concentrations, the dipole-dipole repulsive interaction plays a strong role in controlling the aggregation process. The differences in aggregation at oil-water and air-water interfaces are expected to be due to higher surface charge and dipolar concentrations on the particles in the former system.

It is also worth noting that depending on the salt and the free energy of formation of the electric double layer in the polar phase, ΔG_{DL}, the surface free energy at the particle surface becomes [33] $\sigma_{\mathrm{pw}} = \sigma_{\mathrm{pw},0} + \Delta G_{\mathrm{DL}}$, where $\sigma_{\mathrm{pw},0}$ is the particle-water surface tension in absence of the double layer. Substitution of σ_{pw} into equation (2.11) gives $\cos\theta = \cos\theta_0 - \Delta G_{\mathrm{DL}}/\sigma_{\mathrm{pw}}$. Since, the formation of the double layer is spontaneous, $\Delta G_{\mathrm{DL}} < 0$, making $\theta < \theta_0$, that is, the contact angle of the particle is reduced due to the double layer.

Hydrophobic interaction

The presence of a hydrophobic surface in a polar liquid gives rise to local restructuring of the solvent [5, 14], leading to the attraction between such surfaces, which decays exponentially with surface separation. For a pair of hydrophilic particles, the interaction becomes repulsive as there is a layered arrangement of the solvent molecules at the surface of the particles. These structural or entropic interactions are dependent both on the chemical properties of the interface as well as the surface roughness. Experimentally, the hydrophobic interaction is detectable for $\theta > 64°$, while the hydrophilic repulsion becomes important when $\theta < 15°$ [5]. The Derjaguin approximation is valid as this is a short-range interaction and the interaction potential between two planes is [5]

$$U_{\text{flat}}(h) = W_0 \exp(-\frac{h}{\lambda_0}) \tag{2.22}$$

where W_0 and λ_0 are constants related to the strength and range of the interaction. Typically, for hydrophilic particles, $W_0 = 3 - 30$ mJ/m^2 and $\lambda_0 = 0.6 - 1.1$ nm.

Capillary interactions

For colloidal particles, the deformation of the interface due to gravity is negligible. However, the roughness or chemical heterogeneity, and the resulting non-uniform wetting of the particles, can induce an irregularity of the three-phase contact line. These undulations lead to deformations of the fluid interface and when two particles are close by, they re-orient to minimise the potential energy arising due to the local curvature [31, 34, 5]. After reorientation, there is attraction between the particles to further reduce the local interfacial curvature. This may be considered as an interaction between capillary multipoles. Capillary quadrupoles give the major contribution to the pair potential of capillary attraction, and this is maximum at the most favourable orientation of the particles, as given by [31]

$$U_{cap}(r) = -\frac{3\pi\sigma\delta^2(a\sin\theta)^4}{4r^4}, \tag{2.23}$$

where δ is the amplitude of the three-phase contact line undulations.

2.2.3 Curvature of monolayers

Depending on the wetting behaviour of the particles, as determined by θ, the monolayers will curve such that the larger area of the particle surface remains on the external side of the locally concave interface [4, 39]. Thus, for $\theta < 90°$, air-in-water or oil-in-water dispersed systems will be favoured such as particle-coated bubbles or O/W particle-coated emulsions. While for $\theta > 90°$, water-in-air or water-in-oil interfaces will be preferred as happens for particle-coated liquid marbles [39, 40] or aerosols and W/O emulsions, respectively.

2.2.4 Pickering bubbles

The fact that finely divided solid particles can significantly enhance the stability of emulsions has been known since the beginning of the 20th century [15, 16, 4, 5]. These are termed as ‘Pickering emulsions’, despite the fact that the phenomenon had been described earlier by Ramsden in 1904 [15]. Similarly, particles have been known to stabilise bubbles [15, 4, 18, 5]. These particle-stabilised bubbles are referred to as armoured bubbles or ‘Pickering bubbles’.

Particle-coated bubbles exhibit remarkable stability, with bubbles resisting coarsening, coalescence and drainage in foams over a period of months [41–43, 5, 13]. There are several possible reasons for this. One, small particles with strong aggregation form a cohesive monolayer at the interface which results in an armour that hinders gas dissolution. Two, the local curvature between the particles can diminish or become negative, resulting in decreased Laplace overpressure inside the bubble [44]. A third mechanism predicts that the monolayer imparts an elasticity to the interface which resists compression while the bubble tends to shrink [42].

2.3 Buckling behaviour of particle-coated microbubbles

There have been several investigations on the mechanisms responsible for the remarkable stability of armoured bubbles in resisting dissolution [42, 18, 44, 5]. One such mechanism involves the particles in the monolayer resisting the compression as a bubble tends

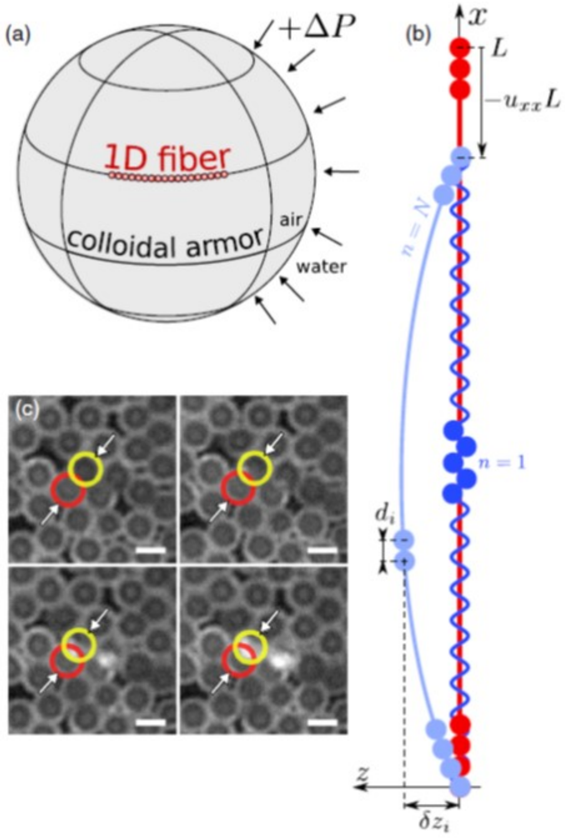

Fig. 2.3 Illustration of model describing the deformations of a colloidal armour on a bubble. (a) Sketch of the colloidal armour with an arbitrary 1D fibre composed of particles, highlighted in red. (b) Sketch of the buckling of the fibre. The red line shows the undeformed initial state of the fibre of length L; the blue lines are the deflected sinusoidal states. Light blue is the lowest frequency mode ($n = N$); dark blue is the highest frequency mode ($n = 1$) with alternating beads. (c) Detail from fluorescence micrographs of the buckling event, where the beads overlaid in red and yellow overlap and come out of the plane of the monolayer. The direction of the compression is indicated by the white arrows. Scale bars are 5 μm. Adapted from reference [45], which is available under the terms of the Creative Commons Attribution 3.0 Licence (CC BY 3.0).

to dissolve. This problem was taken up through an experimental study by Taccoen, et. al. 2016 [45], where the dislocations of particles in the bubble armour were monitored while the ambient pressure was varied. A theoretical description was also provided to explain the observations. The experiments involved trapping individual colloid-coated bubbles in a region with a conical roof, while it was observed from underneath using a microscope. The hydrostatic pressure around the bubble in the zone was systematically controlled to compress or expand the bubble. Image analysis was used to track individual particles and how they interacted with one another as the interface underwent compression or expansion. The model and its implications are briefly described here.

A bubble of radius R_0 neither shrinks nor grows for an equilibrium ambient pressure $P_{\text{eq}}(R_0)$. If the external pressure is increased to $P = P_{\text{eq}} + \Delta P$, then the energy variation due to gas dissolution, per unit area, may be expressed as [45]

$$W_{\text{diss}} = -\Delta P \delta R, \tag{2.24}$$

for a radius variation of $\delta R = R_0 - R$. In presence of a particle monolayer at the interface, upon compression the particles are close packed, and owing to their high desorption barrier, there is a competition between the energy gained from gas dissolution with the energetic cost of displacing individual particles out of the interface. The problem may be recast to the study of a 1D fibre of particles, where the fibre represents an arbitrary line of N rigid spheres, of diameter $p = 2a$, of length L, taken on the shell surface of the bubble. This is schematically presented in Figure 2.3(a). The particles are trapped at the air-water interface due to the surface tension σ_{aw}, which results in a radial restoring force whenever a particle is displaced from its equilibrium position, by a displacement z as shown in Figure 2.3(b). Thus, when a particle is displaced from the interface and into the liquid, by a depth z, then the energy difference between the particle at the interface minus the energy of the same particle completely immersed in the liquid is given as [28, 45]

$$\Delta E = \pi p z(\sigma_{\text{pa}} - \sigma_{\text{pw}} - \sigma_{\text{aw}}) + \pi z^2 \sigma_{\text{aw}}. \tag{2.25}$$

This is valid for a flat interface, yet is physically different from equation (2.16). In the former [equation (2.25)], the energetic cost associated with displacement z of the particle is estimated while it still remains attached to the interface. Whereas, equation (2.16) gives the estimate for the minimum energy required for the detachment of the particle from the interface. The equilibrium position of the particle is given by the Young-Dupré relation as $z_0 = (1 - \cos\theta)p/2$, and the depth of the energy well of the particle in this equilibrium position is $\Delta E_{\text{min}} = -\pi \sigma_{\text{aw}} z_0^2$. Therefore, a capillary potential for the i-th particle in the fibre, for a displacement $z_i = z - z_0$ normal to the interface, may be defined as $w_i = \Delta E - \Delta E_{\text{min}}$, or,

$$w_i = \pi \sigma_{\text{aw}} \delta z_i^2. \tag{2.26}$$

The compression of the armour will cause a longitudinal compression of the fibre, resulting in a uniaxial strain u_{xx}, which will cause the particles to move out of the plane of the shell, while the capillary restoring force will oppose the displacements. A sinusoidal profile of amplitude A may be assumed to describe the out-of-plane displacements as

$$\delta z_i = A\cos\left(\frac{\pi i}{n}\right) \quad \text{with } n \in \mathbb{N}, \quad n \in [1, N], \tag{2.27}$$

as shown in Figure 2.3(b), for different n. The longitudinal (x-axis) distance between two adjacent particles i and $i+1$ at different deflections (z-axis) may be calculated using the Pythagoras theorem, and in the limit $A \ll p$, the uniaxial strain can be expressed as

$$u_{xx} = \frac{\sum\limits_{i=1}^{n} d_i - pn}{pn} = -\frac{nA^2}{2p}\left[1 - \cos\left(\frac{\pi}{n}\right)\right]. \tag{2.28}$$

Thus, the energy cost per unit area, W_{shell}, of the deformed shell can be estimated by summing the energies required to displace each particle over one period of sinusoidal deflection. Combining equations (2.26),(2.27) and (2.28), with the uniaxial strain u_{xx} in any fibre of the shell given as $u_{xx} = \delta R/R$, we get

$$W_{\text{shell}} = \sum_{i=1}^{n} \frac{w_i}{n \times p^2} = -\frac{\pi\sigma_{\text{aw}}\delta R}{R[1 - \cos(\frac{\pi}{n})]}. \tag{2.29}$$

The threshold pressure above which mechanical stability is lost is obtained by equating W_{shell} and W_{diss}, so that

$$\Delta P_n^* = \frac{\pi\sigma_{\text{aw}}}{R[1 - \cos(\frac{\pi}{n})]}, \tag{2.30}$$

which predicts that different threshold pressures exist depending on the buckling mode n, with the lowest threshold ΔP^* being attained for $n = 1$, where, $\Delta P_1^* = \pi\sigma_{\text{aw}}/(2R) \simeq 1.57\sigma_{\text{aw}}/R$, which corresponds to the smallest possible wavelength.

Consequences of buckling expressions for a discrete *'shell'* The predictions of the model, described above, has some readily apparent salient features. First, the threshold pressure is insensitive to the particle size. Second, $n = 1$ is predicted to be the most unstable mode, which corresponds to the highest available spatial frequency with alternating particles [Figure 2.3(b)]. Practically, this leads to the localised dislocations between adjacent particles at the onset of instability. Once this happens, the shell is expected to lose its mechanical stability, which is seen in Figure 2.3(c), where buckling proceeds through localised events that lead to total collapse. This contrasts with the expectation from the case of a continuous elastic hollow shell, where deformation energy cost is proportional to the squared mean curvature of the deflection, that is $W_{\text{shell}} \propto u_{xx}/n^2$, making $n = 1$ as having the highest energetic cost, while larger values of n, leading to long wavelength of deformation, as having the least energetic cost. This illustrates that treating a particulate monolayer as a continuous shell may not give appropriate predictions.

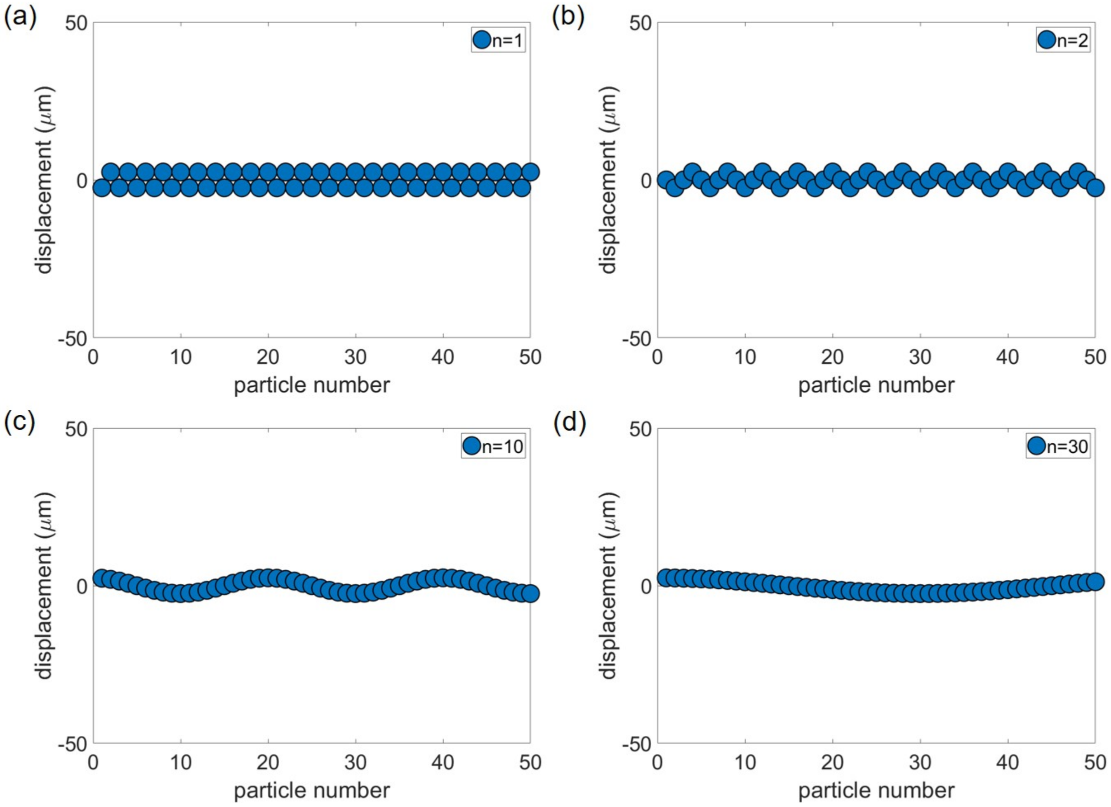

Fig. 2.4 **Bending mode n of particle-fibre with $N = 50$ particles.** The x-axis denotes particle number i, while the y-axis indicates displacement in μm units for a set amplitude of $A = 2.5$ μm. (a) For $n = 1$ all particles are staggered alternately. (b) For $n = 2$ the particles appear to overlap, while the bending wavelength λ has increased. In reality the overlap means that the particles are staggered as for $n = 1$, but are also simultaneously experiencing a longer bending wavelength. Similarly the bending modes for (c) $n = 10$ and (d) $n = 30$ are shown.

A MATLAB [MATLAB. version 9.4.0.813654 (R2018a). Natick, Massachusetts: The MathWorks Inc.] script was written to implement the model, to visualise the buckling modes for a fibre containing $N = 50$ particles for various modes $n = 1, 2, 10$ and 30. These are shown in Figure 2.4. Higher the mode, longer is the bending wavelength, and higher is the energy cost. That is to say higher pressures will lead to long wavelength buckling. This is qualitatively understood by keeping the marker size constant for the circles representing the particles. For $n = 1$, the particles become staggered and for $n = 2$, the particles appear to overlap [Figure 2.4(b)]. In reality it means that for any mode $n > 1$, the particles will remain staggered as for $n = 1$, but will also undergo compaction that will cause the interface to bend with a longer wavelength. As the bending wavelength increases, such that the ratio of the particle size to the wavelength a/λ becomes smaller [as for $n = 10$ or 30 in Figures 2.4 (c-d)], the compression axis of local particles will appear straight. This means more particles will be compacted laterally in a linear direction for a larger bending wavelength λ.

2.4 Interfacial rheometry using pendant drops

2.4.1 Pendant drop tensiometry

The shape of drops or bubbles depends on the balance between gravity and surface tension. This idea was first used by Worthington in 1881 [46, 20], where he projected and sketched the contour of the silhouette of a pendant drop on a paper screen, and evaluated the curvature using a graphical method. The balance between hydrostatic pressure at a given height and the Laplace pressure due to the curved interface can be expressed by the Young-Laplace equation:

$$(\kappa_1 + \kappa_2)\sigma = p - \Delta\rho g z, \tag{2.31}$$

where κ_1 and κ_2 are the two principal curvatures of the interface at a height z, directed opposite to gravity, with $z = 0$ being the attachment point of the drop to the needle, p the pressure difference over the interface at $z = 0$, $\Delta\rho = \rho_\mathrm{l} - \rho_\mathrm{a}$ the difference between the densities of the liquid ρ_l and air ρ_a. g is the acceleration due to gravity. To estimate the surface tension, an algorithm is required [47] to (i) sample the contour coordinates of the drop; (ii) compute a drop profile based on an initial guess value of σ and using equation (2.31); (iii) compare the sampled drop contour with the computationally

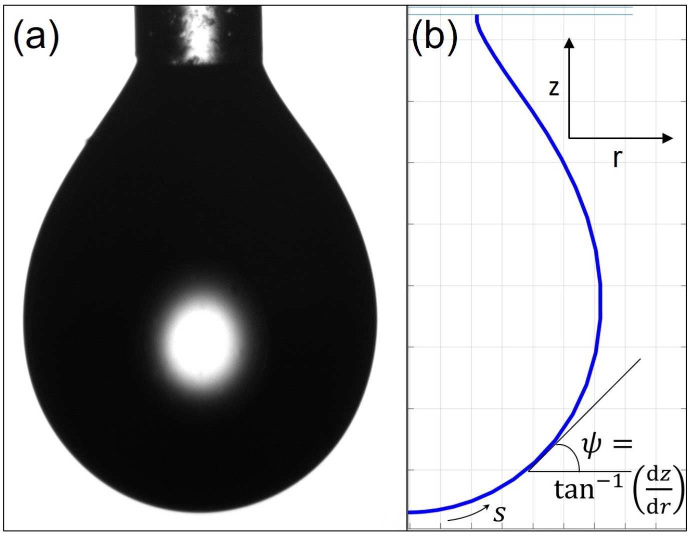

Fig. 2.5 Sampling the contour of a water pendant drop. (a) Original image and (b) its sampled coordinates and representing the coordinate variables (s, ψ) and (r, z).

obtained drop profile; and (iv) iteratively update σ until the error between the two drop profiles is minimised. This method of estimating the interfacial tension between two fluids is known as pendant drop tensiometry [48, 20] or drop shape analysis (DSA). A cylindrical coordinate system is used to define the drop contour, with a radial axis r, azimuthal angle ϕ, and a vertical axis z oriented opposite to the direction of gravity. The experimentally acquired contour is sampled as (r, z) coordinates. This is converted into arc-length s, such that a small arc element is defined as $\mathrm{d}s = \sqrt{\mathrm{d}r^2 + \mathrm{d}z^2}$, and the tangent angle to the arc ψ. This choice of defining the contour avoids assigning $r(z)$ or $z(r)$ to become singular or multi-valued as the arc extends from $s = 0$ at the drop apex to the needle tip, with the assumption of axisymmetry about the drop axis. Thus, the coordinate systems are related by:

$$\frac{\mathrm{d}r}{\mathrm{d}s} = \cos\psi, \quad \frac{\mathrm{d}z}{\mathrm{d}s} = \sin\psi. \tag{2.32}$$

The curvatures are defined as

$$\kappa^s = -\frac{\mathrm{d}^2 r/\mathrm{d}s^2}{\sqrt{1 - (\mathrm{d}r/\mathrm{d}s)^2}} = \frac{\mathrm{d}\psi}{\mathrm{d}s}, \quad \kappa^r = \frac{1}{r}\frac{\mathrm{d}z}{\mathrm{d}s} = \frac{\sin\psi}{r}. \tag{2.33}$$

An example of a water drop suspended from a glass capillary, of which the sampling is done is schematically shown in Figure 2.5 with the coordinate system.

2.4.2 Drop shape fitting elastometry

Drop shape analysis has also been applied to bubbles/drops coated with surface-active agents to measure the effective surface tension. When the drop interfaces exhibit solid-like elastic behaviour due to the presence of interfacial structure, the analysis can be extended to extract the mechanical properties using an approach called *drop shape fitting elastometry* or DSFE. This method involves using rheological constitutive models along with the Young-Laplace equation and was developed by [49, 50, 20]. Assuming purely elastic behaviour of the interface, the 2D solid can be described by a set of elastic parameters [49, 20, 50, 25]. The elastic material parameters include: a 2D Young's modulus Y_{2D}, Poisson ratio ν, compression and shear moduli E_{d} and G_{2D} respectively. They are related [20] as:

$$E_{\mathrm{d}} = \frac{Y_{\mathrm{2D}}}{2(1-\nu)}, \quad G_{\mathrm{2D}} = \frac{Y_{\mathrm{2D}}}{2(1+\nu)}, \quad Y_{\mathrm{2D}} = \frac{4G_{\mathrm{2D}}E_{\mathrm{d}}}{G_{\mathrm{2D}}+E_{\mathrm{d}}}, \quad \nu = \frac{E_{\mathrm{d}}-G_{\mathrm{2D}}}{E_{\mathrm{d}}+G_{\mathrm{2D}}}. \tag{2.34}$$

In presence of the elastic-extra stresses, the Young-Laplace equation is generalised to include the meridional and hoop stresses, that are not necessarily equal, and is given by

$$(\kappa^s\sigma^s + \kappa^r\sigma^r) = p - \Delta\rho g z, \tag{2.35}$$

with κ^s and κ^r being the meridional and hoop curvatures respectively. The stress components, σ, with superscripts s and r denote the meridional and hoop components, respectively. There now being two stresses, an additional equation is needed, which is obtained from the stress balance in the meridional direction [51, 20]

$$r\frac{\mathrm{d}\sigma^s}{\mathrm{d}s} = (\sigma^r - \sigma^s)\cos\psi. \tag{2.36}$$

When a drop with a complex interface is elastically relaxed, that is, the thermodynamic isotropic stress is non-zero, while the elastic-extra stresses are zero, this state may be defined as a reference state. The drop shape obeys the Young-Laplace equation (2.31). When the drop is deflated, meridional and hoop stretch factors, λ^s and λ^r respectively, can be defined with respect to the reference state. The compressional strain is then $\lambda^s\lambda^r - 1$, which is resisted by the dilational modulus E_{d}, while the shear stress $\lambda^s/\lambda^r - 1$ is resisted by the interfacial shear modulus G_{2D}. The deformation of a surface element with respect to the reference state, during compression is schematically represented in Figure 2.6, where the starred quantities denote variables in the reference state.

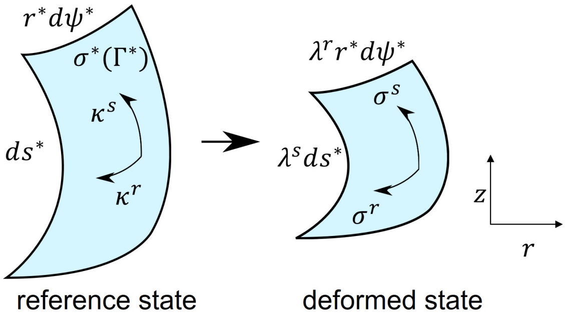

Fig. 2.6 Schematic of an area element on the pendant drop with a complex interface. The reference state has an isotropic stress $\sigma^*(\Gamma^*)$ of thermodynamic origin. It undergoes deformation with stretch factors λ^s and λ^r in the meridional and hoop directions respectively, leading to non-isotropic stress components σ^s and σ^r.

To accommodate for the finite deformations encountered in an experimental setting, and as required for accurately discerning between two states via image analysis, a finite strain measure is required. For this reason, the Hencky strain measure [52] is used to incorporate modest strain non-linearities [20, 53, 52], which is symmetric with respect to extension and recompression. Using the Hencky strain measure, the isotropic dilational stress is given by:

$$\sigma^{\text{iso}} = -\pi(\Gamma) + \frac{1}{2}\text{tr}(\boldsymbol{\sigma_e}) = E_{\text{d}} \ln(\frac{a}{a^*}) = E_{\text{d}} \ln(\lambda^s \lambda^r), \tag{2.37}$$

where a is the area of the new state, while a^* is the area of the reference state. The deviatoric stresses arise due to changes in the aspect-ratio of a surface element, at constant area. This stress is related to the deformation as:

$$\sigma_e^s - \frac{1}{2}\text{tr}(\boldsymbol{\sigma_e}) = G_{\text{2D}} \ln(\frac{\lambda^s}{\lambda^r}), \quad \sigma_e^r - \frac{1}{2}\text{tr}(\boldsymbol{\sigma_e}) = G_{\text{2D}} \ln(\frac{\lambda^r}{\lambda^s}). \tag{2.38}$$

Using these equations, a pseudo-linear Hookean model can be defined as:

$$\sigma^s - \sigma^* = E_{\text{d}} \ln(\lambda^s \lambda^r) + G_{\text{2D}} \ln(\frac{\lambda^s}{\lambda^r}), \tag{2.39}$$

$$\sigma^r - \sigma^* = E_{\text{d}} \ln(\lambda^s \lambda^r) + G_{\text{2D}} \ln(\frac{\lambda^r}{\lambda^s}). \tag{2.40}$$

Here, σ^* denotes the isotropic surface tension of the elastically relaxed reference state, so that $\sigma^* = \sigma_0 - \pi(\Gamma^*)$.

Hence, to estimate the relevant rheological parameters, the algorithm used in pendant drop tensiometry will need to include additional fitting parameters, and equations (2.35),(2.36),(2.39) and (2.40) will have to be solved to predict a drop shape which will be compared to the experimental drop shape. The iterations will continue until the fitting error is minimised and the elastic parameters E_d and G_2D can be determined. Pressure measurement within the drop can simplify the problem and improve accuracy, particularly when small drops are used to amplify the pressure signal [20].

2.4.3 Gibbs elasticity

Simple interfaces may be defined as those where there are no viscous or elastic contributions to the interfacial stress, as happens for clean or loosely packed interfaces [25]. However such interfaces can still exhibit an apparent elasticity due to changes in surface coverage, or excess concentration Γ, with area compression/expansion as $\sigma = \sigma(\Gamma)$. This can happen due to diffusive exchange of surface-active agents between bulk and interface and is dependent on the kinetics of adsorption/desorption [26]. Further, diffusive transport towards curved interfaces may be curvature-dependent. Hence, imposing a time-dependent deformation can lead to a dynamic surface tension. Under this situation, the ratio of the change in surface tension to the areal strain gives rise to an apparent elasticity, but it is more representative of diffusivity and surface coverage of the material rather than the true mechanical response of the interface. So, it differs from the dilational or compression modulus E_d, which appears in the constitutive models to describe the interface [equations (2.39) and (2.40)]. Only in-plane relaxation processes that correspond to a response of the interfacial microstructure to deformation lead to true material functions [25, 54]. For soluble surfactants, both transport and material properties play a role and the apparent elasticity includes both contributions. In experiments, therefore, the measurement of a single quantity, σ, which has many components [as is evident in section (2.1.4): equation (2.10)], it is difficult to distinguish between the two types of elasticities. Material functions should depend only on strain or strain-rate, rather than geometry of the interface.

In absence of mass transfer between bulk and interface, for an insoluble monolayer with $\Gamma \times A =$ constant, and without in-plane relaxation processes, the dynamic surface tension will be in phase with the imposed deformation. For small deformations, this leads to a constant elastic modulus that is only dependent on surface coverage

$$E_{\text{Gibbs}} = -\frac{\mathrm{d}\sigma}{\mathrm{d}\ln\Gamma}. \tag{2.41}$$

E_{Gibbs} is known as the Gibbs' modulus. In absence of in-plane relaxation processes, this is entirely determined by the thermodynamics of the interface, which depends on surface composition, or transport of material between bulk and interface, or both. This contrasts with E_{d}, which accounts for the in-plane relaxations and relates the elastic-extra stresses, within the microstructure, and deformation of the interface through a constitutive model. The distinction between the two types of elasticities are not always clearly made in literature.

This has frequently been the case, in the past, where the effective surface tension was measured, of coated interfaces, using pendant drops, using only the Young-Laplace equation (2.31), without coupling with a constitutive relationship. The obtained apparent elasticity was then, the Gibbs' elasticity, using equation (2.41), instead of the material function E_{d}. This issue was highlighted by [49, 50].

2.5 Theory of bubble dissolution

The rate of dissolution of a clean bubble in an unbounded liquid was first derived by Epstein and Plesset in 1950 [55]. It is assumed that a bubble containing gas of molecular weight M_{w} is suspended in the bulk of a liquid medium of density ρ and surface tension σ at a constant temperature T. The gas diffusivity in the liquid is D, while the solubility is dictated by the Henry's constant $k_{\text{H}} = c_s/P_0M_{\text{w}}$, where it is assumed that $c = c_{\text{s}}$ at the interface $r = R$ and $c = c_i$ at $r \to \infty$, and P_0 is the ambient pressure. The rate of change of the bubble radius R at time t is given as

$$\frac{\mathrm{d}R}{\mathrm{d}t} = -Dk_{\text{H}}R_{\text{g}}T\left[\frac{1 - f + 2M_{\text{w}}\sigma/(\rho R_{\text{g}}TR)}{1 + 4M_{\text{w}}\sigma/(3\rho R_{\text{g}}TR)}\right]\left(\frac{1}{R} + \frac{1}{\sqrt{\pi D t}}\right), \tag{2.42}$$

where R_{g} is the universal gas constant, and $f = c_i/c_{s,0}$ is the ratio of the initial dissolved gas to the concentration at saturation where initially at $t = 0$, gas concentration is $c_{s,0}$ at a planar interface. The equation predicts that even at saturated conditions, i.e., when $f = 1$, the bubble still dissolves due to surface tension.

Assuming a steady state by neglecting the time dependent term $1/\sqrt{\pi D t}$, and integrating the above equation from the initial radius $R(t=0)=R_0$ to $R(t=t_\mathrm{d})=0$, the dissolution time t_d can be estimated for $f=1$ as

$$t_\mathrm{d} = \frac{R_0^2}{3Dk_\mathrm{H}}\left(\frac{\rho R_0}{2M_\mathrm{w}\sigma} + \frac{1}{R_\mathrm{g}}\right). \tag{2.43}$$

Both the dissolution rate and time have been experimentally validated [56]. For bubbles that are near a boundary, as happens when a bubble rests against a gas impermeable horizontal wall due to buoyancy, an empirical correction factor of $\ln 2 = 0.693$ has been found to capture the dissolution times [56]. The effective dissolution time is given by $t_\mathrm{eff} = t_\mathrm{d}/\ln 2$.

2.5.1 Effect of varying temperature on bubble dissolution

If the temperature of the medium varies, then the temperature dependence of $\sigma(T)$, $\rho(T)$, $D(T)$ and $k_\mathrm{H}(T)$ needs to be taken into account. To account for these changes, equation (2.42) may be modified [57] to express the dissolution rate as

$$\begin{aligned}\frac{\mathrm{d}R}{\mathrm{d}t} &= -Dk_\mathrm{H}R_\mathrm{g}T\left(1 - f + \frac{2M_\mathrm{w}}{\rho_0 R_\mathrm{g}T}\frac{2\sigma}{R}\right)\left(1 + \frac{2M_\mathrm{w}}{3\rho_0 R_\mathrm{g}T}\frac{2\sigma}{R}\right)^{-1}\\ &\quad\times\left(\frac{1}{R} + \frac{1}{\sqrt{\pi D t}}\right) + \left[\frac{R_\mathrm{g}T\rho_0 R/M_\mathrm{w} + 2\sigma + 2T(\mathrm{d}\sigma/\mathrm{d}T)}{3T(R_\mathrm{g}T\rho_0/M_\mathrm{w} + 4\sigma/3R)}\right]\frac{\mathrm{d}T}{\mathrm{d}t},\end{aligned} \tag{2.44}$$

where

$$\rho_0 = \frac{P_0 M_\mathrm{w}}{R_\mathrm{g}T} \tag{2.45}$$

is the density of the gas at temperature T. Depending on the liquid, the Henry's constant may increase or decrease with temperature. In water the air solubility decreases with T, so a bubble grows with increasing temperature [57]. Whereas in alkanes, k_H increases leading to faster bubble dissolution at higher temperatures [58].

2.5.2 Effect of bulk and interfacial rheology on bubble dissolution

The bubble dissolution rate is modified by the rheological properties of both the bubble interface and surrounding bulk medium, as has been theoretically considered by Kloek, et. al. 2001 [59].

Effect of interfacial elasticity

For a bubble of instantaneous area $A = 4\pi R^2$ at radius R, the dilational elasticity is defined as [24, 59]

$$E_\mathrm{d} = A\frac{\mathrm{d}\sigma}{\mathrm{d}A} = \frac{2}{R}\frac{\mathrm{d}\sigma}{\mathrm{d}R} \tag{2.46}$$

and the interfacial viscosity is [59]

$$\eta_\mathrm{d} = A\frac{\mathrm{d}\sigma}{(\mathrm{d}A/\mathrm{d}t)}. \tag{2.47}$$

Here it is assumed that the interfacial adsorbed agents do not have in-plane interactions, and therefore, E_d depends only on the surface concentration at a given bubble radius, without the consideration of transport exchanges between bulk and interface. This then, relates to the Gibbs' modulus, defined in equation (2.41). Usually the interfacial elasticity increases by the extent of compression of the bubble from the initial radius R_0 as the interfacial layer undergoes compaction until collapse of the adsorbed layer. Assuming E_d to be proportional to the amount of adsorbed species per unit surface area Γ, it can be expressed as a function of the relative bubble radius $\varepsilon = R/R_0$ and initial elasticity $E_0 = E_\mathrm{d}(R = R_0)$

$$E_\mathrm{d} = E_0\left(\frac{R_0^2}{R^2}\right) = \frac{E_0}{\varepsilon^2}. \tag{2.48}$$

Hence, the radius dependence of the effective surface tension is given as

$$\sigma(R) = \sigma_0 + E_0\left(1 - \frac{R_0^2}{R^2}\right), \tag{2.49}$$

where $\sigma_0 = \sigma(t = 0)$ is the initial effective surface tension when $R = R_0$. Incorporating this radius-dependent effective surface tension into equation (2.42), with $f = 1$ and

$\frac{\mathrm{d}R}{\mathrm{d}t} = 0$, it can be derived [59] that the final relative radius at which bubble dissolution stops completely is

$$\varepsilon = \sqrt{\frac{E_0}{E_0 + \sigma_0}}. \tag{2.50}$$

This predicts that higher the value of the initial dilational elasticity, lesser is the extent to which the bubble shrinks before attaining complete stability against dissolution. It is independent of the initial bubble radius R_0.

Along similar lines, often the Gibbs stability criterion is cited in literature [19, 59] as follows. The general case for a bubble when $\sigma = \sigma_0$ is independent of bubble size, the bubble shrinks due to the increasing Laplace pressure inside the bubble, as

$$\frac{\mathrm{d}P}{\mathrm{d}R} = -\frac{2\sigma_0}{R^2} < 0. \tag{2.51}$$

But when an interfacial elasticity exists and $\sigma = \sigma(R)$,

$$\frac{\mathrm{d}P}{\mathrm{d}R} = -\frac{2\sigma(R)}{R^2} + \frac{4E_\mathrm{d}}{R^2}. \tag{2.52}$$

So, as long as $E_{\mathrm{d,max}} \geq \sigma(R)/2$, a bubble becomes stable against dissolution.

Effect of interfacial viscosity

When the interface exhibits purely viscous behaviour, the effect can be incorporated into the bubble dissolution rate equation (2.42) through $\sigma(R)$ described as

$$\sigma(R) = \sigma_0 + \frac{2\eta_\mathrm{d}}{R}\frac{\mathrm{d}R}{\mathrm{d}t}. \tag{2.53}$$

Interfacial viscosity alone cannot stop bubble shrinkage but can only delay it. The delay is significant only for very high values of η_d and can be understood by comparing the interfacial viscous stress to the interfacial tension. To retard shrinkage it is required that

$$-\frac{2\eta_\mathrm{d}}{R}\frac{\mathrm{d}R}{\mathrm{d}t} > \sigma_0 \tag{2.54}$$

or,

$$\frac{\eta_\mathrm{d}}{\sigma_0} > \frac{-t}{2\ln\varepsilon}. \tag{2.55}$$

Using typical values for food systems $\sigma_0 = 30$ mN/m, $R_0 = 100$ μm and $D = 10^{-10}$ m$^2/s$, if it is desired that shrinkage is delayed by interfacial viscosity effects, and is dominant after the bubble has shrunk to $\varepsilon = 0.9$, then it is required that η_d/σ_0 is 1.9×10^5 s.

Effect of bulk elasticity

In a scenario where only the bulk exhibits purely elastic behaviour, the pressure at the bubble boundary $r = R$ is given by

$$P_0 + \frac{2\sigma}{R} - \tau_{rr} = \frac{nR_\mathrm{g}T}{V}. \tag{2.56}$$

Here n is the number of moles of gas in the bubble, V its volume and τ_{rr} is the excess radial bulk stress tensor. For a single bubble in an infinite elastic medium, with bulk elastic modulus G, the excess radial bulk stress may be expressed as

$$\tau_{rr} = 2G\frac{R_0}{R} + \frac{G}{2}\frac{R_0^4}{R^4} - \frac{5}{2}G. \tag{2.57}$$

This shows that whenever the bubble tends to shrink (or grow), there will be an excess stress opposing the movement of the interface. Equations (2.56) and (2.57) may be incorporated into equation (2.42) through the term $\rho(R)$, which is the radius-dependent density of the gas within the bubble.

Bulk elasticity can arrest bubble dissolution, even when interfacial effects are absent. At saturated conditions, $f = 1$, the stability criterion can be derived as

$$\frac{GR_0}{\sigma_0} = \frac{4\varepsilon^3}{1 - 5\varepsilon^4 + 4\varepsilon^3}. \tag{2.58}$$

With increasing values of G, the bubble shrinks to a lesser extent before attaining stability. If the interface, too, exhibits elastic behaviour, then in equation (2.56), $\sigma = \sigma(R)$ [as given by equation (2.49)]. The combined effects of interfacial and bulk elasticity in stabilising individual bubbles in foams are summarised in Figure 2.7, generated using a MATLAB script, where the rheological parameters used cover a range typical of food systems [59], with $\sigma_0 = 30$ mN/m.

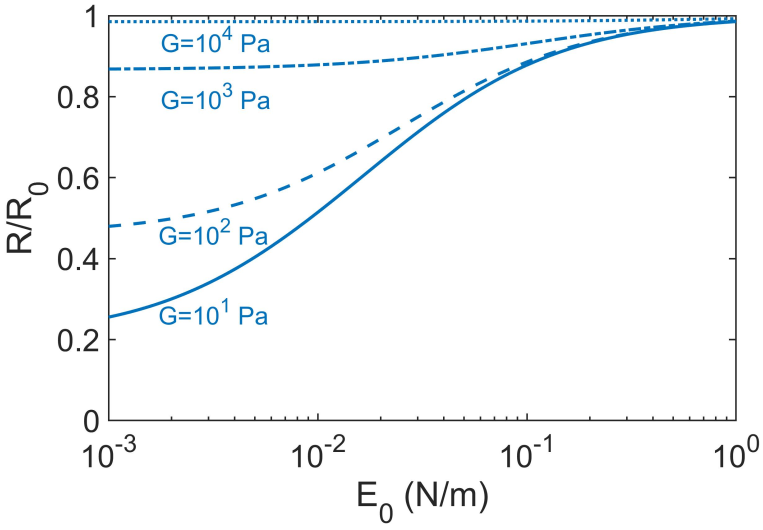

Fig. 2.7 Combined effects of interfacial elastic modulus $E_\mathrm{d}(R) = E_0(R_0^2/R^2)$ and the bulk modulus G on bubble dissolution. The lines indicate the relative radius at which a bubble becomes stabilised. The bulk moduli are indicated in Pa.

Effect of bulk viscosity

When the bulk is a purely viscous liquid with viscosity μ, the bulk excess stress becomes

$$\tau_{rr} = -\frac{4\mu}{R}\frac{\mathrm{d}R}{\mathrm{d}t}. \tag{2.59}$$

Similar to interfacial viscous effects, the presence of bulk viscosity can only retard bubble dissolution, but it cannot stop it. Again, the effect is only pronounced for very high values of μ as becomes evident by comparing bulk viscous stress to the interfacial stress, that is,

$$\frac{2\sigma}{R} < -\frac{4\mu}{R}\frac{\mathrm{d}R}{\mathrm{d}t}. \tag{2.60}$$

With the initial condition $\varepsilon(t=0) = 1$, this can be re-written as

$$\varepsilon(t) = 1 - \frac{2\sigma t}{4\mu R_0^2}. \tag{2.61}$$

The critical viscosity required to oppose the Laplace stress scales linearly with the initial bubble radius. Using the typical values for the parameters, the viscous stress starts dominating when $\varepsilon = 0.9$, if the the critical viscosity is 6×10^7 Pa.s.

The combined effects of bulk and interfacial viscous stresses can only retard bubble dissolution, and only when their magnitudes exceed certain critical values. However, to stop bubble dissolution, either the bulk, the interface, or both, must be elastic.

2.6 Bubbles as rheological probes

2.6.1 Bubble dynamics in an oscillating pressure field

When a spherical gas cavity in an unbounded liquid medium is exposed to a time-varying pressure, it undergoes volumetric oscillations due to the compressibility of the gas inside the bubble. The radial position of the interface $R(t)$ at time t with respect to the bubble centre can be described by carrying out mass and momentum balances at the interface in spherical coordinates. For an incompressible liquid with density ρ, viscosity μ, surface tension σ the bubble dynamics can be described by the equation

$$R\ddot{R} + \frac{3}{2}\dot{R}^2 = \frac{1}{\rho}\left(P_i - P_\infty - \frac{2\sigma}{R} - 4\mu\frac{\dot{R}}{R}\right), \tag{2.62}$$

where P_i is the equilibrium pressure within the bubble and P_∞ is the pressure at infinity. The dots indicate derivatives with respect to time. Equation (2.62) is known as the Rayleigh-Plesset equation [60–63]. For an acoustic pressure field $P_{\mathrm{ac}}(t) = P_{\mathrm{a}}\sin(\omega t)$ of amplitude P_{a}, the pressure outside the cavity becomes $P_\infty = P_0 + P_{\mathrm{ac}}(t)$, with P_0 being the ambient pressure, while ω is the angular frequency of the sound wave. Assuming the gas behaves ideally with polytropic exponent κ, $P_i = (P_0 + P_L)(\frac{R_0}{R})^{3\kappa}$, $P_L = \frac{2\sigma}{R_0}$ the Laplace pressure arising from surface tension acting on the curved interface, and R_0 is the equilibrium radius of the bubble. With these considerations, equation (2.62) may be rewritten as

$$R\ddot{R} + \frac{3}{2}\dot{R}^2 = \frac{1}{\rho}\left[\left(P_0 + \frac{2\sigma}{R_0}\right)\left(\frac{R}{R_0}\right)^{-3\kappa} - P_0 - P_{\mathrm{ac}}(t) - \frac{2\sigma}{R} - 4\mu\frac{\dot{R}}{R}\right]. \tag{2.63}$$

The bubble excursions are maximum when the driving oscillation frequency is close to the natural frequency $f_0 = \omega_0/2\pi$ of the air bubble suspended in an unbounded liquid. This is based on the Minnaert resonance [64], with the effects of surface tension incorporated [65] to get

$$\omega_0 = \sqrt{\frac{1}{\rho R_0^2}\left[3\kappa P_0 + \frac{2\sigma}{R_0}(3\kappa - 1)\right]}. \tag{2.64}$$

The polytropic exponent exhibits strong dependence on the driving frequency ω of the ultrasound [62] as there are three length scales to consider, which are the bubble radius R_0, wavelength of ultrasound in gas $\lambda_\mathrm{g} = 2\pi(\gamma R_\mathrm{g} T/M_\mathrm{w})^{1/2}/\omega$, and the thermal diffusion length $L_\mathrm{th} = (\alpha\omega)^{1/2}$, where α is the thermal diffusivity of the gas. Isothermal behaviour may be expected when $R_0 \ll L_\mathrm{th}$, leading to $\kappa \cong 1$, whereas, for $R_0 \gg L_\mathrm{th}$, adiabatic behaviour may be expected with $\kappa \cong \gamma$, where γ is the ratio of the specific heats for the gas. For small bubble oscillation amplitudes, within the linear regime, κ may be estimated as [66–68]

$$\kappa = \frac{1}{3}\mathfrak{R}(\mathfrak{Z}), \tag{2.65}$$

where $\mathfrak{R}(\mathfrak{Z})$ is the real part of the complex number $\mathfrak{Z}$ given by

$$\mathfrak{Z} = \frac{3\gamma}{1 - 3(\gamma - 1)iPe[(i/Pe)^{1/2}\coth(i/Pe)^{1/2} - 1]}, \tag{2.66}$$

with the Peclet number defined as $Pe = \alpha/(\omega R_0^2)$.

2.6.2 Oscillating bubble as an interfacial rheological probe

Comparing the radial oscillation dynamics of a bare bubble and that coated by surface active agents, in a Newtonian liquid under similar conditions, the interfacial rheological properties, arising from the adsorbed layer, can be determined. By symmetry, the area of an oscillating bubble undergoes pure dilational deformation. So the material properties of interest are the dilational elasticity E_d and dilational viscosity η_d.

This has been done, for instance, for lipid-coated microbubbles that are used as ultrasound contrast agents (UCAs) [69, 70]. Over time, several models associating the Rayleigh-Plesset equation with rheological constitutive models to describe the interfacial coating have been developed [71–73, 69, 74–78], here we focus on the framework developed by Marmottant et. al. 2005 [69], as this allows us to conveniently describe the oscillatory dynamics of colloid-coated bubbles, considered in Chapter 6, where it is combined with a micromechanical description of the buckling of particle-coated bubbles.

For a phospholipid-coated microbubble of initial radius R_0, the state of stress on the bubble surface can be defined in terms of the effective surface tension σ along three linear regimes that depend on the area of the bubble as it pulsates [69]. This is based on the low frequency measurements of effective surface tension variations with area in a flat monolayer. Within a narrow regime, where the monolayer behaves as an elastic solid, the area-dependent surface stress $\sigma(A)$ is a linear function of A, or the square of the radius R, such that around the equilibrium radius, the effective tension can be written as [69]

$$\sigma(R) = \sigma(R_0) + E_\mathrm{d}\left(\frac{R^2}{R_0^2} - 1\right) \simeq \sigma(R_0) + 2E_\mathrm{d}\left(\frac{R}{R_0} - 1\right), \tag{2.67}$$

when $|R - R_0| \ll R_0$.

Hence, the state of stress in the monolayer coating the bubble can be described in three regimes, which depend on the bubble radius. (i) Below a certain radius, R_buckling, compression will lead to the surface buckling, effectively leading to $\sigma = 0$. R_buckling will depend on the surface concentration of the lipids. (ii) Within an elastic regime, with $R_\mathrm{buckling} < R \leq R_\mathrm{break-up}$, the monolayer resists expansion owing to the lipid-lipid lateral attractive interactions. The surface stress is described by equation (2.67), and the upper limit of this regime is given by either $R_\mathrm{ruptured} = R_\mathrm{buckling}\sqrt{1 + \sigma_0/E_\mathrm{d}}$ or $R_\mathrm{break-up} = R_\mathrm{buckling}\sqrt{1 + \sigma_\mathrm{break-up}/E_\mathrm{d}}$. That is, the monolayer is elastic until the bubble expansion leads to a stress strong enough to break up the monolayer. This stress can be σ_water, which is the surface tension of a bare interface, or, if the cohesive interactions are strong enough, some $\sigma_\mathrm{break-up} > \sigma_\mathrm{water}$. (iii) After the break-up, it is assumed that the surface tension relaxes to σ_water. With these assumptions in the model, and that $\sigma_0 = \sigma(R_0) = 0$, the effective surface tension $\sigma(R)$ is defined as:

$$\sigma(R) = \begin{cases} 0 & \text{if} \quad R \leq R_\mathrm{buckling} \\ E_\mathrm{d}\left(\frac{R^2}{R_\mathrm{buckling}^2} - 1\right) & \text{if} \quad R_\mathrm{buckling} < R \leq R_\mathrm{break-up} \\ \sigma_\mathrm{water} & \text{if ruptured and} \quad R \geq R_\mathrm{ruptured} \end{cases} \tag{2.68}$$

Assuming the interfacial lipid layer as a thin solid shell with thickness $\epsilon \ll R$, a mechanical equilibrium balance across the shell gives

$$(P_\mathrm{g} - P_\mathrm{l}) = \frac{2\sigma(R)}{R} = \frac{2}{R}\left[\sigma_0 + E_\mathrm{d}\left(\frac{R^2}{R_0^2} - 1\right)\right], \tag{2.69}$$

with pressure inside the bubble being P_g, while on the liquid side, it is P_l. When the interface is in radial motion, as happens during bubble oscillations, the stress balance has additional terms arising from bulk viscous dissipation and dilational viscous dissipation

$$P_\mathrm{g}(t) - P_\mathrm{l}(t) = \frac{2\sigma(R)}{R} + 4\mu\frac{\dot{R}}{R} + 4\eta_\mathrm{d}\frac{\dot{R}}{R^2} \tag{2.70}$$

where μ is the liquid viscosity and κ_s is the interfacial dilational viscosity. Again, for $\epsilon \ll R$, $\kappa_\mathrm{d} = 3\epsilon\mu_\mathrm{lipid}$, with μ_lipid being the bulk lipid viscosity. The liquid motion hydrodynamics around the bubble, neglecting compressibility of the liquid, is described by the Rayleigh-Plesset equation [equation (2.62)]. Considering ideal gas behaviour with polytropic index κ and incorporating equations (2.69), (2.70) into equation (2.62) we get the model for the dynamics of a coated-bubble

$$\rho\left(R\ddot{R} + \frac{3}{2}\dot{R}^2\right) = \left[P_0 + \frac{2\sigma(R_0)}{R_0}\right]\left(\frac{R}{R_0}\right)^{-3\kappa} - P_0 - \frac{2\sigma(R)}{R} - \frac{4\mu\dot{R}}{R} - \frac{4\eta_\mathrm{d}\dot{R}}{R^2} - P_{ac}(t) \tag{2.71}$$

Here the radius-dependent stress term is defined differently for each regime of the monolayer. However, the elasticity is not radius-dependent.

Examples of the radius-time curves for a phospholipid-coated bubble, as predicted by the Marmottant model [69] is shown in Figure 2.8, where a MATLAB script was used to numerically solve equation (2.71). A bubble of initial radius $R_0 = 0.82\ \mu$m, is subjected to a sine-enveloped sinusoidal pressure wave with amplitude P_a varied over 100, 200, 300 and 400 kPa, at a fixed driving frequency of $f = \omega/2\pi = 2.9$ MHz. The parameters used are $R_\mathrm{buckling} = R_0$, $E_\mathrm{d} = 1$ N/m, $\eta_\mathrm{d} = 15 \times 10^{-9}$ kg/s, $\sigma_\mathrm{break-up} = 1$ N/m (resistant shell) and $\kappa = 1.0$.

The compression modulus K_V of such a coated bubble can be defined as

$$K_V = -V\left(\frac{\mathrm{d}P}{\mathrm{d}V}\right) = \begin{cases} \kappa P & \text{for the buckled state} \\ \kappa P + \frac{4}{3}\frac{E_\mathrm{d}}{R} & \text{for the elastic state} \\ \kappa P + \frac{3\kappa-1}{3}\frac{2\sigma_\mathrm{water}}{R} & \text{for the free bubble with broken shell} \end{cases}$$

with the bubble volume as V, polytropic exponent for the ideal gas as κ, which is close to 1 for slow isothermal compressions. Usually for phospholipids, $E_\mathrm{d} \gg \sigma_0$ and so compression-only behaviour is expected within the elastic regime. This means that the

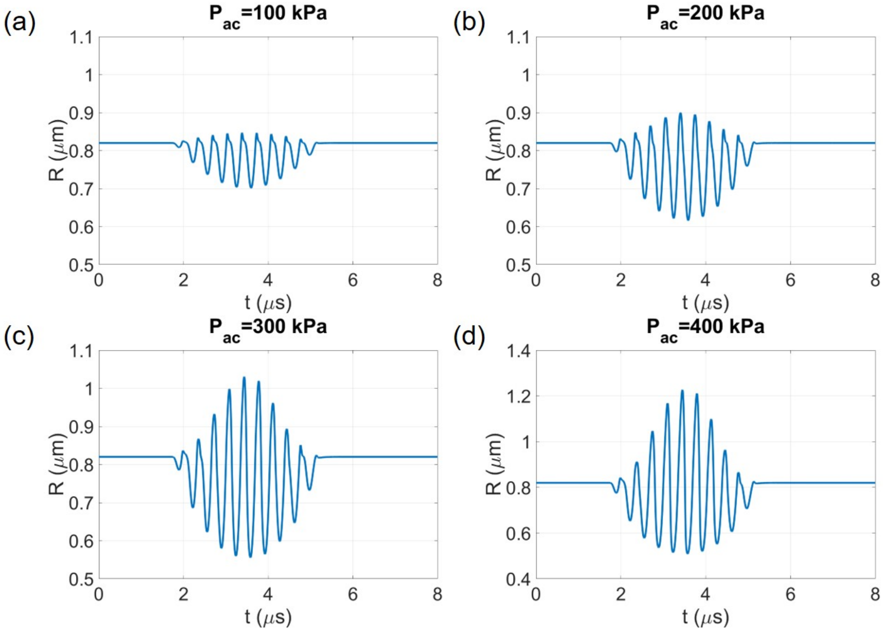

Fig. 2.8 Radius time curves for a phospholipid-coated bubble of size $R_0 = 0.82$ μm as predicted by the Marmottant model [69]. The acoustic pressure amplitude is (a) $P_a = 100$ kPa, (b) $P_a = 200$ kPa, (c) $P_a = 300$ kPa and (d) $P_a = 400$ kPa. The shell elasticity is fixed at $E_\mathrm{d} = 1$ N/m. All other parameters are mentioned in the main text.

compression to expansion ratio of the bubble during oscillations is likely to be higher than unity, as is evident in Figures 2.8 (a,b).

The modified Rayleigh-Plesset equation can be linearised [70, 79, 80] to express the bubble excursions as a linear harmonic oscillator. For small forcing amplitude, $P_\mathrm{a}/P_0 \ll 1$, the excursions of the bubble $x(t) = [R(t) - R_0]/R_0$ can be expected to follow the same temporal dependence as the forcing, such that $x(t) = x_0 \sin(\omega t + \phi)$. The amplitude of oscillations is small, $x_0 \ll 1$, and ϕ is the phase shift between the forcing and the oscillations. With these considerations, equation (2.71) may be linearised as

$$\ddot{x} + 2\beta\dot{x} + \omega_0^2 x = \frac{P_a}{\rho R_0^2} \sin \omega t, \tag{2.72}$$

with x_0 expressed as

$$x_0(\omega) = \frac{P_\mathrm{a}/(\rho_l R_0^2)}{\sqrt{(\omega_0^2 - \omega^2)^2 + (\delta\omega\omega_0)^2}}, \tag{2.73}$$

where $\omega_0 = 2\pi f_0$ is the natural frequency or eigenfrequency of the oscillator and $\omega = 2\pi f$ is the driving frequency, and δ is the damping factor which comprises of viscous, thermal, acoustic effects, in addition to dilational viscosity effects of the interfacial layer. The eigenfrequency of a coated bubble is given by [70]

$$\omega_0 = \sqrt{\frac{1}{\rho_l R_0^2}\left[3\kappa P_0 + \frac{2\sigma_{\text{water}}(3\kappa - 1)}{R_0} + \frac{4E_{\text{d}}}{R_0}\right]}. \tag{2.74}$$

When the oscillations are damped by dissipative effects, the frequency of maximum response, or resonance frequency is defined as

$$\omega_{\text{res}} = \omega_0\sqrt{1 - \frac{\delta^2}{2}}. \tag{2.75}$$

Thus, by varying the acoustic driving frequency, over a wide range of decades, the rheological properties of the interfacial layer can be characterised over varying timescales, by determining the frequency of maximum response [70].

Chapter 3

Experimental methodology

The general details of the materials, methods and setups used in all experimental studies, in this Thesis, are described in this Chapter. Following a description of the materials, the sample preparation protocol for oleofoams, oleogels and the video-microscopy of such samples using a temperature-controlled stage are elaborated. Image analysis algorithms used for measuring the radii of bubbles, both during dissolution and ultrasound-mediated volumetric oscillations, are presented. Next, the rheological characterisations of samples, with a rheometer for characterising bulk properties, and a drop shape analysis method for estimating interfacial properties, in the study of oleofoams and oleogels are briefly outlined. Then, a method used to estimate the surface free energy of solid substrates is explained. Finally, the preparation of colloid-coated bubbles, isolation of such bubbles within a specially designed enclosure, and the subsequent ultrasound-mediated oscillation of the bubbles, are described.

3.1 Materials

Materials used for preparing oleofoams and oleogels The wax used was Hydropel QB (Shamrock Technologies), a blend of paraffin and synthetic waxes. According to the manufacturer's specifications, the mean particle diameter was 9 μm, the density was $\rho_{\mathrm{wax}} = 0.88$ g cm^{-3} and the melting temperature range was $T_{\mathrm{m}} = (50-105)$°C. The wax particles were used as received. Consumer-grade sunflower oil (Tesco supermarket) was used as received. Being obtained from sunflower seeds, it is typically constituted of glycerides of linoleic acid (57.5%), oleic acid (33.4%) and saturated fatty acids such as palmitic acid (3.5%), stearic acid (2.9%), arachidic acid (0.6%), lignoceric acid (0.4%), including some amount of unsaponifiable matter [81]. The density was measured to be $\rho_{\mathrm{oil}} = 0.8879$ g cm^{-3} and the viscosity $\eta_{\mathrm{oil}} = 50$ mPa.s at $T = 25$°C . The variation in viscosity of the oil upon heating from $T = 25$°C to 90°C, followed by reversing the temperature ramp to cool the oil, led to similar trends in viscosity, as seen in Figure 4.8(b) in Chapter 4. This suggests that chemical decomposition was not a problem within the temperature range considered.

Colloid particles for preparing colloid-coated bubbles Colloidal particles used in the experiments were sulfate polystyrene latex microspheres (Molecular Probes, Invitrogen, Thermo Fisher Scientific) with diameters 0.53 ± 0.011 μm, 1.8 μm, 2.4 μm, 3.1 ± 0.29 μm, 4.9 ± 0.29 μm and 11 ± 1.6 μm. Among the properties of the particles, as listed by the manufacturer, were density $\rho_{\mathrm{s}} = 1055$ kg/m^3 at $T = 20$°C and compressive modulus 3000 MPa.

3.2 Preparation of observation cells for optical microscopy

To make observations of wax crystals, or bubbles, using microscopes, samples were prepared on glass slides. Slabs of polydimethylsiloxane (PDMS) were prepared and cut into square pieces with dimensions of 20 mm$\times$ 20 mm$\times$2 mm, which were then cut in the middle to form hollowed volumes of dimensions 15 mm$\times$15 mm$\times$2 mm. These ‘spacers’, were stuck onto the glass slides. The interior of each such cavity was filled with a sample, using pipettes, spatulas or hand-held syringes with needles, and then carefully enclosed with a glass cover slip, with care being taken not to introduce gas pockets while sealing the enclosure.

3.3 Oleofoam preparation and microscopic visualisation

The general method used for the preparation of oleofoams, which was the subject matter of Chapter 4, is described here. The goal was to produce oleofoams with low gas volume fraction, so as to be able to observe the evolution of isolated bubbles. For this, a simple protocol was developed to prepare oleofoams containing a small amount of stable bubbles. This differed from the established whipping protocol [82, 83], in which dense, stable oleofoams are produced. The latter involves heating a mixture of a high-melting crystallising agent in a vegetable oil, to get a solution with crystal melt. The solution is then cooled down to room temperature to form a gel, which is then subsequently whipped to incorporate air and form an oleofoam.

In the current study, sunflower oil and Hydropel QB wax particles were mixed in a vial and heated to a given temperature on a hotplate (UC152, Stuart). Concentrations of wax in the range 0.5-7.5 wt% were used in the experiments. The temperature of the sample was monitored using a thermocouple (RS PRO Digital thermometer, K-type, SYS calibration). When the sample attained the required temperature, the vial was agitated using a vortex mixer (PV-1, Grant) at 3000 rpm, for a given mixing time, during which the sample cooled down. The heating temperature was varied in the range $50-120$°C; the mixing time was varied in the range 30 seconds to 3 minutes. The temperature of the sample was measured again with the thermocouple immediately after mixing.

After the sample attained room temperature, it was carefully scooped from the vial using a spatula and placed onto a microscope glass slide with a polydimethylsiloxane (PDMS) spacer of thickness 1.5 mm and a glass cover slip on top. To prepare samples with wax-coated bubbles without the bulk gel network, the prepared oleofoam was diluted by gently scooping a small sample (≈ 20 μL) and adding sunflower oil to a dilution factor of 12. This was achieved by placing the oleofoam on a microscope slide with a PDMS spacer and sunflower oil was added drop-wise to fill up the enclosure, which was then sealed with a glass cover slip. Except for bubbles within an oleofoam, which were held in place by the bulk oleogel network, buoyancy caused the bubbles to rise to the top of the enclosure. These bubbles were then in the immediate vicinity of the glass cover slip, but no contact line was formed. The bubbles remained mobile when the slide was tilted, giving further evidence that there was no adhesion of the bubbles with the cover slip.

3.4 Sample preparation for use with temperature-controlled stage

3.4.1 Introduction of sample and purging

To introduce a sample into the temperature-controlled microscope stage (THMS600, Linkam), a glass slide containing the sample was placed onto the heating element of the stage. The stage was sealed using a metal lid with a glass window. It was connected to a dewar containing liquid nitrogen, a pump to draw and circulate the cold gaseous nitrogen and a temperature controller. A purging step was carried out to remove any moist air and replace it with nitrogen to prevent condensation at the window. The purging was done at $T = 25°\text{C}$ as the samples considered were otherwise sensitive to higher temperatures. The sample was observed using an upright microscope (BXFM, Olympus).

3.4.2 Calibration of the temperature-controlled stage

The temperature in the chamber, as reported by the software, corresponds to that of the metallic heating element. The true sample temperature differs as the glass slide, PDMS, sample and cover slip have different thermal conductivities. To acquire the true temperature of the sample, and to calibrate it with the temperature profiles recorded with the software, the thermocouple probe was placed into the sample. A small channel was made on one side of the PDMS spacer to dip the wire into the sample, a suspension of 2.5 % w/v of wax in sunflower oil. This method was carried out in triplicate and the calibrations were reproducible. Additionally, the melting points of two reference substances – ice ($T_m = 0°\text{C}$) and cholesterol (Sigma Aldrich, $T_m = 147 - 150°\text{C}$) – were used to check the calibration. The temperatures reported in the remainder of the thesis correspond to the true calibrated temperatures.

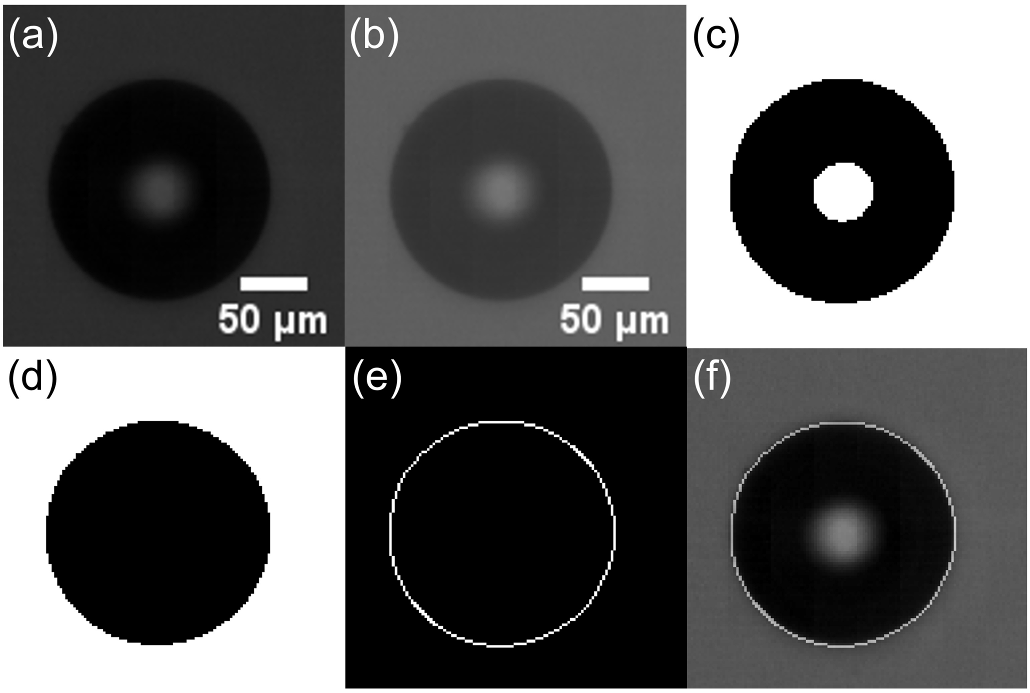

Fig. 3.1 **Steps of image analysis for a bare bubble**. (a) The original frame shows that the video is recorded in low lighting condition to avoid image saturation effects. (b) A brightness and contrast enhancement of the same frame shows the bubble more clearly. This is just to show the bubble, but the actual image analysis is carried out on the original frame (a). (b) After selecting an appropriate threshold the image is binarised. (c) The bright central region is eliminated and the dark pixels corresponding to the bubble are counted. (e) Edge detection using the Sobel method and overlaying the detected edge on the original unprocessed frame (a) is shown in (f). This visually shows that the detected contour overlaps with the perceived actual contour. The estimated equivalent radius of the bubble is $R_0 = 83.2\ \mu$m.

3.5 Image analysis algorithms for measuring bubble size

The bubble radii in each frame was tracked using functions provided with the MATLAB Image Analysis package (MATLAB and Image Processing Toolbox Release 2018a, The MathWorks Inc., Natick, Massachusetts, United States.). In estimating the 2D projected area of a bare bubble in the focal plane, the number of pixels corresponding to and within the bubble region were counted. The threshold for each frame was determined independently using the *greythresh* function which incorporates Otsu's method [84]. The image was rendered into a binary one using *im2bw*, with the bubble being represented by dark pixels, while the background as white. The binarised image is referred to as ‘Image A’. In the event that there were extraneous debris, such as colloids in the vicinity of the bubble, they would be prone to be detected as part of the ’object’. To remove these, the image was inverted and then *bwareaopen* was used to extrapolate and fill up the small regions that corresponded to the debris. The demarcation between objects being recognised as either the bubble or debris was based on the size of the objects as correspondingly being larger or smaller than a set pixel dimension, respectively. Anything below this size was filled up and made part of the background. Finally, as each clean bubble had a central luminous region arising from diffraction and internal reflection effects due to illumination, this was filled up using *imfill*. The image was once again re-inverted. This is referred to as ’Image B’. The number of black pixels were counted to give the area A_{pixel}. From this the equivalent radius was determined as

$$R_{\text{pixel}} = \sqrt{\frac{A_{\text{pixel}}}{\pi}}. \tag{3.1}$$

As a visual check that the bubble had been correctly detected using the steps so far, the contour edge of the bubble was determined using the *edge* function with the ’Sobel’ method. The output was a binary image with the contour represented as a white curve, in this case a circle, of a width of one pixel. This image is referred to as ’Image C’. Images A and C were overlaid with *imfuse* (’blend’). If the detection was correct, the estimated position of the contour coincided with the visually observed contour in the original unprocessed frame. A montage frame was constructed again with *imfuse* (’montage’) to have the overlaid image A-C on the left and B on the right.

The above steps were carried out for each frame in a loop and the estimated radii were stored in an array. An example where the radius of a bare bubble is estimated in a frame using the above algorithm is shown in Figure 3.1.

The algorithm remains valid for both bare and colloid-coated bubbles. The only difference is that when colloids are large, $3 - 10$ μm in diameter, with high surface coverage, the central bright region is not apparent. This makes the image processing faster. An example of a colloid coated bubble, following the desorption of some particles into its vicinity, is illustrated in Figure 3.2, showing that debris do not contribute to the bubble area.

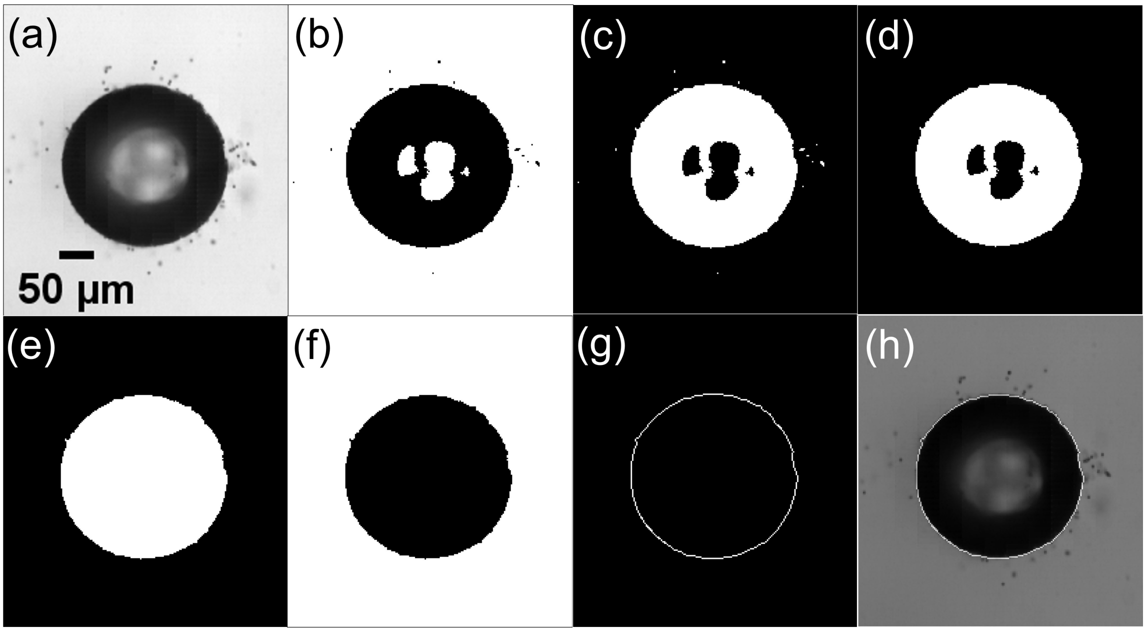

Fig. 3.2 **Steps of image analysis for a coated bubble**. (a) Original frame showing a partially coated bubble with desorbed particles around it. (b) Binarised image; (c) image inversion followed by (d) area opening to fill up the small debris. (e) Elimination of central region and (f) re-inverting image to detect edge in (g). Frames (g) and (a) are overlapped to check if the detected contour matches with perceived contour of the bubble. The estimated equivalent radius of the bubble is found to be $R_0 = 118.5$ μm.

3.6 Bulk rheological characterisation of samples

Bulk rheology of samples were characterised in a rheometer, with a Peltier heating element and water bath temperature control (MCR 302, Anton Paar), using a cone-plate geometry (diameter 50 mm, cone angle 1°) with a minimum gap of 0.101 mm. In some experiments, where the temperature was fixed at room temperature, sandpaper (hydrophobic, P1500 sandpaper, Sungold Abrasives, Port Washington, New York, U.S.A.) was stuck on both the cone and plate surfaces, with a typical roughness of 13 μm to limit wall slip. For temperature ramps, sandpaper was avoided to allow good temperature control. For a given sample, the linear viscoelastic regime was identified by first performing an amplitude sweep at a constant frequency $f = 1$ Hz. The strain amplitude γ up to which the dynamic moduli G' and G'' remained constant was identified as the linear viscoelastic regime. With this value of γ, frequency-sweeps were performed on fresh samples in the range $f = 0.1 - 50$ Hz, with data acquisition occurring in logarithmic time steps. It was noted that above $f = 50$ Hz, the mechanical resonances within the rheometer started affecting the measurements.

3.7 Drop shape analysis

3.7.1 Setup for pendant drop tensiometry and contact angle measurement

To measure the surface tension and perform drop shape fitting elastometry on drops coated with complex interfaces, a custom built pendant drop setup was used. This involved a needle connected to a 1 mL syringe barrel without the plunger, mounted on an optical post. A flexible tubing 1/16” ID (Tygon tubing, Saint-Gobain) was pushed and sealed into the barrel, with the other end of the tube connected to another needle attached to a syringe filled with liquid. The liquid filled syringe was set up on a syringe pump (Harvard Apparatus). Drops at the tip of the needle were observed using a CMOS camera (DCC1545M, Thorlabs) connected to a zoom lens (6.5×, Navitar). A blue LED array (LIU470A 470 nm LED Array, Thorlabs) was collimated using a diffuser lens, acting as the light source behind the drop. Images were captured using a software (ThorCam, Thorlabs). The optical elements of the setup are shown in Figure 3.3. To measure contact angles of droplets, the optical post was substituted by an height-adjustable horizontal stage.

The needles were cleaned by sealing them into micro vials filled with ethanol and agitated using the vortex mixer at 3000 rpm for 1 minute. Then it was repeated with water (ultra-pure water, resistivity 18.2 MΩ cm at 25°C, toc < 5 μg/L from Merck/Millipore-Milli-Q Integral 3). The needles were dried both inside and outside by blowing compressed air. As an immediate check of the cleanliness of the needle and accuracy of the instrument, before each experiment, the surface tension of ultra-pure water was measured using the ‘Pendant Drop’ plugin in ImageJ[85]. This was done for varying drop volumes and further experiments were carried out when the surface tension was reliably found to be in the range $\sigma = 72.0 \pm 2.0$ mN/m.

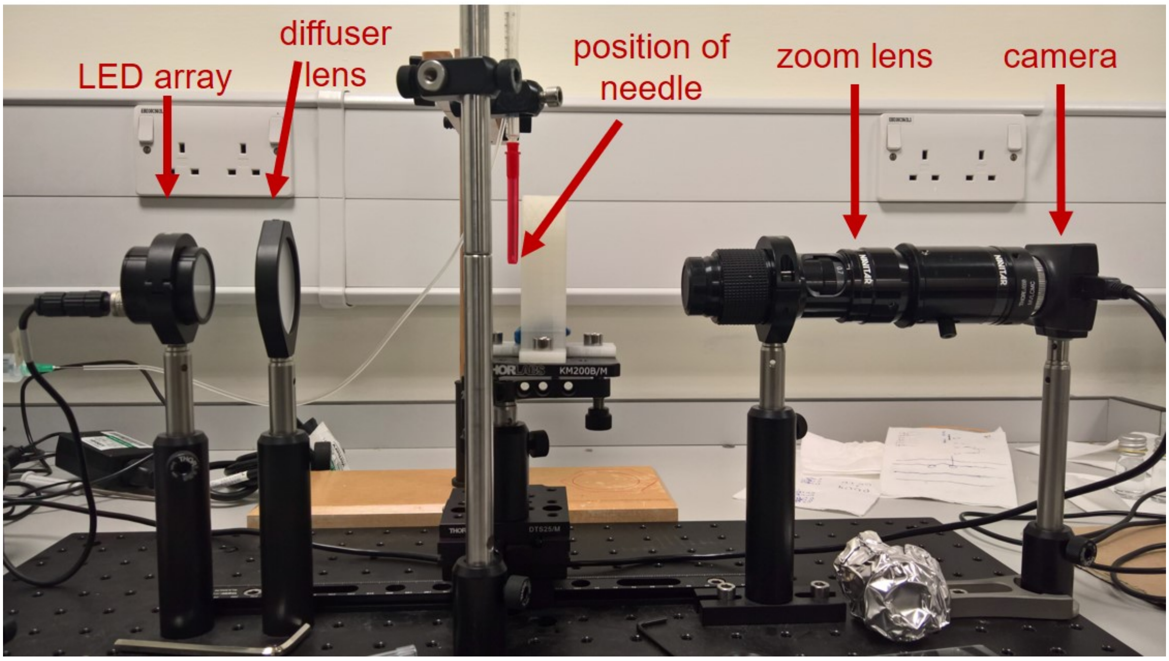

Fig. 3.3 The various elements of the pendant drop setup.

3.7.2 Drop shape fitting elastometry

The estimation of elastic material parameters of a 2D complex interface, using the pendant drop method was done following the Drop Shape Fitting Elastometry (DSFE) analysis described by [49, 20, 50], and summarised in section 2.4.2. A set of MATLAB routines, that were made available under an open source license (http:// tensiomet.sourceforge.net) by Nagel et. al. [20], have been used. In this, the drop shape is sampled by sampling coordinates of the edge. Thereafter, the Young-Laplace equation is solved to predict drop shapes for initial values of an isotropic surface stress σ. The error between the generated drop shape and the sampled shape is compared and an iteration thereon continues until the fitting error is minimised. The final value of the surface stress is taken to be the effective surface tension.

At the start, for each image, a prompt is initiated to interactively locate the drop neck and needle position on the image. The algorithm then samples the discrete coordinates of the edge pixels using a Chebyshev transform [20]. Generally, fitting accuracy increases with increased sampling. However, noise gets amplified with a higher sampling rate, especially when derivatives are computed to estimate the discrete arc lengths corresponding to the drop shape. For the fitting, it is also necessary to have more points at the drop apex and near the attachment point to the needle. For

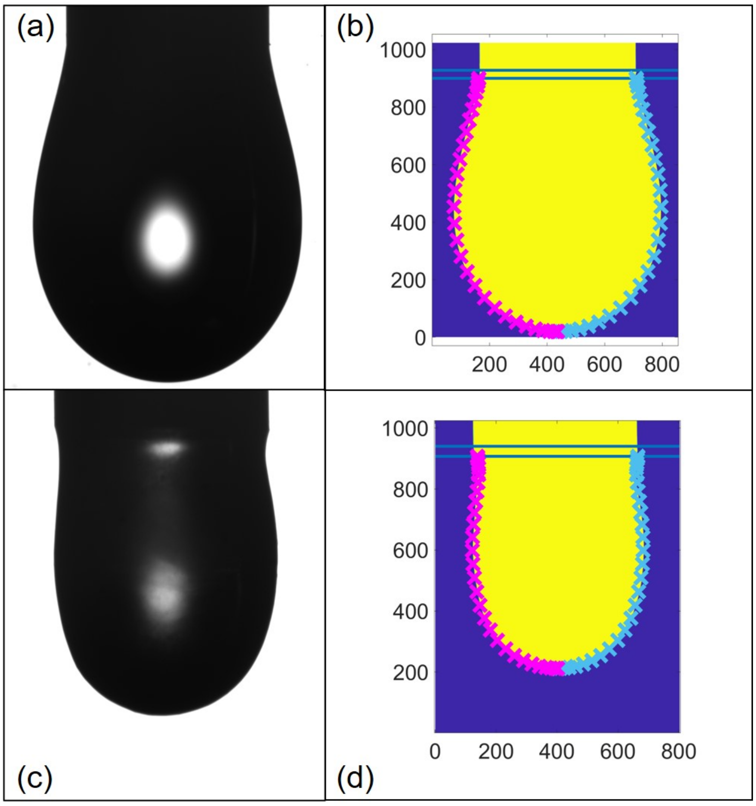

Fig. 3.4 Shape sampling using Chebyshev transform for filtering. (a) An oil drop and (b) its detection using the algorithm. Panels (c) and (d) show a compressed wax-coated pendant drop, and it's detection, respectively, indicating a non-linear curvature profile close to the needle. The numerical coordinates in the processed images correspond to pixel positions. The pairs of horizontal lines mark the positions of the drop neck and needle. The contour markers represent the sampled pixels.

this reason the use of a Chebyshev transform as a filtering allows increased sampling close to the end points of the domain. In other words, assuming a symmetric drop profile, the drop starts at the needle and ends at the apex, so the sampling density is made maximum close to these end points. Meanwhile the sampling is moderate in the intermediate region. This is made clear in Figure 3.4, where the density of the markers, representing sampled points, varies over the domain and is maximum at the end points.

In case the interface is a complex one, a generalised version of the Young-Laplace equation is used along with a constitutive relationship between interfacial stretch factors, defined with respect to a reference state, and the anisotropic stress components (as described in section 2.4.2). The fitting parameters include the interfacial compression modulus E_d and shear modulus G_2D. Assuming purely elastic behaviour, and using Hencky finite-strain measure, a pseudo-linear Hookean model is used [20] as the constitutive model.

The reference state of the drop is one where the interface behaves as a liquid, having an isotropic surface stress equivalent to the effective surface tension $\sigma = \sigma^*$. A drop with a liquid interface should obey the Young-Laplace equation. Equivalently, the meridional curvature profile κ^s should vary linearly with drop height. Compression below this state gives rise to elastic extra-stresses, corresponding to the transition from liquid to solid-like behaviour. Hence, the final drop profile, just before the onset of non-linearity in the κ^s vs z profile, is taken as the reference state and the effective surface tension is defined as σ^*.

3.8 Measurement of surface energy

The surface free energy (SFE) of a substrate in air was estimated, Chapter 5 (section 5.3.6), using the method of Owens and Wendt [86, 87]. For this, sessile drops of liquids, with a wide range of polarity, were deposited on a horizontal substrate which was placed on the height-adjustable stage. The contact angles of the drops were measured using the custom-built optical goniometer.

For a sessile liquid drop on a substrate, the three components of surface energies along the three-phase contact line are the air-substrate surface energy σ_S, the liquid-substrate surface energy σ_LS and the air-liquid surface energy σ_AL. Among these, σ_AL can be obtained using pendant-drop tensiometry as well as from literature. While, σ_S can be determined by estimating the contact angles θ, taken within the liquid phase, for sessile drops of two or more different liquids on the given substrate. It is preferable to use liquids with varying degrees of polarity. The above quantities can be related by the Young-Dupré equation as $\cos\theta = (\sigma_\mathrm{S} - \sigma_\mathrm{LS})/\sigma_\mathrm{AL}$, and σ_LS can be determined for a given liquid with a substrate. The surface energy σ, of a liquid or a substrate, can be divided into a dispersive component arising from interactions such as van der Waals or London dispersion forces [88, 86] as σ^d, and a component arising due to dipole interactions and hydrogen-bonding as σ^p. Thus $\sigma = \sigma^\mathrm{d} + \sigma^\mathrm{p}$.

With the assumption that for a liquid-solid pair, the interfacial energy is given by [86]

$$\sigma_{\mathrm{LS}} = \sigma_{\mathrm{S}} + \sigma_{\mathrm{L}} - 2(\sqrt{\sigma_{\mathrm{L}}^{\mathrm{p}}\sigma_{\mathrm{S}}^{\mathrm{p}}} + \sqrt{\sigma_{\mathrm{L}}^{\mathrm{d}}\sigma_{\mathrm{S}}^{\mathrm{d}}}) \tag{3.2}$$

with σ_L being the surface tension of the liquid and σ_{S} is the SFE for the solid. The terms with superscript 'p' denote components for surface energies arising from polar interactions. Whereas, superscript 'd' denotes dispersive components. When a series of liquids i are deposited on a solid surface, the contact angles θ_i can be incorporated into equation (3.2), using the Young-Dupré equation [89, 87] as

$$\frac{(1+\cos\theta_i)\sigma_{\mathrm{L}i}}{2\sqrt{\sigma_{\mathrm{L}i}^{\mathrm{d}}}} = \sqrt{\sigma_{\mathrm{S}}^{\mathrm{d}}} + \sqrt{\frac{\sigma_{\mathrm{L}i}^{\mathrm{p}}}{\sigma_{\mathrm{L}i}^{\mathrm{d}}}}\sqrt{\sigma_{\mathrm{S}}^{\mathrm{p}}}. \tag{3.3}$$

This is similar to the equation of a straight line

$$y_i = mx_i + c, \tag{3.4}$$

when $x_i = \sqrt{\sigma_{\mathrm{L}i}^{\mathrm{p}}/\sigma_{\mathrm{L}i}^{\mathrm{d}}}$, $y_i = (1+\cos\theta_i)\sigma_{\mathrm{L}i}/(2\sqrt{\sigma_{\mathrm{L}i}^{\mathrm{d}}})$ with slope $m = \sqrt{\sigma_{\mathrm{S}}^{\mathrm{p}}}$ and y-intercept as $c = \sqrt{\sigma_{\mathrm{S}}^{\mathrm{d}}}$. Thus, by determining the corresponding contact angles of the different drops, the polar and dispersive components of the solid SFE can be estimated from fitting a straight line through the data points, using equation (3.3). By using a wide range of polar and non-polar liquids, leading to a wide range of x_i and y_i, the fit becomes more reliable.

3.9 Design of an enclosure made of agarose gel to excite bubbles using ultrasound

To study bubble dynamics under ultrasound, an enclosure was required to isolate a microbubble to be sufficiently far from rigid boundaries, to minimise modifications in the bubble oscillatory dynamics [90, 91], while the bubble rested against a soft upper boundary due to buoyancy of the surrounding liquid medium. Studies have shown that agarose gels, having low bulk elasticity, are compliant and have the least effects in altering the amplitude and frequency of response for the oscillatory dynamics of a bubbles adjacent to the gel boundary, compared to several other materials [91, 66, 92]. Thus, it was chosen as the material for the enclosure. This involved making a gel with a cavity inside to fill up with liquid, serving as the bubble suspending medium, and introduce a microbubble. The ceiling of the cavity, against which the bubble buoyantly rested, would need to be concave to ensure that every time a new bubble was introduced, or when the same bubble was studied multiple times, the position of the bubble within the enclosure would be fixed. This way the pressure field experienced by the bubble would remain constant.

Ideally, it would have been desirable to oscillate microbubbles as they rose in a cuvette, at sufficient distance from all solid boundaries, so that the dynamics would be unaffected by the walls. This was successfully done for bare bubbles that were generated using a microfluidic T-junction with controlled flow rates of air and water. However, it proved to be challenging to produce colloid-coated bubbles with sufficient surface coverage using such T-junctions, using streams of colloid dispersion and air. A high surface coverage required long residence time within the microfluidic channel, which was possible only at low fluid pressure. This made it difficult to inject bubbles into the cuvette as the hydrostatic pressure of the liquid above would have to be overcome as well. Further, this approach would limit studying the same bubble under varying conditions.

3.9.1 Preparation of hydrogel

To prepare the agarose gel, with 2% w/v agarose, a mixture of 30 mL ultra-pure water and 600 mg agarose (Sigma-Aldrich) was mixed in a 50 mL glass beaker. The beaker was covered with an aluminium foil and the mixture was heated to $T \approx 100°\text{C}$ and simultaneously stirred at 500 rpm for 20 minutes using a magnetic stirrer hot plate (Stuart UY-04805). As the water boiled, the agarose powder became completely soluble forming a clear solution. A convex achromatic doublet lens (AC127-025-B, Thorlabs) – of diameter 12 mm, convex radius of curvature 16.2 mm and thickness 7.0 mm– was cleaned with ethanol, rinsed with ultra-pure water and dried using compressed air. The lens was placed at the centre of a plastic Petri dish of diameter 50 mm and depth 20 mm. The hot agarose solution was gently poured onto the lens and up to a 15 mm mark on the side of the Petri dish as shown in Figure 3.5(a). The air-liquid interface was flat at the centre of the Petri dish. The Petri dish cover was put on top and the solution was left to solidify at room temperature on a horizontal surface for 24 hours. Water condensate drops form the interior of the cover and the local environment in the 5 mm gap above the gel kept it moist. After solidification, the gel was cut using a scalpel

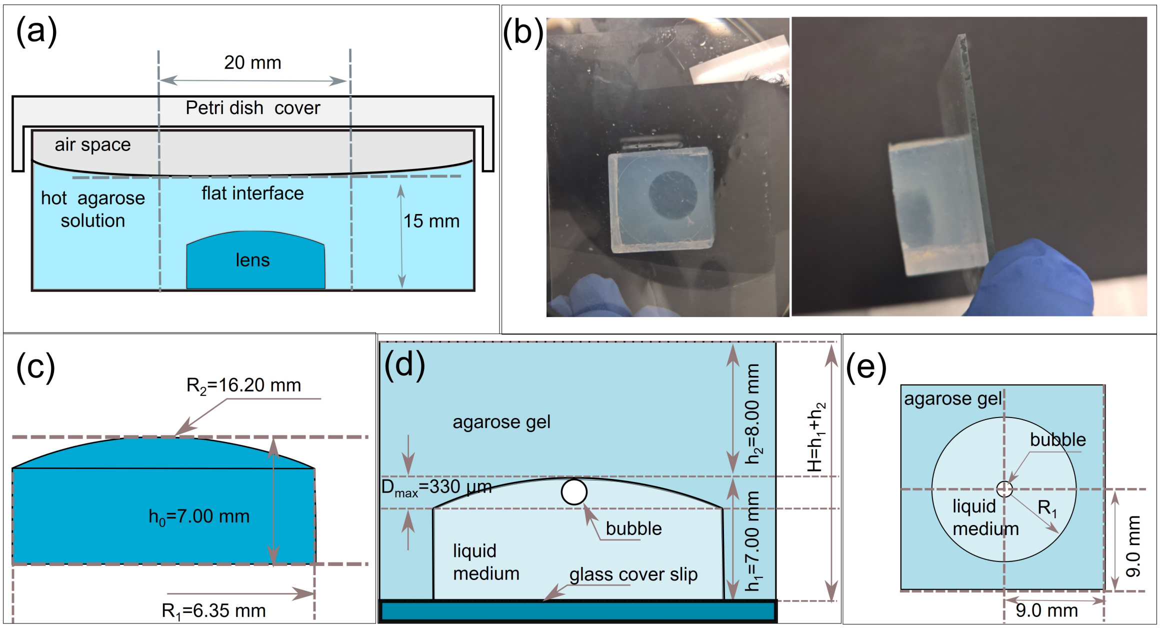
(a)
20 mm
Petri dish cover
air space
hot agarose solution
flat interface
15 mm
lens
(b)
(c)
R2=16.20 mm
h0=7.00 mm
R1=6.35 mm
(d)
agarose gel
h2=8.00 mm
H=h1+h2
Dmax=330 μm
bubble
liquid medium
glass cover slip
h1=7.00 mm
(e)
agarose gel
bubble
liquid medium
R1
9.0 mm
9.0 mm

Fig. 3.5 **Design of agarose gel enclosure** (a) Preparation of the gel in a circular Petri dish, with a cavity moulded by a lens at the bottom of the solution. (b) The gel after cutting, with the flat end adhesively attached onto a glass plate. Tilting the plate does not lead to the gel falling off. The side view also shows the cavity having a concave ceiling. (c) Schematic of the dimensions of the lens used to make the cavity. (d) Dimensions of the gel enclosure with a glass cover slip attached at the bottom. (e) Plan view of the enclosure with the bubble centred.

[Figure 3.5(b)], following the geometrical specifications detailed in Figure 3.5(c-e). The lens was carefully removed from the bottom of the gel using the scalpel, leaving behind a concave cavity within the gel. In the experiments, the cavity was filled with a liquid and a bubble introduced. The cavity was then closed with a circular 18 mm diameter glass cover slip and inverted so that the glass cover slip formed the ‘floor’ of the enclosed volume while the bubble, due to its buoyancy, rested against the soft concave agarose gel ‘ceiling’ as shown schematically in Figure 3.5(d).

3.9.2 Dimensions of the enclosure

The dimensions of the enclosure were selected with the condition that a bubble should be sufficiently far from the glass wall. In the bubble oscillation experiments, the acoustic driving frequency was fixed at $f = 25$ kHz. For bare bubbles this frequency corresponds to a resonance radius R_{res} as

$$R_{\text{res}} = \frac{1}{2\pi f}\sqrt{\frac{3\kappa P_0 + 2\sigma/R_{\text{res}}}{\rho}}, \tag{3.5}$$

where κ is the polytropic exponent of the gas in the bubble. The surface tension is σ, for the liquid with density ρ at an ambient pressure of P_0. For a rough estimate, adiabatic behaviour was assumed, with κ taken to be equal to the ratio of the specific heats of the gas under constant pressure and volume, so that $\kappa = 1.4$. Equation (3.5) is based on the Minnaert resonance [64], with the effects of surface tension incorporated [65].

For a clean bubble in water, this gives $R_{\text{res}} \approx 135$ μm. In an experiment where the effect of bubble radius on excursion amplitude for a fixed frequency is to be studied, the radii are to be at least varied in a domain $R \in [0.7R_{\text{res}}, 1.3R_{\text{res}}]$. Therefore, the maximum bubble diameter that could be studied was $D_{\max} = 330$ μm. To maintain a minimum distance of $10D_{\max}$ from a rigid glass boundary, the distance between the 'floor' of the enclosure to the apex of the concave ceiling [Figure 3.5(d)] must satisfy the condition

$$\frac{h_1 - D_{\max}}{D_{\max}} > 10. \tag{3.6}$$

Also, the ceiling thickness must be such that

$$\frac{h_2}{D_{\max}} > 10. \tag{3.7}$$

As a lens of thickness $h_1 = 7$ mm is used,

$$\frac{h_1 - D_{\max}}{D_{\max}} = 20.21 \tag{3.8}$$

while h_2 is selected as 8.0 mm giving

$$\frac{h_2}{D_{\max}} = 24.24. \tag{3.9}$$

The total height of the enclosure was, therefore, kept at $(h_1 + h_2)$ =15 mm. This allowed flexibility in studying larger bubbles whilst still maintaining the condition $h/D \geq 10$.

3.10 Preparation of colloid-coated bubbles

The preparation method for the colloid-coated bubbles, studied in Chapter 6, is described here. Electrostatic repulsion between the particles was screened by the addition of NaCl to promote aggregation of the colloids at the air-water interface. First a vial containing a particle dispersion was shaken on the vortex mixer at 3000 rpm for 1 minute to homogenise it. Then a few drops of the suspension were taken in a micro-vial and capped and again agitated for a further 30 seconds. An aqueous solution of 500 mM NaCl was added to dilute the dispersion to a desired w/v fraction. The vial was then sealed with paraffin paper and agitated on the vortex mixer at 3000 rpm for 1 minute to generate a foam. The resulting bubbles remained intact, up to several months, when stored at room temperature, while if refrigerated between $2-8$°C, the bubbles were found intact even after an year.

3.11 Placement of a single bubble into the enclosure

The method used to introduce a bubble into the enclosure are described here. A clean stainless steel spatula was slowly immersed into the vial containing the bubbles at the meniscus of the colloidal suspension. Due to capillary effects some bubbles were collected on the spatula. By varying the position of the spatula from the centre of the vial, along a radial direction allowed to pick up bubbles of different sizes as the bubble sizes increased from centre to the periphery of the meniscus in the vial. The spatula was then lightly tapped onto the surface of a 500 mM NaCl (aq) solution, taken in a wide Petri dish, to transfer and spread the bubbles. These steps are schematically represented in Figure 3.6(a).

Next, to extract a specific bubble, a 1 mL hand-held syringe, fitted to a flat ended dispensing needle of gauge 14 with inner diameter 1.70 mm (KDS141P, Kahnetics, RS Components Ltd.) or gauge 18 with ID 0.97 mm (KDS1812P) was filled with the same 500 mM NaCl (aq) solution and gently tapped on the surface of the solution in the Petri dish. As the needle was gently moved near a bubble, the capillary deformation drew the bubble inside the needle. When the needle was removed from the interface, the bubble stayed inside. This is schematically shown in Figure 3.6(b).

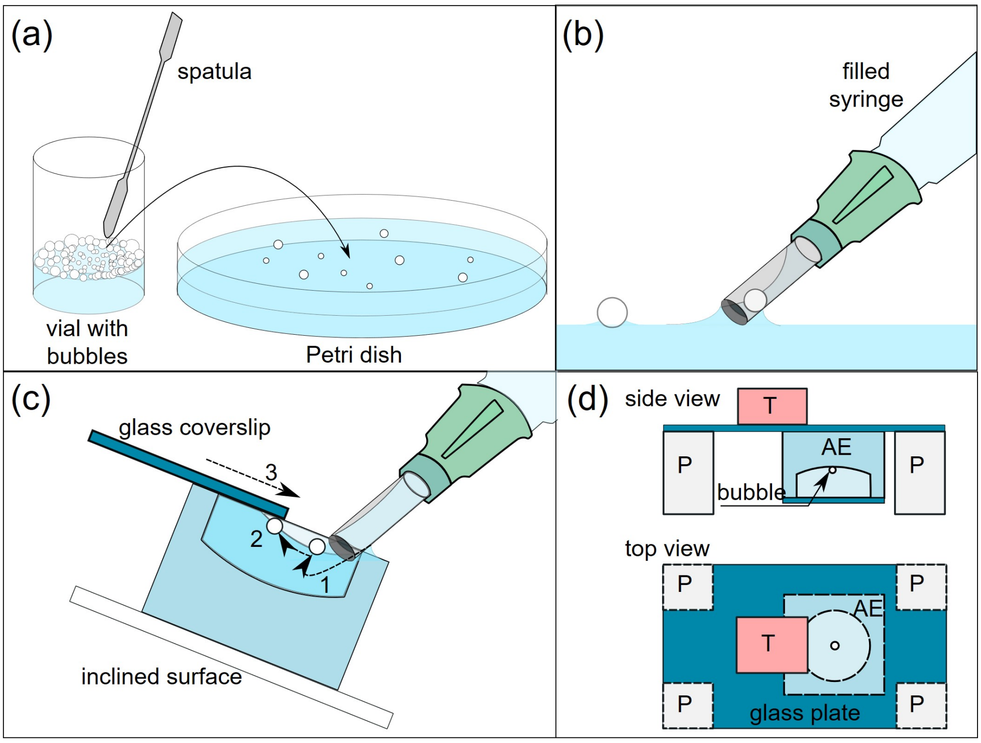

Fig. 3.6 **Isolating a bubble** (a) Transferring bubbles from a vial onto a wide Petri dish, filled with 500 mM NaCl (aq), using a stainless steel spatula. (b) Extraction of a bubble using the capillary deformation induced by a wide flat-ended dispensing needle. (c) Transferring a bubble from the needle into the agarose gel enclosure (AE). Step (1) indicates release of bubble from needle, (2) translation of the bubble up the meniscus due to buoyancy, under the partially closed glass cover slip. Then in step (3), the cover slip is fully closed. (d) Adhesion of the gel with its flat surface onto a glass plate with a transducer (T) glued on. Rectangular PDMS slabs (P) are used to keep the gel enclosure raised from the base. A bubble is shown in the lateral centre of the cavity, resting against the gel ceiling.

The agarose gel enclosure was placed flat on a surface, with the cavity facing up. 500 mM NaCl (aq) solution was filled and a cover slip partially covered it. The needle containing the bubble was brought in contact with the meniscus between the cavity and cover slip while the enclosure was tilted by $10 - 20°$. Gently pushing the plunger, released the bubble which was then drawn into the cavity by capillary action. The cavity was then filled up by more solution and then sealed. The enclosure was then inverted to allow the bubble to rise and rest against the agarose gel ceiling. The steps are schematically shown in Figure 3.6(c). Precision wipes (Kimtech Science paper wipes, Kimberly Clark) were used to dry the level end of the gel.

The flat face of the gel was then pressed against a glass plate on which a transducer had been glued earlier. The gel remained stuck with strong adhesion. The placement of the gel is shown in Figure 3.6(d). It was found in the experiments that varying the wetness of the gel surface led to varying pressure amplitudes within the same gel as the intervening water layer between the gel and the glass modified the transmission of the acoustic vibrations. For this reason, to maintain consistency, the surface of the gel was dried before attachment to the glass plate. The pressure amplitude was then found to be the same as evidenced by observing the bubble excursion amplitudes to be the same at a fixed location, for different bubbles (Chapter 6, section 6.3.1).

To introduce a bare bubble into the cavity, a small air pocket was released into the liquid-filled cavity, and the cavity was sealed. The enclosure was placed onto a glass plate and the plate was tapped to break the large bubble into smaller ones. Bubbles other than the one of the desired size were removed by tilting the enclosure and partially removing the cover slip. More liquid was added to fill up the volume before again sealing the cavity. The enclosure was set upright to make the bubble rise up to the agarose gel ceiling. Tilting the cavity led to the bubble 'rolling' against the agarose ceiling, indicating that it was not stuck to the surface.

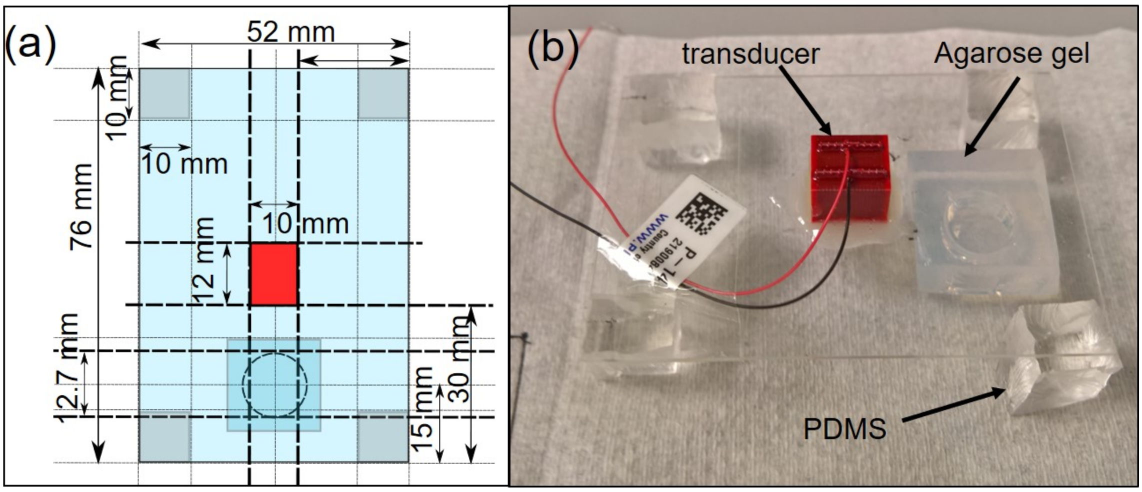

Fig. 3.7 (a) Plan view of glass plate with transducer (red) glued on it. The position of the cavity, below the transducer is shown along with the PDMS pillars (grey). (b) Diagonal view of the actual setup with the agarose gel attached at the bottom of the glass plate, that is, on the opposite side of the above transducer.

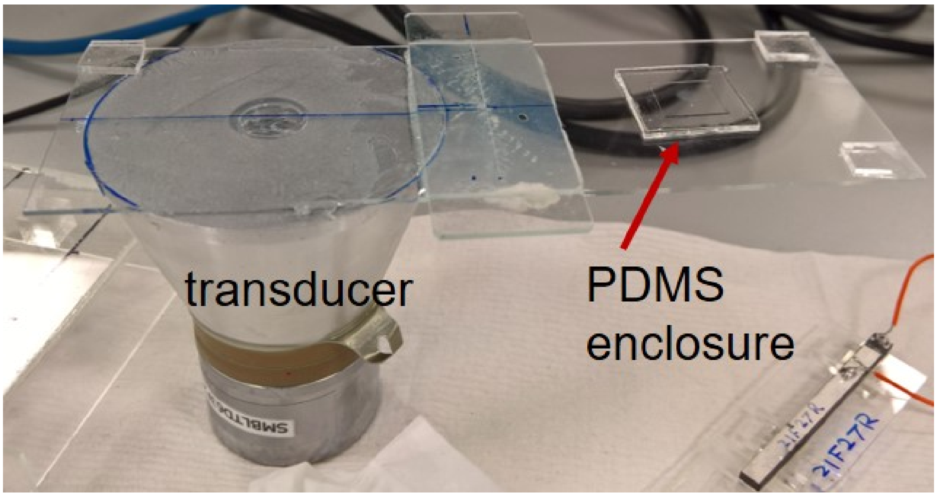

Fig. 3.8 The Langevin transducer used to strongly oscillate bubbles, resulting in particle expulsion for coated microbubbles. When in use, the setup was placed upside down onto the microscope stage.

3.12 Glass plate with transducer

A stacked piezoelectric shear actuator with axial resonant frequency of 100 kHz, travel range 10 μm and dimensions 10 mm×10 mm×12 mm (P141.10, Physik Instrumente Ltd) was glued onto the centre of a 52 mm× 76 mm glass plate, having 90° ground edges, with epoxy glue and left to dry for 24 hours. The transducer produced significant bubble oscillations when used at a driving frequency of f = 25 kHz. PDMS slabs 10 mm×10 mm×20 mm, made of 10:1 elastomer to curing agent ratio (Dowsil Sylgard 184, Univar Ltd) were adhesively attached on each corner of the plate to serve as pillars, vertically raising the plate by 20 mm from the base [Figure 3.6(d)].

The flat side of the gel was attached to the plate, on the opposite side of the transducer. A plan view with the dimensions specified is shown in Figure 3.7(a), while the actual setup is shown in (b). This setup is placed onto the stage of an inverted microscope (IX71, Olympus) after a bubble is introduced into the enclosure.

Oscillating wax-coated bubbles To observe the dynamics of wax-coated bubbles (as in Chapter 5, section 5.3.7), where the aim was to observe phenomena associated with bubble oscillation, such as buckling or crystal expulsion, rather than tracking the temporal radial evolution, a much higher pressure amplitude was required to expel crystals from the interface. For this the volume of the enclosure was reduced by

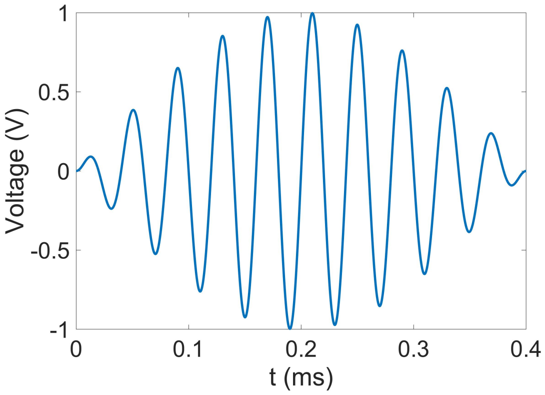

Fig. 3.9 The sine-enveloped sine voltage signal, of peak-peak amplitude of unity, uploaded into the arbitrary waveform generator. The shown signal has a frequency of 25 kHz.

using a hollowed PDMS spacer. The outer dimensions of the resulting cavity were 20 mm×20 mm×2 mm while the inner dimensions were 8 mm×8 mm×2 mm. A more powerful transducer (Bolt clamped Langevin transducer 25 kHz, Steminc) was used. The setup is shown in Figure 3.8.

3.13 Generation of acoustic waves and observation of bubble oscillations

An arbitrary waveform generator (AWG) (Agilent 33220A, Agilent Technologies, Inc.) was linked to an Oscilloscope (OSC) (TDS Oscilloscope, Tektronix, USA), a power amplifier (PA) (AG 1021 Linear Amplifier, T&C Power Conversion, Rochester, USA) and a triggering unit (Sapphire 9214, Quantum composers, Inc.). A 10-cycle sine wave, with a sine envelope, was uploaded to the memory of the AWG. The signal with frequency of $f = 25$ kHz and unit peak-peak amplitude is shown in Figure 3.9. The signal from the AWG went through the amplifier, where the gain value (in %) was set to amplify the voltage, before reaching the transducer. The amplification of the output signal, from the amplifier, was found to vary linearly with gain, as was stated by the manufacturer. This was checked by measuring both the input and output signals using the oscilloscope. As the transducer vibrated, so did the glass plate, which led to the generation of pressure waves in the cavity of the gel and caused the bubble to undergo volumetric oscillations. Keeping the gel slightly raised above the stage, using

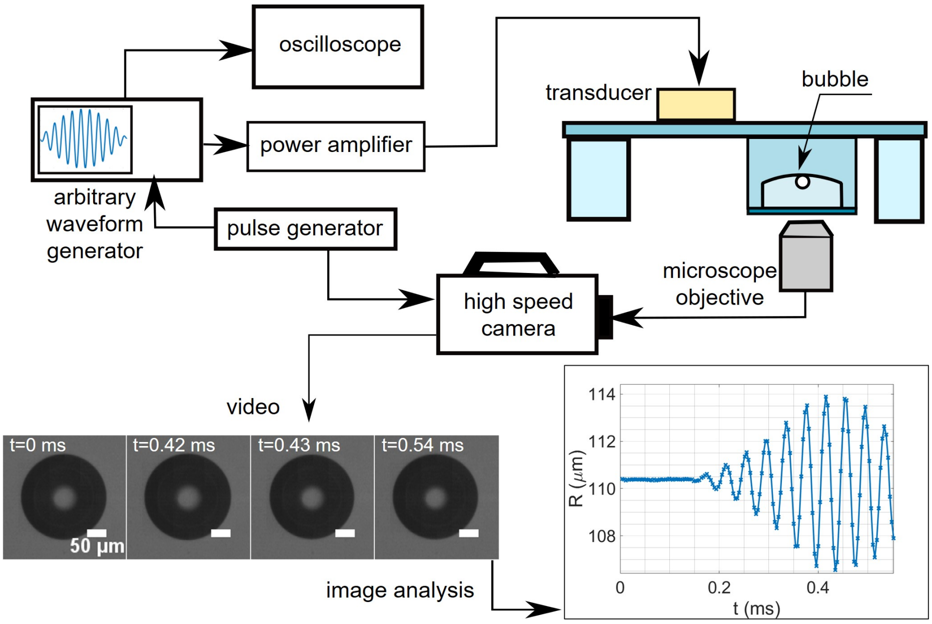
oscilloscope
power amplifier
arbitrary waveform generator
pulse generator
transducer
bubble
microscope objective
high speed camera
video
t=0 ms
t=0.42 ms
t=0.43 ms
t=0.54 ms
50 µm
image analysis
114
112
110
108
R (µm)
0
0.2
0.4
t (ms)

Fig. 3.10 Schematic of the various acoustic and video microscopy elements used to oscillate and observe a bubble simultaneously. An example of the image sequence of a recording of a bare bubble is shown along with the resulting radius-time curve following image analysis.

the PDMS slabs, reduced the dissipation of acoustic energy. The pulse generator was connected to a high-speed camera (HSC) (FASTCAM SA5, Photron, Ltd.), in parallel with the AWG. This allowed triggering of both the HSC and AWG at the same time to simultaneously excite the bubble and record the oscillations. A schematic of the setup is shown in Figure 3.10.

The frame rate used for the HSC was at least 10 times the driving frequency to capture frames with a time resolution of at least 10 points per cycle. For example, for $f = 25$ kHz, the frame rate used was 262,500 frames per second (fps).

Selecting driving frequency to oscillate wax-coated bubbles To expel crystals from the wax-coated bubbles suspended in oil, in Chapter 5, section 5.3.7, the driving frequency was selected close to the natural frequency f_0 of an air bubble, of equivalent radius R_0, suspended in an unbounded liquid. This was obtained by rearranging equation (3.5) to get f_0 in terms of R_0

$$f_0 = \frac{1}{2\pi}\sqrt{\frac{3\kappa P_0 + 2\sigma/R_0}{\rho R_0^2}}. \tag{3.10}$$

This was done to obtain the maximal oscillation amplitude.

Chapter 4

Stability of bubbles in wax-based oleofoams: decoupling the effects of bulk oleogel rheology and interfacial rheology[†]

4.1 Introduction

Foams based on oil instead of water as the liquid phase are known as oleofoams. Foaming of edible oils to form oleofoams is used in the design of food products with reduced fat content [93, 13]. Oleofoams are more difficult to stabilise compared to aqueous foams, because of the limited availability of non-aqueous foaming agents [13]. Recent studies have shown that the addition to vegetable oils of crystallising agents such as fat [94, 95, 93], fatty alcohol [96], fatty acid [82] or food-grade emulsifier [83, 97] crystals improves the foamability and stability of the resulting oleofoams. The benefits of such systems include a long shelf-life at above refrigeration temperatures and a reduced need for additives, which are desirable features for consumers.

The stability of an oleofoam is influenced by several factors. Crystals can adsorb at the air-oil interfaces of the bubbles [95, 13] and impart interfacial elasticity, similar to that observed for aqueous Pickering foams [98, 99, 4, 18, 19, 100], therefore preventing bubble dissolution. Another contributing factor is the rheology of the bulk oleogel formed by the crystals remaining in the oil phase. The size and shape of the crystals influence the rheology of the bulk oleogel [83, 97] surrounding the bubbles. The dominant type of crystal polymorph in the system depends on the method of preparation, involving tempering and agitating the crystal-oil mixture. For instance, it has recently been shown in a model waxy oil that the dynamic moduli of the oleogel vary non-monotonically with cooling rate [101]. The agitation conditions also affect the crystal size and shape. Low shear rates may affect the orientation of crystals and their growth rates [13]. At high shear rates, such as in whipping, the crystal sizes are reduced. Whipping also increases the probability of adsorption of crystals to the air-oil interface [83].

[†] This chapter is adapted from: S. Saha, B. Saint-Michel, V. Leynes, B.P. Binks & V. Garbin. Stability of bubbles in wax-based oleofoams: decoupling the effects of bulk oleogel rheology and interfacial rheology. Rheologica Acta 2020, 59: 255-266.

The classical criteria for bubble stability in the presence of an elastic interface or a viscoelastic bulk predict certain thresholds in (interfacial or bulk) rheological properties for bubble dissolution to be retarded or arrested. Small bubbles are prone to dissolution even in a gas-saturated medium due to the capillary pressure across a curved interface, $\Delta P = \frac{2\sigma_0}{R}$, where σ_0 is the surface tension of the gas-liquid interface [55, 56]. A bubble will continue to dissolve until the rate of change of the capillary pressure P with respect to the bubble radius R becomes zero, $\frac{\mathrm{d}P}{\mathrm{d}R} = -\frac{2\sigma_0}{R^2} = 0$. For bare interfaces, such that σ_0 is a constant, this condition is never satisfied and bubbles dissolve completely. In the presence of an interfacial layer, the surface stress σ changes during bubble dissolution (assuming constant mass of interfacial material on the interface) and becomes dependent on R. The interfacial elasticity of the layer, $E_\mathrm{d} = \frac{\mathrm{d}\sigma}{\mathrm{d}\ln A}$, modifies the stability criterion: $\frac{\mathrm{d}P}{\mathrm{d}R} = -\frac{2\sigma}{R^2} + \frac{4E_\mathrm{d}}{R^2}$. If $E_\mathrm{d} \geq \sigma/2$, bubble dissolution can be arrested. This is known as the Gibbs stability criterion [59] and it has been confirmed experimentally for nanoparticle-stabilised, aqueous foams [19]. The effect of an elastic bulk in retarding or arresting bubble dissolution has been described by Kloek et. al. 2001 [59]. For a bubble surrounded by an infinite elastic medium with constant shear modulus G, a bubble of initial radius R_0 will keep shrinking to a relative radius $\varepsilon = R/R_0$ until the criterion $GR_0 = 4\sigma_0\varepsilon^3/(1 - 5\varepsilon^4 + 4\varepsilon^3)$ is fulfilled. Numerical predictions by Kloek et. al. 2001 [59] show that beyond this, further bubble dissolution will be arrested.

The requirement for formulated products to remain stable in varying environmental conditions poses additional challenges. Oleofoams that are stable at room temperature may be destabilised by heating both because the crystals can melt [82], and because of enhanced bubble dissolution due to the changes in gas solubility with temperature. Enhanced bubble dissolution upon changes in temperature has been previously shown to destroy particle-stabilised bubbles in water, where air solubility increases with cooling [57], and in alkanes, where air solubility increases with heating [58].

To elucidate the link between microstructure and stability imparted by crystals in an oleofoam, in this work experiments have been performed on single bubbles to decouple the bulk and interfacial rheological contributions to stability. In addition, the effect of heating on the stability of single bubbles has been evaluated. The model system for this study was a wax-based oleofoam with low gas fraction to enable observation of individual bubbles. Video microscopy on a temperature-controlled stage was used to visualise directly the microscale phenomena occurring at the single-bubble level for bare bubbles in oil, bubbles stabilised by an interfacial layer of wax, and bubbles stabilised both by an interfacial wax layer and a bulk oleogel phase. To rationalise the observed differences in dissolution times, bulk rheological measurements on the oleogel, and dilational interfacial rheological experiments on a wax layer at the air-oil interface, were performed.

4.2 Methods

4.2.1 Characterisation of wax properties

The details of the paraffin wax and oil used in this study are given in section 3.1. To measure the contact angle of sunflower oil in air on solid wax, powdered wax was put on a glass slide and then heated on a hot plate until the wax melted. Another glass slide was placed on top of the layer of molten wax to obtain a smooth, flat surface. The wax was then allowed to cool down to room temperature and solidify. A sessile drop of sunflower oil was carefully placed on the solid wax layer in air and imaged with a custom-built optical goniometer. The contact angle measured through the oil phase was found to be $\theta = (50 \pm 3)^\circ$ ($n = 8$ repeats) [Figure 4.1 (a)].

Differential scanning calorimetry of the wax was carried out using a DSC Q2000 instrument (TA Instruments). The sample was first brought to 20°C and then heated to 120°C at a rate of 1°C/min. It was maintained at isothermal condition for 1 minute and then cooled down to 20°C at the same rate, after which it was again left for 1 minute at isothermal condition. Similarly, two more heating cycles were carried out

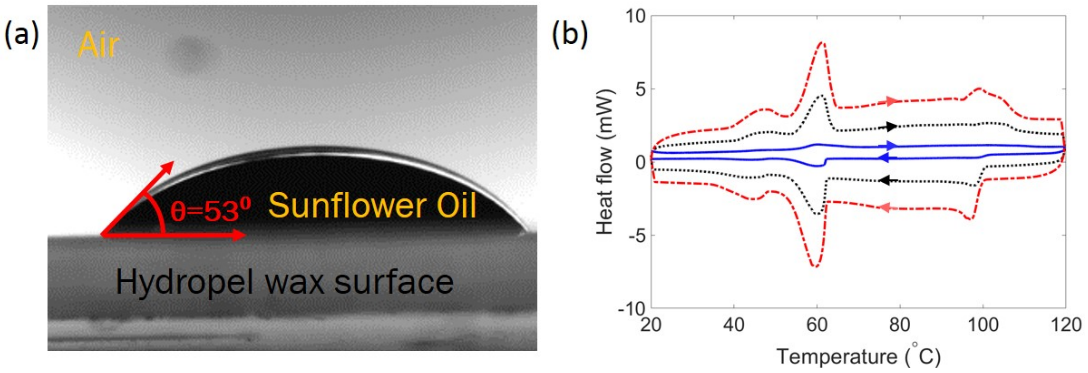

Fig. 4.1 (a) The contact angle of a drop of sunflower oil in air on a solid layer of wax at 18°C, prepared by melting and cooling Hydropel QB wax, is $\theta = 50 \pm 3°$. (b) Differential scanning calorimetry of Hydropel QB wax, first heated from 20°C to 120°C and then cooled. This was performed at rates of 1°C/min (blue, solid line), 5°C/min (black, dotted) and 10°C/min (red, dashed). Adapted from [102], which is distributed under the terms of the Creative Commons CC BY 4.0 licence.

for the same sample at 5°C/min and 10°C/min. A first melting peak is observed at $T \approx 60°$C and a second, broader peak at $T \approx 100°$C [Figure 4.1 (b)].

4.2.2 Foam preparation

The general method used to produce oleofoams with low gas fraction, so as to be able to observe the evolution of isolated bubbles, is described in section 3.3. The selection of specific wax concentration, tempering profile and agitation time in developing a protocol for oleofoam preparation, based on experimental investigations, are highlighted in section 4.3.1.

4.2.3 Video microscopy with temperature control

The slides were placed on a temperature-controlled microscope stage (THMS600, Linkam) and observed with an upright microscope (BXFM, Olympus) using a 10× objective lens. Images were recorded every 10 s in reflection mode with a CMOS camera (Thorlabs).

4.2.4 Image analysis

Image analysis using MATLAB was used to track the size of the bubbles over time. Because the bubble shapes were typically not spherical, the projected area of the bubble in the imaging plane was measured, and then converted into an equivalent radius, that is, the radius of a spherical bubble of the same area. The details are provided in section 3.5.

4.2.5 Bulk rheology

For bulk rheological measurements, the oleofoam preparation followed the protocol described in section 4.2.2. The oleogel was produced using the same protocol, but with the vortex mixer at a lower rate of 750 rpm to promote mixing while preventing bubble inclusion. As seen in Figure A.1, there are hardly any bubbles in the oleogel when prepared this way. The samples were then left to rest in their original vials, on a horizontal surface, for up to 2 hours to attain room temperature. The oleogel and oleofoam were then carefully scooped and inserted in the rheometer geometry (rheometer details in section 3.6). The pure oil and wax suspension did not require such care and were sampled using a pipette. The sample was then naturally squeezed when the cone was lowered to its measuring position. The minimum gap between the cone and plate being 0.101 mm.

Experiments where the temperature was varied were conducted immediately after lowering the cone and without any additional pre-shear. The sample was in direct contact with the smooth metal surfaces of the geometry to ensure good temperature control. The upper limit of the investigated temperature was limited to 95°C. Experiments conducted at fixed temperature were, in many cases, performed using hydrophobic sandpaper surfaces applied on both cone and plate surfaces to limit wall slip. Oscillatory measurements were conducted at a fixed frequency $f = 1$ Hz. All data points for both flow and oscillatory rheology represented 5 s of raw acquisitions. Significant differences were observed compared to smooth surfaces, most notably in oscillatory rheology at medium and high strains for initially undisturbed samples. An effect was also visible at very low shear rates in flow rheology (section 4.3.3).

4.2.6 Dilational interfacial rheology

To estimate the dilational modulus of a wax-coated air-oil interface, a custom-built optical tensiometer was used in a pendant drop configuration (see section 3.7). This was coupled with drop shape analysis techniques. Depending on whether the interfacial layer behaved fluid-like or solid-like, different analysis methods were employed. In general, in the fluid state, the (isotropic) interfacial stress can be obtained as the effective surface tension $\sigma(A)$, where A is the drop surface area [48–50, 20]. From the slopes of the $\sigma(A)$ isotherms, the classical Gibbs modulus, $E_{\mathrm{Gibbs}} = \mathrm{d}\sigma/\mathrm{d}\ln A$ is obtained. A drop shape analysis method for solid-like, elastic interfaces was introduced recently [49, 50, 20]. In this method, called *drop-shape fitting elastometry* (DSFE), the drop shapes are fitted to a model incorporating a constitutive model to extract the interfacial compression modulus, E_{d}, and interfacial shear modulus, G_{2D}.

The constitutive model used in treating the experimental data was a pseudo-linear Hookean model with a finite strain measure using Hencky strain [20]. This is known to incorporate modest strain non-linearities. Also, as image analysis is used to determine the drop area, finite area changes of typically 5% are needed to achieve reasonable accuracy. For these reasons, the Hencky strain measure is quite suitable over infinitesimal strain measures. Given that DSFE is an emerging technique, with limited experimental validation so far, the compression modulus has been obtained in terms of both the Gibbs modulus as well as determined through DSFE.

A pendant drop of neat sunflower oil in air was formed at the tip of a stainless steel needle (inner diameter 1.70 mm, outer diameter 2.11 mm, RS Components) as well as a PTFE-lined stainless steel needle (outer diameter of PTFE tip 1.1 mm, ramé-hart instrument co.) connected to a syringe pump (Harvard Apparatus). An oleogel drop was brought into contact with the pendant drop of oil using another needle (outer diameter 0.5 mm) connected to a 1 mL, hand-held syringe filled with the oleogel. Upon contact, the oleogel drop spontaneously spread over the surface of the pure oil drop. The oleogel was pre-heated to $90 - 110$°C before deposition onto the pendant drop. From the time of transferring the hot oleogel into the syringe to the subsequent contact with the pendant drop, the oleogel temperature decreased by more than 40°C, as measured by depositing a drop of the oleogel from the syringe onto the thermocouple tip.

Other methods were attempted to reproduce conditions closer to the interfacial coating on air bubbles in an oleogel, but were unsuccessful. In a control experiment, to confirm that when spreading the oleogel on an oil drop the wax crystals did not diffuse in the bulk of the drop, microscopy was performed on sessile drops placed on a glass slide. A vertical scan of the drop with the small depth of focus of the 10× lens revealed that the crystals remained confined at the drop interface, even after a waiting time of 10 minutes.

The Bond number, $Bo = \Delta\rho g R_0^2/\sigma$, was in the range $0.40 \leq Bo \leq 0.51$; the Worthington number, $Wo = \Delta\rho g V/(2\pi r_c \sigma)$, was in the range $0.32 \leq Wo \leq 0.81$. Here $\Delta\rho$ is the density difference between the inner and outer fluids, in this case oil and air; g the gravitational acceleration, R_0 the drop radius at the apex, σ the surface tension of the wax-coated air-oil interface, V the drop volume and r_c the needle radius. With these values of Bo and Wo, good precision can be expected in surface tension measurements from drop shape analysis [48].

The volume of the pendant drop was slowly varied in small steps using the syringe pump, at a flow rate of ±0.05 mL/s. The interfacial dilational strain rate for each step was $|\dot{\alpha}| = A^{-1}|\mathrm{d}A/\mathrm{d}t| = 4.5 \times 10^{-3}$ s^{-1}, with an areal strain of $|dA|/A = 0.14 \pm 0.01$ for each step change. Upon attaining the desired volume and allowing 60 s for the drop shape to equilibrate, an image was recorded. The characteristic time at which the surface properties were probed was then around 90 s. After this interval the drop size was changed.

To implement the two drop-shape analysis techniques, open-source routines were used. The effective surface tension was determined by fitting the drop shapes to the Young-Laplace equation, using open-source numerical routines [20] in MATLAB. The method was validated on a pendant drop of pure oil to determine the surface tension during expansion and compression, which remained constant with $\sigma_\mathrm{oil} = (30.7 \pm 0.2)$ mN/m. To implement the DSFE method, the library of open-source MATLAB functions developed by Nagel et. al. 2017 [20] was used.

4.3 Results

4.3.1 Effect of preparation temperature and wax concentration on bubble formation

In a first set of experiments, the temperature, to which the suspension of wax microparticles in sunflower oil was heated prior to mixing and bubble formation, was varied. The concentration of wax was 2.5% w/v in all the experiments. After heating to the desired preparation temperature, each sample was shaken for 2 minutes on a vortex mixer, at 3000 rpm. The temperature at the end of mixing was measured, and was found to have decreased by $\Delta T \approx 20 - 40$°C, corresponding to a cooling rate of $10 - 20$°C/min. The samples were allowed to cool down to room temperature after mixing and prior to imaging.

Figure 4.2(a) shows optical micrographs of samples prepared with different preparation temperatures in the range $T = 50 - 120$°C. For preparation temperatures below $T = 65$°C, which corresponds to the first melting peak of the wax, few or no bubbles were formed. A significant number of bubbles were formed in the range $T = 80 - 115$°C. The bubbles formed in this temperature range were also non-spherical and exhibited buckled and wrinkled interfaces, characteristic of an elastic interfacial layer. At $T = 120$°C the number of bubbles was reduced again (Figure A.2). The bubbles formed for temperatures below $T = 65$°C and at $T = 120$°C tended to be spherical and possessed smooth interfaces. Micrographs with higher magnification in Figure 4.2(b) show non-spherical shapes and buckled interfaces for $T = 75 - 110$°C, which are characteristic of bubbles stabilised by elastic layers. Further, above 65°C, less wax crystals were prominent in the bulk. The bulk appeared like a network with fine material present in it.

The samples were stored at room temperature [Figure A.3(a)] and the stability of the bubbles was tested by optical microscopy after one week [Figure A.3(b)] and again after 4 months [Figure A.3(c)]. Except for the bubbles prepared at temperatures between $T = 80 - 110$°C, the bubbles in the other samples had shrunk significantly with respect to their initial size and many had disappeared at the locations where there were previously many bubbles.

The effect of wax concentration was tested, while keeping the preparation temperature and the mixing time the same for all the samples, $T = 90$°C and 2 minutes,

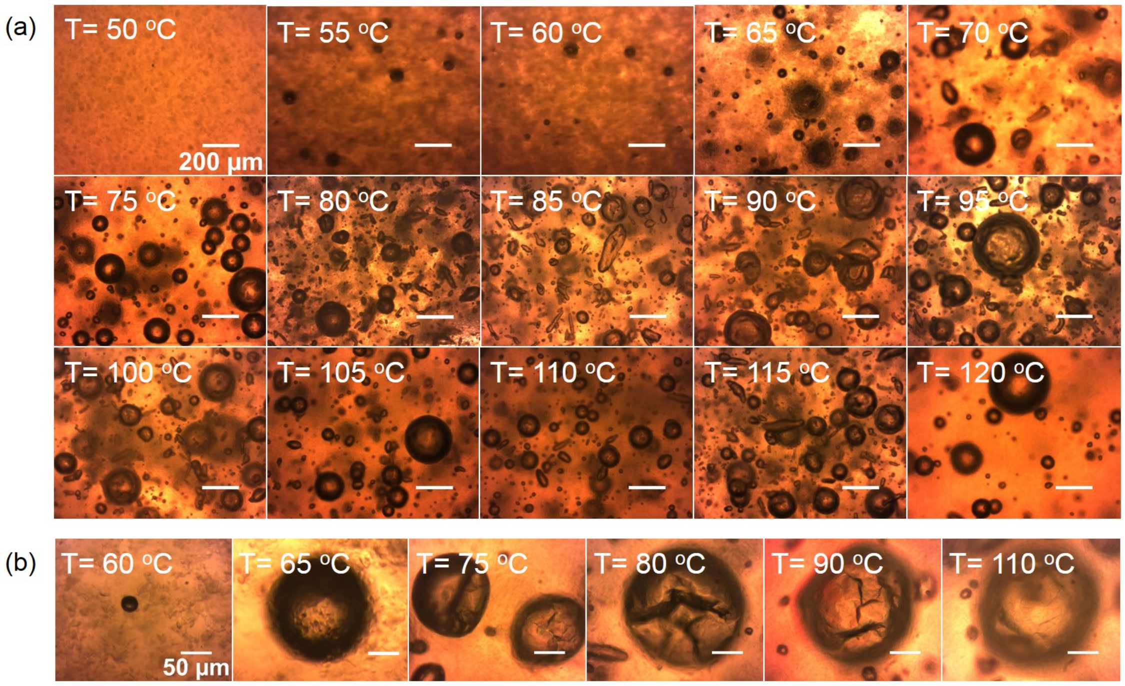

Fig. 4.2 **Effect of preparation temperature on formation of bubbles in oleogels of Hydropel QB wax in sunflower oil.** (a) Optical micrographs of samples (wax concentration 2.5% w/v, mixing time 2 minutes) after preparation and cooling to room temperature. The preparation temperature was varied in the range $T = 50 - 120°\text{C}$. (b) Magnified images of bubbles at selected temperatures showing the non-spherical shapes and buckled interfaces characteristic of bubbles stabilised by elastic layers. The gel of wax crystals in the surrounding oil phase is also visible. Adapted from [102], which is distributed under the terms of the Creative Commons CC BY 4.0 licence.

respectively. The wax concentration was varied in the range 0.5-7.5% w/v. Below a concentration of 2.5% w/v, the bubbles were few, as seen in Figure 4.3, and they dissolved within minutes to hours. Above 2.5% w/v, the mixtures became very viscous as they cooled during mixing, resulting in fewer bubbles and optically opaque mixtures which were difficult to image using optical microscopy.

Finally, keeping the wax concentration fixed at 2.5% w/v, the mixing times were varied from 30 s to 3 minutes for a narrower range of temperatures, $T = 75 - 95°\text{C}$. The temperatures at the end of mixing were recorded and were found to have decreased by $\Delta T \approx 30 - 40°\text{C}$ for mixing times of 2-3 minutes. The number of bubbles increased with increasing mixing time up to 2 minutes. For longer mixing time, the number of bubbles did not increase significantly, as shown in Figure 4.4.

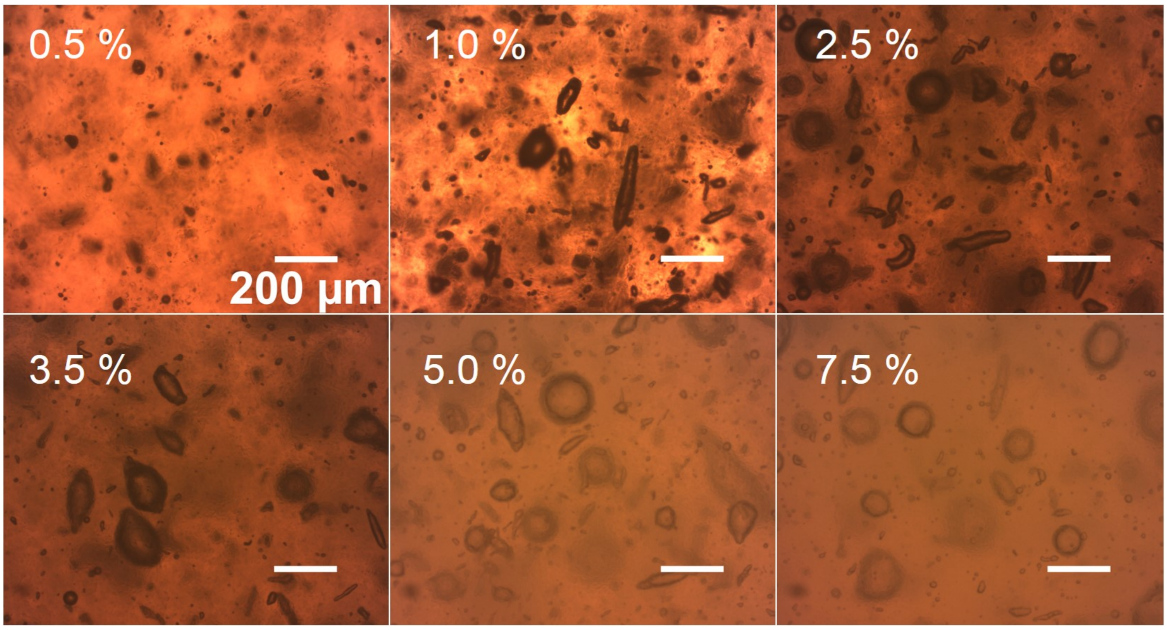

Fig. 4.3 Optical micrographs of oleofoam samples prepared at 90°C and mixing time of 2 minutes. The wax concentrations (indicated in figures) were varied from 0.5 to 7.5 % (w/v). The samples were then allowed to cool to room temperature, and stored at room temperature. Adapted from [102], which is distributed under the terms of the Creative Commons CC BY 4.0 licence.

Based on these results, the parameters were selected for the oleofoam preparation protocol to be used in the rest of the study: preparation temperature $T = 90$°C, wax concentration of 2.5% w/v and mixing time of 2 minutes, followed by cooling to room temperature before use.

4.3.2 Microscopic imaging of single bubble dissolution during heating

The dynamic evolution of the size of single, isolated bubbles upon heating was studied. Three different experiments were conducted so as to gain insights into the roles of the bulk rheology of the oleogel network and of the interfacial rheology of the adsorbed crystal layer:

1. bare bubble in sunflower oil (control experiment).
2. wax-coated bubble: a bubble was extracted from the oleofoam and resuspended in sunflower oil; care was taken to ensure that no bulk gel or crystals were left in

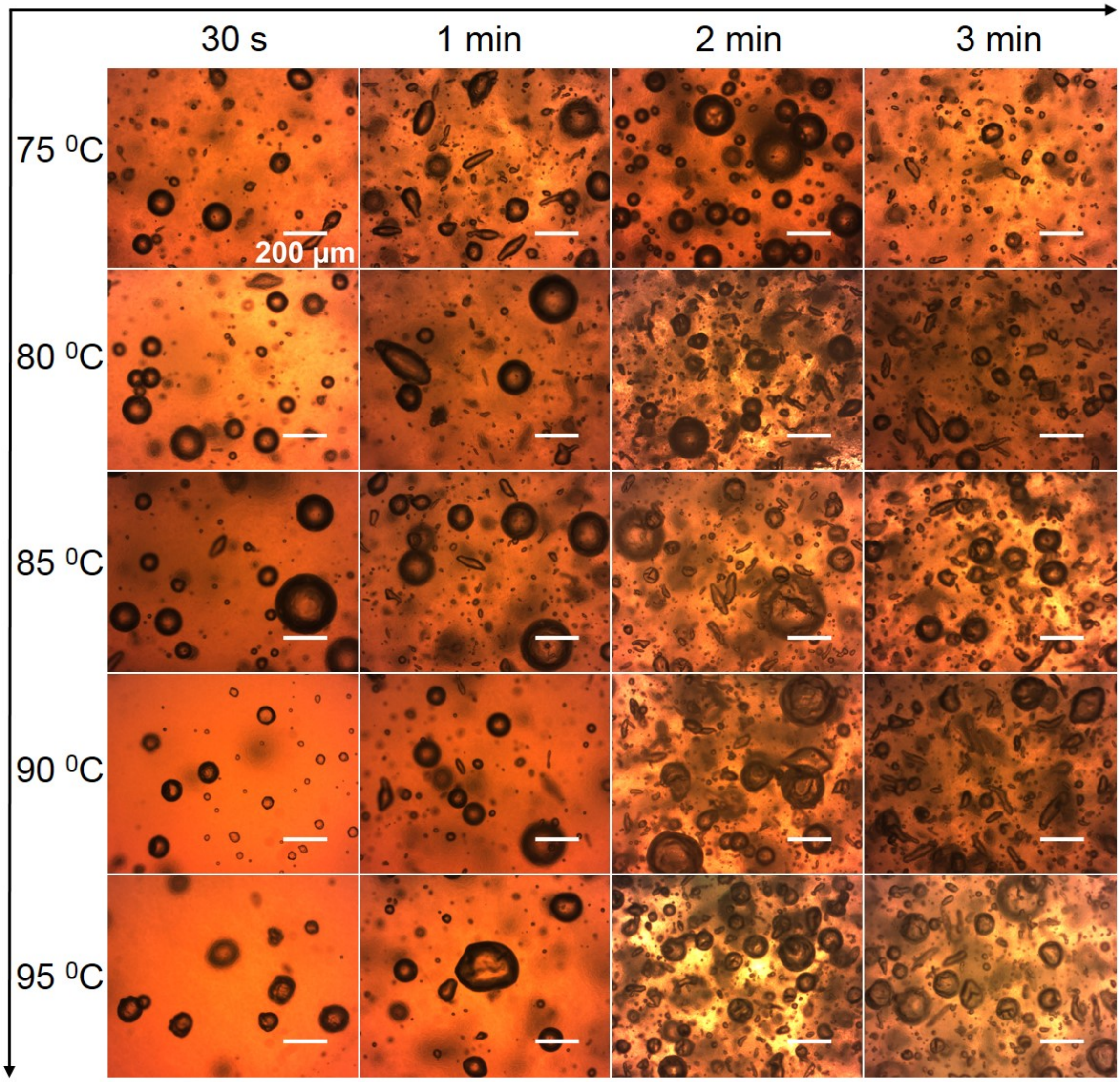
30 s
1 min
2 min
3 min
75 ⁰C
80 ⁰C
85 ⁰C
90 ⁰C
95 ⁰C
200 µm

Fig. 4.4 Optical micrographs of oleofoam samples prepared at temperatures 75 – 95°C for mixing times of 30 s, 1 min, 2 min and 3 min. The samples were then allowed to cool to room temperature, and stored at room temperature. Adapted from [102], which is distributed under the terms of the Creative Commons CC BY 4.0 licence.

the oil surrounding these bubbles. The interfacial layer was still present on the bubbles, as confirmed by their buckled interface.

3. bubble within oleofoam, that is, a bubble in the sample as prepared. These bubbles were therefore coated with an interfacial layer of wax crystals and also embedded in the bulk gel network.

All bubbles considered had initial radii in the range $R_0 = 100 \pm 20$ μm. Care was taken to observe individual, isolated bubbles, in order to prevent unwanted Ostwald ripening effects from neighbouring bubbles, particularly important for bare and wax-coated bubbles. However, this was not possible for the bubbles in oleofoams, because the sample was used without any modification and inevitably contained multiple bubbles. The samples were inserted in the temperature-controlled stage at an initial temperature $T_0 = 21$°C. The temperature was then increased to the desired final temperature at a heating rate of 5°C/min. The temperature was then maintained constant while images were recorded every 10 s. The values of the final temperature were chosen below the melting range of the wax, $T_1 = 25$°C, and above the first melting peak, $T_2 = 74$°C.

The dissolution behaviour of the three types of samples at the two different final temperatures is shown in Figure 4.5. The radius R has been normalised by the initial (effective) bubble radius, R_0. Time has been normalised by t^*, the theoretical dissolution time of a bare bubble in oil, with the same initial radius R_0, at a reference temperature $T = T_1 = 25$°C, and including a correction factor to account for the presence in the experiments of a gas impermeable wall next to the bubbles (section 4.2.2). This theoretical dissolution time was computed using the theory Epstein and Plesset 1950 [55, 56] and is given by

$$t_{\mathrm{th}} = \frac{R_0^2}{3Dk_{\mathrm{H}}}\left(\frac{R_0\rho}{2M_{\mathrm{w}}\sigma} + \frac{1}{R_{\mathrm{g}}T}\right). \tag{4.1}$$

The gas diffusivity in the liquid D, the liquid density ρ, the gas-liquid surface tension σ, and the Henry's constant k_{H}, were evaluated at the reference temperature T. M_{w} is the molar mass of the gas, and R_{g} the universal gas constant. The correction for confinement effects is given by $t^* = t_{\mathrm{th}}/\ln 2$ [56].

The control experiment with bare bubbles in sunflower oil provided qualitative information on the net effect of change in physico-chemical properties of the air-oil

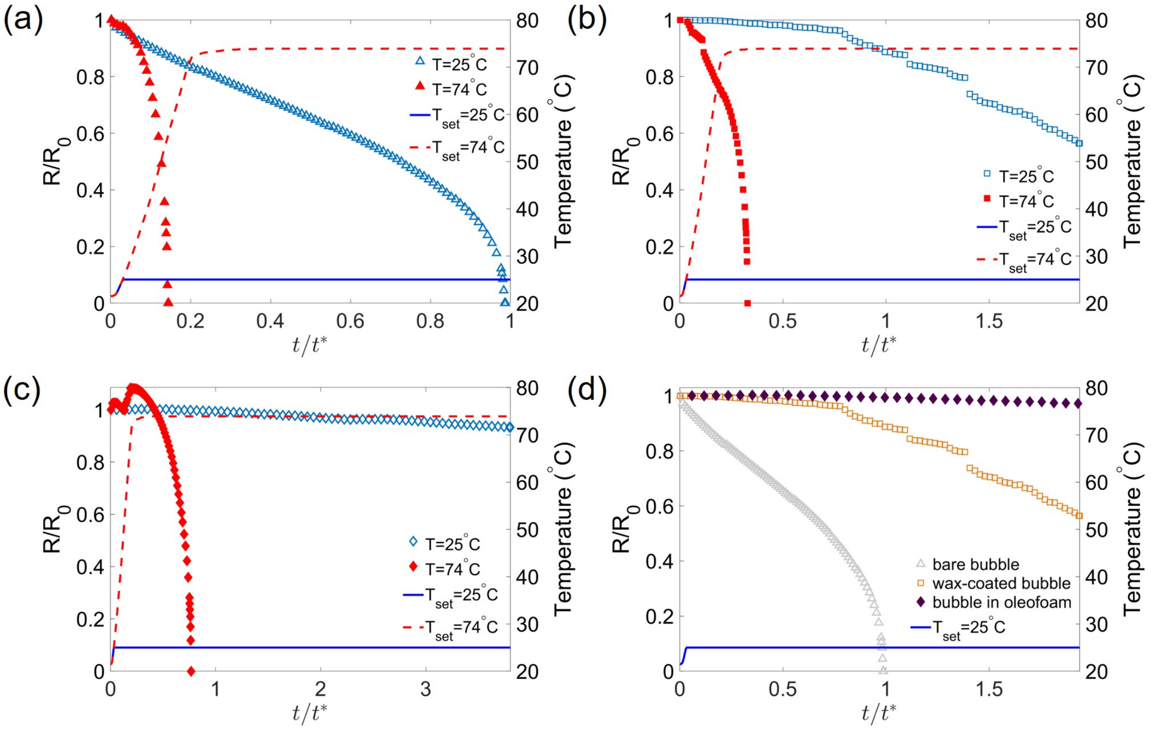

Fig. 4.5 **Dissolution behaviour of bubbles for set temperature profiles.** The temperatures were increased from room temperature (21°C) to 25°C (blue curve) and 74°C (red dashed curve) at a rate of 5°C/min. The corresponding bubble dissolution behaviour is shown by blue open symbols and red filled symbols respectively, in (a-c). (a) Bare bubble dissolving in oil, (b) wax-coated bubble in oil and (c) bubble in oleofoam. (d) Comparison of bubble dissolution at $T_{\text{set}} = 25°\text{C}$ for bare bubble (grey triangles), wax-coated bubble (orange squares) and bubble in oleofoam (filled purple diamonds). Time is normalised by t^*, the theoretical dissolution time of a bare bubble with the same initial radius in oil at 25°C, and corrected for the effect of confinement. Adapted from [102], which is distributed under the terms of the Creative Commons CC BY 4.0 licence.

system with increasing temperature. A bare bubble held at a temperature $T_1 = 25°\text{C}$ took over 4,000 s to completely dissolve. That is, this happened when $t/t^* = 1$, as seen in Figure 4.5(a). Upon heating to $T_2 = 74°\text{C}$, a bare bubble dissolved nearly 5 times faster than this. For the wax-coated bubbles too, the dissolution rate is enhanced with temperature, as seen in Figure 4.5(b). While, a bubble embedded within the oleogel, at $T_1 = 25°\text{C}$, hardly changed size over the observation timespan, lasting over more than 3 times the dissolution time t^* for a bare bubble of equivalent radius. This is shown in Figure 4.5(c), where it is also shown that at $T = 74°\text{C}$ a bubble within the oleogel completely dissolves and this happens on a timescale that is slightly slower than the case of wax-coated bubbles at the same temperature. Finally, in Figure 4.5(d), the dissolution behaviours of the three types of bubbles at $T = 25°\text{C}$ are compared directly. It is clear that the wax-coated bubbles dissolve on a much slower timescale than bare bubbles, while the dissolution of the ones embedded in the oleogel, that is a bubble in the oleofoam, is practically arrested. Additional data sets for bubble dissolution are provided in Table A.1 and show that for wax-coated bubbles, with repeats, there is a large variability in dissolution times. This may be attributed to the differences in surface coverage between different bubbles. Nevertheless, the additional data confirms the qualitative trends shown in Figure 4.5.

Figure 4.6 shows image sequences for three representative experiments at $T_1 = 25°\text{C}$, below the melting range of the wax. The bare bubble dissolved completely [Fig. 4.6(a)]. For a wax-coated bubble, the interfacial layer remained solid and in a few instances it could be seen unfolding around the bubble [Fig. 4.6(b)]. Over the same time scale, a bubble embedded in the oleogel remained stable [Fig. 4.6(c)].

At elevating temperatures, for the oleofoam, there appeared convective flows within the enclosed volume as the bubbles were displaced, as seen in the image sequence for the oleofoam in Figure 4.7, particularly when the temperature rises from $T = 21.5 - 54.5°\text{C}$, where the field of focus was kept fixed. This suggests that there is reduced resistance to flows, originating from built up stresses caused by temperature-induced density gradients within the gel. The field of view was subsequently adjusted to focus on the bubble of interest by keeping it centred. Thereafter, the flow reduced as the magnitude of the displacements of the bubbles became less than their respective radii, indicating a uniformity in temperature. The whole medium's optical density decreased at $T = 73.4°\text{C}$, which lies within the melting range of the wax [Figure 4.1 (b)], with the background becoming more bright. The illumination was adjusted for the subsequent

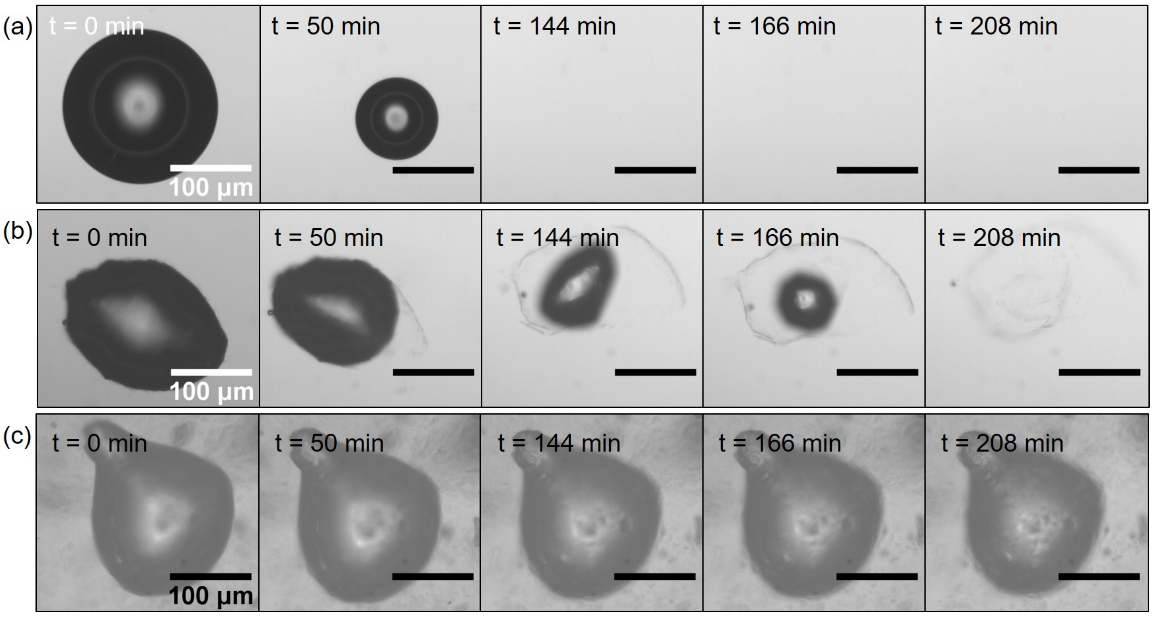
(a)
t = 0 min
t = 50 min
t = 144 min
t = 166 min
t = 208 min
100 µm
(b)
t = 0 min
t = 50 min
t = 144 min
t = 166 min
t = 208 min
100 µm
(c)
t = 0 min
t = 50 min
t = 144 min
t = 166 min
t = 208 min
100 µm

Fig. 4.6 **Image sequences of evolution of bubbles at $T_1 = 25°\mathrm{C}$.** (a) A bare bubble quickly dissolves. (b) Solid interfacial layer unfolding around a dissolving, wax-coated bubble. (c) A bubble in the oleogel remains stable over the same timescale. Adapted from [102], which is distributed under the terms of the Creative Commons CC BY 4.0 licence.

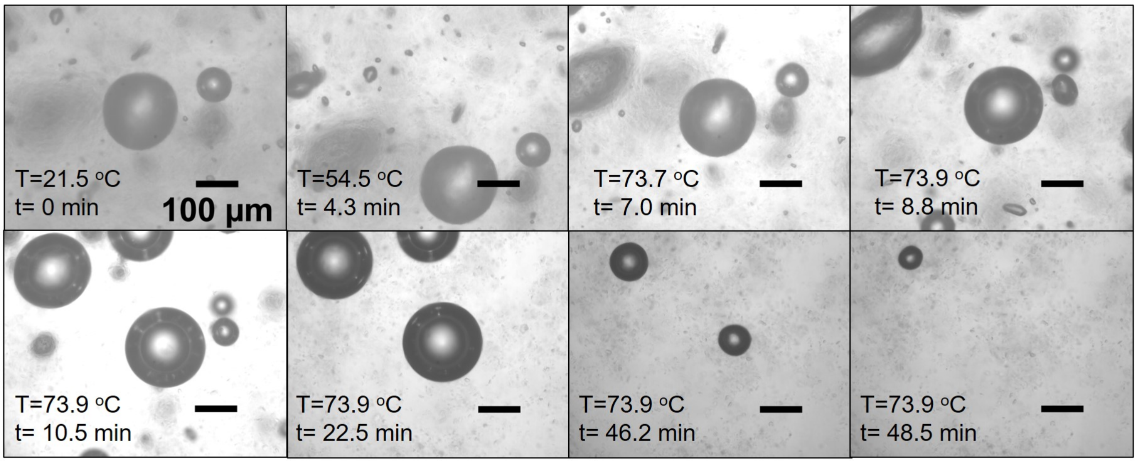
T=21.5 °C
t= 0 min
100 µm
T=54.5 °C
t= 4.3 min
T=73.7 °C
t= 7.0 min
T=73.9 °C
t= 8.8 min
T=73.9 °C
t= 10.5 min
T=73.9 °C
t= 22.5 min
T=73.9 °C
t= 46.2 min
T=73.9 °C
t= 48.5 min

Fig. 4.7 **Image sequences of evolution of bubbles in oleofoam as temperature varies from $T = 21.5 - 74°\mathrm{C}$.** The bubble, usually at the centre of these frames, is the same bubble as shown in Figure 4.5 (c).

frames to prevent saturation effects in image processing. Simultaneously it was also observed that bubbles that were out of focus initially ($t = 0$ min) started rising and appeared in focus, all the while attaining more spherical shapes ($t = 7 - 10.5$ min). The surfaces appeared more reflective suggesting that the interfacial crystals had started melting or desorbing. Overall, at $T = 73.9$°C, the crystal network constituting the gel seemed readily discrete around the bubbles and loosely connected ($t = 22.5$ min). Finally, as the larger bubbles became very small, they again appeared to be slightly non-spherical.

4.3.3 Rheological measurements

To help explain the behaviour observed in bubble formation experiments, the viscosity of all samples were measured as a function of temperature. To interpret the trends observed in the bubble dissolution experiments, characterisations of the bulk rheology of the oleogels and oleofoams and the interfacial rheology of a layer of wax crystals at the air-oil interface were done.

Flow rheology of wax suspensions, oleogels and oleofoams

The shear viscosities were measured for pure sunflower oil, a suspension of wax particles in sunflower oil, an oleogel, and an oleofoam for increasing temperatures between $T = 25$°C and 95°C with a heating rate $\mathrm{d}T/\mathrm{d}t = 10$°C/min. For the samples that contained wax, the wax concentration was the same, namely 2.5% w/v. These measurements were conducted at a shear rate of 50 s^{-1} to prevent wall slip and also to be consistent with the conditions of mixing during bubble formation. The results are shown in Figure 4.8(a). Sunflower oil viscosity is seen to decrease from 50 mPa.s at 25°C to 8 mPa.s at 95°C, following an Arrhenius-like behaviour [103]. For temperatures above 70°C the viscosities, of the other three samples containing wax, decrease and could be due to most of the solid content having melted. At lower temperatures, the viscosities of the oleogel and oleofoam deviate significantly from the wax suspension. Repeat experiments showed a sample variability of around ±30% [Figure A.4] for the oleogel and oleofoam, confirming that the preparation protocol and rheological characterisation were sufficiently controlled. Comparison with the literature on waxy crude oils [104–106] suggests that in the current system, $T = 70$°C roughly corresponds to the rheological wax appearance temperature below which wax crystals nucleate and

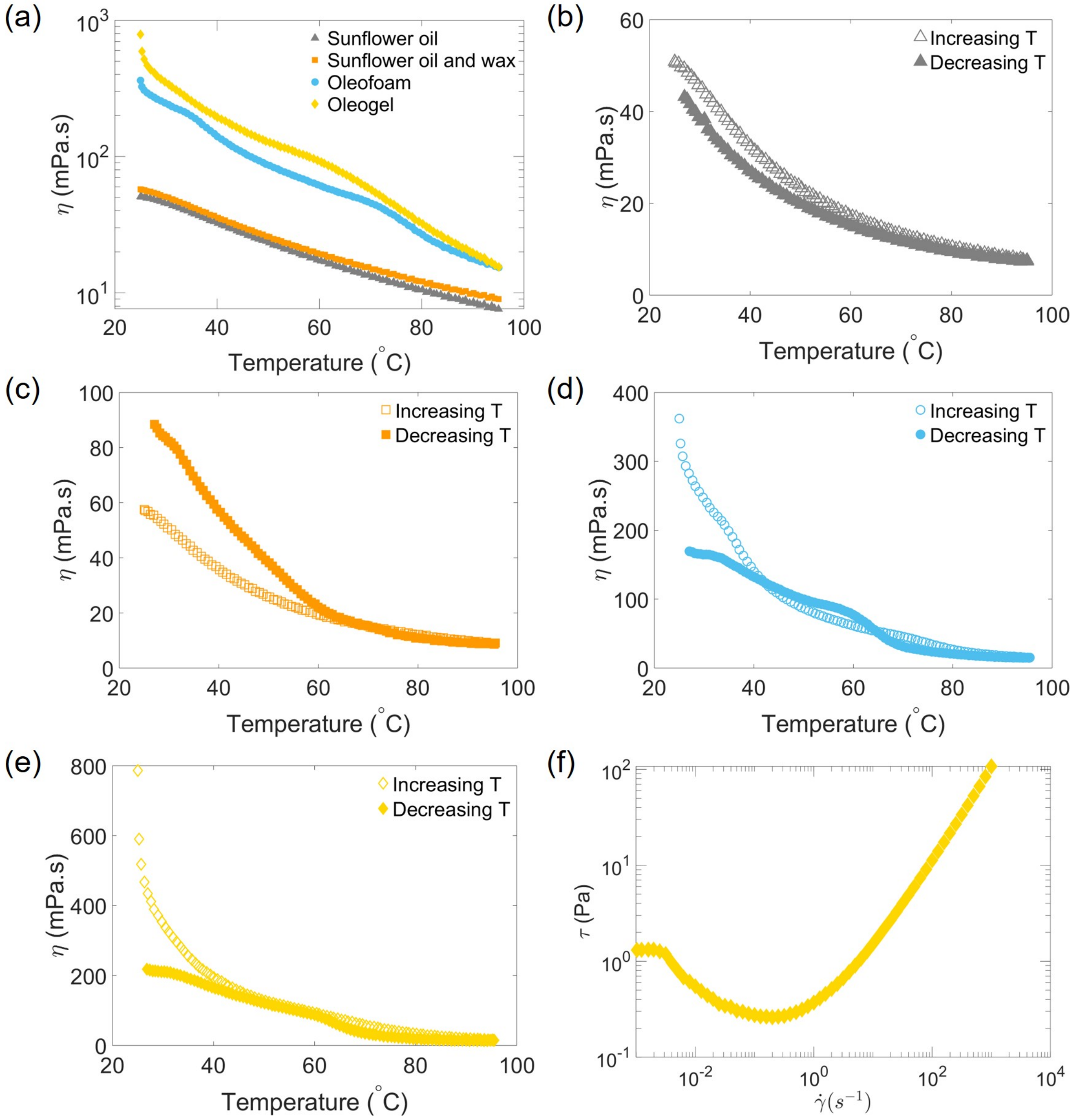

Fig. 4.8 (a) Viscosity of sunflower oil (grey triangles), mixture of oil and wax (orange squares), oleofoam (cyan circles), oleogel (yellow diamonds) for increasing temperatures between $T = 25°C$ and $T \leq 95°C$, with $\mathrm{d}T/\mathrm{d}t = 10°C/\mathrm{min}$ and a constant shear rate of 50 s^{-1}. For all the samples that contained wax, the wax concentration was 2.5% w/v. (b-e) Effect of heating (open symbols) and cooling (filled symbols), between 25°C to 95°C with $\mathrm{d}T/\mathrm{d}t = 10°C/\mathrm{min}$ and shear rate of 50 s^{-1}, for (b) sunflower oil, (c) suspension of wax in sunflower oil, (d) oleofoam and (e) oleogel. (f) Flow curve for oleogel using sand paper, with decreasing shear rates. Panels (a,f) adapted from [102], which is distributed under the terms of the Creative Commons CC BY 4.0 licence.

grow in the oil to a sufficient extent so as to form a percolating network. The presence of bubbles in the oleogel, producing the oleofoam, does not result in a dramatic change in rheology and may be due to the small bubble volume fraction [107], or possibly because the foam releases the bubbles under strong shear.

The samples were also subjected to cooling at the same temperature and shear rates, immediately after the heating step. Except for sunflower oil [Figure 4.8(b)], all samples containing wax – that is, suspension of wax in sunflower oil, oleofoam and oleogel – show a remarkable change in viscosity upon being cooled, when compared to the curves for the heating step [Figure 4.8(c,d and e)]. The differences between the trends for heating and cooling become more apparent at $T \leq 65°\text{C}$. The similarities in behaviour of the oleofoam and oleogel upon cooling support the above hypothesis that the foam releases bubbles upon strong shear or that the bubbles have dissolved. Whereas, in the suspension, the viscosity may have increased due to the formation of weak links among crystals during recrystallisation, which is stronger than the interactions in the suspension form.

Figure 4.8(f) offers a more in-depth understanding of the rheology of the oleogel at $T = 25°\text{C}$ using rough boundary conditions. The flow curve was obtained for decreasing shear rates after a 20 s pre-shear step performed at 1000 s^{-1}. The shape of the curve is identical those of waxy crude oils below wax appearance temperature presented in [108, 106]. The presence of a local stress minimum around $\dot{\gamma} = 0.1$ s^{-1} is a signature of thixotropic behaviour below which the oleogel experiences ageing. Additional experiments with smooth boundary conditions [Figure A.5 (a,b)] confirms this flow curve shape down to the local minimum, below which wall slip significantly affects the measurements. The stress minimum of 0.35 Pa can be used as an estimate of the oleogel yield stress just after being stirred.

Oscillatory rheology of the oleogel

Figure 4.9(a) shows an amplitude-sweep of the oleogel at $T = 25°\text{C}$ using a rough geometry. Two runs were preformed in succession, first for increasing strain amplitudes from $\gamma = 0.01 - 1000\%$, then for decreasing amplitudes. The gel is observed to be initially stiff with a shear modulus around 16 kPa and a limited linear visco-elastic plateau, up to 0.2% in deformation. Experiments conducted with smooth boundary conditions [Figure A.5(c,d)] yielded $G' = 9$ kPa in the linear plateau, which is most

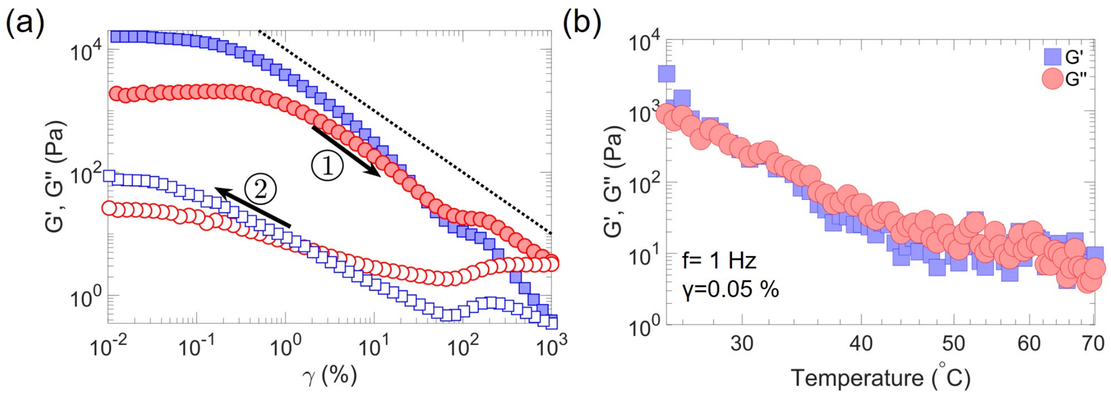

Fig. 4.9 (a) Amplitude sweep of the oleogel for $T = 25$°C and $f = 1$ Hz using a rough geometry. There was a waiting time of 500 s right after loading (with no subsequent pre-shear) after which the sweep was started, first for increasing strains (filled symbols) and immediately afterwards for decreasing strains (open symbols). Blue squares represent the storage modulus G' and the red circles the loss modulus G''. The dashed line shows $G' \propto \gamma^{-1}$ for reference. (b) Effect of temperature sweep on the storage and loss moduli of the oleogel for an applied strain amplitude $\gamma = 0.05\%$, $f = 1$ Hz and a smooth geometry. The sweep was started immediately after sample loading (no pre-shear or waiting time) at a heating rate of $\mathrm{d}T/\mathrm{d}t = 7°\mathrm{C/min}$. Same colour and symbol scheme as in (a). Adapted from [102], which is distributed under the terms of the Creative Commons CC BY 4.0 licence.

likely due to a combination of limited slip in the linear elastic regime and sample variability.

For strain amplitudes above $\gamma = 1\%$, the gel quickly yields: the storage modulus G' decreases so steeply (with an exponent below -1) that the applied stress amplitude decreases with increasing deformation, indicative of the oleogel failure. The stress amplitude maximum reached before failure, $\tau = 43$ Pa, is an upper bound of the yield stress for an initially undisturbed sample. More classical estimates – for instance, the $G' = G''$ crossover point [109]– results in a yield stress around 21 Pa. It is also noted that the data obtained for decreasing strain amplitude are not superposed to the data for increasing amplitude: after failure, the oleogel remains softer for all applied deformations. This is further evidence of thixotropic behaviour.

Figure 4.9(b) shows the evolution of the storage and loss moduli of the oleogel during heating for an applied frequency of 1 Hz and with a smooth geometry. The strain was set to 0.05%, which is in the linear viscoelastic regime, to limit slip and damage to the microstructure. The temperature ramp was measured to be $\mathrm{d}T/\mathrm{d}t = 7°\mathrm{C/min}$. The shear modulus at $T = 25$°C is slightly lower than in Figure 4.9(a), indicating moderate wall slip. The measured shear modulus then decreases sharply and reaches values as low as 100 Pa for $T \geq 40°\text{C}$. At this point the instrument torque falls below 0.5 μN.m, which severely limits the measurement precision. The frequency-sweep at $T = 70°\text{C}$ is shown in Figure A.6. Upon cooling (Figure A.7), the gel strength recovers at $T = 25°\text{C}$.

Dilational rheology of wax-coated air-oil interface

Interfacial rheological effects due to the wax layer [see Figure 4.6(b)] can also contribute to bubble stability against dissolution [59]. Since such effects could not be investigated directly on the oleofoam bubbles, the pendant drop geometry was used as a model system for a wax-coated air-oil interface.

To produce a wax-coated air-oil interface on a pendant drop, a layer of hot oleogel was deposited on the surface of a clean oil drop as described in Section 4.2.6. After deposition of the oleogel, the drop was first expanded in steps to facilitate spreading of the wax over the interface. The drop volume was then decreased to compress the interface, and finally increased to re-expand the interface. The variation of effective surface tension σ_{eff} for compression followed by the second expansion is shown in Figure 4.10. The drop area, A, is normalised by the area corresponding to the maximum volume reached after the first expansion, A_0. In the experiment shown in Figures 4.11, corresponding to the same drop, it is $A_0 = 31.25\ \text{mm}^2$. There appears to be a hysteresis between the two curves which may be attributed to either exchange of crystals between bulk and interface, or to microstructural rearrangements. Figures 4.11(a) and (b) show image sequences for the compression and expansion, respectively. Compression below $A/A_0 = 0.82$ led to drop shapes characteristic of elastic interfaces [49, 50], where a 'neck' (drop becomes inwardly concave) develops near the needle. As shown in Figure 4.11(a), the effect is more pronounced for $A/A_0 = 0.46$. Upon expansion, the signature of solid-like behaviour is no longer apparent for $A/A_0 \geq 0.66$, see Figure 4.11(b). Magnified images of the drop revealed a continuous rough surface in the compressed state, while the surface appeared patchy in the expanded states (Figure A.8).

The transition from liquid to solid-like behaviour can be identified quantitatively by plotting the meridional curvature profile of the drop, $\kappa(z)$. Here z is the vertical axis, oriented opposite gravity with the needle tip at $z = 0$ [as indicated by an arrow in the first panel of Figure 4.11(a)]. For a fluid interface, the curvature varies linearly

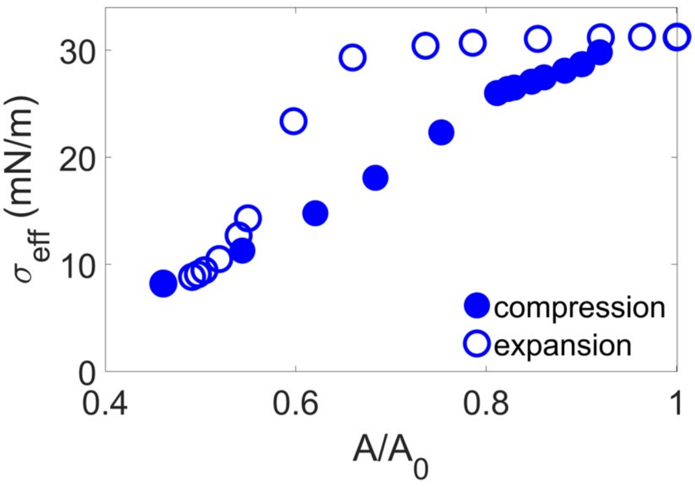

Fig. 4.10 Variation of effective surface tension with compression (filled symbols) and expansion (open symbols). The slope was estimated between each point to determine $E_{\text{Gibbs}} = \mathrm{d}\sigma/\mathrm{d}\ln A$. Adapted from [102], which is distributed under the terms of the Creative Commons CC BY 4.0 licence.

with height, obeying the Young-Laplace equation. For an elastic interface, the profile is no longer linear [20]. The curvature profiles for the compression of the drop, in Figure 4.11(c), show that the deviation from linearity increases for decreasing A/A_0.

The interfacial compression modulus, E_{d}, was determined as the Gibbs modulus over the entire area range, where the interface behaved both fluid-like and solid-like, and from *drop shape fitting elastometry* (DSFE) applied only within the elastic regime. The reference state for DSFE was selected based on the curvature profiles [Figure 4.11(c)]. The state (A/A_0) just below which compression led to the curvature profile becoming non-linear was taken as the reference state. To capture the hysteresis effects, the reference states for compression and expansion were chosen to be $A/A_0 = 0.82$ and $A/A_0 = 0.66$, respectively [Figures 4.11(a, b, c) and Figure A.9].

The classical estimate for the interfacial compression modulus has been the Gibbs modulus [19, 42, 24], defined as $E_{\text{Gibbs}} = \mathrm{d}\sigma/\mathrm{d}\ln A$. This was obtained between each state of the drop by estimating the slope of the effective surface tension σ_{eff} with area A (Figure 4.10).

The Gibbs modulus, E_{Gibbs}, and the compression modulus obtained from DSFE, $E_{\text{d}}^{\text{DSFE}}$, are plotted as a function of area for the compression and expansion experiments in Figures 4.11(d) and (e), respectively. Drop shape fitting elastometry, strictly

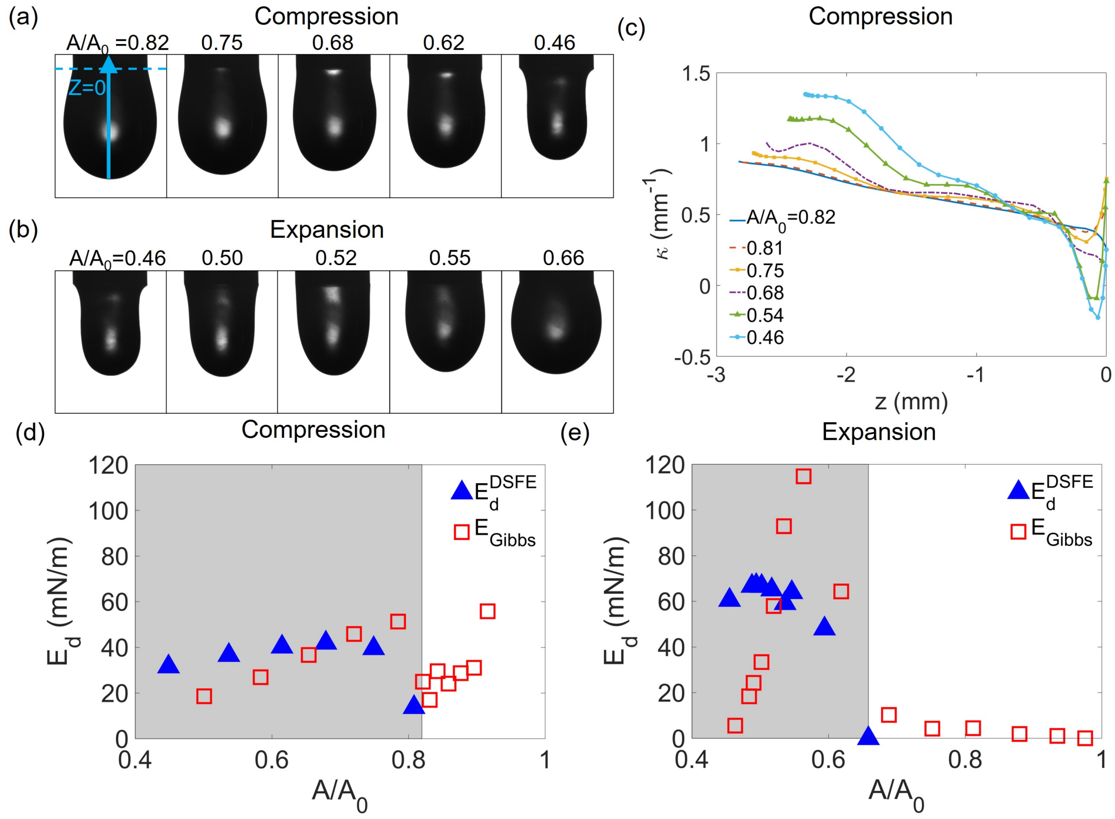

Fig. 4.11 **Interfacial rheology of oleogel layer at the air/oil interface.** Image sequence of a pendant drop of oil coated by an oleogel layer in air undergoing (a) compression followed by (b) expansion. The labels indicate the compression state (A/A_0). (c) Curvature profiles for different values of A/A_0 during compression. The drop is attached to the needle at $z = 0$ and z is directed opposite gravity [as marked on the first panel in (a)]. Estimated compression modulus E_d, at 18°C for the (d) compression series and (e) expansion series using drop shape fitting elastometry $E_\mathrm{d}^\mathrm{DSFE}$ (blue triangles) and the Gibbs modulus E_Gibbs (red squares). The reference state is indicated by the vertical line which corresponds to $A/A_0 = 0.82$ and $A/A_0 = 0.66$ for the two series respectively. The shaded region is where the interface is expected to behave as a purely elastic 2D solid. Panels (a,c,d) adapted from [102], which is distributed under the terms of the Creative Commons CC BY 4.0 licence.

applicable for purely elastic interfaces, is expected to give better estimates of E_d for compressed states below the reference state (grey shaded region) while E_Gibbs is expected to be a more reliable measure for fluid interfaces (outside shaded region). Within the elastic regime, upon compression, the compression modulus is found to be approximately $E_\mathrm{d} \approx 40$ mN/m, which may be used for testing the Gibbs criterion. The interfacial shear modulus, found by DSFE, was small compared to E_d and being in the range 0.02 mN/m$\leq G_\mathrm{2D} \leq$0.12 mN/m. For the expansion series [Figure 4.11(e)], the trends in E_d are different. Following area compression, possibly with crystal desorption into the oil, expansion causes sharp changes in the slopes of σ_eff with increasing A as seen in Figure 4.10. This directly affects the computation of E_Gibbs [25], which is known to be dependent on bulk-interfacial exchanges of adsorbed species. The variation of the effective surface tension and estimates of the moduli for all the expansion/compression series considered for this drop are given in Figures A.10 and A.11, respectively.

As a check for repeatability, additional sets of experiments were done, using both stainless steel and PTFE-coated needles. The results of one of such experiments, using the latter needles, is shown in Figure A.12. For the many cycles considered there, the maximum values for the moduli are found to be $E_\mathrm{d}^\mathrm{DSFE} = 24.9$ mN/m, $E_\mathrm{Gibbs} = 53.2$ mN/m and $G_\mathrm{2D} \approx 0$ mN/m. The transition from fluid to solid-like behaviour occurs at slightly different values of A/A_0 and could be due to differences in surface coverage or microstructure.

4.4 Discussion and Conclusions

4.4.1 Effect of temperature on bubble formation

The effect of preparation temperature on bubble formation (Figure 4.2) can be rationalised from the measurements of viscosity as a function of temperature (Figure 4.8) and bulk rheology as a function of temperature [Figure 4.9(b)]. As the viscosity of the oleogel falls with increasing temperature, turbulent mixing is enhanced, and it aids to incorporate air into the mixture. Therefore, it can be expected that at higher temperatures the number of bubbles will increase. Following bubble formation, if both the bulk viscosity (Figure 4.8) and elasticity G' [Figure 4.9(b)] is too small at the elevated temperatures at which mixing occurs, the bubbles are more mobile and susceptible to coalescence and buoyancy forces, eventually rising to the free surface before being entrapped by the gel as it cools. This balance may explain why the bubble population increases with temperature up to $T = 90°\text{C}$ and then subsequently falls at higher mixing temperatures, with typically larger bubbles [Figure 4.2(a) and Figure A.2].

4.4.2 Effect of bulk rheology on bubble stability

Typical bubbles ($R_0 \approx 100$ μm) in the oleofoam are stable against dissolution at room temperature. Ignoring the effect of the interfacial layer for now, a simple analysis based on [59] (section 2.5.2) would suggest that bulk elasticity of the oleogel may be responsible for the observed stability, as shown for instance by the large value of the elasto-capillary number $GR_0/2\sigma_0 \simeq 50$. For the capillary pressure, $2\sigma/R$, to be balanced by the mechanical load τ_{rr} under static conditions, a stress of over 600 Pa is required, assuming $\sigma = \sigma_0 = 0.031$ Nm^{-1} and $R = R_0 = 100$ μm. However, this analysis assumes that the elastic medium may sustain infinite deformation with a constant shear modulus. While it is found that for the oleogel used here, it flows for shear stresses above 40 Pa. The corresponding plasto-capillary number [107] $\tau_Y R_0/2\sigma_0 \leq 0.15$ is insufficient to arrest dissolution in the framework of [59]. The dynamics of yielding around a spherically deforming bubble have been analysed by [110] for an elastoviscoplastic fluid, in the absence of thixotropy.

As the oleogel is found to be thixotropic [Figure 4.8(f), Figure 4.9(a)], its linear elastic modulus G' and yield stress τ_Y increase with time if the gel is left undisturbed or sheared too slowly. The magnitude of the strain rate around a spherical bubble of radius $R(t)$ is $\epsilon = 2R^2\dot{R}/r^3$, with r being the distance to the bubble centre. Since bare bubbles in oil dissolve on a typical timescale $t^* \simeq 4200$ s [Figure 4.5(a) and Table A.1], the strain rate at the bubble surface can be estimated as $2\dot{R}/R \simeq 2/t^* = 4.8 \times 10^{-4}$ s^{-1}, and it decays as $1/r^3$ away from the bubble. This strain is far below the shear rate of the local stress minimum in Figure 4.8(f) below which strong ageing of the oleogel can be expected, especially away from the bubble edge. It may then be hypothesised that this ageing can be efficient enough for the yield stress of the gel to reach 600 Pa and prevent bubble dissolution at $T = 25°\text{C}$ whereas it may no longer be the case at $T = 70°\text{C}$ given the drastic reduction of both G' and G'' measured at that temperature [Figure 4.9(b), Figure A.6 and Figure A.7].

Waxy systems also present the peculiar property of forming a stronger network after a more intense pre-shear step [111] which means that the more intense mixing step applied to the oleofoam might actually add to its stability. Therefore, directly extrapolating the results presented here to whipped oleofoams then proves to be extremely challenging.

The effect of bulk viscosity in retarding bubble dissolution may be significant only when it is comparable to the critical value of $\eta \sim 10^{10}$ mPa.s, required to retard dissolution through viscous stress in similar oil-based systems [59] (section 2.5.2). While the oleogel viscosity, measured at a shear rate of 1 s^{-1} is found to be 1.1×10^4 mPa.s, as shown in Figure A.4, to make a meaningful comparison, it would have to be ideally measured at shear rate comparable to the inverse of the timescale for bubble dissolution.

4.4.3 Local effects versus bulk rheology

An additional mechanism could contribute to the unexpectedly high bubble stability against dissolution in the oleofoam. In the experiments, the typical bubble size $R_0 \approx 100$ μm is only around 10 times the typical crystal size (of the order of 10 μm), and it may be questioned whether the bubble “sees” the same oleogel as the one probed at a larger scale by a rheometer. Recent experiments performed in attractive, fibrous bacterial cellulose gels [112, 113] showed that the critical bubble size at the onset of rising motion was larger than what was expected from bulk rheological measurements, especially for the smallest solid volume fractions. It was observed [113] that the cellulose gel locally restructured around bubbles, all the more for looser fibre networks. It was proposed that this restructuring allowed the gel to locally withstand the mechanical stresses associated with the bubble buoyancy. By extending those ideas here, it may be speculated that the local restructuring within crystal networks enhances the ability of the oleogels to locally withstand the high, yet strongly localised stresses associated with bubble dissolution.

4.4.4 Effect of interfacial rheology on bubble stability

The presence of a wax layer at the bubble surface also has a stabilising effect, first by reducing the surface tension σ and also through the appearance of an interfacial elasticity E_d. The Gibbs criterion [59, 19] requires that $E_{\mathrm{d,max}} \geq \sigma/2$ to arrest bubble dissolution due to interfacial elasticity alone. The surface tension σ of the wax-coated bubble interface is not known precisely, and it is not a constant as the surface coverage gradually increases during bubble dissolution. Since $\sigma \leq \sigma_0$, where σ_0 is the surface tension of the bare air-oil interface, and σ_0 is known more precisely, fulfilling the more stringent condition $E_{\mathrm{d,max}} \geq \sigma_0/2$ would also fulfil the Gibbs criterion. The DSFE measurements (Figure 4.11) give an approximate value in the range $E_{\mathrm{d}} \approx 40$ mN/m during compression up to $A/A_0 = 0.44$, and therefore the condition $E_{\mathrm{d}} > \sigma_0/2 \approx 15$ mN/m is in principle satisfied. Furthermore, in the oleofoam samples, the crystals at the bubble interface are expected to be more densely packed than in the DSFE experiments; this is qualitatively evidenced by observing the buckled bubble interfaces occurring both in the oleofoam [Figure 4.2(b)] and wax-coated bubbles suspended in oil [Figure 4.6(b)]. The surface elasticity of these bubbles may, therefore, be even higher than estimated from the DSFE experiments and one would expect the wax-coated bubbles to be stable against dissolution even in absence of bulk elasticity. Yet the experiments show that the wax-coated bubbles dissolve in sunflower oil at room temperature, albeit slower than bare bubbles [Figure 4.5(b) and Figure 4.6(b)]. Interestingly, an intact interfacial layer delaminates as dissolution proceeds [Figure 4.6(b)]. The reason for this may be that as the bubble dissolves and E_{d} increases, it eventually becomes energetically more favourable for the wax layer to detach from the air-oil interface rather than be further compressed. The layer therefore peels intactly, exposing local bare air-oil interface with $E_{\mathrm{d}} = 0$ mN/m, such that the wax-coated bubble dissolves. Thus, $E_{\mathrm{d}} > \sigma/2$ is not a relevant criterion for dissolution arrest in this system, and Pickering stabilisation is not effective in this system. This is in contrast with the observations of [83] for lipid-based oleofoams. It is therefore not possible to generalise the applicability of the findings presented here to other types of oleofoams.

Despite the wax-coated pendant-drop surface not being a true representative of the wax-coated bubble interface, the changes in effective surface tension (Figures 4.10 or A.10) and the interfacial moduli [Figures 4.11(d,e)] upon cyclic area changes suggest that the crystals either undergo desorption or reorganisation. Crystal desorption upon compression is in line with the observations of the wax-layer delaminating around a wax-coated bubble as it dissolves.

4.4.5 Effect of heating on oleofoam stability

At elevated temperatures, $T \geq 70°\mathrm{C}$, the crystal network weakens as evidenced by the decreasing bulk viscosity (Figure 4.8) and moduli [Figure 4.9(b), Figure A.6 and Figure A.7] of the oleogel. Further, while the gel around a bubble weakens, the bubble shrinkage is simultaneously accelerated due to increased gas solubility, inducing stresses in its immediate surroundings. This can yield the gel further, leading to a cascading effect where the bubble shrinks while the gel integrity diminishes. This scenario seems likely as (i) the opacity of the gel is seen to decrease while the bubbles become more spherical with heating between $T = 21.5 - 74°\mathrm{C}$ (Figure 4.7); and (ii) at $T \approx 74°\mathrm{C}$, the crystal network within the bulk appears loose. A similar behaviour is expected of the crystal interfacial layer, explaining why the wax-coated bubbles dissolve at a rate not too different from bare bubbles at higher temperatures [Figure 4.5(b)] while bubbles in the oleofoam dissolve completely [Figure 4.5(c)]. The oleofoam is therefore unstable at temperatures above the peak crystal melting point [Figure 4.1(b)], which roughly corresponds here to the rheological wax (dis)appearance temperature [106].

For the oleofoam as a whole, it is possible that with larger bubbles rising first as the gel weakens locally with increasing T, a stirring effect will be produced that will globally weaken the gel further. Thus, the oleofoam may become unstable even at temperatures close to the peak crystal melting point, if there are many large bubbles.

The effect of temperature cycling – heating and cooling – will change the properties of the oleofoam. Besides the above mechanism, whereby air volume is reduced, the viscosity curves in Figure 4.8 and the oscillatory bulk moduli measurements in Figure A.7 suggest that upon cooling, the oleogel properties change as well. This has implications for transport, storage and processing of such oleofoams, where large temperature changes can change properties irreversibly.

4.4.6 Summary

In this study, the dissolution of bubbles in a model wax-based oleofoam, in conjunction with bulk and interfacial rheological measurements, has shown that although crystals adsorb to the interfaces of bubbles, the Pickering mechanism of stabilisation is insufficient to arrest bubble dissolution. It is found that for bubbles isolated from the oleogel matrix but possessing an interfacial wax layer, even though the Gibbs criterion for bubble stability is met, dissolution is not arrested: peeling of the wax layer from the air-oil interface is energetically more favourable than elastic compression of the layer. Bulk rheological properties of the oleogel surrounding the bubbles therefore play the dominant role in arresting bubble dissolution. Additionally, within the oleofoam, the bulk and interfacial effects may produce synergistic effects. Measuring the oleogel bulk elastic properties that are relevant to prevent bubble dissolution is however challenging due to the thixotropic nature of the oleogel used in the experiments. Finally, given the relatively modest size ratio between bubble size and the oleogel crystals, it may be questioned whether a continuous medium approach of bubble dissolution based on bulk rheological measurements is justified.

Chapter 5

Formation and dynamics of crystal-coated air-oil interfaces

5.1 Introduction

In the creation of particle-coated bubbles, or Pickering Bubbles, particle shape, size and wettability influence the adsorption energy of the particles [5, 4], the bubble size and long-term stability [4, 18, 13, 45, 44]. The corresponding foams are generally created through the agitation of an aqueous particle dispersion, to introduce gas pockets through turbulent mixing. Additionally, the vigorous mixing increases the probability of the air-liquid interfaces coming in contact with particles, and increasing surface coverage to create a compact armour.

Oleofoams can be prepared using crystallising agents [93, 95, 83, 13, 97] with the significant difference that the crystal properties change depending on the protocol used to prepare the foams. This affects the characteristics of the final bulk and interfacial networks formed by the crystals. The nature of an oleofoam is then more strongly dependent on preparation history than for the case for colloid-based aqueous foams. Hence, if an oleofoam is prepared by agitating a hot crystal melt, where crystallisation occurs as it cools, as was done in Chapter 4, several concurrent events will contribute towards the formation of individual crystal-coated bubbles. By varying the tempering protocol, the desired dominant crystal polymorphs can be selected to constitute the oleofoam [97, 95, 13]. Furthermore, shearing a crystal melt, as it cools, can affect the crystallisation process as shear flow can orient crystallites as they grow [13] and, hence, favour growth along certain crystallographic axes. This will influence the dominant polymorph, or also produce tiny crystals due to collision and breakage. In addition to the combined effects of shearing and tempering, the simultaneous introduction of air pockets will partition the crystallising nuclei and crystallites to either in the bulk phase the air-oil interface. The growth of crystals at the interface will be influenced by wettability, local curvature [114], surface tension [115] and heterogeneous cooling, which will be different from the cooling rate in the bulk. Heterogeneous nucleation at interfaces is thermodynamically preferred because of a lower nucleation barrier compared with bulk crystallisation [115]. This is because, when crystallisation is induced by cooling a hot saturated solution, faster cooling occurring at the air-liquid interface makes supersaturation highest at this location. Nucleation at interfaces facilitates nucleation in the bulk [115–118]. Further, as agitation continues, the partially formed interfacial layer is impacted by other bubbles and pre-crystallised debris from the bulk.

In this experimental study, the influence of some of these effects on the properties of the crystal networks forming the bulk oleogel and the interfacial microstructure is investigated. In particular, the effect of shear during crystallisation, on the morphology of crystals at the two locations is focused on. It is examined if there exists any qualitative correlation between the crystal characteristics in the bulk and the interface. Also, an attempt is made at estimating the adhesion energy of a crystal layer at the air-oil interface.

Finally, the effect of dynamic deformation of the curved crystal-coated air-oil interfaces under two extreme timescale regimes, $t \sim 10^3 - 10^4$ s and $t \sim 10^{-4}$ s, is studied qualitatively by observing dissolution of the wax-coated bubbles and the oscillation of such bubbles using acoustic waves, respectively. The link between microstructural evolution and timescale of deformation are considered.

5.2 Methods

5.2.1 Preparation of oleogels and oleofoams

As was the case in Chapter 4, the model system was comprised of a paraffin wax and sunflower oil. The details of preparing the oleofoam and oleogels, through different shearing protocols, are described below. The temperature profiles measured during the preparation of the samples were used with the calibrated temperature-controlled stage to generate a tempering profile that could be used to mimic and recreate the oleofoam/oleogel preparation process, but without the presence of agitation. This was done to better understand the effects in presence and absence of agitation in the properties of the oleogels.

Oleogel and oleofoam preparation through agitative fast-cooling A vial containing 2.5%w/v mixture of wax in sunflower oil was agitated using the vortex mixer at 3000 rpm for 2 minutes to form a well mixed suspension by breaking the aggregated wax. The suspension was then heated on the hotplate to melt the wax, with the temperature of the sample being monitored using the thermocouple. The heating rate was estimated to occur at 9.2°C/min. Upon attaining $T = 90°\text{C}$, the sample appeared as a clear solution. The vial was immediately agitated using the vortex mixer for 2 minutes. Vortexing was either done at 3000 rpm to incorporate air to form an oleofoam; or at 750 rpm to get an oleogel. Temperatures of the sample before and after this vortexing were recorded, which gave an estimated *fast-cooling* rate of $-23.5°\text{C/min}$ occurring due to the agitation, for both vortexing rates. This meant that the sample had cooled to $T \approx 43 - 45°\text{C}$. The vial was then placed upright on a flat surface and allowed to cool to room temperature, undisturbed, for 1 hour. The rate of cooling was monitored with a thermocouple placed into the sample, through a small perforation made in the vial cap. The sample was found to cool from $T \approx 45°\text{C}$ to room temperature $T = 23.4°\text{C}$ at a relatively *slow-cooling* rate of $-3.7°\text{C/min}$. The oleogel prepared this way shall be referred to as ‘oleogel750’ in the remainder of the text.

Oleogel samples prepared without agitation or with controlled agitation The tempering profile measured above, as shown in Figure 5.1(a), was used to generate other oleogel samples but with different degrees of agitation during the fast-cooling step.

Oleogel samples that were prepared by implementing the tempering profile on the calibrated temperature-controlled stage, where there was no agitation during the fast-cooling step, are referred to as ‘unagitated-oleogel’ or ‘U-oleogel’.

Some oleogel samples were also prepared in-situ in the rheometer. For this, a suspension of 2.5%w/v wax-oil suspension was transferred onto the rheometer plate using a pipette. The cone was lowered to a minimum gap of 0.101 mm, followed by

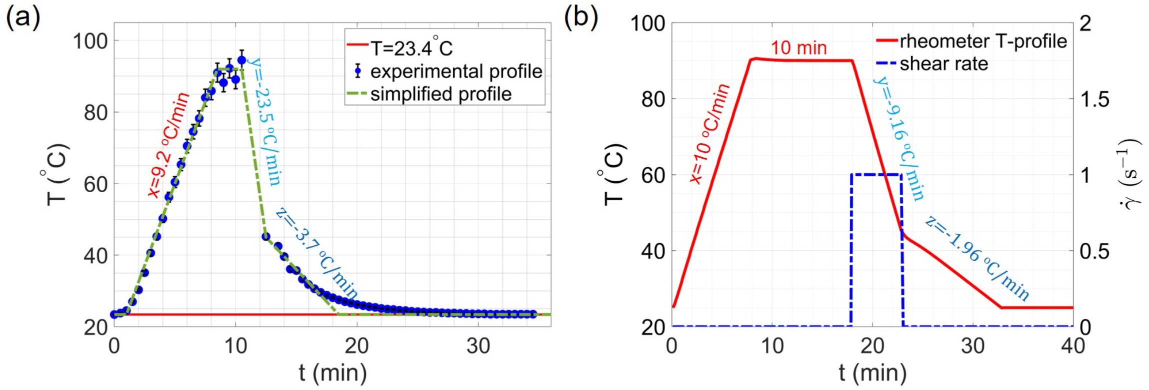

Fig. 5.1 **Tempering profiles used to prepare oleofoams and oleogels.** (a) The room temperature was measured to be $T = 23.4$°C (solid red line), while the temperature of the sample in the vial undergoing heating, agitation and cooling was recorded (blue filled circles with error bars) while preparing the oleofoams and oleogels. The simplified tempering profile (dashed green line) to mimic the experimental preparation protocol was used to prepare oleogels without agitation. This involved a heating rate of $x = +9.2$°C/min, a fast-cooling step at $y = -23.5$°C/min and a slow-cooling step at $z = -3.7$°C/min. (b) The actual tempering profile used to prepare the rheometer-oleogels is shown (red solid line) with $x = +10$°C/min, $y = -9.16$°C/min and $z = -1.96$°C/min. The shear rate $\dot{\gamma}$ was switched on only during the fast-cooling step. A representative shearing profile is shown for $\dot{\gamma} = 1$ s^{-1} (dashed blue line).

trimming of the excess sample. The base temperature was set at $T = 25$°C. The sample was then heated, at a rate of 10°C/min, to $T = 90$°C and left at that temperature for 10 minutes to allow the sample to attain a uniform temperature. The fast heating was possible due to the Peltier element present in the plate. Whereas, the use of the water bath to cool the system, limited the cooling rate to −9.16°C/min to mimic the fast-cooling step. During this latter step, the sample was simultaneously sheared at a rate $\dot{\gamma}$ to mimic the effect of agitation with fast-cooling. Separate samples were prepared using different values of shear rates varying with $\dot{\gamma} = 0, 1, 10$ and 100 s^{-1}. The shearing was stopped when the sample reached $T = 45$°C and then the cooling rate was switched to a rate of −1.96°C/min, to allow for a slow-cooling until $T = 25$°C. The sample was left undisturbed for 1 hour before further tests were conducted using the rheometer. The typical tempering and shear profile using the rheometer is shown in Figure 5.1(b).

The oleogels prepared using the rheometer shall be referred to as 'RO-0' (rheometer-oleogel-0), 'RO-1', 'RO-10' and 'RO-100' for the shear rates $\dot{\gamma} = 0, 1, 10$ and 100 s^{-1} used during the fast-cooling step, respectively.

The differences in base temperatures $T = 23.4°\text{C}$, for the oleogels prepared in vials, and $T = 25°\text{C}$, for the rheometer-oleogels, were not expected to contribute to differences in properties as both temperatures were below the first crystal melting peak temperature $T_\text{m} = 65°\text{C}$ [Chapter 4, Figure 4.1(b)].

5.2.2 Microscopic imaging of samples

Samples were introduced into microscope slides using the method described in section 3.2. Polarised light microscopy was achieved using two dichroic film polariser sheets (Thorlabs LPVISE2X2), one placed before the condenser and another after the sample in the inverted microscope.

The shape and size distribution for the observed crystals was measured using ellipse-fitting methods using the open-source software ImageJ. This was done after appropriately diluting the samples to avoid agglomerated crystal clusters. An appropriate threshold was selected to distinguish between image background and the crystals.

5.2.3 Surface free energy measurements

To assess the surface energy of an oleogel surface in air or sunflower oil, the method of Owens and Wendt 1969 [86], and further described by Hejda, et. al. 2010 [87], was used. This was repeated with glass surfaces to test the accuracy of the method by comparing values of the surface energy for the same reported in literature. Sessile drops of liquids, with a wide range of polarity were deposited on oleogel and glass surfaces, to determine the surface energy of these substrates. The general procedure is described in section 3.8, while the preparation of the oleogel substrate is described below.

An unagitated-oleogel sample was prepared using the temperature-controlled stage to act as a substrate for surface energy measurements. For this a rectangular 76 mm ×26 mm slab of PDMS with 1.5 mm thickness was cut in the middle to form a hollowed volume of 60 mm×10 mm×1.5 mm. This PDMS ‘spacer’ was then stuck onto a 76 mm ×26 mm cleaned glass slide. A 2.5 % w/v wax-oil suspension was filled into the volume and gently placed into the temperature-controlled stage without a cover-slip. The tempering protocol described in section 5.2.1 for the U-oleogel was followed. After one hour of leaving the sample undisturbed, the sessile drop experiments were conducted. For this the slides containing the oleogel surface were placed on a custom-built goniometer. Then the sessile drop of a liquid was placed onto the surface carefully using a hand-held syringe with a needle (outer diameter 0.5 mm).

Table 5.1 Surface tension σ, with dispersive σ^{d} and polar σ^{p} components of liquids used for determining surface energies of solid substrates. For the sunflower oil, the surface tension was measured using pendant drop tensiometry at $T = 25$°C.

Liquid	σ (mN m^{-1})	σ^{d} (mN m^{-1})	σ^{p} (mN m^{-1})
n-decane	23.8	23.8	0
CH_2I_2	50.8	49	1.8
DMSO	44	36	8
NMP	40.8	29.2	11.6
EG	47.7	26.3	21.4
Glycerol	62.4	29	33.4
Water	72.8	22.1	50.7
Oil	33.0	-	-

The surface energy of the unagitated-oleogel was determined using sessile drops of solvents of n-decane, diiodomethane (CH_2I_2), N-methyl-2-pyrrolidone (NMP), ethylene glycol (EG), dimethyl sulfoxide (DMSO), glycerol and ultrapure water. The surface tensions and their components for these liquids were obtained from [119, 120] and are summarised in Table 5.1. The surface energy of borosilicate glass microscope slides were also obtained using the above liquids to serve as a check for the accuracy of the method. Images of the sessile drops were taken using a CMOS camera (Thorlabs DCC1545M) and the contact angles were determined by ellipse-fitting using the ImageJ plugin ‘Contact Angle’.

5.2.4 Ultrasound-induced bubble oscillations

Wax-coated bubbles, suspended in oil, were subjected volumetric oscillations through acoustic forcing. To achieve this, bubbles from the oleofoam were transferred onto a glass plate with a PDMS spacer forming an enclosure, and the volume was filled with oil to dilute and remove the bulk crystal network. The plate had a transducer stuck to it as described in section 3.12.

While the absolute acoustic pressure P_{a} generated by the transducer was unknown, it was varied by changing the gain value of the amplifier. The power output from the amplifier was known to vary linearly with gain. But the pressure amplitude P_{a}

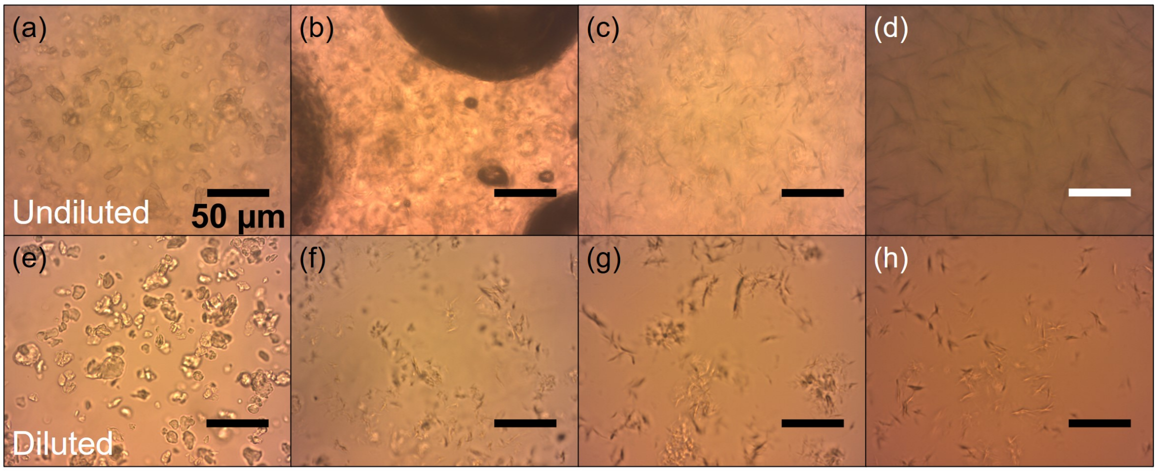

Fig. 5.2 **Micrographs of crystals, with original samples in top row and respective diluted samples in bottom row.** Wax-oil suspension at (a) 2.5 % w/v concentration, (e) diluted by oil; (b) oleofoam interstitial gel, (f) diluted oleofoam; (c) oleogel750, (g) diluted oleogel750; (d) unagitated oleogel prepared using temperature-controlled stage and (h) the diluted sample. All samples were observed 1 hour after preparation.

generated by the transducer could not be calibrated as it was not possible to measure the pressure field within the small enclosure using a hydrophone. For this reason, the amplification or gain value A (in %) is used as a representative for P_a in this chapter.

5.3 Results

5.3.1 Morphology of crystals

Oleofoam, oleogel750 and U-oleogel

Following oleogel and oleofoam preparation and leaving it undisturbed for 1 hour, microscopic images were taken to visualise the crystals. These samples were diluted with oil to better visualise the crystals. The same was done for the U-oleogel. The crystal morphologies for the wax-oil suspension and the other samples are shown in Figure 5.2, for both undiluted [panels (a-d)] and diluted samples [panels (e-h)].

The crystals in the wax-oil suspension appeared platelet-like with a mean size of 9 μm [Figure 5.2(a,e)]. Crystals in the oleofoam, which had been subjected to strong shear during the fast-cooling, mostly appeared to be small and platelet-like

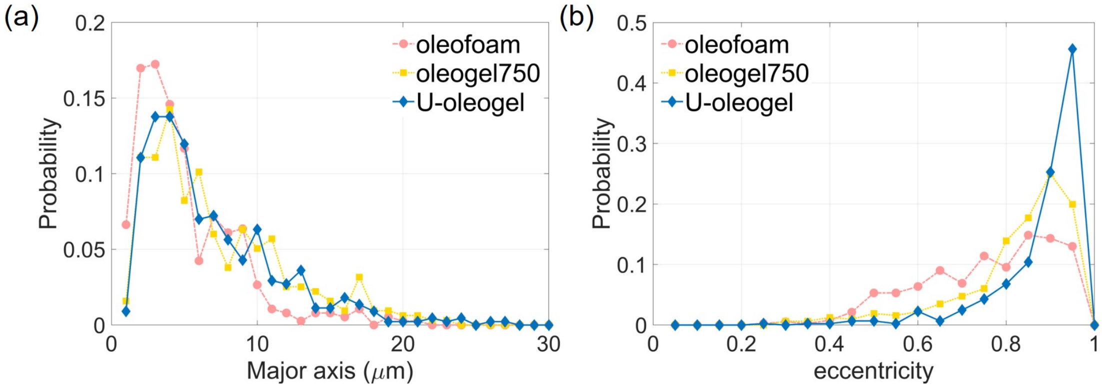

Fig. 5.3 **Ellipse-fitting to determine size and shape distribution of crystals.** (a) The size distribution of the crystals in terms of the length of major-axis of the fitted ellipses. (b) 2D shape distribution of the crystals in terms of eccentricity (e); where $e = 0$ means a circular shape, while $e \to 1$ represents an elongated elliptical shape. The distributions are shown for the crystals of the diluted oleofoam (pink circles), oleogel750 (yellow squares) and unagitated-oleogel (or U-oleogel as blue diamonds).

[Figure 5.2(b,f)]. In the oleogel750, some needle-like crystals were also apparent [Figure 5.2(c,g)]. Whereas, in the U-oleogel, needle-like crystals appeared to be the dominant polymorph shape along with a few star-shaped crystals [Figure 5.2(d,h)]. Platelet-like crystals were not noticed.

The above qualitative descriptions in size and shape are quantitatively supported by ellipse-fitting. The crystal sizes are expressed in terms of the length of the major axes of the fitted ellipses and the eccentricity, $e = \sqrt{1-(b/a)^2}$, of the ellipses gives a rough representation of how circular or needle-shaped the crystals are. Here a is the length of the major-axis, while b is the length of the minor axis. An eccentricity of 0 represents a circle, while a value close to 1 represents a needle or elongated elliptical shape. It appears that the oleofoam crystals are on average smaller than the crystals occurring in the oleogel750 or the U-oleogel, as seen in Figure 5.3(a). In terms of shape distribution in Figure 5.3(b), the crystals in the U-oleogel have a narrow eccentricity close to 1, supporting the observation that the crystals are mostly needle-like [Figure 5.2(d,h)]. The crystals in oleogel750 seem to be a mixture of both needle-like and platelet-like crystals, distribution of which is intermediate between the oleofoam and U-oleogel crystal shapes.

Rheometer-prepared oleogels

The micrographs of the crystals of the four types of oleogels prepared in the rheometer are shown in Figure 5.4 with the shear rates $\dot{\gamma}$, used during fast-cooling, given in the respective panels.

The RO-0 crystals appear to have equal populations of star-shaped crystals with platelet-like crystals, with the longest average dimension for the star-shaped crystals being $\approx 18\ \mu$m. For the RO-1, RO-10 and RO-100 samples, correspondingly, the star-shaped crystals decreased both in size and number. The dominant crystal population is platelet-like.

The occurrence of platelet-like crystals for the RO-0 oleogel contrasts with the fact that there are no noticeable platelet-like crystals in the U-oleogel [Figure 5.2(d,h)] For both the RO-0 and U-oleogel, there was no agitation during the fast-cooling step. This discrepancy in crystal morphologies between the two was hypothesised to arise from the differences in the cooling rates during the 'fast-cooling' step, in the rheometer and temperature-controlled stage respectively. For the U-oleogel this was $\mathrm{d}T/\mathrm{d}t = -23.5$°C/min while for the RO-0 oleogel $\mathrm{d}T/\mathrm{d}t = -9.16$°C/min [compare Figures 5.1(a) and (b)]. To test this hypothesis, an unagitated oleogel was prepared using the temperature-controlled stage using $\mathrm{d}T/\mathrm{d}t = -9$°C/min and this time also star-shaped crystals were found along with the needle-like crystals, without any platelets. Finally, the effect of non-uniform tempering was checked. For this an oleogel sample was prepared using the temperature-controlled stage with $\mathrm{d}T/\mathrm{d}t = -23.5$°C/min by placing only part of the slide within the region of the heating element, while the remainder was outside, which would lead to non-uniform tempering within the sample. Following the tempering, microscopic visualisation revealed the presence of numerous platelet-like crystals, with a few star-shaped crystals, for the part of the sample that was outside the heated region. Whereas, within the uniformly heated region, only star and needle shaped crystals were found. These trends are summarised by the micrographs of the gels in Figure B.1 – for (i) U-oleogel, (ii) U-oleogel prepared with $\mathrm{d}T/\mathrm{d}t = -9$°C/min, (iii) RO-0, and (iv) U-oleogel prepared with non-uniform tempering.

The above experiments and observations suggest that platelet-like crystals form as a consequence of non-uniform cooling coupled with a fast cooling rate in the sample, as happens in the cone-plate geometry of the rheometer [Figure B.1(d)], rather than

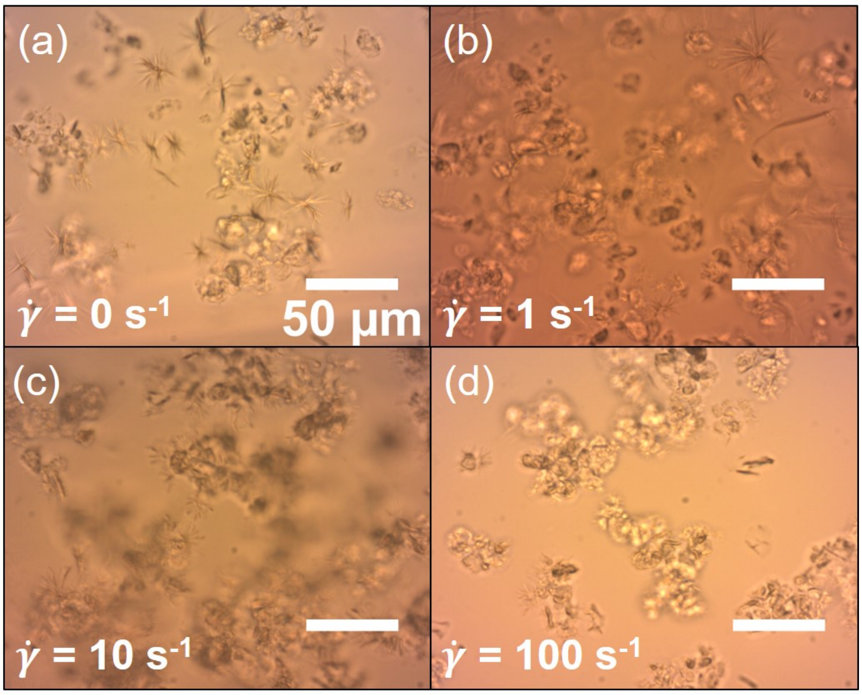
(a)
$\dot{\gamma}$ = 0 s^{-1}
50 µm
(b)
$\dot{\gamma}$ = 1 s^{-1}
(c)
$\dot{\gamma}$ = 10 s^{-1}
(d)
$\dot{\gamma}$ = 100 s^{-1}

Fig. 5.4 **Micrographs of rheometer-prepared oleogels.** Crystal morphologies observed in oleogels prepared in-situ in the rheometer for (a) RO-0; (b) RO-1; (c) RO-10 and (d) RO-100. The rheometer-oleogels (RO) were prepared using a shear rate of $\dot{\gamma} = 0, 1, 10$ and 100 s^{-1}, respectively, during the fast-cooling step where $\mathrm{d}T/\mathrm{d}t = -9.16$°C/min.

solely due to differences in cooling rates. Uniform cooling leads to the formation of needle-shaped and star-shaped crystals only [Figure B.1(a,b)].

5.3.2 Oscillatory rheology of oleogels

Frequency-sweeps for the U-oleogel, oleogel750 and oleofoam, were performed at $\gamma = 0.05$ %, as this was identified to lie within the linear viscoelastic regime for the oleogel750 as already seen in Figure 4.9. No pre-shear was applied to the samples, before testing, as the aim was to probe initial properties with minimal destruction of the existing crystal networks, either in the bulk or at bubble interfaces. The storage moduli G' at $T = 25$°C for the three samples are compared in Figure 5.5(a). The effect of frequency on both storage and loss moduli for each sample are also shown separately in Figure B.2(a,c,e). The samples were allowed to relax for 5 minutes before performing amplitude-sweeps at $f = 1$ Hz as shown in Figure B.2(b,d,e). Interestingly,

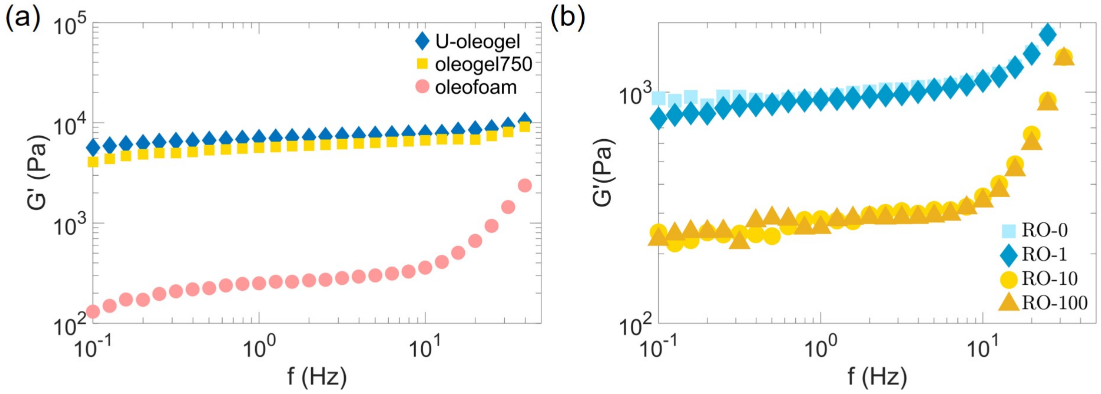

Fig. 5.5 **Oscillatory frequency-sweep of oleogels and oleofoam.** (a) Comparison of the behaviour of storage moduli with frequency-sweeps for the U-oleogel (blue diamonds), oleogel750 (yellow squares) and oleofoam (pink circles) at a constant strain of $\gamma = 0.05$ %. (b) Comparing storage moduli for the rheometer-prepared oleogels RO-0 (cyan squares), RO-1 (blue diamonds), RO-10 (yellow circles) and RO-100 (deep yellow triangles). All samples were tested at $T = 25$°C.

the values of the initial G' for both the U-oleogel and oleogel750 are similar despite the crystal morphologies being quite different [Figure 5.2(c,g), (d,h) and Figure 5.3]. For the oleofoam G' is roughly two orders of magnitude smaller, possibly due to the presence of bubbles.

Similarly, oscillatory bulk rheological tests were performed on the rheometer-prepared samples RO-0, RO-1, RO-10 and RO-100. The frequency sweeps are shown in Figure 5.5(b), where again the strain amplitude was fixed at $\gamma = 0.05\%$. Both bulk moduli for each gel are separately shown in Figure B.3 for frequency-sweeps and Figure B.4 for the amplitude-sweeps performed at fixed $f = 1$ Hz and $T = 25$°C. Here it is noticed that the RO-0 and RO-1 have similar behaviour with $G' \sim 10^3$ Pa initially. Whereas, both RO-10 and RO-100 behave similarly with $G' \sim 10^2$ Pa. This grouped behaviour among the gels suggests an intermediate threshold shear rate $\dot{\gamma}_{\text{th}}$ lying between $\dot{\gamma}$ =1-10 s^{-1}. During the fast-cooling step, when crystal growth is maximum (Section 5.3.4), application of a shear $\dot{\gamma} < \dot{\gamma}_{\text{th}}$ may lead to oleogels with similar properties, while for $\dot{\gamma} > \dot{\gamma}_{\text{th}}$, the oleogels will exhibit comparatively weaker gel strengths. Yet this contradicts with what is observed between the U-oleogel and oleogel750 [Figure 5.5(a)]. For the latter the shear applied during crystallisation was much higher than 100 s^{-1}. Thus, there seems to be a non-monotonic dependence of G' with $\dot{\gamma}$.

5.3.3 Wax-coated bubbles in oleofoams

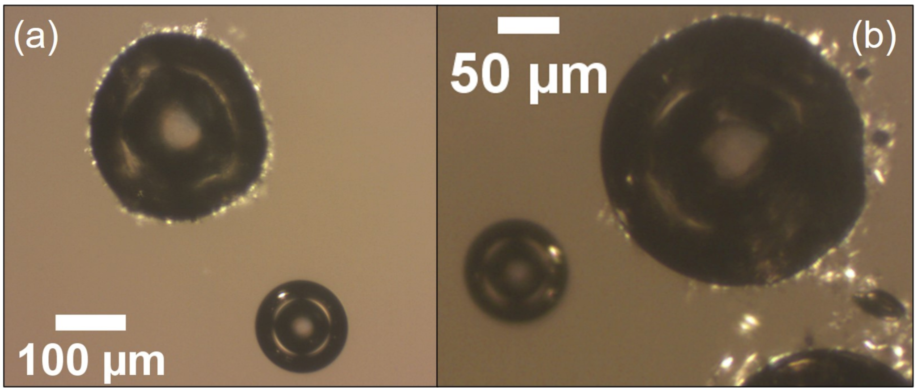

Fig. 5.6 **Polarised light optical microscopy of wax-coated bubbles resuspended in oil.** (a) A wax-coated bubble (top) compared to an injected bare bubble (bottom). (b) Close-up view of a bubble which appears to be partially coated (top right).

Wax-coated bubbles from the oleofoam were isolated and resuspended in oil to remove bulk crystals, as was described in section 3.3. The use of cross-polarisers, during microscopy, highlighted the differences between a coated and a bare bubble. The apparent shape and illumination of the bubble contours differed for the two cases. The crystal-coated bubbles were typically non-spherical and exhibited a halo of light at their contours, originating from the birefringence of the crystals. This illuminated contour was found to be absent for bare bubbles, as seen in Figure 5.6 and Figure B.5. Further, for bubbles that are partially covered with crystals on one side, for example, as evidenced from the localised bright contour on the right side of the bubble in Figure 5.6(b), the curvature appears non-uniform locally. Whereas, on the left side, the curvature appears uniform where the interface is locally devoid of crystals. This suggests that crystal clusters or rafts may induce local interfacial elastic effects, wherever they are present. Also, that the crystal layer does not expand to fill the uncovered area, as would be expected for a cohesive layer.

Close examination of bubbles as in Figure B.7 indicate that there is a multilayer of wax crystals at the air-oil interface in some regions.

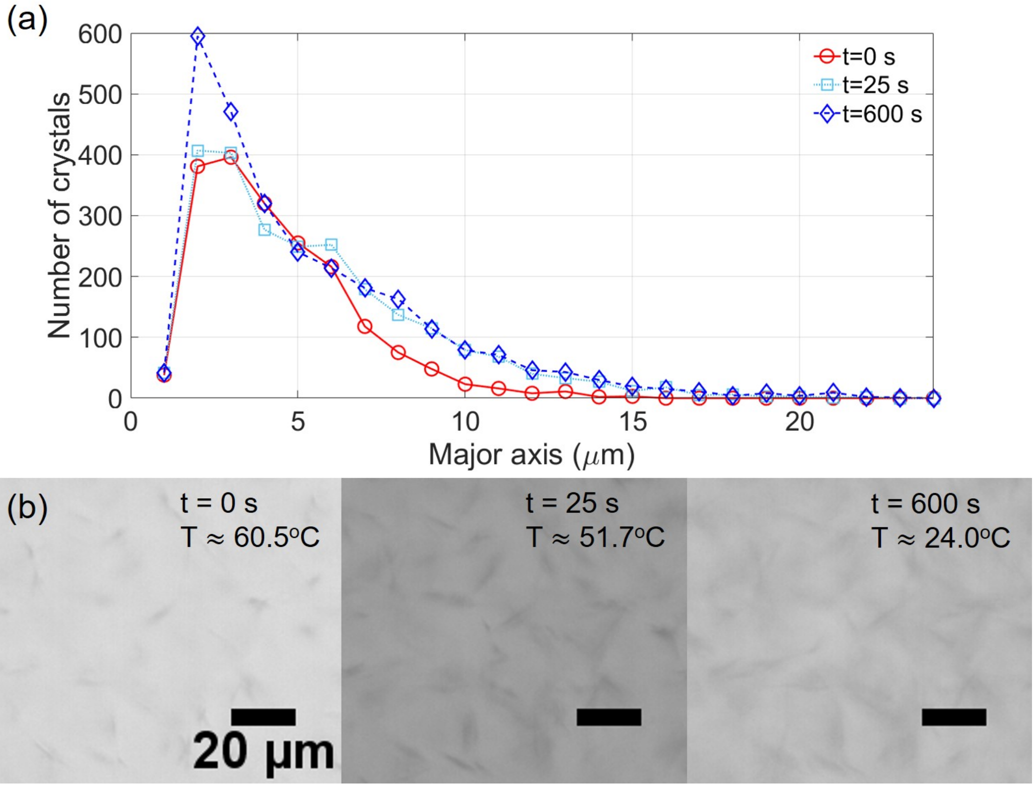

Fig. 5.7 **Crystal size distribution during cooling.** (a) The size distribution of crystals during the first noticeable appearance at $t = 0$ s (red circles), then after $t = 25$ s (cyan squares) and $t = 600$ s (blue diamonds). (b) The micrographs of the sample at a fixed location at the same times, with the temperatures T also marked. A zoomed region of the frames is provided to show the crystals. Whereas, each frame contained around 1000 crystals. The contrasts in the images vary as the illumination during the experiments had to be adjusted manually as the opacity of the samples varied with temperature and time.

5.3.4 Crystal growth in oleogels

The crystal appearance and growth during the cooling of a heated wax-oil mixture, while preparing the U-oleogel, was observed using a 10× magnification objective. During the fast-cooling step, crystals become visually apparent at $T = 60.5 \pm 1.5$°C, based on 3 repeats, which is close to $T_{\mathrm{m}} = 65$°C. From the time of first appearance at $t = 0$ s, the successive growth in the number of crystals at $t = 25$ s ($T \approx 52$°C) and 600 s ($T \approx 24$°C) are summarised by Figure 5.7(a).

The zoomed frames at these times are shown in Figure 5.7(b). The full frames typically contained around 1000 crystals and are provided in Figure B.6. Image analysis beyond $t = 25$ s becomes unreliable as it is difficult to distinguish crystals that are not in the focal plane.

While most crystals appear to form during the fast-cooling step, the gel stiffens mainly during the slow-cooling step. This is indirectly evidenced by tilting a vial containing oleogel750 just after the fast-cooling step, where the sample flows as a viscous liquid. But when tilted after the 1 hour slow-cooling step, the gel does not flow, even upon inversion of the vial. This is likely to be due to linking and sintering of neighbouring crystal networks as growth may still continue [97].

5.3.5 Crystallisation at interfaces

Crystallisation at bubble interfaces

To gain insights into how crystals appear at the bubble interface, and also to decouple the effects of tempering from agitation, an unagitated-oleogel was prepared where air bubbles were present in the system beforehand. To achieve this, bubbles were introduced using a hand-held syringe into a wax-oil suspension filled into a thin PDMS enclosure on a glass slide. A glass cover-slip was put on top to seal the system, which was then placed into the temperature-controlled stage. The thin spacing between the glass slide and cover slip, caused the large bubbles to form a ‘pancake’ shape [sketched in Figure 5.12(a)]. This facilitated visualisation of the bubble contour with a reduced depth perpendicular to the focal plane. The tempering protocol to prepare the U-oleogel was followed. One of the bubbles is shown in Figure 5.8(a). It has an initial diameter of $D_0 \approx 930$ μm in the focal plane, and is surrounded by the platelet-like crystals. The bubble appears dark near its periphery because of the light having to pass through the curved air-liquid interfaces [121–123]. At $T = 90$°C, the bulk appears clear as the crystals have melted [Figure 5.8(b)]. After cooling, the final state is shown in Figure 5.8(c), where the bulk crystals appear needle-shaped and the bubble has attained a non-circular shape in the focal plane.

Figure 5.8(d) shows some of the intermediate image sequences for the same bubble, with a closer view of the air-oil interface, as the system cooled from $T = 90 - 22$°C. Crystals become visible, both in the bulk and at the interface, at $T = 63$°C. Further cooling leads to crystal growth and eventually the bubble interface contracts and attains a locally non-uniform curvature. As the bubble shrinks, the interface moves

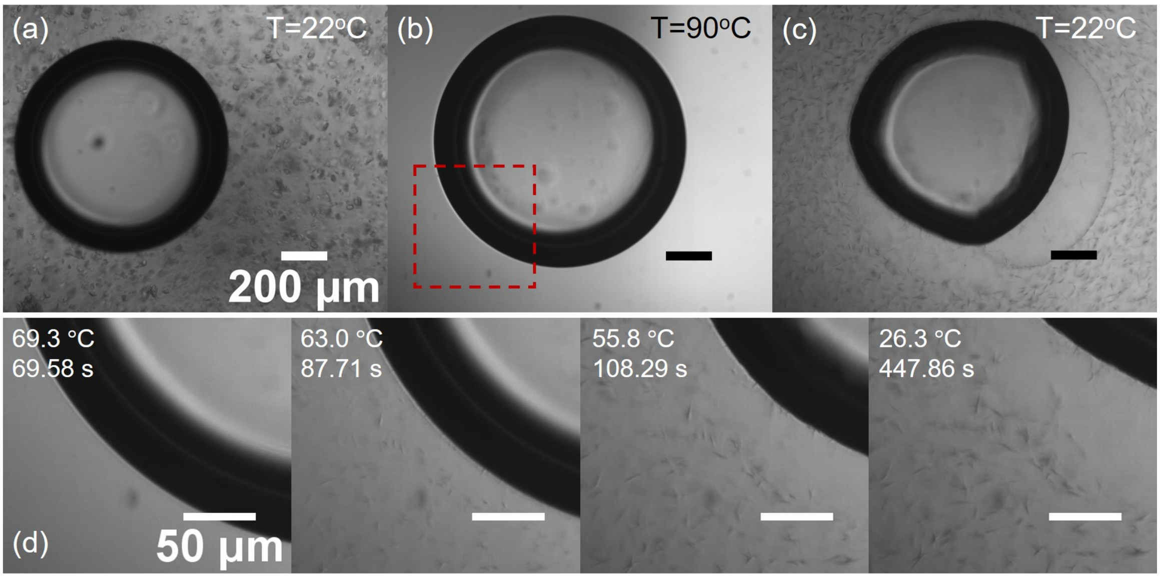

Fig. 5.8 **Unagitated crystallisation in presence of an air bubble.** (a) A bubble of initial diameter $D_0 \approx 930\ \mu$m in the wax-oil suspension at $T = 22°$C. The surrounding crystals are platelet-like. (b) The bubble at $T = 90°$C, following coalescence with a neighbouring bubble, with the bulk appearing clear. (c) The same bubble as in (b), but at $T = 22°$C, after crystallisation has occurred. The bubble curvature appears to vary discontinuously along its perimeter in the focal plane passing through the diameter. The bulk crystals appear needle-like. (d) Image sequences in the highlighted red-dashed square region in panel (b): showing crystallisation occurring at the air-oil interface of the bubble as the system cools at $d\mathrm{T}/\mathrm{dt} = -25°\mathrm{C}/\mathrm{min}$. Crystals become visible at $T = 63°$C and at $T = 55.8°$C, the interface curvature profile is not smooth. As the bubble interface recedes further, the interfacial crystals move with the interface ($t = 447.86$ s).

towards the bubble centre and the crystals at the interface move with it [Figure 5.8(d) $t = 108.29 - 447.86$ s]. This indicates that the crystals are adsorbed at the interface.

A more elaborate image sequence exhibiting these observations, on a larger scale and time interval, is shown in Figure 5.9 where $t = 0$ s marks the onset of the cooling from $T = 90°$C. In section 5.3.6, this sequence is used to estimate the adhesion energy of the crystal layer with the air-oil interface. It is seen that between $t = 24.50 - 75.63$ s the bubble in focus coalesces with another to form a larger bubble. As the system cools, crystals start appearing in the bulk between $T = 61.3 - 67.2°$C, and closely agrees with what was observed during crystallisation in the U-oleogel samples, without bubbles (section 5.3.4). At $T = 61.3°$C, the bubble's projected shape starts deviating from a circle and this is more pronounced at $T = 54.5°$C, when the crystals are prominent in the bulk. While the bubble shrinks, the lower left part of the interface contracts and a region devoid of crystals is seen, which was previously occupied by the bubble (t = 141.03 s and T = 44.8°C). This probably happens as both the bulk viscosity and the elastic modulus of the gel increase with the drop in temperature, effectively immobilising the crystals by the strengthening cohesive interactions. Figures 4.8 and 4.9(b) in Chapter 4, even though presented for the oleogel750, supports this notion. At the same time, beyond the crystal-devoid region, there are crystals, adsorbed at the interface, moving with the contracting bubble interface. This is prominent in Figure 5.9 at $t = 112.6 - 141.03$ s [and closely, in Figure 5.8(d) at $t = 108.29 - 447.86$ s]. Then suddenly the bubble tries to attain a uniform curvature with the interface moving outward. This is followed by the lower right part of the interface contracting. A sharp phase separation boundary appears, lined with crystals separating the oil from the oleogel crystals. Almost no crystals are apparent within the region between the phase line and the bubble. Interestingly, the bubble interface now has a locally smooth curvature profile even as it contracts ($t = 196.56 - 613.77$ s). This suggests that just before the abrupt detachment leading to the phase-line at $t = 141.03$ s, the crystals at that locale are subjected to a pull on both sides– (i) to move with the receding interface and (ii) to remain cohesively bonded to the bulk crystals. When the latter is stronger, the phase-line is created. Additionally, it appears that the needle-like crystals are tangentially oriented at the phase-line. If these were indeed crystals that were previously adsorbed at the interface of the bubble, then it indicates that the crystals were adsorbed with their major-axes oriented parallel to the interface. This would then agree with the findings by [124, 95], where X-ray diffraction techniques were used to probe the distribution and orientation of vegetable oil fat crystals around oil-water emulsions [124] and bubbles [95]. In the former, lamellar planes of fat crystals, formed at the oil-water interface, were found to be parallel to interface. While in the latter, similar observations were made of the fat crystals being oriented parallel close to and at the bubble interfaces.

Crystallisation at a planar interface

In order to verify that crystallisation indeed occurs independently at interfaces, additional sets of experiments were undertaken. First, a PDMS enclosure, on a glass slide, was filled to the brim with wax-oil suspension to get a flat interface at the centre of the enclosure [Figure 5.10(a)]. No cover-slip was placed on top. This was placed carefully

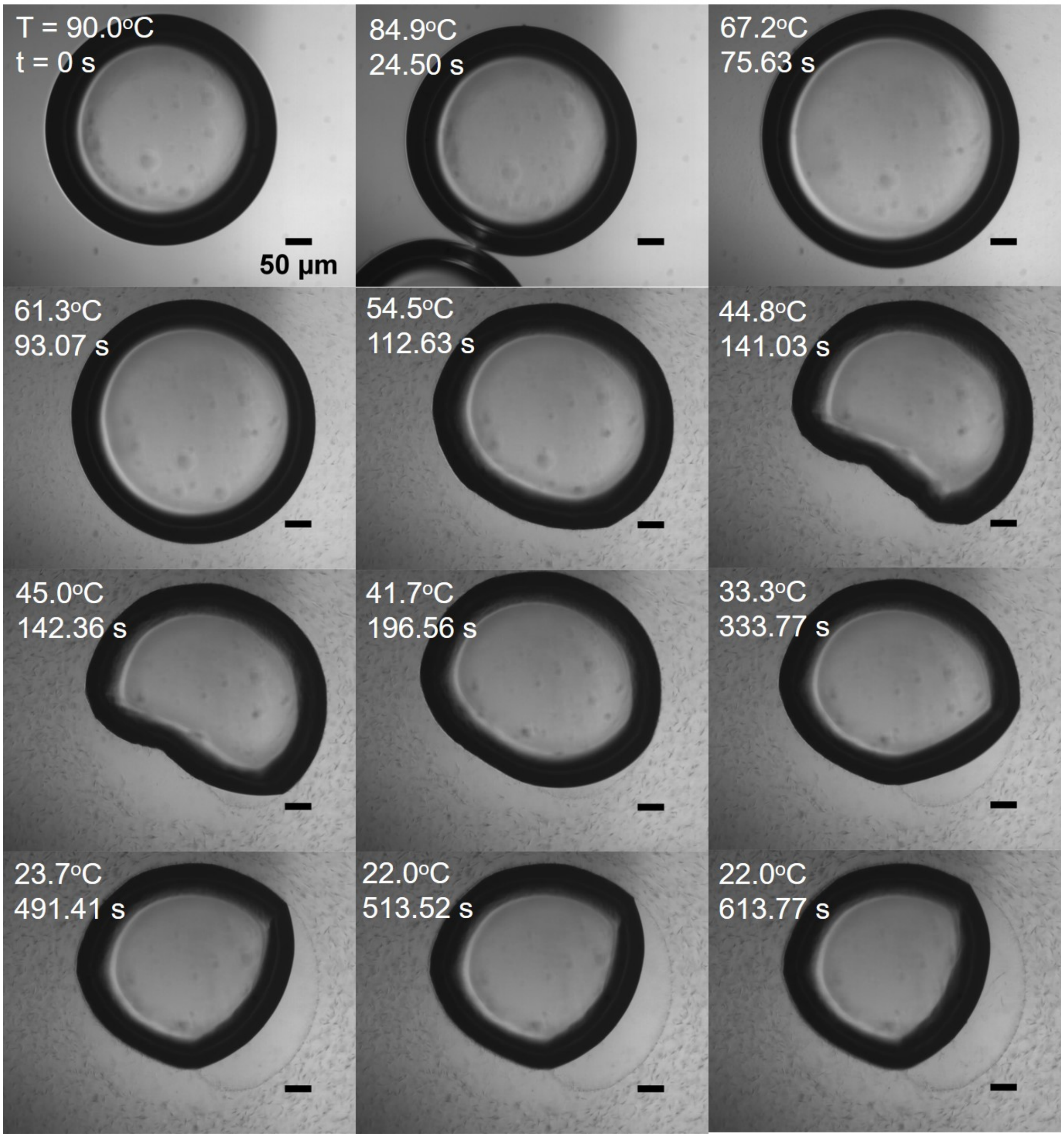
T = 90.0°C
t = 0 s
50 µm
84.9°C
24.50 s
67.2°C
75.63 s
61.3°C
93.07 s
54.5°C
112.63 s
44.8°C
141.03 s
45.0°C
142.36 s
41.7°C
196.56 s
33.3°C
333.77 s
23.7°C
491.41 s
22.0°C
513.52 s
22.0°C
613.77 s

Fig. 5.9 Image sequence of crystallisation occurring in presence of an air bubble in the wax-oil suspension. $t = 0$ s marks the start of the cooling steps, where initially $T = 90°\text{C}$ and the final room temperature is $T = 22°\text{C}$.

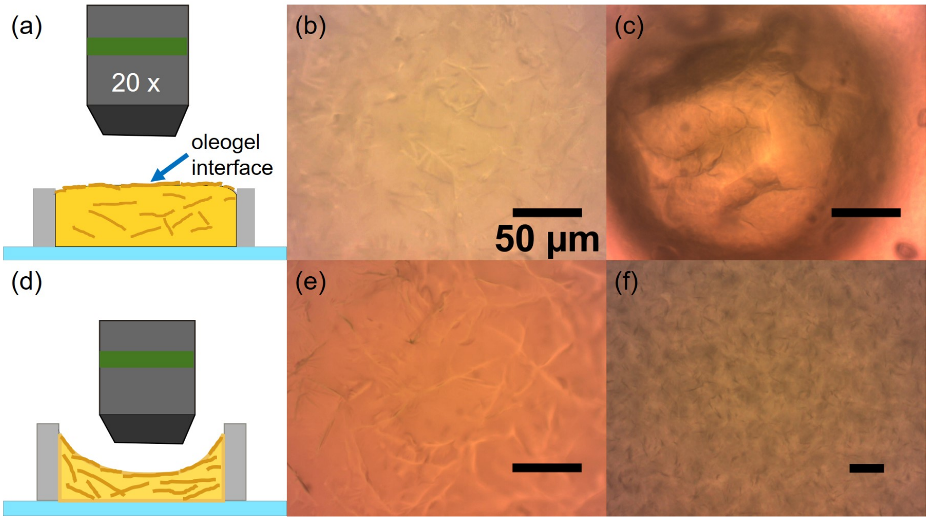

Fig. 5.10 **Crystallisation at oleogel interface.** (a) The schematic of the setup is shown where a 20× objective is moved towards the bulk of the oleogel. The oleogel is contained within a PDMS enclosure, on a glass slide. (b) Micrograph showing the wrinkled interface. Individual crystals are not identifiable. (c) A bubble in an oleofoam observed with a 20× objective shows similar wrinkles on its surface. (d) Schematic of an oleogel interface with a radius of curvature ~ 0.1 mm with a micrograph (e) showing the interface. (f) Crystals in the oleogel for the gel in (b) visualised using a 10× objective reveals discernable crystals in the bulk, unlike at the interface.

into the temperature-controlled stage. The usual tempering protocol to prepare the U-oleogel was followed and the objective was focused at the interface. Crystal growth was observed to occur at the interface. To confirm that the crystallisation had occurred at the interface itself, the sample was taken out of the cooling-stage and a 20× objective with a depth of field of ≈ 2.6 μm was used to slowly move towards the sample, into the bulk. The interface appeared rough with wrinkles as seen in Figure 5.10(b), similar to what is observed for a bubble in the oleofoam [Figure 5.10(c)].

To check if curvature played any role on surface texture, another sample was prepared with a PDMS enclosure of thickness 2 mm. This time the wax-oil suspension partially filled the volume so that the interface had a radius of curvature of around 1 mm. During observation, the 20× objective had to be adjusted vertically as the interface went out of focus as it curved upwards away from the centre [Figure 5.10(d)]. This is seen in Figure 5.10(e), where the right side of the image is a little hazy. Finally, in both the prepared gels, using the 10× objective, with a greater depth of field, showed that the crystals in the bulk were distinguishable [Figure 5.10(f)], and smaller than the typical wrinkle lines at the interface.

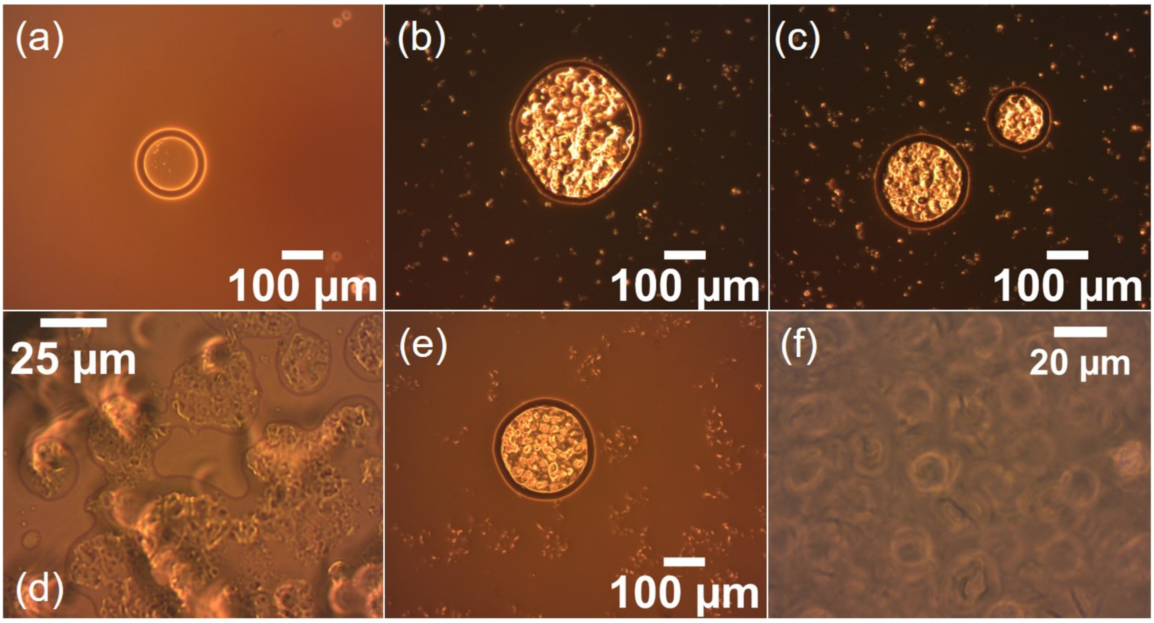

Fig. 5.11 **Bubbles flattened between glass plates.** The spacing between the glass plates is between $20 - 50$ μm and is filled with oil. (a) A bare bubble appears quite clear, with two bright rings. (b-d) Bubbles extracted from oleofoams; and (e-f) bubbles that were prepared in the U-oleogel.

Overall, even upon using high magnification, the interface appears to be constituted of fine, indistinguishable crystals.

Crystal polymorphs at bubble interfaces

To compare interfacial crystals adsorbed on bubbles within the oleofoam, that were subjected to vigorous agitation during crystallisation, and bubbles present in the U-oleogel, where agitation during crystallisation was absent, isolated bubbles were observed. The bubbles from their respective preparation samples were transferred onto a glass slide with sessile oil drops. The oil was added to remove bulk crystals away from the bubbles. Then a cover-slip was pressed onto it to squeeze the bubbles between the glass planes, without a spacer, resulting in a spacing of $20 - 50$ μm. This allowed clear visualisation of crystals confined within the region of the flattened bubbles. For comparison, bare bubbles under the same configuration were also observed [Figure 5.11(a)]. In Figure 5.11(b-d), crystals confined within the bubble rims for oleofoam bubbles are presented. They appear platelet-like that are joined to form large aggregates. Whereas, Figure 5.11(e-f) shows that bubbles, that were extracted from the U-oleogel, have needle-like crystals within the bubble region along with platelet-like crystals. The bubbles prepared within the U-oleogel were delicate to recover as they ruptured when trying to extract them from the prepared sample, and so only a few were observed. This prevented generalising the features observed for the surface crystals on bubble prepared without agitation.

5.3.6 Determination of adsorption energy of an adsorbed crystal layer

The observations of the bubble interface separating from the bulk oleogel-network, in Figures 5.8(c) and 5.9 ($t = 141.03 - 613.77$ s), provides an opportunity to get an estimate of the adhesion energy of a wax-crystal layer with an air-oil interface. The side view of this 'pancake' bubble, which is confined between two glass plates with a gap $h = 200\ \mu$m, is sketched in Figure 5.12(a). As the bubble shrinks, oil has to fill up the volume that was previously occupied by the bubble. Oil that is confined within the crystal gel network, or cage, will have to be pulled into the vacant volume. Provided that the crystal network is permeable to oil, the oil should be able to flow unhindered. This is verified by stacking the corresponding frames [Figures B.8(a-b)], which show that the bulk crystals themselves do not move – implying that the crystal network itself is not effectively strained.

The bubble is observed to shrink in abrupt steps with only the lower right part of the interface contracting. This contraction will be resisted by the interfacial crystals in this region as the substitution of the air-oleogel boundary by an oil-oleogel boundary has an energetic cost that prevents the interface from retracting. The concept of estimating the adhesion energy between two media in presence of a third medium [14] may then be used to calculate the change in the surface free energy of the adsorbed layer where the adjoining air phase is substituted by the oil phase.

For a meaningful estimate of the adhesion energy, two thermodynamically equilibrium states have to be compared. For this the states of the bubble shown in Figure 5.9 at times $t = 513.52$ s and 613.77 s, where the temperature is the same $T = 22°$C, may be considered. Using ImageJ, the two image frames are stacked to create a third image, wherein each pixel stores the standard deviation of the pixel values of the parent images. This is shown in Figure 5.12(b) and reveals that the main changes between the two states occur on the side of the bubble that lies within the oil phase, interior

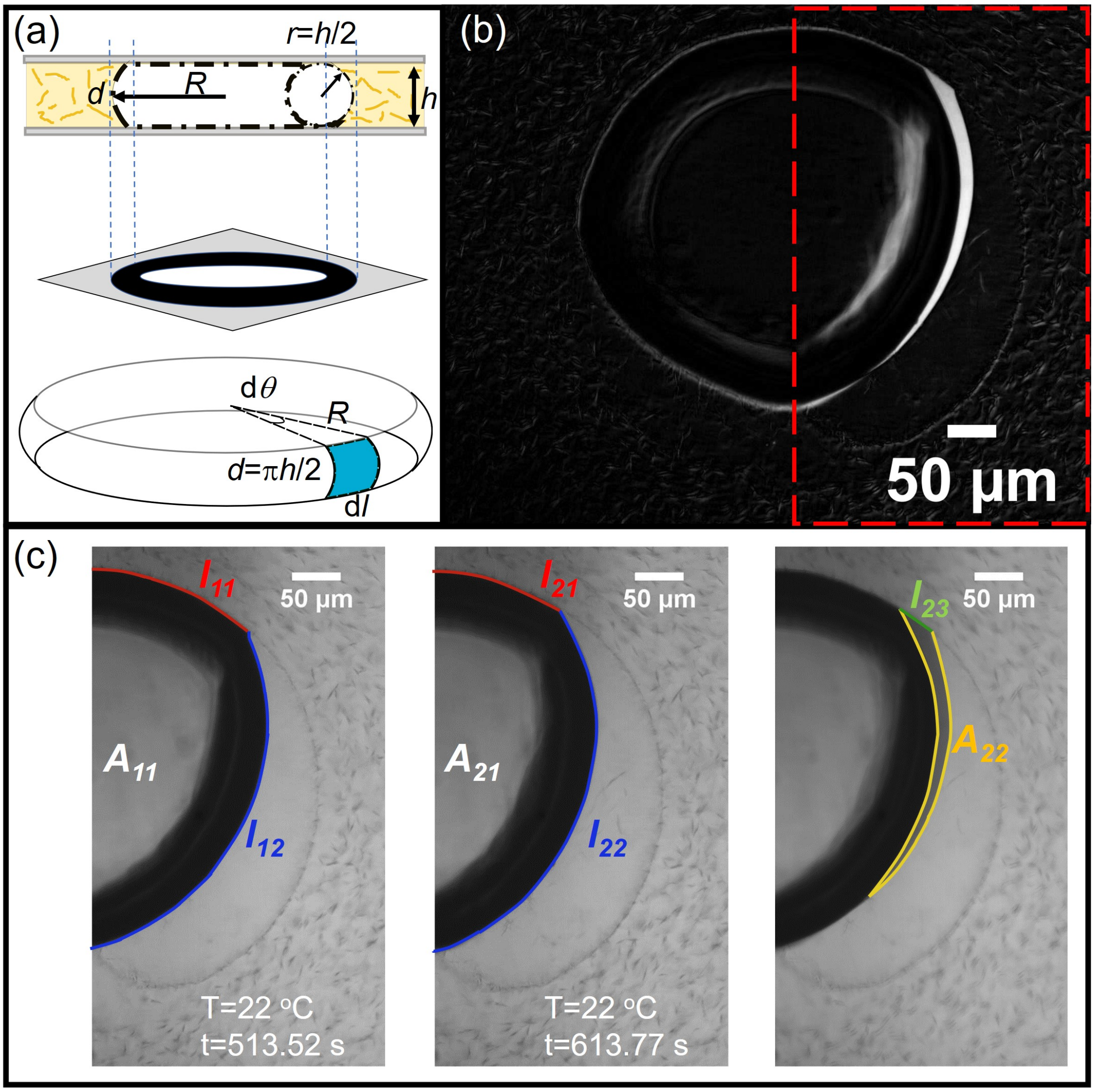

Fig. 5.12 **Estimation of adhesion energy of wax-crystal layer at bubble interface between two thermal equilibrium states.** (a) Schematic illustrating side-view of the bubble confined between two glass planes. The projected 2D image of the bubble, as seen in the actual frames, is also depicted. A differential area element (in blue), in the lateral curved surface, is depicted for the 'pancake' bubble. (b) Stack made by taking standard deviation of pixel values of two parent images corresponding to states $i = 1$ and 2 with red-dashed box indicating region of interest (ROI). (c) ROI in parent images for $i = 1$ ($t = 513.52$ s) and $i = 2$ ($t = 613.77$ s) with labelling to show the arc elements and area elements described in the main text. Further, the stacked image, obtained by taking median of the pixel values in the two images, is used to show the area A_{22} where the air-glass interface is replaced by the oil-glass interface.

of the oil-oleogel phase line, as highlighted by the dashed red box. More specifically there are changes in the lengths of the bubble interface in contact with the oil and the oleogel; and the area of the bubble in contact with glass. It may be considered that the largest radius of the bubble, occurring in the mid-plane (same as the focal plane) is R [Figure 5.12(a)]. While the radius of curvature of the bubble between the two glass surfaces may be approximated as $r = h/2$. Hence, the arc-length of the bubble in the gap is $d = \pi h/2$. Finally, a differential area element (blue planar element) of the bubble between the glass planes is given as $\mathrm{d}A = d \times \mathrm{d}l = \pi h/2 \times \mathrm{d}l$, with $\mathrm{d}l$ being the length of arc lying in the focal plane of the image.

In Figure 5.12(c), the parent images are used to estimate the dimensional changes between the two states. For $t = 513.52$ s, which is state $i = 1$, l_{11} denotes the length of the bubble arc between air and the oleogel; l_{12} the arc length for the air-oil interface; and A_{11} the area of the bubble in contact with the glass. Only the bright region represents the flat air-glass contact, while the curved part is dark [121–123] and represents the air-oil interface, not in contact with glass. Similarly for $i = 2$, where $t = 613.77$ s, l_{21} is the length of the air-oleogel interface; l_{22} is the air-oil interface and A_{21} is the air-glass contact area. The right most image of Figure 5.12(c) is the stack of the two parent images where the pixels represent the median of the pixels from the parent images. The stacks of the entire frames, using both standard deviation and median of the pixels, are shown in Figure B.8(a), where it becomes clear that all changes to the system between states $i = 1, 2$ are confined within the limited region within the red box. A_{22} denotes the difference in areas occupied by the bubble in going from state 1 to state 2. During this same transition, an area element of length l_{23} of the adsorbed crystal layer delaminates from the bubble interface. This area element, initially exposed to air on one side, is now exposed to oil.

The free energy of the system for state 1 is

$$E_1 = \sigma_{\mathrm{A-Gel}} l_{11} d + \sigma_{\mathrm{AO}} l_{12} d + 2A_{11}\sigma_{\mathrm{A-Glass}} \tag{5.1}$$

where $\sigma_{\mathrm{A-Gel}}$ is the surface energy of the oleogel in air, σ_{AO} is the air-oil surface tension and $\sigma_{\mathrm{A-Glass}}$ is the surface energy of glass in air. The prefactor 2 before A_{11} accounts for there being two air-glass contact regions, one above and one below the bubble. Similarly, the free energy for state 2 is given as

$$E_2 = \sigma_{\mathrm{A-Gel}} l_{21} d + \sigma_{\mathrm{AO}} l_{22} d + 2A_{12}\sigma_{\mathrm{A-Glass}} + \sigma_{\mathrm{O-Gel}} l_{23} d + 2A_{22}\sigma_{\mathrm{O-Glass}}, \tag{5.2}$$

with $\sigma_{\mathrm{O-Gel}}$ being the oil-oleogel interfacial energy and $l_{23} = (l_{11} + l_{12}) - (l_{21} + l_{22})$ is the arc-length of the oil-oleogel phase-line created as the bubble interface recedes. The term $2A_{22}\sigma_{\mathrm{O-Glass}}$ accounts for the oil wetting the two glass faces as the air-glass interface is displaced.

The change in free energy of the system in going from states 1 to 2 is

$$\Delta E = E_2 - E_1, \tag{5.3}$$

or,

$$\Delta E = \sigma_{\mathrm{A-Gel}}(l_{21} - l_{11})d + \sigma_{\mathrm{AO}}(l_{22} - l_{12})d + 2\sigma_{\mathrm{A-Glass}}(A_{21} - A_{11}) + 2\sigma_{\mathrm{O-Glass}}A_{22} + \sigma_{\mathrm{O-Gel}}l_{23}d. \tag{5.4}$$

As mentioned that all changes occurring in the system between the two states is mainly confined to the volume within the red-dashed box in Figures 5.12(b) and B.8(a), so that equation (5.3) is approximately valid. Hence the change in free energy per unit area, of the crystal-layer, or the adhesion energy ΔG_{ads} is

$$\Delta G_{\mathrm{ads}} = -\frac{\Delta E}{\Delta A_i}, \tag{5.5}$$

with ΔA_i denoting the area of the desorbed crystal layer as

$$\Delta A_i = l_{23}d = \frac{\pi}{2}hl_{23}. \tag{5.6}$$

The various arc-lengths and areas concerned are determined via image analysis using MATLAB, as schematically represented in Figure B.8(c,d) and tabulated in Table B.1. However, the interfacial energies need to be determined experimentally.

Ideally, to estimate the adhesion energy, using the concept of 'free energy', it is required that the process occurs reversibly. The transition between the states occurs over $\Delta t = 100.2$ s. The length of the crystal-layer desorbed during this is $l_{23} = 19.76$ μm, which in comparison to the bubble size is quite small ($l_{23}/D_0 \approx 0.02$) and so the process may be assumed to be quasi-static.

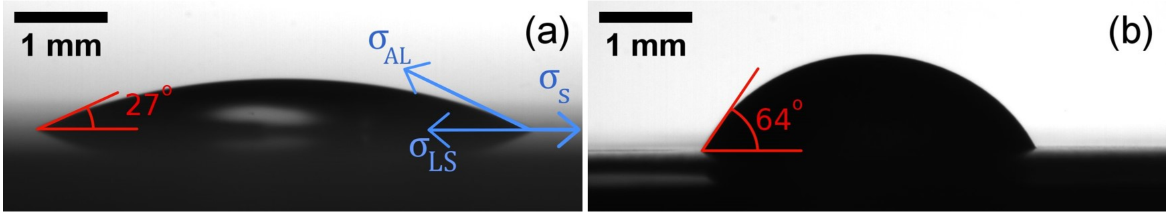

Fig. 5.13 Sessile drops of DMSO on (a) a borosilicate glass slide and (b) an U-oleogel.

Table 5.2 Contact angles of various liquids on borosilicate glass and U-oleogel. The number of drops analysed is indicated by n. *Oil was not used for the OW-fit, but instead used for the calculation of $\sigma_{\mathrm{L-Glass}}$ and $\sigma_{\mathrm{L-Gel}}$.

Liquid	Borosilicate glass	Unagitated gel
n-decane	$3.8 \pm 1°$ $(n = 7)$	$16.3 \pm 3.7°$ $(n = 3)$
CH_2I_2	$44.6 \pm 2°$ $(n = 10)$	$38.9 \pm 2.3°$ $(n = 5)$
DMSO	$26.5 \pm 2.7°$ $(n = 10)$	$63.5 \pm 1.3°$ $(n = 6)$
NMP	$33.7 \pm 3.9°$ $(n = 4)$	$64.1 \pm 1.9°$ $(n = 4)$
EG	$39.2 \pm 1.6°$ $(n = 8)$	$72.8 \pm 0.9°$ $(n = 6)$
Glycerol	$30.0 \pm 2.3°$ $(n = 10)$	$80.7 \pm 0.9°$ $(n = 5)$
Water	$22.4 \pm 4.2°$ $(n = 5)$	$89.1 \pm 0.9°$ $(n = 5)$
Oil*	$29.8 \pm 0.9°$ (n=10)	$27.8 \pm 1.3°$ (n=4)

Estimation of surface free energy

The solids, for which the surface free energies (SFEs) were to be estimated were borosilicate glass – which is the material of the glass slides and cover slips – and the unagitated oleogel (U-oleogel). As examples, two images of sessile DMSO drops on a clean glass slide and on an unagitated oleogel are shown in Figure 5.13(a) and (b) respectively. Even on a microscopic level, the U-oleogel surface appears flat and smooth. The contact angles measured for the various liquids are presented in Table 5.2, with the number of repeats n provided. For each liquid, a fresh substrate surface was prepared.

The fit to the data using the Owens-Wendt (OW) fit, is shown in Figure 5.14. Linear regression using MATLAB was used to fit the data series. From the fitting it is found that the surface free energy components, consisting of dispersive σ^{d} and polar σ^{p} contributions, for the two solids in air are: $\sigma^{\mathrm{d}}_{\mathrm{Glass}} = 17.6$ mN/m; $\sigma^{\mathrm{p}}_{\mathrm{Glass}} = 38.4$ mN/m, while $\sigma^{\mathrm{d}}_{\mathrm{Gel}} = 24.9$ mN/m and $\sigma^{\mathrm{p}}_{\mathrm{Gel}} = 2.6$ mN/m. This gives $\sigma_{\mathrm{Glass}} = 56.0 \pm 4.0$ mN/m, while $\sigma_{\mathrm{Gel}} = 27.5 \pm 1.5$ mN/m . The estimates for the SFE and its components for glass is close to what is reported by [87]. The low polar contribution to the U-oleogel SFE is coherent with the fact that both sunflower oil and the wax are non-polar.

The above method has some drawbacks. The estimation requires a highly reliable characterisation of the liquid samples used, which is difficult to do. Also, uncertainties become large due to the use of square-roots, particularly if a liquid has low $\sigma_{\mathrm{L}}^{\mathrm{p}}$. This becomes an issue for glycerol, which changes its surface tension due to its hygroscopic nature. There is also the issue of volatility. For these reasons the times of experiments were kept as low as possible. Substrate roughness also contributes to errors. As mentioned above, on a microscopic scale, the surfaces used appeared smooth (Figure 5.13).

Using the above, the interfacial tensions between oil and the respective surfaces are calculated using the Young-Dupré equation $\sigma_{\mathrm{LS}} = \sigma_{\mathrm{S}} - \sigma_{\mathrm{AL}} \cos\theta$. The values with regards to the U-oleogel and glass are respectively $\sigma_{\mathrm{O-Gel}} = -1.7 \pm 2.0$ mN/m and $\sigma_{\mathrm{O-Glass}} = 27.4 \pm 4.4$ mN/m. Taking into account the experimental uncertainties involved, it may be reasonable to consider $\sigma_{\mathrm{O-Gel}} \approx 0$ mN/m, since the U-oleogel is constituted of sunflower oil and a wax.

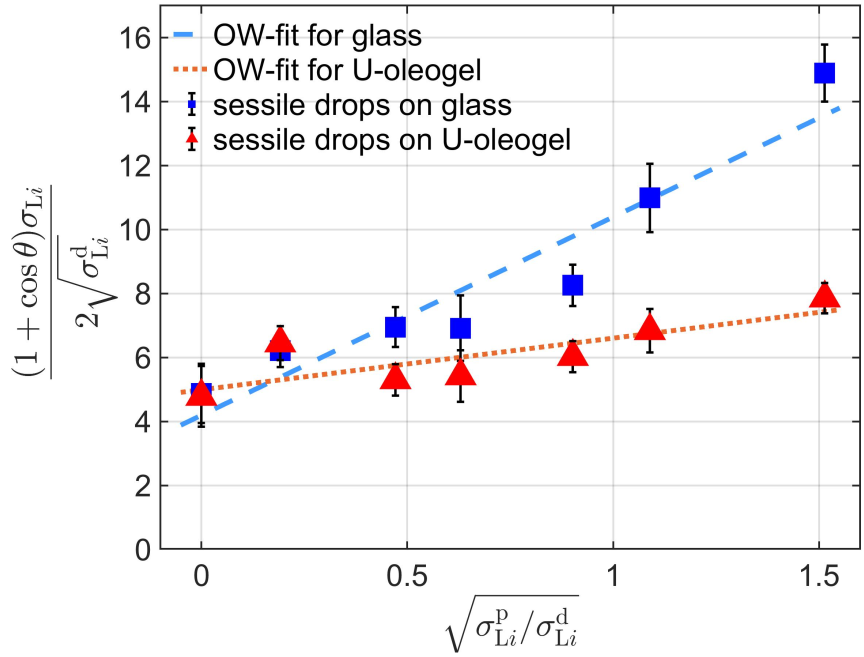

Fig. 5.14 **OW-fit to determine solid SFE.** The surface free energy components for the borosilicate glass and U-oleogel were obtained by fitting straight lines through the data points for sessile liquid drops deposited on glass slides (blue squares) and U-oleogel surfaces (red triangles). The fitted straight line, using linear regression, for the glass (dashed blue line) gives $\sigma_{\mathrm{Glass}}^{\mathrm{d}} = 17.6$ mN/m; $\sigma_{\mathrm{Glass}}^{\mathrm{p}} = 38.4$ mN/m. While for the U-oleogel, the fitting (orange dotted line), gives $\sigma_{\mathrm{Gel}}^{\mathrm{d}} = 24.9$ mN/m and $\sigma_{\mathrm{Gel}}^{\mathrm{p}} = 2.6$ mN/m.

Substituting the relevant values in equation (5.4) we get $\Delta E = -3.75 \times 10^{-10}$ J. With $|\Delta A_i| = 6.21 \times 10^{-9}$ m^2 we get

$$\Delta G_{\text{ads}} = 60.40 \text{ mJ/m}^2 \tag{5.7}$$

at $T = 22°$C. This value is of the same order of magnitude as the compression modulus E_{d} of a wax-coated pendant drop, as estimated in Chapter 4, section 4.3.3.

This way we have lower limit estimates on both the adhesion energy, of the crystals with the interface, and interfacial compression modulus. Since they remain comparable, the hypothesis, presented in the conclusion of Chapter 4 (section 4.4.4), still holds that if $E_{\text{d}} \times \Delta A \geq \Delta G_{\text{ads}} \times \Delta A$, then the interfacial layer may prefer delamination over further compression.

In the above, the estimate of adhesion energy is considered as a 'lower' limit as the crystal layer was formed at the bubble interface (section 5.3.5) without agitation. For the bubbles in oleofoams, where there is vigorous agitation in their preparation, a higher surface coverage of crystals may be expected resulting in more crystals per unit area in the delaminating strip considered. A denser interfacial network may be expected to give rise to a higher adhesion energy. However, as regards to practicality, it is suspected that even bubbles in oleofoams have voids in the interfacial layer as noted by the wide variation in dissolution times for wax-coated bubbles (Table A.1).

5.3.7 Behaviour of crystal-coated bubbles under varying deformation timescales

Phenomena observed when deforming the crystal-coated air-oil interfaces of wax-coated bubbles, at two extreme timescales – one during bubble dissolution and second during ultrasound-induced volumetric oscillations – are described here.

Phenomena during dissolution of a coated-bubble

Bubble dissolution occurs over a timescale of $\sim 10^3 - 10^4$ s (section 4.3.2). To better visualise the behaviour of the interfacial layer at the bubble surface, as it undergoes dissolution, wax-coated bubbles were extracted from the oleofoam and re-suspended in sunflower oil and were observed with cross-polarisers.

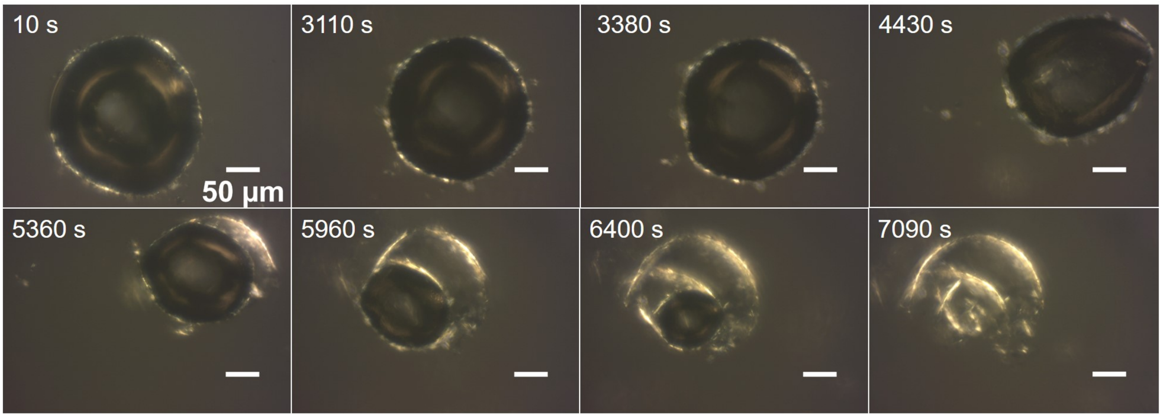

Fig. 5.15 Time sequence of a wax-coated microbubble undergoing slow dissolution, observed using polarised light microscopy.

An image sequence of such a bubble is shown in Figure 5.15. The bubble, with a halo of crystals around it in the form of a 'shell', initially appears non-spherical, implying high surface coverage. As it dissolves, the shell distorts sharply ($t = 4430$ s, top right) and just after this the interfacial layer is seen to unwrap like a sheet. It may be hypothesised that at this point both the compression and bending moduli of the layer resist further distortion and instead favour desorption of the interfacial layer from the air-oil interface. As the bubble shrinks further, it transits through non-spherical shapes, suggesting that there is still significant crystal material remaining at the interface. The unwrapping layer remains intact and eventually settles at the bottom of the enclosure, after complete dissolution of the bubble. The layer appears to be composed of large crystal subunits with individual dimensions being comparable to the initial bubble radius ($R_0 \approx 100\ \mu$m). This contrasts with the observed morphologies and sizes observed for bulk crystals [Figure 5.3(a)], where individual crystals typically had dimensions $\leq 10\ \mu$m.

More micrographs of remnant crystal layers of dissolved bubbles, shown in Figure B.9, that were prepared within the U-oleogel as well as oleofoam, reveal similar structures, where the individual crystals appear larger than the oleogel bulk crystals. It is worth noting that the bubbles prepared in the U-oleogel [Figures B.9(a-b)] in these samples had dissolved within a week and the structure of the interfacial layer remained intact even after six months.

Volumetric oscillations of crystal-coated bubbles using acoustic waves

The behaviour of the wax-coated interface, undergoing deformation on a much shorter timescale $\sim 10^{-4}$ s, using ultrasound-induced coated-bubble oscillations was studied. To ensure that only bubbles with high surface coverage were considered, bubbles that had a halo of crystals and were initially non-spherical were focused upon. The bubbles, of initial radii R_0, were positioned at least $20 \times R_0$ away from their closest neighbours to avoid acoustic radiation effects [125].

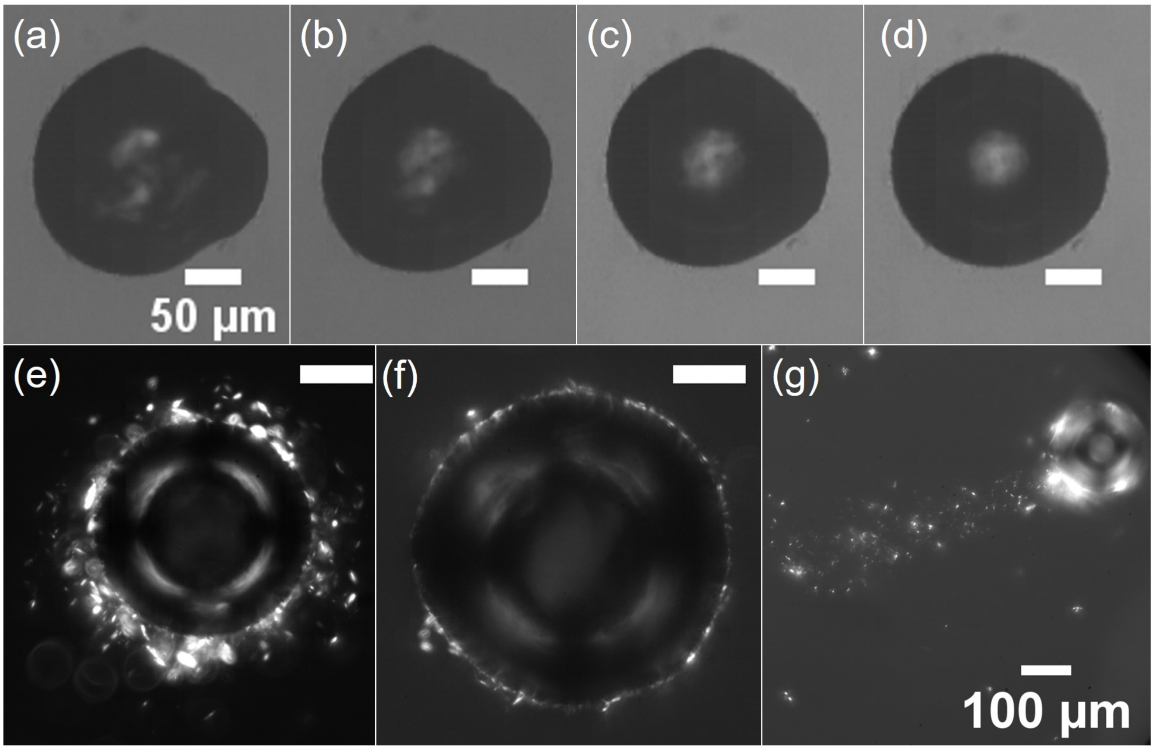

Fig. 5.16 **Bubble-shape change and crystal expulsion at high-frequency volumetric oscillations.** (a) A wax-coated bubble with initial $R_0 = 100.8$ μm; (b) after having undergone 50 cycles of oscillations at $A = 10\%$, at $f = 25$ kHz. (c) Slight shape change after two more periods of similar oscillations. (d) After 80 cycles at $A = 20\%$. (e) Crystal expulsion for the same bubble after $N = 100$ and $A = 70\%$. A different bubble with $R_0 \approx 108$ μm, before (f) and after (g) oscillations is observed using cross-polarisers. A trail of desorbed crystals is left behind due to simultaneous oscillation and translation of the bubble.

Shape change and crystal expulsion by acoustic cycling

Shape change: For a set ultrasound frequency, the bubbles were found to undergo volumetric compression-expansion oscillations, and the oscillatory behaviour was found to depend on the acoustic pressure P_a, or equivalently gain value A (section 5.2.4), and the number of cycles N. For low acoustic pressures, the bubbles underwent volumetric oscillations while maintaining their initial shapes, independent of the number of cycles ranging between $N = 10 - 100$. Whereas, for higher pressures and number of cycles $N = 20 - 50$, the bubbles underwent shape changes during the oscillations and attained shapes closer to spherical at the end of the forcing. When these were left undisturbed for $\Delta t \approx 300 - 600$ s, they again acquired non-spherical shapes that differed slightly from their initial shapes, with a slight decrease in the area of the bubble projected in the focal plane. For example, when the non-spherical wax-coated bubble of Figure 5.16(a), with $R_0 = 100.8$ μm, was subjected to $N = 50$ cycles of ultrasonic forcing at $f = 25$ kHz and $A = 10\%$, there was no perceptible change in bubble shape at the end of the oscillations as seen in Figure 5.16(b). For $A = 20\%$ and the same N, however, the bubble shape changed slightly, as seen in Figure 5.16(c). With $N = 80$, the shape became closer to spherical as seen in Figure 5.16(d). When left for 10 minutes, the shape again transited into a non-spherical one, with the radius having decreased by $\Delta R = 8.2$ μm. Over this course, negligible amount of crystals desorbed from the bubble.

Crystal expulsion: At higher P_a and N, the volumetric oscillations became larger in amplitude, and upon compression of the bubble, crystals were observed to desorb from the interface. This appears similar to the case of colloid-coated microbubbles, in aqueous solutions, under ultrasonic fields [126]. When the bubble in Figure 5.16(a-d) was subjected to higher pressures ($A = 70$ %) and $N = 100$, crystals started desorbing from the interface. The final state of the bubble, after the end of the oscillations is shown in Figure 5.16(e) with cross-polarisers, where it appears perfectly spherical. This behaviour was observed with different bubbles, of different sizes, when the appropriate f, N and gain values were selected.

In Figure 5.16(f) an initially non-spherical bubble with $R_0 \approx 108$ μm is shown using cross-polarisers. After an acoustic forcing with $f = 25$ kHz, $N = 100$ and $A = 70\%$, crystals were expelled, while at the same time the bubble moved from left to right in the view field due to acoustic radiation forces [127]. This left behind a trail of crystals similar to the appearance of a comet, as seen in Figure 5.16(g).

Interestingly, both in Figures 5.16(e) and (g), the crystals appear much smaller than those appearing in the delaminated layers of dissolved bubbles in Figure B.9, which had not been oscillated.

Bubble dissolution following ultrasound-induced bubble oscillations

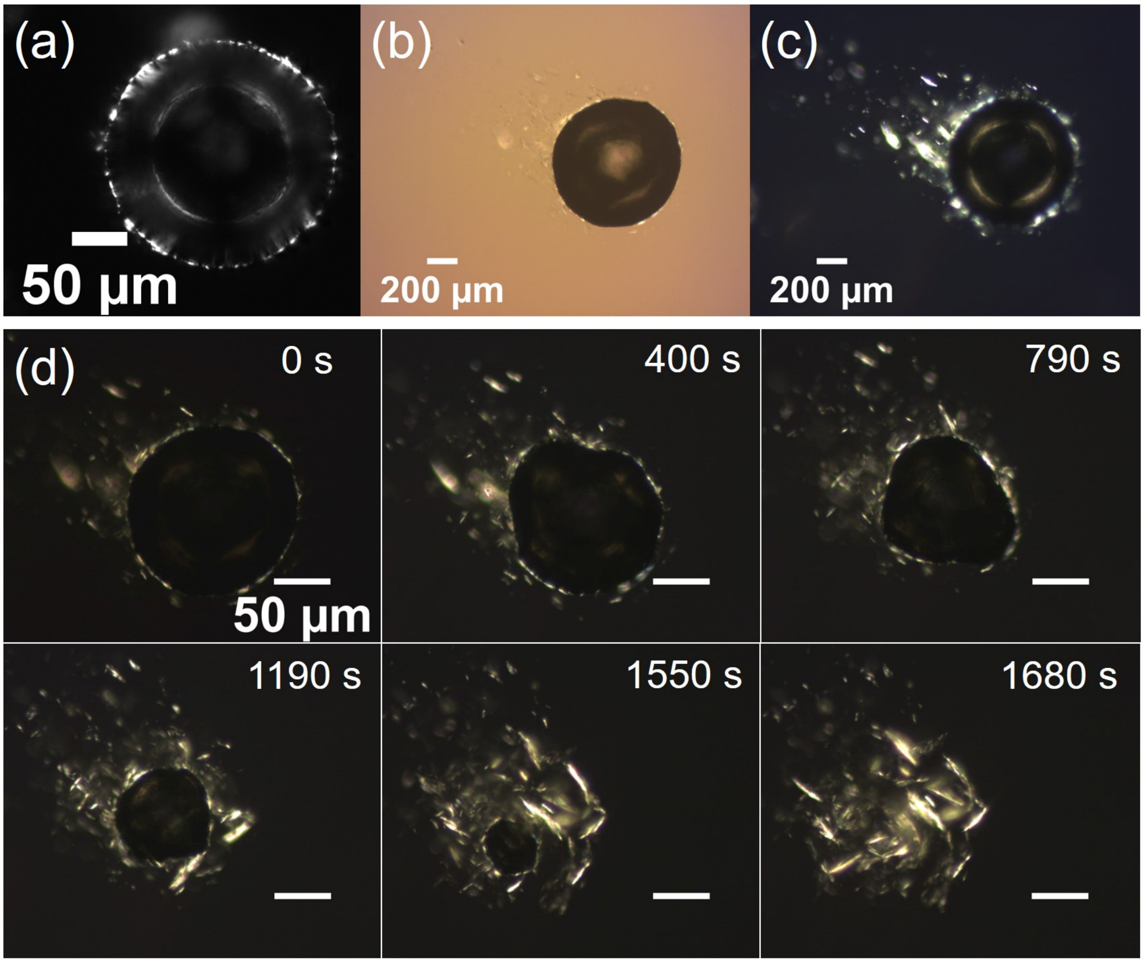

Fig. 5.17 **Wax-coated bubble dissolution following crystal expulsion mediated by acoustic driven bubble oscillations at $f = 25$ kHz.** (a) The initial state of the coated bubble observed using cross-polarisers. The bubble following the crystal expulsion protocol is shown in (b) and with cross-polarisers in (c). Image sequences of the bubble subsequently dissolving are shown in (d).

To gain insights into the nature of the interfacial layer, following bubble oscillations, the bubbles were left to dissolve completely after a period of acoustic-driven oscillations. This would leave behind the interfacial crystals. A wax-coated bubble of initial radius $R_0 \approx 103$ μm [Figure 5.17(a)] was oscillated using $f = 25$ kHz in a controlled manner to desorb a limited amount of crystals without complete desorption. The protocol followed is provided in terms of successive steps of (gain%,N) pairs as: (40%,$N = 80$), (40%,$N = 20$), (70%,$N = 80$), (70%,$N = 100$), (80%,$N = 100$) and (80%,$N = 200$).

The micrographs of the bubble after all these steps is shown in Figure 5.17(b) and with cross-polarisers in Figure 5.17(c). Following this, the bubble was left undisturbed as images were recorded every 10 s and an image sequence of the bubble dissolution steps at the fixed temperature $T = 22$°C is shown in Figure 5.17(d). The crystals at $t = 1680$ s, when the bubble has completely dissolved, appear larger compared to those that were desorbed at $t = 0$ s, when the recording was started. This can mean either two things – (i) the small crystals that were not able to be integrated into a collective cohesive network have been expelled; or (ii) the interfacial crystals are broken and then expelled from the interface during bubble oscillations.

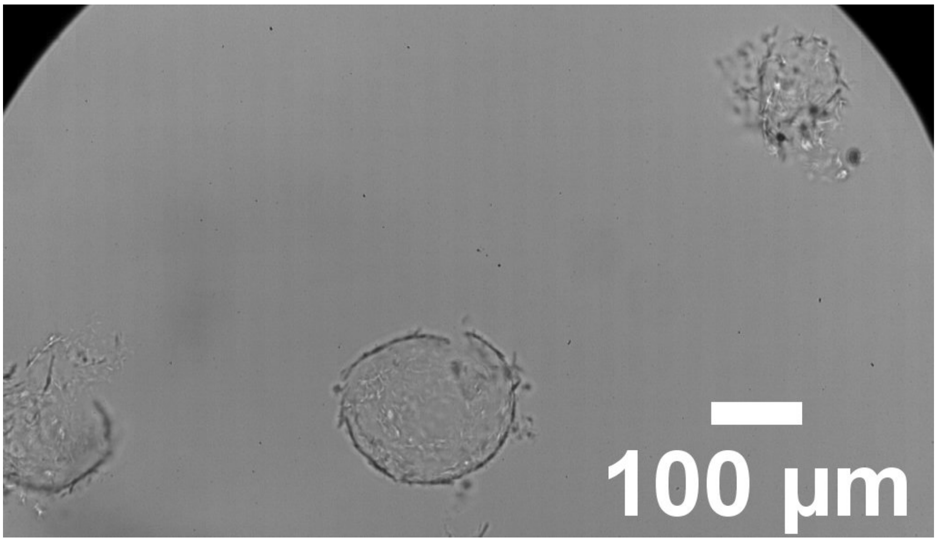

Fig. 5.18 Effect of bubble deformation history on remnant interfacial layer. Following ultrasonic pulsing at $f = 28 - 29$ kHz, only bubbles close to the resonance radius underwent strong oscillations. This induced crystal desorption, leaving behind fragmented remnant interfacial layers on the left and right of the image. While a larger bubble, in the centre, left behind a more intact remnant layer since it did not oscillate significantly.

Finally, selecting the driving frequency in turn selects the bubbles that will undergo forced oscillations (section 3.13). In a sample containing spaced bubbles, with varying bubble sizes, observing the remnant interfacial layers after the bubbles have completely dissolved, following a period of ultrasound-driven oscillations, reveals interesting aspects. For example, in Figure 5.18, it is seen that for $f = 28 - 29$ kHz and gain between $40 - 65\%$, there was strong oscillations of the two bubbles on the left and right of the figure. The resulting remnant layer appears shattered. Whereas, a larger bubble in the centre, that underwent a reduced excursion, has left behind a more intact remnant layer after complete dissolution. The amplitude of oscillations is dependent on the initial bubble radius [64].

5.4 Discussion

5.4.1 Effect of shear and tempering history on bulk oleogel network

By studying the model paraffin wax-sunflower oil system, there is direct evidence showing that the dominant crystal polymorphs occurring in the oleogel are influenced by shear rate (section 5.3.1, Figures 5.2,5.3 and 5.4) applied during the fast-cooling of the crystal melt, as the major crystallisation appears to occur during this step (section 5.3.4 and Figure 5.7). The oleogel hardens over the slow-cooling step, but it is reasonable to believe that the crystal polymorphs will dictate the final gel strength. While the tempering profiles for the rheometer-prepared oleogels (RO) differed slightly from that used in preparing the oleofoam, oleogel750 and unagitated-oleogel (U-oleogel) samples (Figure 5.1), qualitative interpretations can still be extracted from their oscillatory rheological measurements. It was found that the oscillatory shear moduli for the oleogels appear to vary non-monotonically with $\dot{\gamma}$. This is then, analogous to the observation of the non-monotonic dependence of the dynamic moduli on cooling rate $\dot{T}$ of the crystal melt for a model waxy crude oil [101].

5.4.2 Formation of a crystal-coated interface

From observations (section 5.3.5), it is understood that the formation of the crystal-coated air-oil interfaces of individual bubbles occurs due to: (i) independent heterogeneous nucleation and crystal growth at the interface; and (ii) transfer of crystallites from bulk to interface. When bubbles are introduced into the crystal melt, without any agitation prior to cooling, only the former mechanism is active. Whereas, when bubbles are introduced into the cooling melt through turbulent agitation, both mechanisms occur simultaneously.

Owing to experimental challenges, it was not possible to comprehensively compare the dissolution times for crystal-coated bubbles prepared with and without agitation to assess impact on bubble stability when these two distinct routes were used. It seems sensible to anticipate that agitation increases the probability of attaining higher surface coverage in these bubbles. Yet it remains non-trivial to hypothesise whether the crystallites, from the bulk, impacting the interfacial layer, already formed due to intrinsic crystal growth at the interface, disrupts to weaken or strengthen the interfacial network. Comparing dissolution times should shed more light onto this matter.

5.4.3 Qualitative comparison of crystals in bulk and interface

Depending on tempering protocols, in absence of any shear, the bulk crystals are either needle or star shaped [Figures 5.2(d,h), B.1(a,b)]. Non-uniform tempering leads to the formation of platelet-like crystals [Figure B.1(d) and description in section 5.3.1]. Yet the interfacial crystals, at the planar interfaces, are superfine in size and indistinguishable unlike the bulk oleogel crystals (Figure 5.10). Adding the effect of increasing shear, during crystallisation, leads to the crystals in the bulk being either platelet-like or fragmented [Figures 5.2(f,g), 5.4(b-d)].

The observations of the remnant crystal-layers, left behind after bubble dissolution [Figures 5.15 and B.9], that appear to be composed of linked disparate, long and slender crystal domains, with typical dimensions being of the order of the initial bubble radii, appear to be inline with the observations and analysis described regarding the growth of 2D colloidal crystal domains at the surface of spherical droplets [114]. In that study, by changing the droplet sizes, the curvature of the interfaces were varied. It was found to be energetically favourable for crystal domains to grow into branched, ribbon-like domains, with large voids and no topological defects, especially when the droplets were a few micrometres in radii. The droplet curvature was proposed to bend the lattice vectors of crystallising domains, promoting anisotropic growth.

Surface tension too plays a role in orienting crystals at interfaces [115], with the characteristic reorientation time being dependent on the balance of viscous and capillary torques. The reorientation timescale, $\tau = \eta a/\sigma$, for a crystal of size a at an interface with surface tension σ and bulk liquid viscosity η, being of the order of 0.1 to 1 μs for an air-water interface, or ranging up to a few milliseconds for more viscous liquids. Hence, in the current study it may be inferred that when crystallites from the bulk impact the bubble interfaces in the cooling crystal melt, during oleofoam formation, the subsequent growth and integration of the crystallites will be influenced by the effective surface tension.

The above facts suggest that, at least qualitatively, there may be a weak correlation between the dominant crystal polymorphs located at the interface and within the bulk in oleofoams that are prepared using similar protocols as presented in this study. It will then, be useful to study the transition of the crystal domain features when tracing the network bridging the bulk oleogel structure to the interfacial structure, in oleofoams formed with or without agitation. This will shed light on how bubble dissolution may be retarded due to local effects as the local gel yield strength is very likely to differ from the macroscopic yield strength, obtained through bulk rheological measurements [112]. This will supplement in explaining the remarkable stability of bubbles embedded within an oleogel, where macroscopic rheological reasoning alone was found to be somewhat inadequate, as was concluded in sections 4.4.2 and 4.4.3.

5.4.4 Deformation of crystal-coated interfaces at varying timescales

Quasi-static deformation during bubble dissolution

Observations of the dissolution of wax-coated bubbles (section 5.3.7) indicate that the crystal layer detaches from the air-oil interface when the local distortion of the layer, both by compression and bending, increases the stress within the interfacial network to the point that deformation starts competing with the adhesive interaction between the wax-layer and the air-oil interface. Lower estimates of both the compression modulus E_d (as determined in section 4.3.3) and the adhesion energy ΔG_ads (section 5.3.6) being of comparable magnitudes supports this hypothesis.

Given that bubble dissolution occurs over a timescale of $10^3 - 10^4$ s, it may be hypothesised that the crystals at the interface have sufficient time to reorganise and form a network that opposes the stress due to decreasing area. This is similar to the mechanism of jammed colloids self-organising in response to support an external load [128]. It is a possibility that the compressive stresses may lead to the fusion of crystal domains to form larger domains at the interface. This in addition to the process of domain growth on a curved surface, as described in section 5.4.3, may explain why the unwrapped crystal layer appears to be composed of large crystal domains [Figure B.9].

High-frequency periodic deformation through bubble pulsations

Interestingly, when a wax-coated bubble is compressed during the first compressive phase of the acoustic wave, the interfacial layer does not delaminate, as one might expect from the bubble dissolution experiments (Figure 5.15). This suggests that the timescale of $\sim 10^{-4}$ s is too small to form 2D jammed cohesive structures to oppose the externally applied stresses. Instead, the crystals, possibly, are more free to slide past each other. At low acoustic pressures ($A \leq 20\%$), the interface also buckles.

Under higher acoustic pressures, with large number of cycles ($N \approx 50 - 100$), with the onset of bubble shape oscillations, discrete crystal elements of characteristic dimensions l much smaller than R_0, the bubble radius, are observed to be expelled [Figure 5.16(e,g)]. The mechanism of expulsion is expected to be similar to that proposed for the expulsion of spherical solid colloidal particles from the anti-nodes of colloid-coated bubbles undergoing shape oscillations, under high acoustic pressures [126]. The cumulative push of crystals in locally concentrated regions may be significant to overcome the desorption barrier of the crystals, similar to what was observed for colloidal particles [126, 129].

The desorbed crystals being much smaller than the ones constituting the delaminated structure, observed after bubble dissolution [compare Figures 5.15, B.9 and 5.16(e,g)], imply that under fast deformation timescales $\sim 10^{-4}$ s, crystals cannot orient favourably to fuse with one another. Instead, the fast collisions lead to breakage and fragmentation of the overall interfacial structure.

Finally, coated bubbles when allowed to dissolve following a limited period of ultrasound-driven oscillations, reveal the remnant interfacial crystals to be comprised of crystal sizes varying throughout the range $l \ll R_0$ and $l \sim R_0$ (Figure 5.17). This suggests that either (i) the interfacial network is partially fragmented by bubble oscillations; or (ii) following crystal expulsion, the remaining crystals at the interface bond to form larger crystal domains. By tuning the moment and period and of ultrasound-induced pulsing, protocols can be devised for the use of crystal-coated microbubbles for systematic crystal release, in terms of size and amount in an application [Figures 5.16(g) and 5.17]. Also, depending on the requirement, the bubble shapes can be altered.

5.5 Conclusion

In this chapter the incorporation of wax crystals at air-oil interfaces, leading to the formation of crystal-coated bubbles, in a model oleofoam are studied. The dominant crystal polymorphs and the resulting nature of the crystal networks, occurring both at the interface or within a bulk oleogel, are found to be influenced by the tempering profile, and the shear applied when the crystal melt cools. Observations of flat interfaces constituted of crystals, or of interfacial layers left behind after the dissolution of wax-coated bubbles, reveal that the interfacial crystal structures differ from those within bulk oleogel networks, despite following the same tempering and shear protocols. This difference is ascribed to interfacial nucleation and crystal growth being also dependent on the effects of heterogeneous cooling, surface tension, local curvature, which occur in simultaneity and take place intrinsically at the interface. Additionally, turbulent agitation, during crystallisation, causes impaction of the intrinsic interfacial layer with crystallites from the bulk, which are then to be integrated into the growing interfacial structure. It is quantitatively presented that the work needed to compress a wax-coated interface is comparable to the adhesion energy of the wax-layer with the air-oil interface, so that, as a wax-coated bubble shrinks, the interfacial layer cannot resist compression. Finally, the deformation of the crystal-coated bubbles, or equivalently, highly curved surfaces, is observed under two separate timescale decades, $10^3 - 10^4$ s and 10^{-4} s. A rich diversity of phenomena is observed concerning the interfacial layer during either bubble dissolution or ultrasound-driven bubble pulsations. It is illustrated that protocols can be devised for the use of crystal-coated microbubbles for systematic crystal release in terms of size and amount in an application. These observations and their interpretations hold significant consequences in applications pertaining to the design of food, pharmaceutical or cosmetic formulations.

Chapter 6

Dynamics of colloid-coated bubbles in ultrasound

6.1 Introduction

Bubbles stabilised by particles [16, 4, 5, 18, 43, 19, 13], known as armoured bubbles, or sometimes Pickering bubbles, exhibit remarkable stability with bubbles resisting coarsening and coalescence in foams over a period of months [42, 43, 5, 13, 41]. In the last few decades there has been great interest in understanding the stability against dissolution of particle-coated bubbles [44, 19, 45]. There are several possible reasons for this. Small particles with strong aggregation form a cohesive monolayer at the interface which results in an armour that hinders gas dissolution. It is also predicted that the monolayer imparts an elasticity to the interface which resists compression while the bubble tends to shrink [42]. The investigations of the physical properties of such bubbles and particle-coated monolayers in general, have mostly been considered under static or quasi-static conditions.

However, in many practical applications, with multiphase flows and interactions prevalent, interfaces undergo rapid deformation. The deformation timescales allow little time for the interfacial microstructure to relax to an equilibrium configuration. For instance, in the flow of crude oil, droplets stabilised by asphaltenes or impurities, collide or coalesce causing a rapid change in surface area between water and oil. At high flow rates, which is the norm in real scenarios, the dilational deformations occur very fast, with typical areal strain rates $\dot{\alpha} = \mathrm{d}A/A\mathrm{d}t$ between $10^1 - 10^5$ s^{-1}, or above.

Conventional interfacial rheological methods [130] seldom allow the higher deformation rates to be accessed.

An oscillating bubble, driven by ultrasound, can serve as an interfacial rheological probe [70], where the above strain rates can be achieved by tuning the driving acoustic frequency. Linking the microstructural evolution of the interfacial layer with the dynamic response of the bubble can shed light into the micromechanics and stresses occurring at the interface.

In a step towards developing a bubble as an interfacial rheological probe, the oscillatory dynamics of a bubble coated with micron-sized colloidal particles is studied. Using high-speed video-microscopy, the time-dependent bubble size and shape, the surface coverage by particles, and some details of the rearrangements of the particles can be visualised. Thus, under such conditions, the bubble dynamics can be expected to reveal rich micromechanical properties of a colloidal monolayer.

6.2 Methods

Bubbles, both bare and colloid-coated were prepared as described in section 3.10 and section 3.11, and were isolated, following the methods described in section 3.11. These isolated bubbles were subjected to two classes of separate experiments with ultrasound. In both cases, the exciting ultrasound pulse consisted of 10 cycles of a sine-enveloped sine wave. The corresponding voltage signal was generated by the arbitrary waveform generator (AWG) with a peak-to-peak amplitude of 180 mV. This was amplified using the power amplifier by varying the amplification gain value A in % (percentage). The oscillations were recorded using high-speed video-microscopy, with the details of the setup described in section 3.13. Image analysis, using MATLAB, was used to extract the time-varying radii of the bubbles. Both the AWG and high-speed camera were triggered using a pulse generator, with the AWG being triggered 100 μs after the camera. This way the bubble dynamics before the onset of forced oscillations were recorded. The duration of the AWG signal, with driving frequency $f = 25$ kHz, for the 10 cycles, lasted for 400 μs, while the total recording time was 1.9 ms.

Details of the colloidal particles, used in preparing the armoured bubbles, are given in section 3.1. The radii of the particles were $a = 0.25, 1.2, 2.5$ and 5 μm. Each bubble was covered by only one size of particles in a given experiment.

6.2.1 Pressure amplitude sweep experiments

In the first series of experiments, the ultrasound pressure amplitude was varied by changing the amplification in steps, while maintaining the initial bubble radius R_0 constant. The bubble excursions were measured as a function of acoustic pressure, or equivalently amplifier gain A. As mentioned in section 3.13, the output power from the amplifier was known to vary linearly with gain. The excursion amplitude is defined as

$$x_0 = \frac{R_{\max} - R_{\min}}{2R_0} \tag{6.1}$$

where $R_{\max}$ and $R_{\min}$ are the maximum and minimum bubble radii attained during bubble oscillations. This class of experiments will be referred to as *pressure-sweep* experiments.

To maintain R_0 nearly constant, by minimising bubble dissolution during the experiments, 500 mM NaCl aqueous solution, saturated with air, was used as the medium. This salt concentration also ensured that the colloids at the interface of the Pickering bubbles maintained an aggregated state (section 2.2.2). The density of ultrapure water, at $T = 18°\text{C}$ was measured to be $\rho = 1003$ kg/m^3, while for the brine solution $\rho = 1029 \pm 5.6$ kg/m^3. This small change in density is expected to have negligible effect on the bubble excursions, as was also confirmed by numerically solving the Rayleigh-Plesset equation and comparing the differences in oscillation amplitude. The solutions showed a change in x_0 to be $\approx 0.5\%$.

A bubble was oscillated with the 10-cycle pulse, having a driving period of 400 μs, after which it was left undisturbed for $\Delta t \approx 30$ s for the oscillation effects to relax. This was repeated by increasing A in steps, and continued to cover the range $A = 5 - 100\%$. Hence, for a step change of $\Delta A = 5\%$, this led to 20 runs of oscillations, spanning over a period of $\Delta t \approx 600$ s. For small bare bubbles, with $R_0 \leq 100$ μm, while the addition of salt retarded the dissolution rate, to further minimise changes in R_0 during sampling, the steps ΔA were increased to $10 - 20\%$. This way, it was ensured that over the course of the runs, the change in bubble size was limited to $\Delta R_0 < 1.2\%$. For larger bubbles, $\Delta R_0 < 1\%$, even when smaller step changes in ΔA were used. Where dissolution was negligible, for the same bubble, the amplifier gain was decreased in the series $A = 100 - 5\%$, in the same way, to check if there were any hysteresis effects.

6.2.2 Radius sweep experiments

The effect of bubble radius R_0 on excursion amplitude x_0, at constant acoustic pressure, was studied by introducing bubbles with varying initial radii R_0 into the enclosure, one at a time, and oscillating them. This class of experiments will be referred to as *radius-sweep* experiments. At a given frequency, bare bubbles are expected to exhibit a maximum excursion amplitude at a particular bubble radius R_{res}. This is akin to a resonance frequency f_{res} in frequency-sweep experiments [70, 92]. Hence, the initial bubble radius corresponding to the maximum excursion amplitude is termed as the resonance radius R_{res}. Radius-sweep experiments were preferred, instead of frequency-sweep experiments, as it was difficult to produce monodisperse colloid-coated bubbles, that is, having the same R_0, and isolate them away from rigid boundaries. Therefore, bubbles needed to be isolated in an enclosure with a compliant hydrogel boundary, as described in section 3.9. Within this enclosure it was not possible to calibrate the acoustic pressure at different acoustic frequencies. Yet both frequency-sweep and radius-sweep methods may be considered similar as they allow to explore the resonance behaviour of the bubbles.

For bare bubbles this was done by introducing a bubble of radius ≈ 250 μm and allowing it to dissolve. To increase the dissolution rate, the ultrapure water was degassed. The bubble was oscillated with the 10-cycle pulse, lasting for 400 μs, after which it was left undisturbed for 1 minute. Then again it was oscillated. This way, the oscillations of the same bubble were recorded every minute, at different R_0, as the bubble dissolved. However, during the pulsing period itself, the dissolution, and hence, change in R_0, was negligible. This way, as R_0 decreased from 250 μm to 50 μm, the oscillations were recorded for $n \approx 40$ values of R_0. The excursions, x_0, were estimated for each run and a plot of x_0 against R_0 was generated. These are referred to as *excursion versus radius* plots or *resonance curves*.

Radius-sweep experiments on bare bubbles were performed to confirm that the implementation of this method gave reproducible results. All bare bubbles of similar size were required to exhibit the same excursion x_0 for a fixed amplification A. Ideally, for a given gel, the curves of excursion amplitude with varying bubble radii, as a bubble dissolves, should be identical each time a new bubble is introduced into the enclosure, at the same position. For $f = 25$ kHz, the wavelength of sound would be $\lambda = f/c$, where c is the speed of sound in the medium. In water, $c \approx 1480$ m/s and so $\lambda \approx 0.06$ m. Therefore, a slight change in position of a bubble by a few micrometres

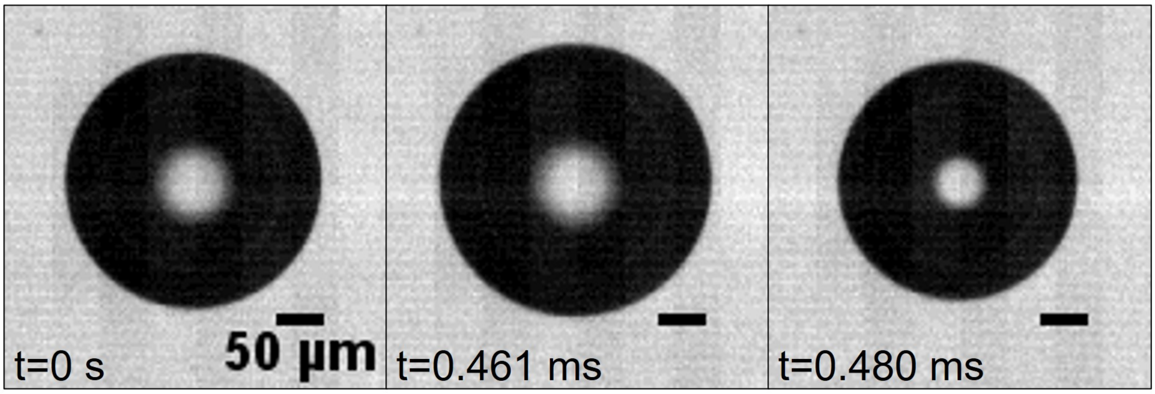

Fig. 6.1 Image sequences of an oscillating bare bubble with $R_0 = 134.1$ μm, $A = 100\%$. The initial state $R = R_0$ is at $t = 0$ s, while the maximum and minimum radii are attained at $t = 0.461$ ms and $t = 0.480$ ms respectively.

should not significantly affect the excursion amplitude at a fixed pressure amplitude. There would however, be a slight delay of the order of milliseconds, due to the time of flight of the acoustic wave.

For colloid-coated bubbles, the radii were varied by introducing a new bubble each time, into the cavity filled with 500 mM NaCl (aq). This was done since such bubbles were too stable against dissolution. For a given bubble of radius R_0, the bubble was subjected to three pulses, with an interval of 1 minute in between, to measure the average and standard deviations in the excursion amplitudes.

6.3 Results

6.3.1 Radius-sweep experiments on bare bubble

A typical image sequence for an oscillating bare bubble is shown in Figure 6.1, with $R_0 = 134.1$ μm at amplifier gain $A = 100\%$. The radius-time curves for a bubble during a radius-sweep experiment are shown in Figure 6.2. It is clear that the excursions change non-monotonically with R_0. The acoustic forcing started at $t_1 = 100$ μs and stopped at $t_2 = 500$ μs, therefore the bubble oscillation amplitude should gradually have decreased after t_2. Yet there appeared to be a second driving pulse, leading to an increase in the oscillations at $t_3 \approx 760$ μs. This is likely to be due to ringing of the transducer, or in combination with reflections of the ultrasound within the cavity. Our analysis involves only the driven excursions, during the 10-cycle pulse. Hence, in the subsequent figures, data points only up to the end of the driven part of the bubble oscillations will be shown in the radius time curves.

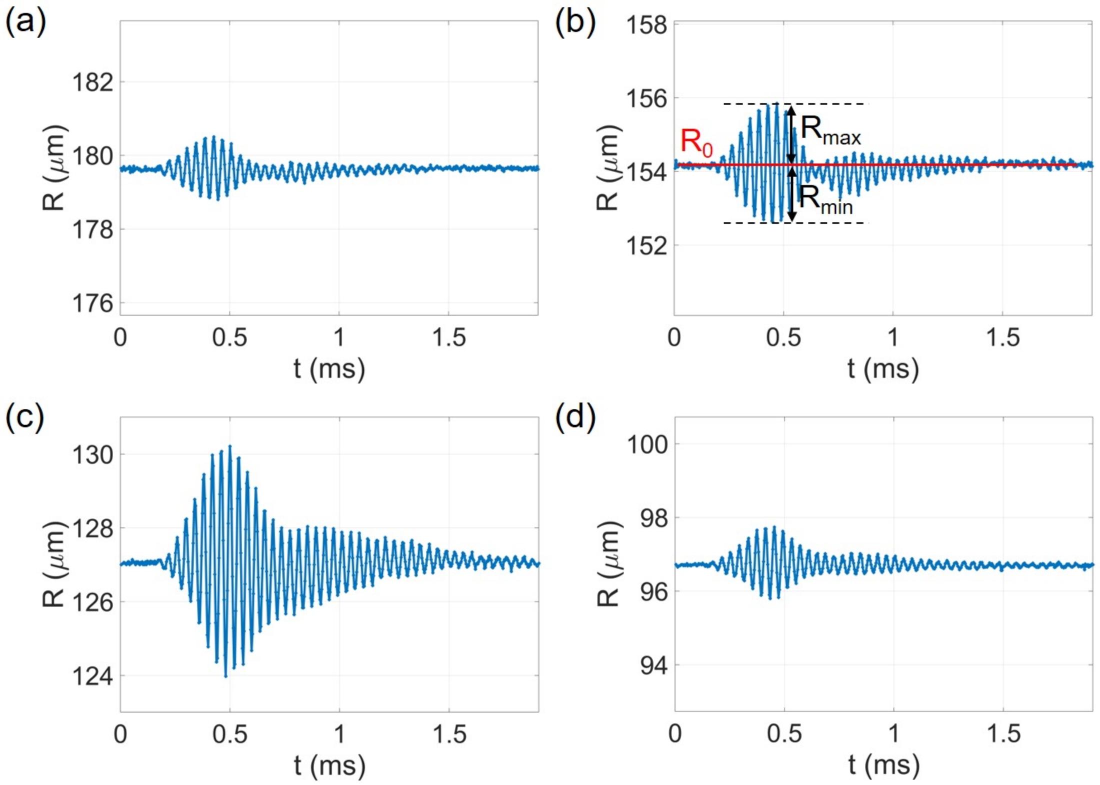

Fig. 6.2 **Radius-time curves for a bubble at different radii as it dissolved.** The initial radii before oscillations are (a) $R_0 = 179.6$ μm, (b) $R_0 = 154.1$ μm, (c) $R_0 = 127.0$ μm and (d) $R_0 = 96.7$ μm, where it is explicitly shown that after the oscillations, the initial radius is recovered, indicating that the bubble dissolution is negligible during the acoustic excitation. Panel (b) is annotated to represent the quantities R_0, R_{max} and R_{min}. All at $A = 40\%$.

The excursion amplitudes of three bare bubbles at different radii are shown in Figure 6.3. It is evident that the experiments for a given gel, give reproducible results, with the radius for maximum response occurring at $R_{\text{res}}^{\text{exp}} \approx 128.4 \pm 2$ μm. For similar conditions, but using different gel samples, the observed excursion amplitudes of bubbles varied across the gel samples. An example is given in Figure C.1 where bubble excursion amplitudes are shown for different bubbles. The variation in bubble excursions across different gel samples may be due to slight changes in the outer volumes of the enclosures during the cutting of the gel from the mould. For an increased volume of the gel, assuming that the density was fixed, more acoustic power was expected to be dissipated

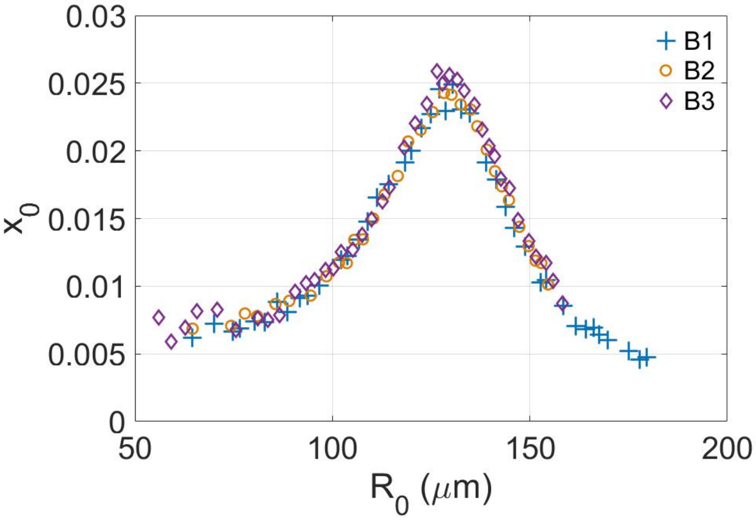

Fig. 6.3 **Bubble excursion amplitude x_0 against varying bubble radius R_0** for experiments using bare bubbles B1 (blue plus), B2 (orange circles) and B3 (violet diamonds) at $A = 40$ %.

into the gel, leading to reduced bubble excursions. However, within each gel, the results were reproducible, as demonstrated by the reproducibility of the radius-sweep experiments in each enclosure, using different bubbles, which are illustrated in the same figure.

To test the effect of ageing in a given gel, radius-sweep experiments were done at $A = 40, 60$ and 80 %, using different bubbles on different days. These are summarised in Figure C.2. The similarity of the excursions even on the 10th day [Figure C.2(b)] suggested that the gels, if completely immersed in ultrapure water at $T = 16 - 18°\text{C}$, did not undergo significant physical or chemical changes and their bulk rheological properties remained unchanged. This control experiment would be important for later experiments involving colloid-coated bubbles, where the effect of particle size on bubble dynamics was investigated.

To test if the pressure amplitude is linear with gain A, and if the bubble response is linear with the pressure amplitude, the radius-sweep experiments were performed in the same gel at different amplifications A, using different bubbles. This way *resonance curves* for varying pressure amplitudes were obtained as shown in Figure 6.4(a). The excursions x_0 as a function of A, for the same R_0 were obtained by linear interpolation. An example is shown in Figure 6.4(b) for $R_0 = 128$ μm. The linear fit to the

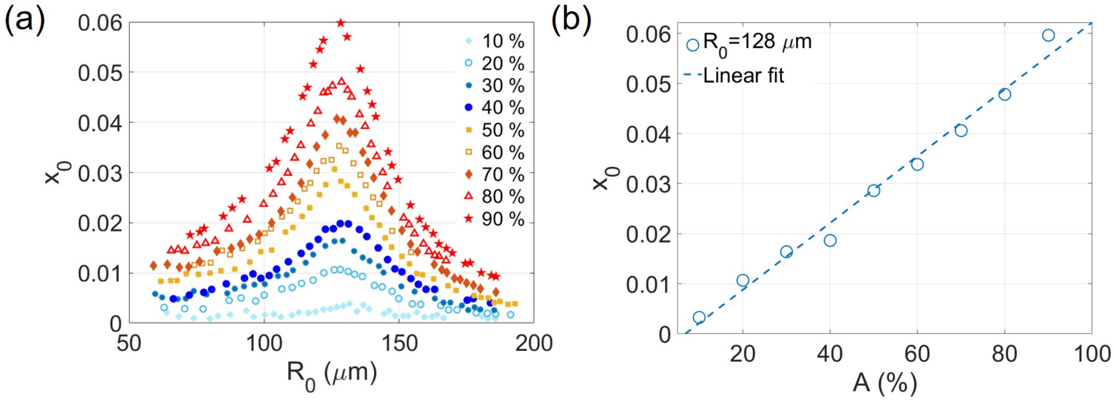

Fig. 6.4 (a) **Resonance curves for increasing pressure amplitude:** excursion amplitude x_0 with varying bubble resting radius R_0 for different acoustic pressure amplitude in terms of amplification $A(\%)$. Only one set of data is shown for each value of $A = 10$ % (plus), $A = 20$ % (open circle), $A = 30$ % (star), $A = 40$ % (filled circle), $A = 50$ % (cross), $A = 60$ % (open square), $A = 70$ % (filled diamond), $A = 80$ % (open triangle) and $A = 90$ % (filled pentagram). (b) Using the resonance-radius excursion map in (a), the excursion amplitudes of a bubble with radius $R_0 = 128$ μm is estimated by linear interpolation (blue circles). The linear fit to the data is shown by the blue dashed line.

data suggests that the amplitude of oscillations varies linearly with the amplification. Additional supporting data are shown in Figure C.3.

6.3.2 Pressure-sweep experiments on bare bubbles

The effect of pressure variation on excursion amplitude of a bubble is presented in Figure 6.5(a), where the initial bubble radius is $R_0 = 97.9$ μm before the first run at $A = 5\%$ and it decreases to $R_0 = 96.7$ μm when $A = 100\%$. Despite the decrease in radius of 1.2%, the trend of x_0 against A appears linear. Another example, where the step change in A was by 5%, leading to a prolonged observation time, for a larger bubble with initial $R_0 = 167$ μm, where the change in bubble size is $\Delta R = 1.1\%$, the trend again appears linear as seen in Figure C.4.

For a given gel, excursion is plotted against amplification for different bubbles with fixed R_0 in Figure 6.5(b). Linear fitting of the data for each bubble are also shown. As expected, bubbles close to the resonance radius exhibit the maximum response compared to bubbles with R_0 either smaller or greater than R_{res}.

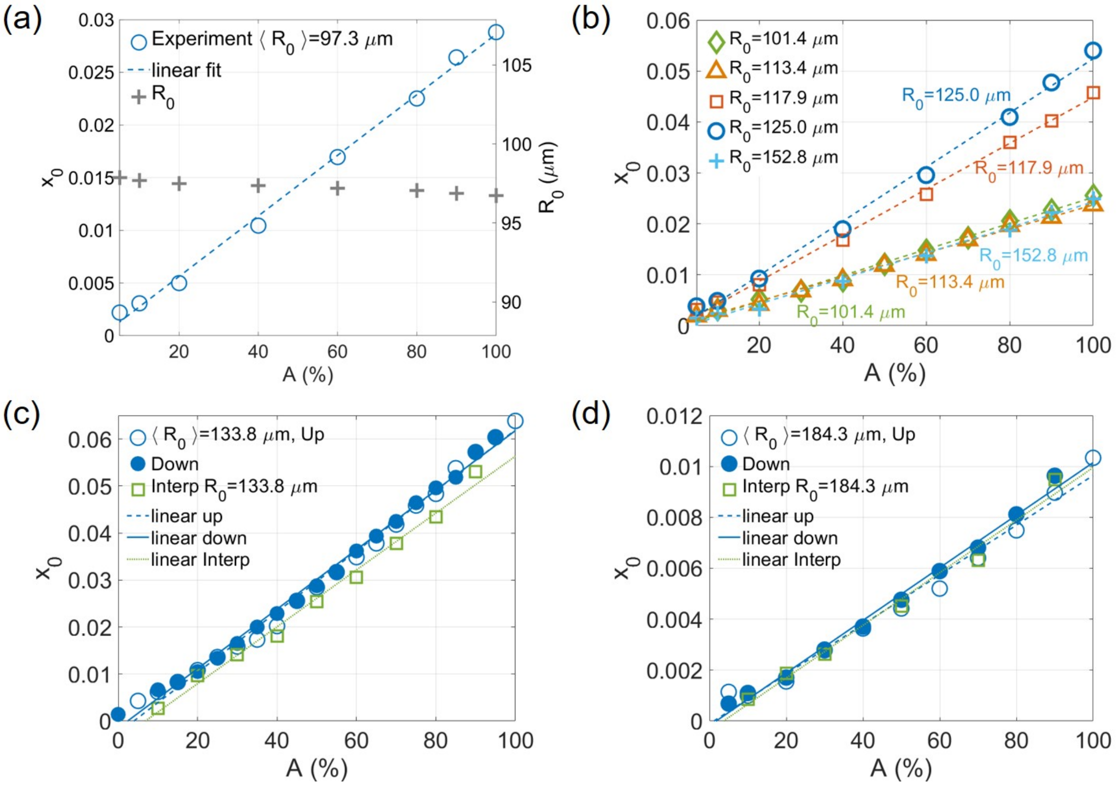

Fig. 6.5 **Variation of excursion amplitude (x_0) with acoustic pressure in terms of amplification A (%) for bare bubbles.** (a) The excursions (open circles) for a bubble with mean radius $\langle R_0 \rangle = 97.3$ μm is plotted against A. The bubble radii just before and after the oscillations, for each point, are shown by the grey plus symbols (right y-axis). A linear fit to the $x_0 - A$ data is shown by the dashed blue line. (b) $x_0 - A$ plots for different bubbles with $R_0 = 101.4$ μm (green diamonds), linear fit (green dashed line); $R_0 = 113.4$ μm (orange triangles), linear fit (orange dashed line); $R_0 = 117.9$ μm (light orange squares), linear fit (light orange line); $R_0 = 125.0$ μm (blue circles), linear fit (blue line); and $R_0 = 152.8$ μm (cyan plus), linear fit (cyan line). (c) Excursions of a bubble of radius $\langle R_0 \rangle = 133.8$ μm with amplifications going up (open blue circles) and amplifications going down (filled blue circles). The respective linear fits to the data are shown by blue dashed and blue solid lines. The $x_0 - A$ data interpolated from the excursion map [Figure 6.4(a)], for a bare bubble of same radius is also shown (open green squares) with its linear fit (green dotted line). (d) The same as in (c) but for $\langle R_0 \rangle = 184.3$ μm.

In Figure 6.5(c), a bubble, with mean radius $\langle R_0 \rangle = 133.8$ μm, is first subjected to increasing pressures (referred to as 'Up' series in figures), and then to decreasing pressures ('Down' series). The data for the two series coincide because the change in radius is negligible ($\Delta R_0 < 1\%$) over all the runs. There is then, practically, no hysteresis between the series corresponding to the amplification steps going up or down. The same remains true for another example where the mean radius is $\langle R_0 \rangle = 184.3 \pm 1.1$ μm as shown in Figure 6.5(d).

The excursions observed in the pressure-sweep experiments were expected to be similar to the excursions observed in the radius-sweep experiments at different amplifications [section (6.3.1) and Figure 6.4]. As a comparison, x_0 is estimated for a bubble with $R_0 = 133.8$ μm at different A by interpolating the data from the resonance-radius excursion map for that gel [Figure 6.4(a)]. The obtained excursions, and the linear fit to the data, are overlaid in Figure 6.5 (c). The trends are indeed similar in both classes of experiments. It is further supported by similar comparisons made for the bubble with $\langle R_0 \rangle = 184.3 \pm 1.1$ μm, in Figure 6.5(d).

The equivalence of the two classes of experiments, radius-sweep and pressure-sweep, in this manner, will be used when investigating the behaviour of colloid-coated bubbles.

6.3.3 Surface microstructure of colloid-coated bubbles

Monodisperse colloidal microspheres of given sizes, adsorbed at the air-water interface in the aggregated state, formed an armour around the colloid-coated bubbles. This is shown in Figure 6.6. Even in presence of multiple bubbles in contact, coalescence was inhibited by the particles at the periphery, as seen in [Figure C.5(b)]. Forced oscillation of bubble pairs in contact, did not cause them to coalesce. Under static conditions, at very low surface coverage, the colloids exhibited ordering up to several particle diameters [Figure C.6 (a,b)]. For very high coverage, a bubble attained a buckled shape [Figure C.6(c)].

6.3.4 Oscillations of colloid-coated bubbles

The colloid-coated bubbles were subjected to ultrasound-induced oscillations with varying pressure amplitude. The radius-time curves for such bubbles exhibited an *expansion-only* behaviour, that is, the bubbles had a higher excursion during expansion,

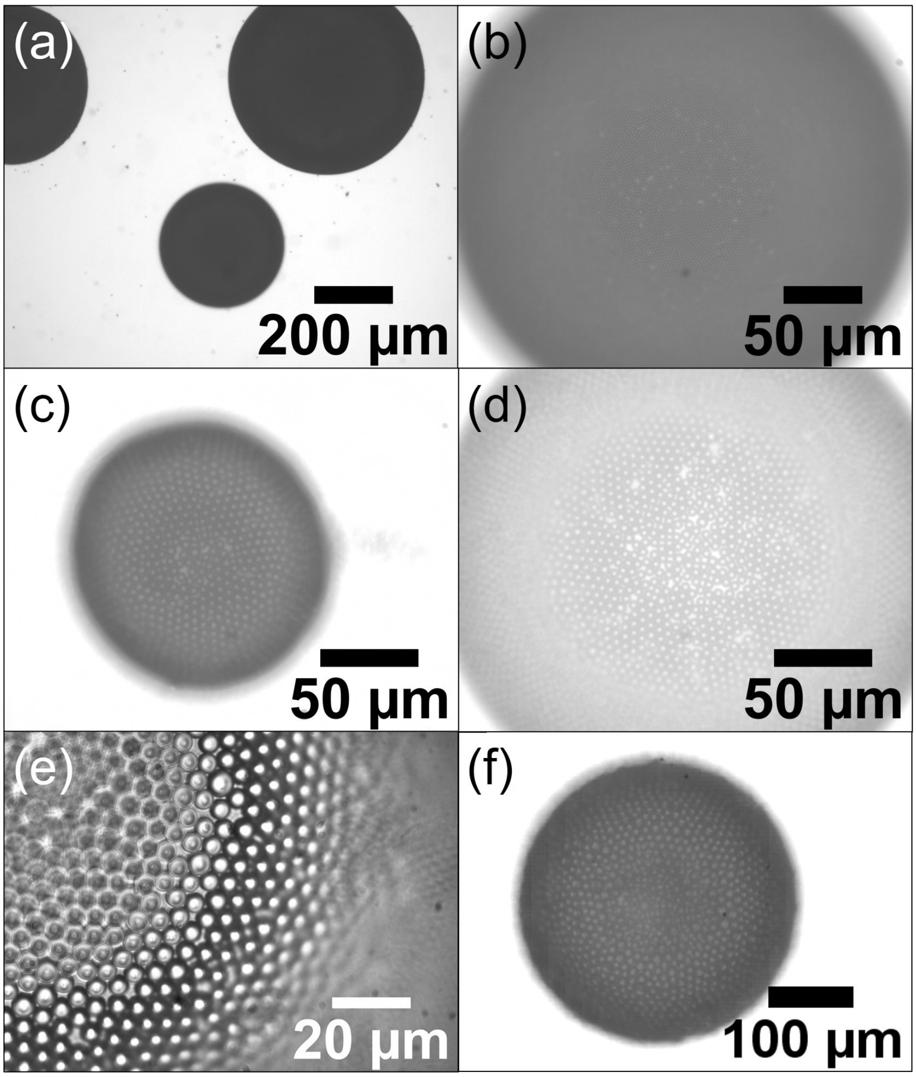
(a)
200 μm
(b)
50 μm
(c)
50 μm
(d)
50 μm
(e)
20 μm
(f)
100 μm

Fig. 6.6 **Colloid-coated microbubbles.** (a,b) Bubbles coated by $a = 1.2$ μm colloids; (c,d) $a = 2.5$ μm, with the bubble in (c) being an oblate spheroid. (e) A higher magnification used to observe particles, $a = 2.5$ μm, in a given focal plane. (f) A bubble coated by $a = 5.0$ μm particles.

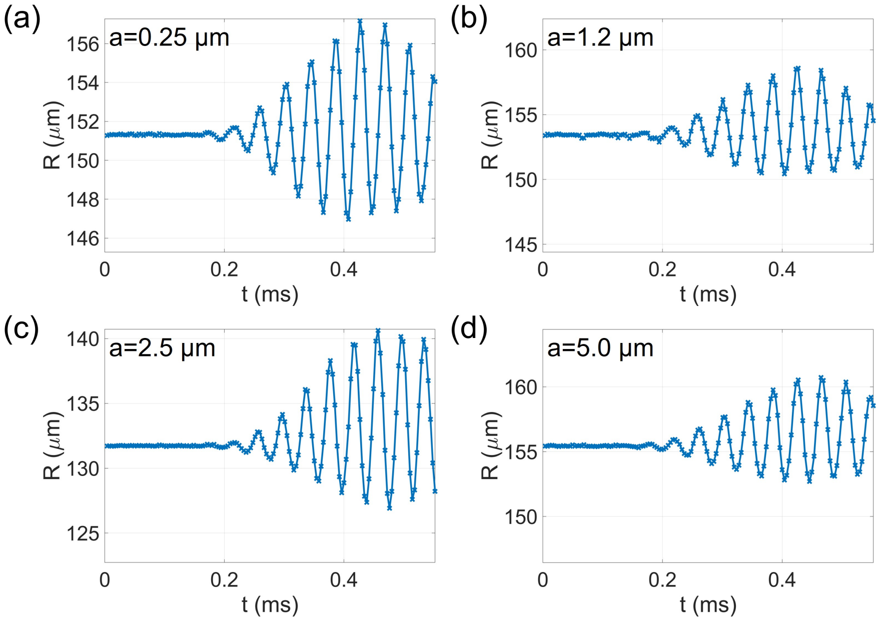

Fig. 6.7 **Radius-time curves of colloid-coated bubbles.** (a) A bubble with $R_0 = 151.3$ μm coated by spherical colloids of radius $a = 0.25$ μm; (b) $R_0 = 153.4$ μm, $a = 1.2$ μm; (c) $R_0 = 131.7$ μm, $a = 2.5$ μm; and (d) $R_0 = 155.4$ μm, $a = 5$ μm, all at $A = 100\%$.

while the extent of compression was smaller. This is shown in Figure 6.7 for various particle sizes. The behaviour is similar to what has been observed for bubbles coated with liposomes attached to lipid monolayers [131], as well as for gold nanoparticle-coated microbubbles [76, 77]. Quantitatively, the excursion during expansion may be defined as

$$x_{\mathrm{e}} = \frac{R_{\mathrm{max}} - R_0}{R_0} \tag{6.2}$$

while the extent of compression can be defined as

$$x_{\mathrm{c}} = \frac{R_0 - R_{\mathrm{min}}}{R_0}. \tag{6.3}$$

For bare bubbles at similar pressure amplitudes, $x_{\mathrm{e}}/x_{\mathrm{c}} \approx 1$. This is shown in Figure 6.8 (a,c). Whereas, for coated bubbles it is experimentally observed that typically $x_{\mathrm{e}}/x_{\mathrm{c}} > 1$. An example for a bubble coated by 2.5 μm colloids is shown in Figure 6.8(b,d).

Even for a prolonged acoustic cycling period, the oscillations exhibited this asymmetry. An example for a bubble coated by $a = 1.2$ μm colloids with 20 cycles of ultrasonic driving is shown in Figure C.7.

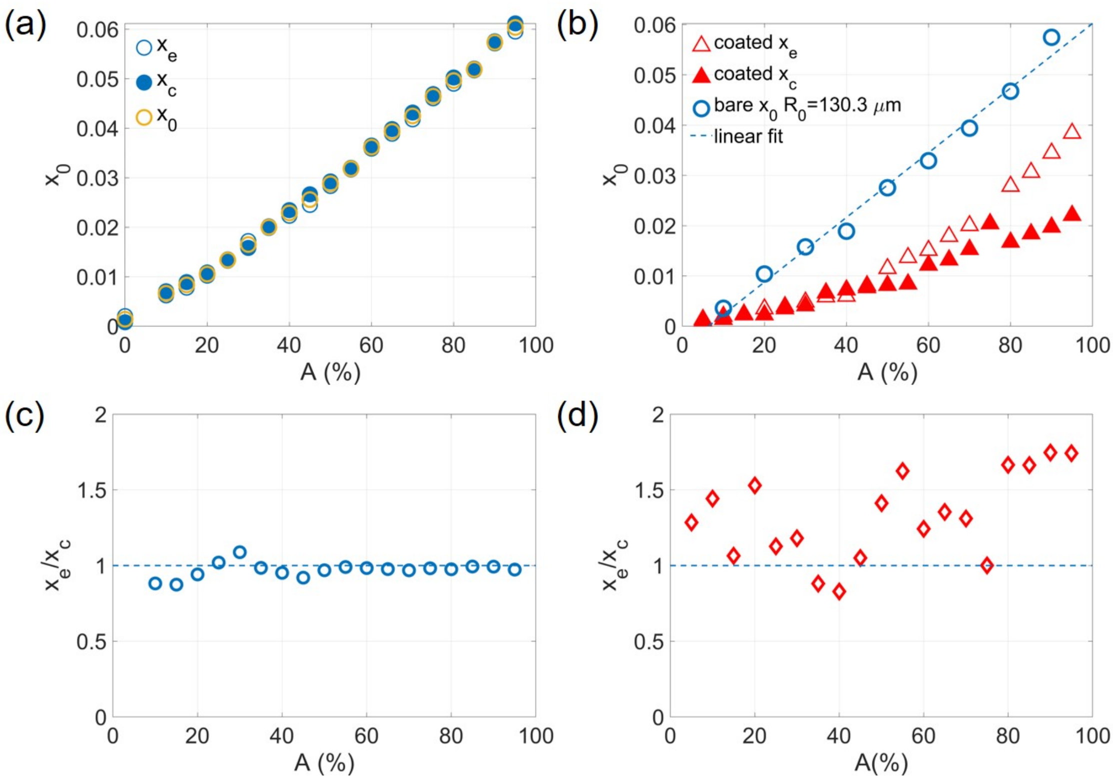

Fig. 6.8 Comparing bubble excursions during expansion (x_e) and compression (x_c). (a) A bare bubble with $\langle R_0 \rangle = 134.4$ μm for increasing gain. x_e (open blue circles), x_c (filled blue circles) and x_0 (open orange circles) all overlap. (b) For a $\langle R_0 \rangle = 130.3$ μm, coated by $a = 2.5$ μm colloids, x_e (open triangles) is greater than x_c (filled triangles) at higher pressures. For comparison, the excursions x_0 (open circles) for a bare bubble of the same radius is shown along with its linear fit (dashed line). The ratio of x_e/x_c for (c) the bare bubble is close to unity, while for (d) the coated bubble, it is usually above unity.

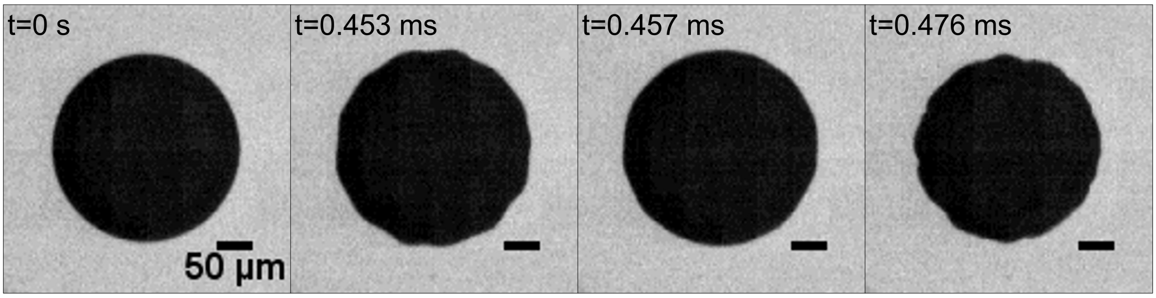

Fig. 6.9 Image sequence of bubble oscillations for $R_0 = 131.7$ μm and $a = 2.5$ μm. At $t = 0$, $R = R_0$. The bubble was just about to attain the maximum radius at $t = 0.453$ ms and $t = 0.457$ ms was just after this. The maximum compression occurred roughly at $t = 0.476$ ms.

As the bubbles compressed, the particle monolayer underwent buckling without any particle desorption. This is shown by the image sequence for a bubble in Figure 6.9 with $R_0 = 131.7\ \mu$m, with $a = 2.5\ \mu$m and is the same as the one shown in Figure 6.7. Different buckling modes are active at different instances, as seen by the wavelength of the undulations throughout the series.

6.3.5 Pressure-sweep experiments on colloid-coated bubbles: a = 2.5 μm colloids

Colloidal particles of size $a = 2.5\ \mu$m were most easy to observe. For this reason, they were taken as candidates for extensive study. Pressure-sweep experiments were performed using armoured bubbles. For a bubble with $R_0 = 132.6 \pm 1.7\ \mu$m, $a = 2.5\ \mu$m, the excursions for increasing and decreasing acoustic pressure, are shown in Figure 6.10(a). This is compared with a bare bubble of similar radius $R_0 = 133.9 \pm 0.7\ \mu$m under the same changes in pressure, within the same gel enclosure. The excursions of the coated bubble are of lower magnitudes than those of the bare one. Further, the excursions of the former initially follow a non-linear increase with pressure.

To test the effect of multiple perturbations and ageing, a coated-bubble was oscillated at $A = 40\%$ after different waiting times, as shown in Figure 6.10(b). First it was subjected to increasing pressures, of which the excursion amplitude at $A = 40\%$, is represented at $t = 0$ min in the figure. Then at $t = 8$ min, during the gain Down series. After this, it was again oscillated at different times, up to $t = 13$ min, being driven only at $A = 40\%$. During this the radius varied by 0.8% while the excursion amplitude by 21.8%.

It was not possible to always get a bare bubble and a colloid-coated bubble of the same size for direct comparison. For this reason, the equivalence shown to hold for bare bubbles under pressure-sweep and radius-sweep experiments, as shown in section 6.3.2: Figure 6.5(c,d), was valuable. For every coated bubble of radius R_0, the excursions of a bare bubble with the same radius could be obtained by interpolating the data available in the excursion map for the gel used (Figure 6.4). This way, a coated bubble with $\langle R_0 \rangle = 155\ \mu$m and $a = 2.5\ \mu$m was compared with a bare bubble with the same radius as shown in Figure 6.10(c). Further, in Figure 6.10(d), it is shown that the amplitudes of excursion, for a coated bubble, overlap for both increasing and decreasing pressures.

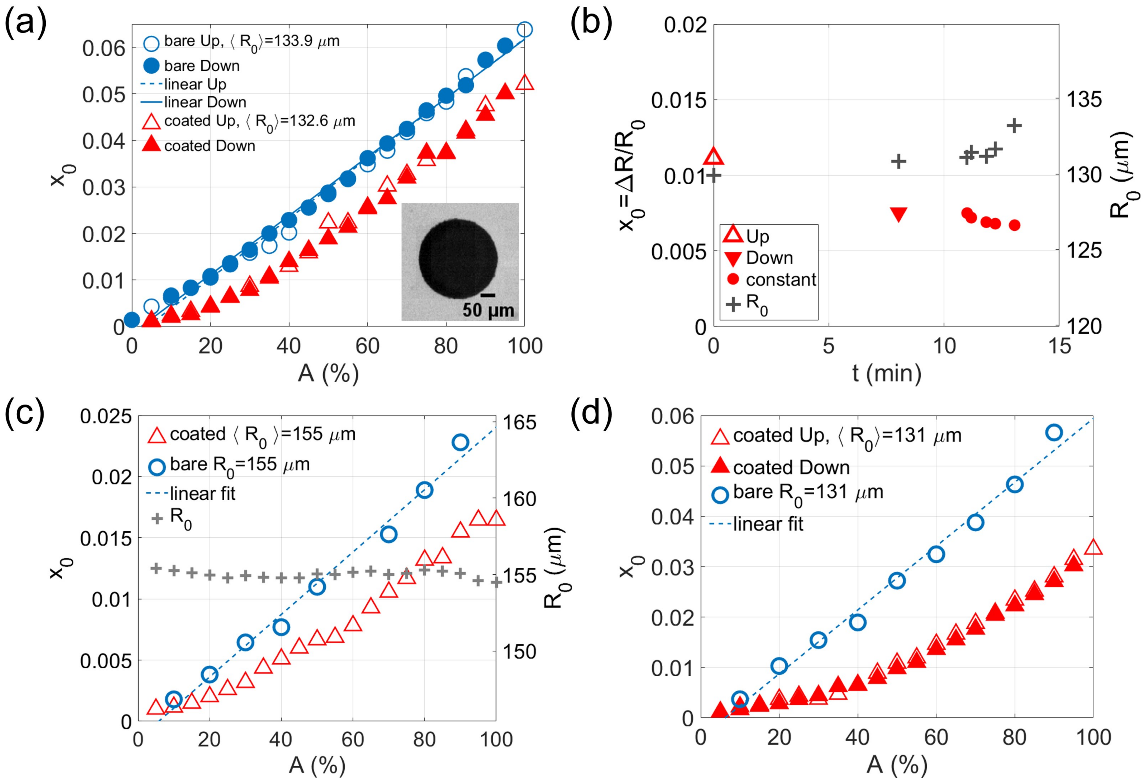

Fig. 6.10 **Excursions of bubbles coated by colloids with a = 2.5 μm.** (a) Excursion amplitudes of a bare bubble, with $R_0 = 133.9\ \mu$m, as amplification went up (open blue circles) and then down (filled blue circles), with the corresponding linear fits as shown by dashed and solid lines respectively. Overall change in radius $\Delta R < 1\%$. These are compared to the excursion amplitudes of a coated bubble, with $\langle R_0 \rangle = 132.6\ \mu$m, as amplification went up (open red triangles) and then down (filled red triangles). The coated-bubble at the start of the experiment is shown in the inset. (b) Examining ageing effect on a particle coated bubble at $A = 40\%$. Excursion amplitudes during increasing pressure (open upward triangle), decreasing pressure (filled downward triangle) and constant pressure (filled red circles) are shown. The radius R_0 of the bubble during these times are also shown (plus symbols, right y-axis). (c) Comparing excursions of a coated bubble, of radius $\langle R_0 \rangle = 155\ \mu$m, with that of a bare bubble (open circles) of the same radius. The excursions of the latter are obtained by linear interpolation from the excursion map for the gel [Figure 6.4(a)]. (d) Excursions of a coated bubble, $\langle R_0 \rangle = 131\ \mu$m, for increasing (open triangles) and decreasing (filled triangles) pressures, compared with a bare bubble of the same radius (obtained by interpolation).

Colloid-coated bubbles are expected to be very stable against dissolution [19, 44]. It is possible that, during bubble oscillations, the particle configuration is disrupted and momentarily the bubble becomes prone to dissolution until a new jammed state is attained. In the jammed state, the bubbles were typically not perfectly spherical. Applying a few cycles of oscillations could make them change towards more spherical shapes. Therefore, the equivalent radius of the projected bubble in the focal plane could increase or decrease marginally. Yet the excursion behaviour of the bubble remains the same despite the shape changes as shown for a coated bubble in Figure C.8.

For bare bubbles, the amplitude of oscillations is symmetric around the resting radius, $x_0 = x_\mathrm{e} = x_\mathrm{c}$ [Figure 6.8 (a,c)]. It may be reasoned that since for the coated bubbles $x_\mathrm{e}/x_\mathrm{c} > 1$, the average excursion x_0 is reduced by the limited compression. To check this, the excursions of a coated bubble were separated into x_e and x_c [Figure 6.8(b)]. It is seen that $x_0(\text{bare}) > x_\mathrm{e}$, and so the amplitude of response of a bubble coated with 2.5 μm colloids is still smaller than its counterpart bare bubble. Further, rarely $x_\mathrm{e} \approx x_\mathrm{c}$ for the coated bubbles [Figure 6.8(d)]. Thus, only x_0 is shown in the following figures, unless stated otherwise.

To tune the surface coverage fraction ϕ, a coated bubble, with $a = 2.5$ μm, was placed into the enclosure undisturbed for 30 minutes, at supersaturated conditions and allowed to grow by gas diffusion. The bubble was then found to be spherical with patches of its surface devoid of particles. In a pressure-sweep with increasing amplitude, $x_0(\text{coated}) < x_0(\text{bare})$ as seen in Figure 6.11 (a). In a pressure-sweep with decreasing amplitude, $x_0(\text{coated}) \approx x_0(\text{bare})$ for $A \leq 60\%$. This difference may be because at small excursions (at small A), particularly during compression, the particles at the interface are not impacted by their neighbours as the colloidal network is sparse. At higher compressions (typically $A > 60\%$), the particles interact with each other and the compression of the interface is resisted. This hypothesis is supported by observing the radius-time curves at $A = 50\%$ and $A = 90\%$ for decreasing pressure amplitude in Figure 6.11(c,e) respectively. At $A = 50\%$ [Figure 6.11(c)], the oscillations are symmetric about R_0, while at $A = 90\%$ [Figure 6.11(e)], expansion-only behaviour occurs.

Further, the apparent hysteresis between the up and down series, may be attributed to changes in the microstructure of the interfacial monolayer. Interestingly, at $A = 50\%$ during the pressure sweep with increasing amplitude [Figure 6.11(b)] the oscillations are expansion-only, while at the same amplification during the pressure sweep with

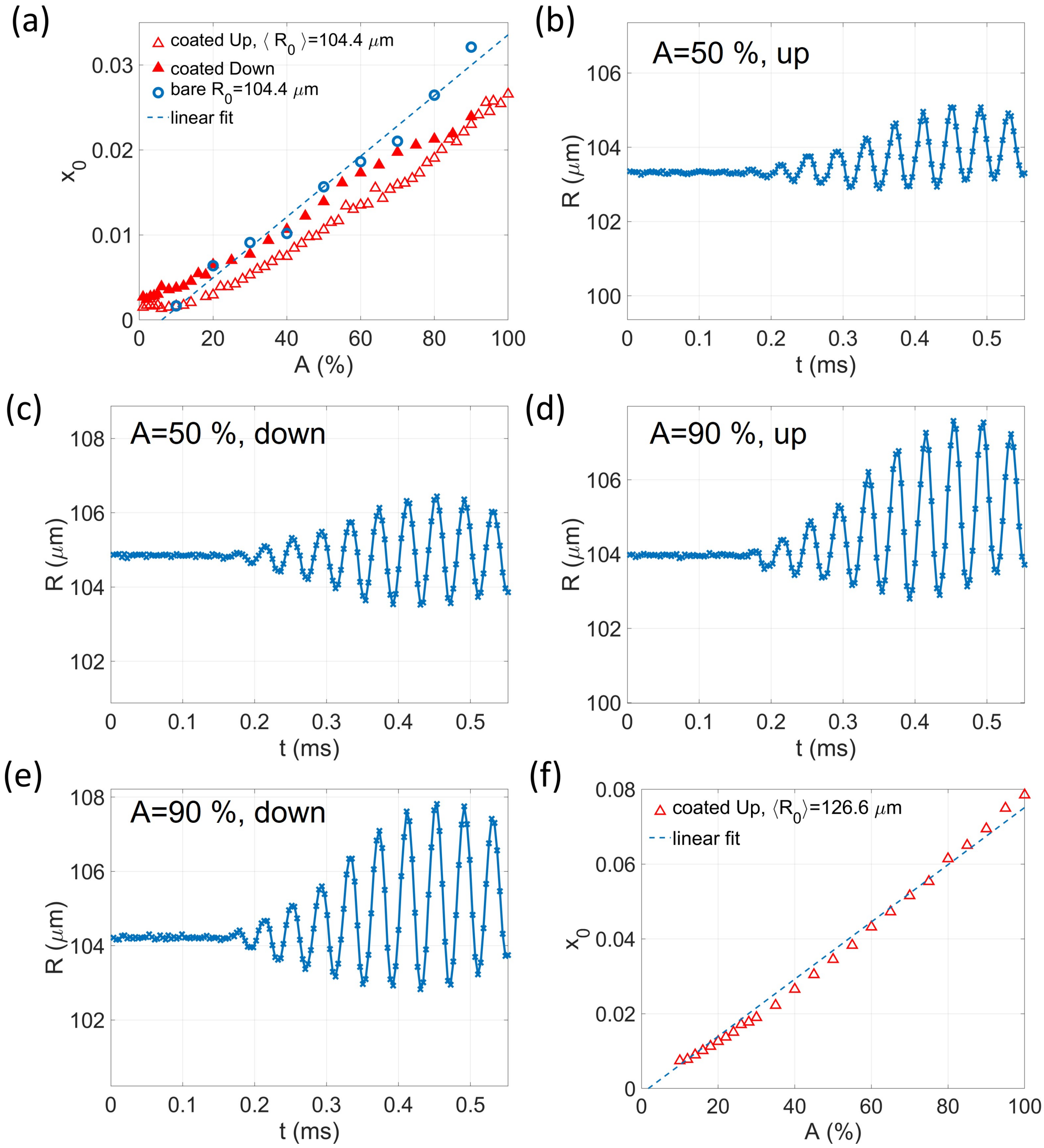

Fig. 6.11 **Hysteresis in the response of a coated bubble with reduced coverage.** (a) Comparing excursions of a coated bubble with gain going up (open red triangles) and then down (filled red triangles). Overall, $\langle R_0 \rangle = 104.4\ \mu$m with change in $\Delta R_0 = 1.7\%$. For comparison, excursions of an equivalent bare bubble are shown (open blue circle with its linear fit (dashed blue line). Radius-time curves for the coated bubble at (b) $A = 50\%$ during the 'Up' series and (c) $A = 50\%$ during the 'Down' series. Similarly at $A = 90\%$ during the (d) 'Up' series and (e) 'Down' series. (f) The same bubble after being left undisturbed for 101 minutes, grew larger with $\langle R_0 \rangle = 126.6\ \mu$m from $\langle R_0 \rangle = 104.4\ \mu$m. The excursions are apparently linear.

decreasing amplitude, the oscillations are symmetric [Figure 6.11(c)]. For $A = 90\%$, the oscillations are identical [Figure 6.11(d,e)]. When the same bubble was left unperturbed for an additional 101 minutes, the bubble size changed from $R_0 = 104.4$ μm to $R_0 = 126.6$ μm leading to the surface coverage being $\phi \approx 0.57$, since the number of particles at the surface was constant. The oscillations of this larger bubble were symmetric for all A, a few examples of which are shown in Figure C.9. And the magnitude of the excursions were both linear and comparable to that of a bare bubble as seen in Figure 6.11(f). This apparent hysteresis in oscillation dynamics was observed for bubbles with a surface coverage fraction between $0.7 \leq \phi < 0.8$.

6.3.6 Effect of particle size

Pressure-sweep experiments with bubbles with interfaces decorated with colloidal particles with other sizes revealed similar trends as those with $a = 2.5$ μm, when contrasted with bare bubbles. The excursions varied non-linearly at low pressures, and the magnitudes were below those of their respective counterpart bare bubbles. Examples for $a = 1.2$ μm and $a = 5.0$ μm are shown in Figure 6.12 in panels (a,b) and (c,d) respectively. So far, as the data stands, no remark can be made when comparing bubbles of the same size for different particle sizes as it was not possible to study bubbles with the same R_0. Pressure-sweep experiments for bubbles, coated by $a = 0.25$ μm colloids, led to expulsion of the particles beyond certain pressure amplitudes. An example is given in Figure C.10. The expulsion of colloid particles from coated bubble interfaces has been studied previously [126]. Therefore, to perform experiments with a constant number of particles in the monolayer, sub-micron particles were not considered.

6.3.7 Coated bubbles radius-sweep experiments

Radius-sweep experiments were performed using bubbles coated with particles of size $a = 1.2$ μm. The results at $A = 40\%$ are shown in Figure 6.13(a), where the excursions of the coated bubbles are contrasted with those of bare bubbles at the same gain. The spectral density of the radius-time curves for each bubble, bare and coated, were analysed. The analysis described by van der Meer et. al. [70] was used. Since the driving frequency was fixed at $f = 25$ kHz, a quantitative estimate of the response of the bubble was obtained by integrating the area under the power spectrum in a band

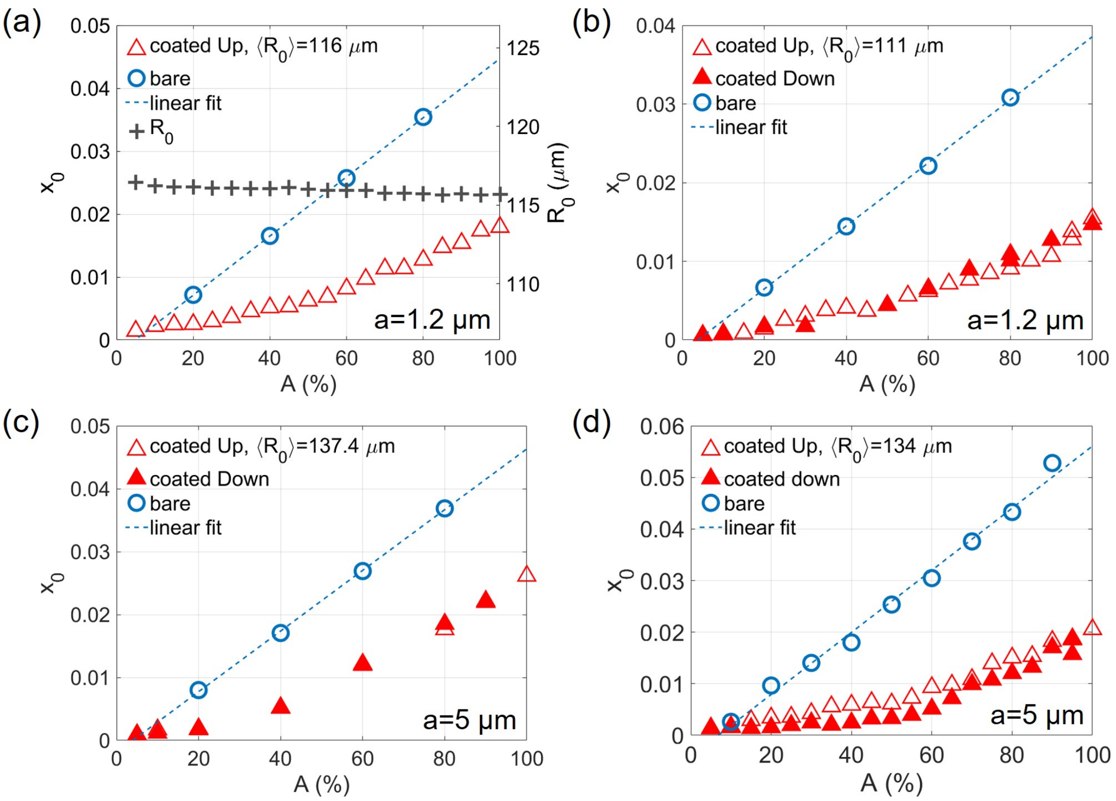

Fig. 6.12 **Bubbles coated with other particle sizes**. (a) The excursion amplitudes (red open triangles) for a bubble with $R_0 = 116$ μm coated with $a = 1.2$ μm colloids, as gain A goes up in steps. The equivalent bare bubble excursions (through interpolation) and the linear fits are shown by the open blue circles and the blue dashed line respectively. The radius R_0 (grey plus symbols, right y-axis) does not change significantly. (b) Another bubble with $R_0 = 111$ μm and $a = 1.2$ μm with gain going up (open red triangles) and then down (filled red triangles). (c,d) Bubbles coated by $a = 5$ μm colloidal microspheres. The excursions as the gain is both increased and then decreased is shown for (c) $R_0 = 137.4$ μm and (d) $R_0 = 134$ μm.

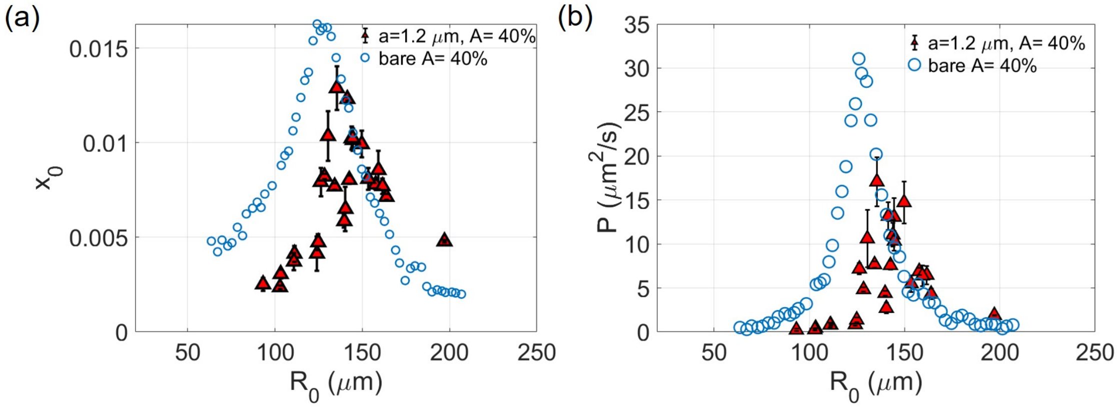

Fig. 6.13 **Radius-sweep experiments for coated bubbles, with particle size $\boldsymbol{a = 1.2\ \mu}$m.** (a) Comparison of bare and coated bubble responses for varying R_0 at fixed $A = 40\%$. (b) The same data recast in terms of the power spectrum.

of $\Delta f = 2$ kHz around the driving frequency. This integral P corresponding to the acoustic energy gone into the oscillations of the bubble was defined as

$$P = \int_{f-\frac{1}{2}\Delta f}^{f+\frac{1}{2}\Delta f} p_f \mathrm{d}f, \tag{6.4}$$

where p_f is the power spectrum, with units of μm^2, of the time-varying signal $x(t) = R(t) - R_0$, in units of μm. The units of P are μm^2/s. The discrete Fourier transform of the signal was computed using the MATLAB functions *fft* and *fftshift*.

The results of x_0 against R_0 for the bare and coated bubbles are recast in terms of a response P against R_0 plot in Figure 6.13(b). For the given sample of coated bubbles, the resonance radius appears at $R_{\text{res}}^{\text{coated}} \approx 135.4\ \mu$m, in contrast to $R_{\text{res}}^{\text{bare}} \approx 126.0\ \mu$m, for the bare bubble series. Also, as expected from the previous experiments, the response of the coated bubbles exhibit smaller amplitude than the corresponding bare bubbles. Similar trends are observed for $A = 60\%$, in a separate set of experiments as shown in Figure C.11.

6.4 Discussion

Here, the characteristic behaviour of colloid-coated bubbles are first summarised. Following this the possible micromechanical and viscoelastic effects responsible for the behaviours are discussed.

6.4.1 Summary of experimental results

In summary, the results for colloid-coated bubbles showed the following trends:

1. In pressure-sweep experiments, the excursion amplitude is reduced compared to bare bubbles in the same conditions; and the trend with respect to pressure amplitude is non-linear in the same conditions in which it is linear for bare bubbles.

2. The radius-time curves of coated bubbles exhibit expansion-only behaviour. The reduced excursions with respect to bare bubbles are not completely explained in terms of the excursion asymmetry.

3. During the compression phase of the oscillations, the monolayer is observed to buckle.

4. Hysteresis is observed for bubbles with surface coverage typically $\phi < 0.80$, when the $x_0 - A$ plots for increasing gain are compared with the decreasing gain series for the same bubbles. At low pressures, the bubbles appear to oscillate as their bare counterparts once the initial microstructure has been disrupted. When the bubbles are allowed to grow, further reducing surface coverage to $\phi \approx 0.57$, they behave as bare bubbles for all amplifications explored.

5. No conclusive remarks can be made on the effect of particle size, for the sizes considered here: $a = 1.2, 2.5$ and 5 μm. This was because it was not possible to directly compare bubbles with the same R_0.

6. In radius-sweep experiments performed using $a = 1.2$ μm, the resonance-radius of the coated bubbles was found to be 6.9% higher than that for bare bubbles under similar conditions, at a constant gain $A = 40\%$. At $A = 60\%$, $R_{\text{res}}^{\text{coated}}$ was 8.5% higher than $R_{\text{res}}^{\text{bare}}$. In addition, the excursions of the bubbles were lower than their corresponding bare bubble counterparts.

6.4.2 Expansion-only behaviour of colloid-coated bubbles

To explain the expansion-only behaviour observed for coated bubbles, a model is proposed that combines a model for bubble dynamics for lipid-coated microbubbles by Marmottant et. al. 2005 [69], with the buckling model for colloid-coated bubbles developed by Taccoen et. al. 2016 [45]. These models have been reviewed in section 2.6.2 and section 2.3, respectively. Among the existing models to describe the dynamics of lipid-coated bubbles, the one developed in [69] has been considered here because it can be easily combined with the micromechanical description of the compressive stresses within particle monolayers developed in [45].

In experiments, the colloid-coated bubbles were found to have high surface coverage, as was visually apparent (Figures 6.6 and 6.9). Hence the interface may be considered to be fully packed, with a surface coverage $\phi \approx 0.91$, when the bubble is at its resting radius R_0. As the bubble radius decreases, the monolayer undergoes compression. Then there is a competition between particle desorption against monolayer compression. For strong particle adsorption, the monolayer will buckle and this has indeed been observed in experiments [42, 132, 45, 133]. The model developed by [45] considered the energetic cost of compressing the monolayer to be balanced by the high desorption energy of particles. During compression, the out-of-plane deformation of the 'shell' was described by a sinusoidal profile with amplitude smaller than a particle diameter, that is, $B < 2a$. The expression for the energy per unit area to compress the packed bubble monolayer was given as

$$W_{\text{shell}} = -\frac{\pi \sigma_{\text{water}} \delta R}{R_0[1 - \cos(\frac{\pi}{n})]}, \tag{6.5}$$

where δR is the change in bubble radius as the bubble is compressed, σ_{water} is the surface tension of the pristine air-water interface and n is the bending mode. The threshold differential pressure, outside the bubble, needed to induce a mechanical instability to cause buckling was given as

$$\Delta P_n^* = \frac{\pi \sigma_{\text{water}}}{R_0[1 - \cos(\frac{\pi}{n})]}. \tag{6.6}$$

In the derivation it was shown that the energy needed to compress the monolayer was independent of particle size. However, since $n \leq N$, the accessible mode and the number of particles may be expected to depend on the particle size. For a shell composed of discrete particles, $n = 1$ corresponds to highest frequency mode with particles staggered in an alternating manner. Longer the wavelength of the undulations, higher is the mode number, which has a higher energetic cost [equation (6.6)]. The undulations of the monolayer are schematically plotted, on a polar plot using a MATLAB script, as presented in Figure 6.14.

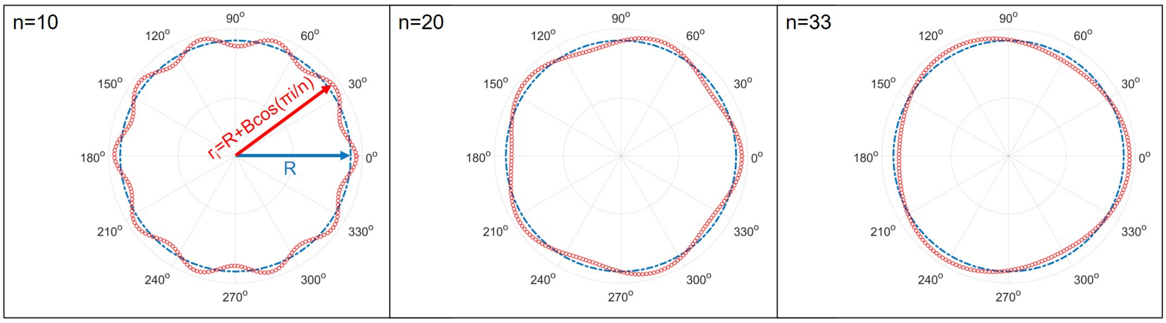

Fig. 6.14 **Polar plot of bending modes with $\mathbf{n = 10, 20}$ and 33.** A bare bubble with initial radius R_0, when compressed would have its contour described by the fixed radius $R < R_0$ (dashed blue line). But in presence of a compact particle monolayer at the interface, each particle will be displaced, relative to the interface at radius R, as the monolayer buckles. Thus, the radial position of each i-th particle can be described by $r_i = R + B\cos(\pi i/n)$ (red circles). The number of particles shown is $N = 200$.

When the bubble expands with $R > R_0$, the elasticity arising from the attractive lateral particle-particle interactions is expected to resist the expansion. Following the approach developed by [69] to describe the bubble dynamics of lipid-coated bubbles, where the elasticity E_d was assumed to be constant, the radius-dependent surface stress can be given as

$$\sigma(R) = \sigma(R_0) + E_\mathrm{d}\left(\frac{R^2}{R_0^2} - 1\right). \tag{6.7}$$

In the high-speed image sequences of colloid-coated bubbles, oscillated at high pressures, the colloids in the monolayer broke apart during bubble expansion, revealing air-water interface between them. Above a critical radius R_break, the average surface stress is therefore approximated as the surface tension of the bare interface σ_water.

Combining the effects of buckling [45] and surface elasticity [69], the surface stress can be defined as

$$\sigma(R) = \begin{cases} \sigma(R_0) + \frac{\pi\sigma_\mathrm{water}(\delta R/R_0)}{1-\cos(\pi/n)}, & \text{if} \quad R \le R_0 \\ \sigma(R_0) + E_\mathrm{d}\left(\frac{R^2}{R_0^2} - 1\right), & \text{if} \quad R_0 < R < R_\mathrm{break} \\ \sigma_\mathrm{water}, & \text{if ruptured and} \quad R \ge R_\mathrm{break} \end{cases} \tag{6.8}$$

For a packed monolayer on a Langmuir trough, the effective surface tension for $a = 1.5$ μm sulfate-latex particles [126], is found to be $\sigma_\mathrm{eff} \approx 20$ mN/m, and $E_\mathrm{d} \approx 25$ mN/m. So, in the above equation the surface stress at $R = R_0$ may be taken as

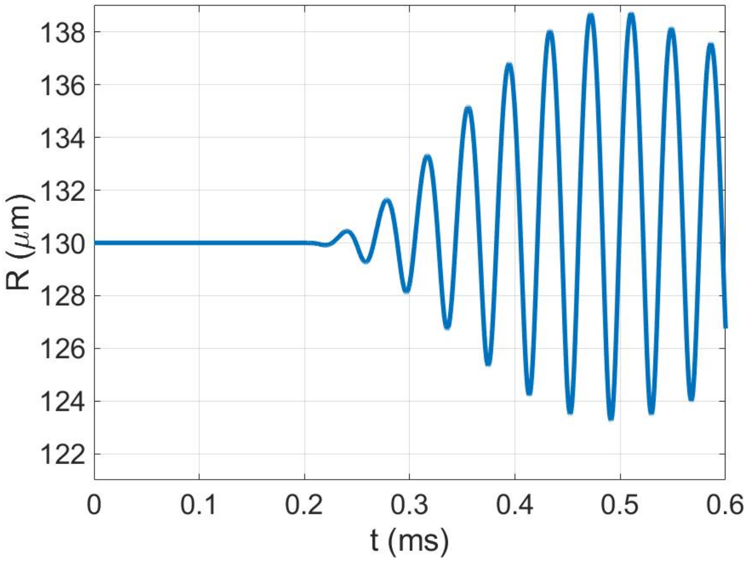

Fig. 6.15 Numerical solution of the model, presented in the main text, illustrating the radius-time curve for a bubble with radius $R_0 = 130$ μm and parameters as $n = 20$, $E_\mathrm{d} = 25$ mN/m, $\eta_\mathrm{d} = 0$ and $P_\mathrm{a} = 3$ kPa. The ratio expansion to compression ratio is $x_e/x_c = 1.30$.

$\sigma(R_0) = 20$ mN/m. This is in contrast to the effective surface tension for lipid-coated bubbles being $\sigma(R_0) = 0$ in the compressed state [69, 79].

It is noted that for $R < R_0$, the surface stress $\sigma(R)$ will gradually become negative as $\delta R = (R - R_0)$ increases in magnitude. When a particle monolayer is compressed by external forcing, the monolayer will develop internal stresses that will tend to expand the interface to attain a more relaxed configuration. While for $R > R_0$, the stress is always positive, meaning that work needs to be done to stretch the interface.

The surface stress function is introduced into the modified Rayleigh-Plesset equation as given by Marmottant et. al. 2005 [69],

$$\rho_l\left(R\ddot{R} + \frac{3}{2}\dot{R}^2\right) = \left[P_0 + \frac{2\sigma(R_0)}{R_0}\right]\left(\frac{R}{R_0}\right)^{-3\kappa} - P_0 - \frac{2\sigma(R)}{R} - \frac{4\mu\dot{R}}{R} - \frac{4\eta_\mathrm{d}\dot{R}}{R^2} - P_\mathrm{ac}(t), \quad (6.9)$$

where the dots indicate derivatives with respect to time. ρ_l is the liquid density with viscosity μ, κ the polytropic exponent for the gas assumed to behave ideally, P_0 is the ambient pressure, η_d is the dilational interfacial viscosity. $P_\mathrm{ac}(t) = P_\mathrm{a}\sin(\omega t)$ is the time-varying acoustic pressure of amplitude P_a and angular frequency ω.

The buckling mode n may be estimated a priori through equation (6.6), if the acoustic pressure amplitude is known. However, the presence of the compliant agarose ceiling in contact with the oscillating bubble is likely to introduce further sources of mechanical instabilities. In experiments, high bending modes, with long wavelengths are indeed observed during bubble oscillations (Figure 6.9 at $t = 0.457$ ms). Another reason for the appearance of higher bending modes may be due to instabilities arising from the rapid monolayer compression and expansion cycles occurring at a timescale $t \sim 10^{-4}$ s. Thus, higher buckling modes may be attained even though the threshold pressure needed for that mode is not reached by the acoustic pressure. Also it is observed that at different instants the buckling mode, as seen in the focal plane, can change (compare Figure 6.9 and 6.14). As an example, the radius-time curve for a colloid-coated bubble is plotted using equation (6.9) with $n = 20$, $\eta_\mathrm{d} = 0$ and $P_\mathrm{a} = 3.2$ kPa for $R_0 = 130$ μm. This is shown in Figure 6.15. According to this $x_\mathrm{e}/x_\mathrm{c} = 1.30$, which appears to be in the range seen for a coated bubble as seen in Figure 6.8(d).

6.4.3 Limitations of the model

There have been other models to explain the dynamics of particle-coated bubbles [76, 77], but these consist of a number of empirical parameters. The approach here has been to develop a model with a smaller number of empirical parameters, with a focus on describing behaviour through a micromechanistic view.

While it is able to explain the expansion-only behaviour, even at low pressure amplitudes, for colloid-coated bubbles, there are limitations. The dilational modulus E_d is taken to be constant as in the Marmottant model [69]. But in experiments it is observe that the slope of the bubble excursions change with pressure [Figures 6.10, 6.12 and 6.8(b)].

The functional form of the surface viscosity η_d is needed. There have been theoretical considerations of spheres adsorbed at fluid interfaces that give rise to dissipative mechanisms [134, 135]. Besides the dissipation occurring in the thin gaps between particles, the particle collisions are also expected to have an effect in dissipating the energy that would otherwise go into bubble oscillations.

Finally, the thermal dissipative mechanisms between the gas inside the bubble and the liquid outside, through the particle-laden interface, need a careful consideration when selecting the appropriate value of the ideal gas polytropic exponent κ.

6.4.4 Link to interfacial rheology

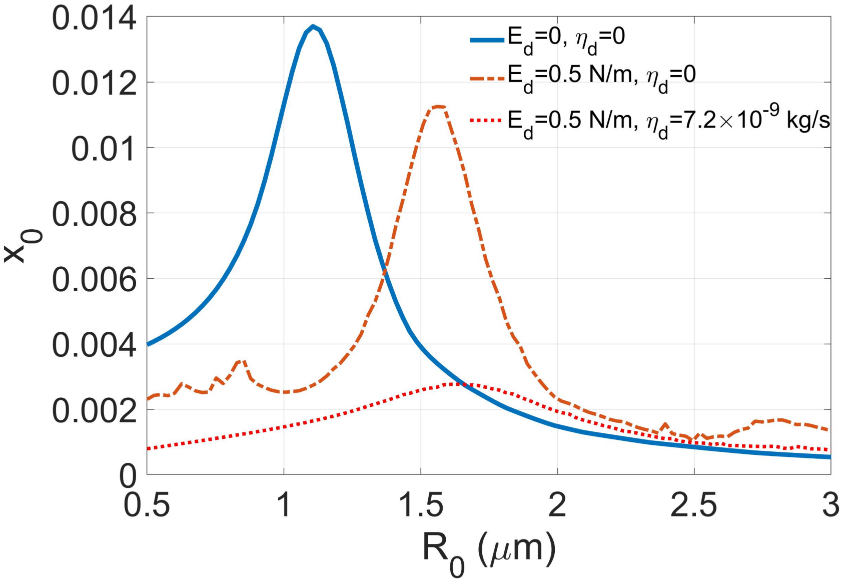

Fig. 6.16 **Numerical analysis of the effect of interfacial viscoelasticity on radius-sweep on lipid-coated bubbles.** The Marmottant model [69] is used to illustrate the effect of interfacial viscoelasticity. Three cases are shown: uncoated bubbles $E_\mathrm{d} = 0$, $\eta_\mathrm{d} = 0$ (solid line); bubbles with purely elastic interfaces $E_\mathrm{d} = 0.5$ N/m, $\eta_\mathrm{d} = 0$ (dashed line); and bubbles with viscoelastic interfaces $E_\mathrm{d} = 0.5$ N/m, $\eta_\mathrm{d} = 7.2 \times 10^{-9}$kg/s (dotted line). The parameters are typical representative of lipid-coated bubbles [70] with $f = 2.5$ MHz and $P_\mathrm{a} = 1$ kPa.

Viscoelastic properties of lipid-coated bubbles, oscillating at MHz frequencies, have been characterised by measuring the response of the bubbles, when oscillated at different frequencies, while keeping R_0 fixed [70, 79]. Typically, bubbles of size $R_0 \sim 1$ μm have been studied. By determining the frequency of maximum response, the dilational modulus and dilational viscosity of the lipid layer have been estimated. In the present case, due to experimental constraints (as mentioned in section 6.2.2), radius-sweep experiments were performed instead of frequency-sweep experiments. However, in the determination of the properties of the colloid monolayer, an analogous approach, as used for lipid-coated bubbles, may be adopted.

In general, in a radius-sweep experiment, interfacial elasticity can be expected to increase the radius of maximum response, for coated bubbles. Whereas, the dilational viscosity will tend to dampen the response of the bubbles. This hypothesis can be tested using numerical analysis. For lipid-coated bubbles, the results of performing a radius-sweep experiment on bubbles with $R_0 = 0.5 - 3$ μm may be predicted using numerical analysis. This is illustrated in Figure 6.16, where the Marmottant model [69] was used to numerically obtain the excursions for lipid coated bubbles. Equation (2.68), from section 2.6.2 was used to evaluate the surface stress $\sigma(R)$ with the modified Rayleigh-Plesset equation [equation (6.9)]. The parameters used were $E_\mathrm{d} = 500$ mN/m and $\eta_\mathrm{d} = 7.2 \times 10^{-9}$ kg/s, as typically reported for lipid-coated bubbles [70, 79, 136, 69].

From this, analogously, it can be inferred that the shift in resonance radius R_res and the reduction in excursion amplitudes x_0, for the colloid-coated bubbles with respect to bare bubbles (Figures 6.13 and C.11) is due to surface viscoelasticty of the monolayer.

The modified Rayleigh-Plesset equation can be linearised [70, 79, 136] to express the bubble excursions as a linear harmonic oscillator, as described in section 2.6.2 with x_0 expressed as

$$x_0(\omega) = \frac{P_\mathrm{a}/(\rho_l R_0^2)}{\sqrt{(\omega_0^2 - \omega^2)^2 + (\delta\omega\omega_0)^2}}, \tag{6.10}$$

where $\omega_0 = 2\pi f_0$ is the natural frequency or eigenfrequency of the oscillator and $\omega = 2\pi f$ is the driving frequency, and δ is the damping factor which comprises of viscous, thermal, acoustic effects, in addition to dilational viscosity effects of the interfacial layer. The eigenfrequency of a coated bubble is given by [70]

$$\omega_0 = \sqrt{\frac{1}{\rho_l R_0^2}\left[3\kappa P_0 + \frac{2\sigma_\mathrm{water}(3\kappa - 1)}{R_0} + \frac{4E_\mathrm{d}}{R_0}\right]}. \tag{6.11}$$

For the case of a radius-sweep experiment, it is worth noting the effect of interfacial elasticity can be expected to be more pronounced in the oscillations of smaller bubbles as the elastic contribution appears in the form E_d/R_0. When the oscillations are damped by dissipative effects, the frequency of maximum response, or resonance frequency is defined as

$$\omega_\mathrm{res} = \omega_0\sqrt{1 - \frac{\delta^2}{2}}. \tag{6.12}$$

In absence of measurements of the acoustic pressure, a practical approach to assess the viscoelasticity of the monolayer would be to directly compare the excursion

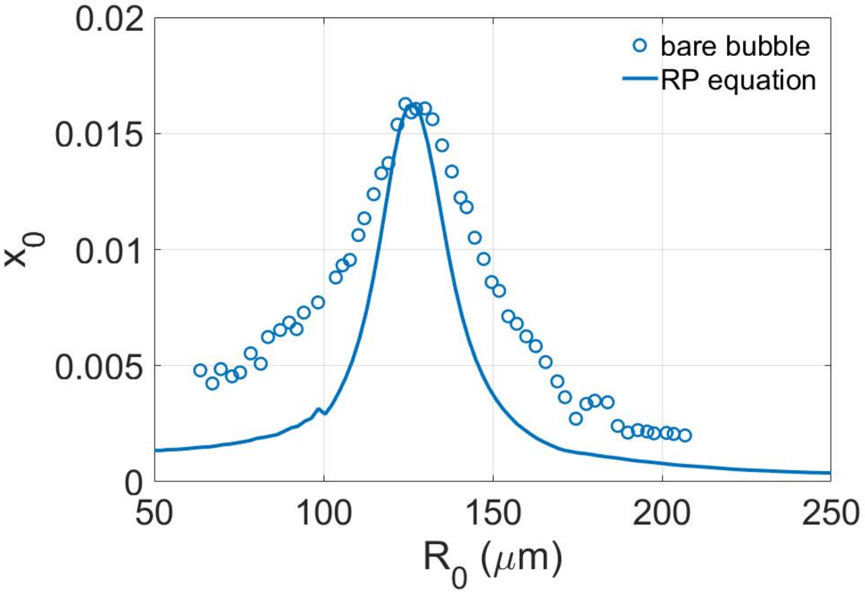

Fig. 6.17 **Radius-sweep curves for bare bubbles: experiment and theory.** The excursions x_0 of a bare bubble, for a radius-sweep experiment (open circles), is compared to the excursions obtained by numerically solving the Rayleigh-Plesset equation (solid line). The data from experiments are the same as presented in Figure 6.13(a). In solving the RP equation, the parameters used are $P_\mathrm{a} = 400$ Pa, with κ estimated for each R_0 at $f = 25$ kHz. The resonance radius from the experiments is $R_\mathrm{res}^{exp} \approx 126$ μm, and for the numerical solution $R_\mathrm{res}^{RP} = 126.8$ μm.

behaviour of the coated bubbles with the bare bubbles as follows. The excursion amplitude for a bare bubble can be expressed as

$$x_{0,\mathrm{bare}}(\omega) = \frac{P_\mathrm{a}/(\rho_l R_0^2)}{\sqrt{(\omega_{0,\mathrm{bare}}^2 - \omega^2)^2 + (\delta_\mathrm{bare}\omega\omega_{0,\mathrm{bare}})^2}}, \tag{6.13}$$

where $\omega_{0,\mathrm{bare}}$ is obtained by substituting $E_\mathrm{d} = 0$ in equation (6.11). For a coated bubble,

$$x_{0,\mathrm{coated}}(\omega) = \frac{P_\mathrm{a}/(\rho_l R_0^2)}{\sqrt{(\omega_{0,\mathrm{coated}}^2 - \omega^2)^2 + (\delta_\mathrm{coated}\omega\omega_{0,\mathrm{coated}})^2}}. \tag{6.14}$$

Squaring followed by division of equation (6.13) by (6.14) gives

$$\left(\frac{x_{0,\mathrm{bare}}}{x_{0,\mathrm{coated}}}\right)^2 = \frac{(\omega_{0,\mathrm{coated}}^2 - \omega^2)^2 + (\delta_\mathrm{coated}\omega\omega_{0,\mathrm{coated}})^2}{(\omega_{0,\mathrm{bare}}^2 - \omega^2)^2 + (\delta_\mathrm{bare}\omega\omega_{0,\mathrm{bare}})^2} \tag{6.15}$$

which is independent of the driving acoustic pressure amplitude. If for the bare bubbles, δ_{bare} is known, for the coated bubble $\omega_{0,\text{coated}}$ and δ_{coated} can be estimated for each R_0. From this, subsequently, $E_{\text{d}}(R_0)$ and $\eta_{\text{d}}(R_0)$ can be estimated. In the current case, determining δ_{bare} is challenging due to the contribution arising from the agarose ceiling, against which each bubble oscillates during the experiments. The agarose gel ceiling introduces a resistance to the bubble oscillations and is likely to cause the dissipation of acoustic energy into the gel as the bubble oscillations also oscillate the boundary. This is evident from the damped response of the bubbles in experiments in Figure 6.17.

A rough estimate for the dilational modulus of the colloid monolayer, for particles of size $a = 1.2$ μm, may be made as follows. At the resonance radius,

$$\omega - \omega_{\text{res}}(E_{\text{d}}, \delta, R_{\text{res}}) = 0. \tag{6.16}$$

Combining equations (6.11),(6.12) and (6.16),

$$\omega - \sqrt{\frac{1}{\rho_l R_{\text{res}}^2}\left[3\kappa P_0 + \frac{2\sigma_{\text{water}}(3\kappa - 1)}{R_{\text{res}}} + \frac{4E_{\text{d}}}{R_{\text{res}}}\right]\left(1 - \frac{\delta^2}{2}\right)} = 0. \tag{6.17}$$

Solving this equation gives $\delta = 0$ and $E_{\text{d}} = 1.89$ N/m. For lipid-coated bubbles, oscillated at MHz frequencies, E_{d} has been reported to be in the range $0.06 - 3.5$ N/m [79, 136]. However, the large value of E_{d} for the colloid monolayer is in stark contrast with the quasi-static value of $E_{\text{d}} \approx 25$ mN/m [126]. Further, the value of the total damping factor being zero appears unphysical. Yet, for a shift in resonance radius of colloid-coated bubbles by $\approx 7\%$, with respect to bare bubbles (Figure 6.13), E_{d} has to be large as the bubbles considered in the current experiments have $R_0 \sim 100$ μm. To have a higher resonance frequency, or analogously, a higher resonance radius, the ratio $4E_{\text{d}}/R_0$ has to be at least comparable to the other terms in equation 6.11.

6.4.5 Conclusions

An oscillating bubble, coated with monodisperse colloidal microspheres, can serve as a model system for understanding the micromechanical phenomena occurring in monolayers at liquid interfaces, at high dilational deformation frequencies. The colloids can be visualised by optical microscopy, allowing one to track the evolution of the interfacial microstructure. In this preliminary experimental study, the range for linear response of uncoated bubbles in a pressure-sweep experiment was identified. The response of colloid-coated bubbles was then characterised in the same range of pressure amplitudes. The coated bubbles exhibited a non-linear relationship between excursion and acoustic pressure. Additionally, the bubbles showed expansion-only behaviour with buckling occurring during bubble compression. This was found to be dependent on particle surface coverage. A model was proposed to explain both the buckling and expansion-only behaviours. The effect of varying particle size within a decade showed no remarkable differences in bubble dynamics. A more extensive study needs to be undertaken to assess the effects of particle size.

Comparing the excursions of bare and coated bubbles at fixed pressure amplitudes, in a radius-sweep experiment showed that the resonant radius is $7 - 8.5$ % higher for the coated bubbles. This along with the reduced excursion amplitude is a measure of the surface viscoelasticity due to the monolayer. Overall, an oscillating bubble, driven by ultrasound has potential for studying microscopic/nanoscopic phenomena occurring at very small timescales, which otherwise by conventional methods is difficult to achieve.

Chapter 7

Conclusions

In this thesis, bubbles were used as probes to study the dynamics of particle-coated interfaces under two extreme timescales. First, in a crystal-stabilised foam, rheological properties of particle networks, both in the bulk and at an interface were evaluated to explain their relative contributions in inhibiting bubble dissolution. Second, after removing bulk effects, the dynamic behaviours of the crystal-coated bubbles were explored through observations of the bubbles undergoing either dissolution or ultrasound-induced volumetric oscillations. In this way interfacial phenomena were probed at two extreme timescales of deformation, specifically for $t \sim 10^4$ s and $t \sim 10^{-4}$ s, through video microscopy techniques. Third, a quantitative study of the oscillation dynamics of colloid-coated bubbles, driven by ultrasound, was taken up to understand the mechanical responses of a monolayer under high-frequency deformations. The observations were explained through micromechanistic and rheological interpretations.

In Chapter 4, the dissolution time for wax-coated bubbles, in presence or absence of a bulk crystal network, was used as a parameter to evaluate the contributions of bulk and interfacial rheology to oleofoam stability. The bubbles were considered as subunits of the oleofoam. It was found that interfacial effects alone were insufficient to arrest bubble dissolution. Rather the bulk crystal network, possibly in synergy with the interfacial network, played the crucial role in the long-term stability of the bubbles and perhaps the oleofoam as a whole. However, measurements of the macroscopic viscoelastic parameters alone proved to be somewhat inadequate in explaining the stability of the bubbles embedded within the oleogel network. This suggested additional stabilising influences of the local microstructure in the immediate vicinity of the bubbles.

In Chapter 5, the formation of the crystal networks was investigated under controlled shear and tempering histories. Qualitatively, there appeared to be a weak correlation between the bulk and interfacial crystal morphologies. It was, therefore, hypothesised that there is a transition, in crystal domain features, spanning from the bulk interstitial gel network to the bubble interface, in the oleofoams. The stability of bubbles is likely to be dependent on the local mesoscopic effects associated with this transition.

Focus was then shifted towards investigating the dynamic behaviour of crystal-coated interfaces during the dissolution of the wax-coated bubbles. As dissolution progressed, delamination of the wax layer from the air-oil interface occurred. Following complete bubble dissolution, the remnant layer was intact and found to be comprised of large crystal subunits, of length scales comparable to the initial bubble radius R_0. It was hypothesised that over a timescale of $t \sim 10^4$ s, the interfacial crystals had sufficient time to reorganise into a rigid 2D structure to oppose the decrease in area. Eventually, when the work needed to compress the interface exceeded the adhesion energy of the layer with the air-oil interface, it was more favourable for the crystal layer to desorb than undergo further compression. This reasoning was partially supported by determining the lower estimates on the interfacial compression modulus and the adhesion energy of the crystal layer. Both quantities were found to have similar values. Yet, when the same type of bubbles were subjected to rapid volumetric oscillations, using acoustic waves, small crystals were found to desorb at high acoustic pressures. These crystals were much smaller than R_0 and it was hypothesised that at timescales of $t \sim 10^{-4}$ s, there was insufficient time for the crystals to reorganise at the interface.

Finally, in Chapter 6, with the aim of implementing an oscillating bubble, with oscillations driven by ultrasound, as a high-frequency interfacial rheological probe, the oscillatory dynamics of a model system comprising of a bubble, in an aqueous solution, stabilised by a monolayer of monodisperse colloidal microspheres was studied. Colloids with diameters in the range $2.4 - 10$ μm, were used so that they could be resolved by optical microscopy. Owing to the high desorption barrier and low acoustic pressure amplitudes used, the number of particles in a given monolayer was a constant. The armoured bubbles exhibited non-linear dynamics with varying pressure amplitudes which contrasted with the linear dynamics of bare bubbles under similar conditions. The coated bubbles also exhibited buckling during compression and hysteresis effects for intermediate surface coverage. Within the decade of particle diameters considered, no discernable effects were noticed by varying particle size.

The observed buckling behaviour was explained using a micromechanical description. Further, a qualitative framework was presented to extract interfacial viscoelastic parameters from the differences observed between the oscillatory dynamics of coated and bare bubbles.

The outcomes of this thesis can be summarised as follows:

1. in Chapter 4, bulk rheological effects were found to play the dominant role in the long-term stability of bubbles in the system. This is possibly coupled with local mesoscopic effects connecting the bulk crystal network to the interfacial network at the bubbles, as supported by observations in Chapter 5, where the formation of crystal-coated interfaces were investigated.
2. In Chapter 5, a study of the dynamic behaviour of the crystal-coated air-oil interfaces at quasi-static and sub-millisecond timescales, suggested that the timescale of deformation determined how the crystals organised in response to the external stresses.
3. In Chapter 6, the oscillatory dynamics of colloid-coated bubbles, driven by ultrasound, were linked to microstructural events in the colloid monolayer. The dynamic behaviour was explained in terms of a continuum-based rheological model, and a micromechanical description in keeping with the visualisations of the monolayer.

Future work and Outlook

A pulsating bubble, driven by ultrasound allows a vast possibility of devising experiments to study microscale phenomena at high frequency. For instance, the model system comprising of colloid-coated bubbles may be extended to understand the dynamics of monolayers with bidisperse or polydisperse particles, which is frequently encountered in real applications. Surface rheological properties have been probed in such systems through studying the propagation of capillary waves along particle laden interfaces over a range of frequencies up to 900 Hz [133, 132]. Using ultrasound-driven bubbles, this range can be further extended and add to our understanding of particulate interfaces over a broad range of deformation timescales. Additionally, particle-tracking methods can be applied, on such optically resolvable colloids, to link the local evolution of the interfacial microstructure to the emergent dynamics of the interface as a whole [137, 126].

The surface coverage of colloid-coated bubbles can be controlled by protocols of forced particle desorption, and be used to investigate the fundamental effects associated with pair-wise interactions between particles or contact-angle hysteresis when the interface is perturbed rapidly through bubble oscillations. Squeezing such a bubble between two transparent plates (as was done in Figure 5.11), giving rise to a ring of particles, similar to a Saturn-ring, at the interface, and then oscillating it may allow clearer visualisations of interparticle interactions.

The high-frequency interfacial rheology of insoluble surfactants, such as phospholipids, have been extensively characterised [69, 70, 136, 79]. An interesting system to study would be bubbles coated with soluble molecular surfactants. Bubble oscillation timescales can be made faster, or comparable to the diffusion timescales associated with the exchange of surfactant molecules between bulk and interface. In this situation, the surface elasticity may be completely different from what is observed using conventional methods to assess the rheology of soluble surfactant monolayers.

The intrinsic effects of surface tension, local curvature and heterogeneous surface cooling, leading to a weak interdependence of interfacial crystal properties in relation to bulk oleogel crystal properties, as found in the model wax-based oleofoam, may serve as an additional degree of freedom in the design of formulation products, where different degrees of deformability are desired among the two phases. A systematic understanding to selectively tune these properties would further add to the applicability of oleofoams, that already exhibit stability at above refrigeration conditions without the need for additives.

Furthermore, crystal-coated bubbles can be used as delivery agents, as exemplified by the wax crystals released by the bubble as shown in Chapter 5, Figure 5.16(g). With the systematic and timely release of crystals of varying amount and size, into an environment, through stimulated bubble dissolution, ultrasound-mediated desorption, or a combination of the two, such bubbles offer potential for future research. The applicability of microbubbles as drug delivery agents has been investigated [138–140]. A similar biomedical application, but with the novelty of using viral crystals [141], in particular oncolytic virus particles [142, 143], can involve growing the crystals onto micrometric bubbles, followed by controlled release and monitoring the uptake of the particles in cells. The lack of a suitable delivery technique has been a limiting factor [142] in applying this virotherapy.

Finally, bubbles with particle-coated interfaces can serve as a platform for the study of diverse and fundamental interfacial phenomena. By tuning the particle to bubble aspect ratio, the interfacial layer may be studied in the limits of it behaving as a continuous or discrete shell. The timescale of deformation, can be varied to resonate with specific intrinsic relaxation timescales, which are inherent in the hierarchical structure and relaxation mechanisms spanning over various length scales of the interfacial microstructure. This way the dominant relaxation pathway can be identified, pertaining to specific phenomena. Such knowledge will pave the way for directed assembly in the design of functional materials.

References

[1] Denis Weaire and Stefan Hutzler. *The Physics of Foams.* OUP, Oxford, 1999.

[2] Duncan J. Shaw. *Introduction to Colloid and Surface Chemistry.* Butterworth-Heinemann, Oxford, 4th ed. edition, 1992.

[3] Robert Aveyard and Denis A. Haydon. *An Introduction to the Principles of Surface Chemistry.* Cambridge chemistry texts. Cambridge University Press, London, 1973.

[4] Bernard P. Binks. Particles as surfactants—similarities and differences. *Current Opinion in Colloid & Interface Science*, 7(1-2):21–41, 2002.

[5] Bernard P. Binks and Tommy S. Horozov (Eds.). *Colloidal Particles at Liquid Interfaces.* Cambridge University Press, Cambridge ; New York, 2006.

[6] Valeria Garbin. Colloidal particles: Surfactants with a difference. *Physics Today*, 2013.

[7] Reinhard Sigel. Concepts for soft interfaces. *Soft Matter*, 13(10):1940–1942, 2017.

[8] Eugene M. Terentjev. Searching for equilibrium. *Nature Materials*, 1(3):149–150, 2002.

[9] George M. Whitesides and Bartosz Grzybowski. Self-assembly at all scales. *Science*, 295(5564):2418–2421, 2002.

[10] Robert Hołyst. Some features of soft matter systems. *Soft Matter*, 1(5):329–333, 2005.

[11] Douglas Durian and Haim Diamant. Condensed-matter physics: In search of soft solutions. *Nature*, 412(6845):391–392, 2001.

[12] Valeria Garbin. Collapse mechanisms and extreme deformation of particle-laden interfaces. *Current Opinion in Colloid and Interface Science*, 39:202–211, 2019.

[13] Robbe Heymans, Iris Tavernier, Koen Dewettinck, and Paul Van der Meeren. Crystal stabilization of edible oil foams. *Trends in Food Science and Technology*, 69:13–24, 2017.

[14] Jacob N. Israelachvili. *Intermolecular and Surface Forces.* Academic Press, 3rd ed. edition, 2011.

[15] Walter Ramsden. Separation of solids in the surface-layers of solutions and 'suspensions' (observations on surface-membranes, bubbles, emulsions, and mechanical coagulation). – preliminary account. *Proceedings of the Royal Society of London*, 72(477-486):156–164, 1903.

[16] Spencer Umfreville Pickering. CXCVI.—Emulsions. *Journal of the Chemical Society, Transactions*, 91:2001–2021, 1907.

[17] Bernard P. Binks, Jhonny A. Rodrigues, and William J. Frith. Synergistic interaction in emulsions stabilized by a mixture of silica nanoparticles and cationic surfactant. *Langmuir*, 23(7):3626–3636, 2007.

[18] Timothy N. Hunter, Robert J. Pugh, George V. Franks, and Graeme J. Jameson. The role of particles in stabilising foams and emulsions. *Advances in Colloid and Interface Science*, 137(2):57–81, 2008.

[19] Antonio Stocco, Wiebke Drenckhan, Emanuelle Rio, Dominique Langevin, and Bernard P. Binks. Particle-stabilised foams: an interfacial study. *Soft Matter*, 5(11):2215, 2009.

[20] Mathias Nagel, Theo A. Tervoort, and Jan Vermant. From drop-shape analysis to stress-fitting elastometry. *Advances in Colloid and Interface Science*, 247(May):33–51, 2017.

[21] J. S. Vermaak, C. W. Mays, and D. Kuhlmann-Wilsdorf. On surface stress and surface tension. I. Theoretical considerations. *Surface Science*, 12(2):128–133, 1968.

[22] Dominik Kramer and Jörg Weissmüller. A note on surface stress and surface tension and their interrelation via Shuttleworth's equation and the Lippmann equation. *Surface Science*, 601(14):3042–3051, 2007.

[23] Tom Verwijlen, Luna Imperiali, and Jan Vermant. Separating viscoelastic and compressibility contributions in pressure-area isotherm measurements. *Advances in Colloid and Interface Science*, 206:428–436, 2014.

[24] E. H. Lucassen-Reynders. Interfacial Viscoelasticity in Emulsions and Foams. *Food Structure*, 12(1):1–12, 1993.

[25] Nick Jaensson and Jan Vermant. Tensiometry and rheology of complex interfaces. *Current Opinion in Colloid and Interface Science*, 37:136–150, 2018.

[26] M. Van Den Tempel. Surface rheology. *Journal of Non-Newtonian Fluid Mechanics*, 2(3):205–219, 1977.

[27] Thomas Young. An Essay on Nature. *Philosophical Transactions of the Royal Society of London*, 95(2):65–87, 1805.

[28] Pawel Pieranski. Two-dimensional interfacial colloidal crystals. *Physical Review Letters*, 45(7):569–572, 1980.

[29] Tsuneo Okubo. Surface tension of structured colloidal suspensions of polystyrene and silica spheres at the air-water interface. *Journal of Colloid and Interface Science*, 171(1):55–62, 1995.

[30] Tommy S. Horozov, Robert Aveyard, John H. Clint, and Bernard P. Binks. Order-disorder transition in monolayers of modified monodisperse silica particles at the octane-water interface. *Langmuir*, 19(7):2822–2829, 2003.

[31] Tommy S. Horozov, Robert Aveyard, Bernard P. Binks, and John H. Clint. Structure and stability of silica particle monolayers at horizontal and vertical octane-water interfaces. *Langmuir*, 21(16):7405–7412, 2005.

[32] Tommy S. Horozov, Robert Aveyard, John H. Clint, and Bernd Neumann. Particle zips: Vertical emulsion films with particle monolayers at their surfaces. *Langmuir*, 21(6):2330–2341, 2005.

[33] Valeria Garbin, John C. Crocker, and Kathleen J. Stebe. Nanoparticles at fluid interfaces: Exploiting capping ligands to control adsorption, stability and dynamics. *Journal of Colloid and Interface Science*, 387(1):1–11, 2012.

[34] F. Martínez-López, M. A. Cabrerizo-Vílchez, and R. Hidalgo-Álvarez. Colloidal interaction at the air-liquid interface. *Journal of Colloid and Interface Science*, 232(2):303–310, 2000.

[35] Boris Vladimirovich Derjaguin, Nikolai Vladimirovich Churaev, and Vladimir Markosovich Muller. *Surface Forces.* Springer Science+Business Media, LLC, New York, 1987.

[36] Robert J. Hunter. *Introduction to Modern Colloid Science.* Oxford University Press, Oxford, 1993.

[37] Lee R. White. On the deryaguin approximation for the interaction of macrobodies. *Journal of Colloid And Interface Science*, 95(1):286–288, 1983.

[38] Kasper Masschaele, Bum Jun Park, Eric M. Furst, Jan Fransaer, and Jan Vermant. Finite ion-size effects dominate the interaction between charged colloidal particles at an oil-water interface. *Physical Review Letters*, 105(4):1–4, 2010.

[39] Bernard P. Binks and Ryo Murakami. Phase inversion of particle-stabilized materials from foams to dry water. *Nature Materials*, 5(11):865–869, 2006.

[40] P. Aussillous and D. Quéré. Liquid marbles. *Nature*, 411(6840):924–927, 2001.

[41] Tommy S. Horozov. Foams and foam films stabilised by solid particles. *Current Opinion in Colloid and Interface Science*, 13(3):134–140, 2008.

[42] A. Cervantes Martinez, E. Rio, G. Delon, A. Saint-Jalmes, D. Langevin, and B. P. Binks. On the origin of the remarkable stability of aqueous foams stabilised by nanoparticles: Link with microscopic surface properties. *Soft Matter*, 4(7):1531–1535, 2008.

[43] Maria V. Tzoumaki, Dimitris Karefyllakis, Thomas Moschakis, Costas G. Biliaderis, and Elke Scholten. Aqueous foams stabilized by chitin nanocrystals. *Soft Matter*, 11(31):6245–6253, 2015.

[44] Seung I. Kam and William R. Rossen. Anomalous capillary pressure, stress, and stability of solids-coated bubbles. *Journal of Colloid and Interface Science*, 213(2):329–339, 1999.

[45] Nicolas Taccoen, François Lequeux, Deniz Z. Gunes, and Charles N. Baroud. Probing the mechanical strength of an armored bubble and its implication to particle-stabilized foams. *Physical Review X*, 6(1):1–11, 2016.

[46] Arthur Mason Worthington. On pendent drops. *Proceedings of the Royal Society of London*, 32(212-215):362–377, 1881.

[47] Y. Rotenberg, L. Boruvka, and A. W. Neumann. Determination of surface tension and contact angle from the shapes of axisymmetric fluid interfaces. *Journal of Colloid And Interface Science*, 93(1):169–183, 1983.

[48] Joseph D. Berry, Michael J. Neeson, Raymond R. Dagastine, Derek Y. C. Chan, and Rico F. Tabor. Measurement of surface and interfacial tension using pendant drop tensiometry. *Journal of Colloid and Interface Science*, 454:226–237, 2015.

[49] Sebastian Knoche, Dominic Vella, Elodie Aumaitre, Patrick Degen, Heinz Rehage, Pietro Cicuta, and Jan Kierfeld. Elastometry of deflated capsules: Elastic moduli from shape and wrinkle analysis. *Langmuir*, 29(40):12463–12471, 2013.

[50] Jonas Hegemann, Sebastian Knoche, Simon Egger, Maureen Kott, Sarah Demand, Anja Unverfehrt, Heinz Rehage, and Jan Kierfeld. Pendant capsule elastometry. *Journal of Colloid and Interface Science*, 513:549–565, 2018.

[51] Daniel Carvajal, Evan J. Laprade, Kevin J. Henderson, and Kenneth R. Shull. Mechanics of pendant drops and axisymmetric membranes. *Soft Matter*, 7(22):10508–10519, 2011.

[52] L. Anand. On H. Hencky's approximate strain-energy function for moderate deformations. *Journal of Applied Mechanics, Transactions ASME*, 46(1):78–82, 1979.

[53] Jordan T. Petkov, Theodor D. Gurkov, Bruce E. Campbell, and Rajendra P. Borwankar. Dilatational and shear elasticity of gel-like protein layers on air/water interface. *Langmuir*, 16(8):3703–3711, 2000.

[54] Gerald G. Fuller and Jan Vermant. Complex Fluid-Fluid Interfaces: Rheology and Structure. *Annual Review of Chemical and Biomolecular Engineering*, 3(1):519–543, 2012.

[55] P. S. Epstein and M. S. Plesset. On the stability of gas bubbles in liquid-gas solutions. *The Journal of Chemical Physics*, 18(11):1505–1509, 1950.

[56] P. Brent Duncan and David Needham. Test of the Epstein-Plesset model for gas microparticle dissolution in aqueous media: Effect of surface tension and gas undersaturation in solution. *Langmuir*, 20(7):2567–2578, 2004.

[57] Vincent Poulichet and Valeria Garbin. Cooling particle-coated bubbles: Destabilization beyond dissolution arrest. *Langmuir*, 31(44):12035–12042, 2015.

[58] Kanvara Achakulwisut, Chak Tam, Axel Huerre, Rafaella Sammouti, Bernard P. Binks, and Valeria Garbin. Stability of Clay Particle-Coated Microbubbles in Alkanes against Dissolution Induced by Heating. *Langmuir*, 33(15):3809–3817, 2017.

[59] William Kloek, Ton Van Vliet, and Marcel Meinders. Effect of bulk and interfacial rheological properties on bubble dissolution. *Journal of Colloid and Interface Science*, 237(2):158–166, 2001.

[60] Lord Rayleigh. VIII. On the pressure developed in a liquid during the collapse of a spherical cavity . *The London, Edinburgh, and Dublin Philosophical Magazine and Journal of Science*, 34(200):94–98, 1917.

[61] M. S. Plesset. The Dynamics of Cavitation Bubbles. *Journal of Applied Mechanics*, 16(3):277–282, 1949.

[62] M. S. Plesset and A. Prosperetti. Bubble dynamics and cavitation. *Annual Review of Fluid Mechanics*, 9(1):145–185, 1977.

[63] Andrea Prosperetti. A generalization of the Rayleigh-Plesset equation of bubble dynamics. *Physics of Fluids*, 25(3):409–410, 1982.

[64] M. Minnaert. XVI. On musical air-bubbles and the sounds of running water . *The London, Edinburgh, and Dublin Philosophical Magazine and Journal of Science*, 16(104):235–248, 1933.

[65] Andrea Prosperetti. Thermal effects and damping mechanisms in the forced radial oscillations of gas bubbles in liquids. *Journal of the Acoustical Society of America*, 61(1):17–27, 1977.

[66] Fumiya Hamaguchi and Keita Ando. Linear oscillation of gas bubbles in a viscoelastic material under ultrasound irradiation. *Physics of Fluids*, 27(11), 2015.

[67] Andrea Prosperetti. Thermal effects and damping mechanisms in the forced radial oscillations of gas bubbles in liquids. *Journal of the Acoustical Society of America*, 61(1):17–27, 1977.

[68] Andrea Prosperetti, Lawrence A. Crum, and Kerry W. Commander. Nonlinear bubble dynamics. *The Journal of the Acoustical Society of America*, 83(2):502–514, 1988.

[69] Philippe Marmottant, Sander van der Meer, Marcia Emmer, Michel Versluis, Nico de Jong, Sascha Hilgenfeldt, and Detlef Lohse. A model for large amplitude oscillations of coated bubbles accounting for buckling and rupture. *The Journal of the Acoustical Society of America*, 118(6):3499–3505, 2005.

[70] Sander M. van der Meer, Benjamin Dollet, Marco M. Voormolen, Chien T. Chin, Ayache Bouakaz, Nico de Jong, Michel Versluis, and Detlef Lohse. Microbubble spectroscopy of ultrasound contrast agents. *The Journal of the Acoustical Society of America*, 121(1):648–656, 2007.

[71] N. de Jong, R. Cornet, and C. T. Lancée. Higher harmonics of vibrating gas-filled microspheres. Part two: measurements. *Ultrasonics*, 32(6):455–459, 1994.

[72] Charles C. Church. The effects of an elastic solid surface layer on the radial pulsations of gas bubbles. *The Journal of the Acoustical Society of America*, 97(3):1510–1521, 1995.

[73] Dhiman Chatterjee and Kausik Sarkar. A Newtonian rheological model for the interface of microbubble contrast agents. *Ultrasound in Medicine and Biology*, 29(12):1749–1757, 2003.

[74] Alexander A. Doinikov and Paul A. Dayton. Maxwell rheological model for lipid-shelled ultrasound microbubble contrast agents. *The Journal of the Acoustical Society of America*, 121(6):3331–40, 2007.

[75] Matthieu Guédra, Tony Valier-Brasier, Jean-Marc Conoir, François Coulouvrat, Ksenia Astafyeva, and Jean-Louis Thomas. Influence of shell compressibility on the ultrasonic properties of polydispersed suspensions of nanometric encapsulated droplets. *The Journal of the Acoustical Society of America*, 135(3):1044–1055, 2014.

[76] Eleanor Stride. The influence of surface adsorption on microbubble dynamics. *Philosophical Transactions of the Royal Society A: Mathematical, Physical and Engineering Sciences*, 366(1873):2103–2115, 2008.

[77] E. Stride, K. Pancholi, M. J. Edirisinghe, and S. Samarasinghe. Increasing the nonlinear character of microbubble oscillations at low acoustic pressures. *Journal of the Royal Society Interface*, 5(24):807–811, 2008.

[78] Alexander A. Doinikov and Ayache Bouakaz. Review of shell models for contrast agent microbubbles. *IEEE Transactions on Ultrasonics, Ferroelectrics, and Frequency Control*, 58(5):981–993, 2011.

[79] Tim Segers, Emmanuel Gaud, Michel Versluis, and Peter Frinking. High-precision acoustic measurements of the nonlinear dilatational elasticity of phospholipid coated monodisperse microbubbles. *Soft Matter*, 14(47):9550–9561, 2018.

[80] Jordan S. Lum, Jacob D. Dove, Todd W. Murray, and Mark A. Borden. Single Microbubble Measurements of Lipid Monolayer Viscoelastic Properties for Small-Amplitude Oscillations. *Langmuir*, 32(37):9410–9417, 2016.

[81] George S. Jamieson and Walter F. Baughman. The chemical composition of sunflower-seed oil. *Journal of the American Chemical Society*, 44(12):2952–2957, 1922.

[82] Bernard P. Binks, Emma J. Garvey, and Josélio Vieira. Whipped oil stabilised by surfactant crystals. *Chemical Science*, 7(4):2621–2632, 2016.

[83] D. Z. Gunes, M. Murith, J. Godefroid, C. Pelloux, H. Deyber, O. Schafer, and O. Breton. Oleofoams: Properties of Crystal-Coated Bubbles from Whipped Oleogels-Evidence for Pickering Stabilization. *Langmuir*, 33(6):1563–1575, 2017.

[84] Nobuyuki Otsu. A threshold selection method from gray-level histograms. *IEEE Transactions on Systems, Man, and Cybernetics*, 9(1):62–66, 1979.

[85] Adrian Daerr and Adrien Mogne. Measuring liquid surface tension through the pendent drop method : description of a measurement bench and an ImageJ Plugin. *Journal of Open Research Software*, pages 1–12, 2016.

[86] D. K. Owens and R. C. Wendt. Estimation of the surface free energy of polymers. *Journal of Applied Polymer Science*, 13(8):1741–1747, 1969.

[87] F Hejda, P Sola, and J Kousal. Surface Free Energy Determination by Contact Angle Measurements – A Comparison of Various Approaches. *WDS'10 Proceedings of Contributed Papers*, (3):25–30, 2010.

[88] Frederick M. Fowkes. Additivity of Intermolecular Forces At Interfaces. I. Determination of the Contribution To Surface and Interfacial Tensions of Dispersion Forces in Various Liquids 1 . *The Journal of Physical Chemistry*, 67(12):2538–2541, 1963.

[89] Frederick M. Fowkes. Attractive Forces At Interfaces. *Industrial & Engineering Chemistry*, 56(12):40–52, 1964.

[90] M. Strasberg. The Pulsation Frequency of Nonspherical Gas Bubbles in Liquids. *Journal of the Acoustical Society of America*, 25(3):536–537, 1953.

[91] Brandon L. Helfield, Ben Y.C. Leung, and David E. Goertz. The effect of boundary proximity on the response of individual ultrasound contrast agent microbubbles. *Physics in Medicine and Biology*, 59(7):1721–1745, 2014.

[92] Akaki Jamburidze, Marco De Corato, Axel Huerre, Angelo Pommella, and Valeria Garbin. High-frequency linear rheology of hydrogels probed by ultrasound-driven microbubble dynamics. *Soft Matter*, 13:3946–3953, 2017.

[93] Bernard P. Binks and Ioannis Marinopoulos. Ultra-stable self-foaming oils. *Food Research International*, 95:28–37, 2017.

[94] Mathieu Brun, Mathieu Delample, Etienne Harte, Sophie Lecomte, and Fernando Leal-Calderon. Stabilization of air bubbles in oil by surfactant crystals: A route to produce air-in-oil foams and air-in-oil-in-water emulsions. *Food Research International*, 67:366–375, 2015.

[95] Shoko Mishima, Atsushi Suzuki, Kiyotaka Sato, and Satoru Ueno. Formation and Microstructures of Whipped Oils Composed of Vegetable Oils and High-Melting Fat Crystals. *JAOCS, Journal of the American Oil Chemists' Society*, 93(11):1453–1466, 2016.

[96] Anne Laure Fameau, Stephanie Lam, Audrey Arnould, Cédric Gaillard, Orlin D. Velev, and Arnaud Saint-Jalmes. Smart Nonaqueous Foams from Lipid-Based Oleogel. *Langmuir*, 31(50):13501–13510, 2015.

[97] Robbe Heymans, Iris Tavernier, Sabine Danthine, Tom Rimaux, Paul Van der Meeren, and Koen Dewettinck. Correction: Food-grade monoglyceride oil foams: the effect of tempering on foamability, foam stability and rheological properties. *Food and Function*, 9(7):4036, 2018.

[98] Elka S. Basheva, Peter A. Kralchevsky, Nikolay C. Christov, Krassimir D. Danov, Simeon D. Stoyanov, Theodorus B.J. Blijdenstein, Hyun Jung Kim, Eddie G. Pelan, and Alex Lips. Unique properties of bubbles and foam films stabilized by HFBII hydrophobin. *Langmuir*, 27(6):2382–2392, 2011.

[99] Peter J. Beltramo, Manish Gupta, Alexandra Alicke, Irma Liascukiene, Deniz Z. Gunes, Charles N. Baroud, and Jan Vermant. Arresting dissolution by interfacial rheology design. *Proceedings of the National Academy of Sciences*, page 201705181, 2017.

[100] Antonio Stocco, Emmanuelle Rio, Bernard P Binks, and Dominique Langevin. Aqueous foams stabilized solely by particles. *Soft Matter*, 7(4):1260–1267, 2011.

[101] Diogo E.V. Andrade, Moisés A. Marcelino Neto, and Cezar O.R. Negrão. Non-monotonic response of waxy oil gel strength to cooling rate. *Rheologica Acta*, 57(10):673–680, 2018.

[102] S Saha, B Saint-Michel, V Leynes, B P Binks, and V Garbin. Stability of bubbles in wax-based oleofoams: decoupling the effects of bulk oleogel rheology and interfacial rheology. *Rheologica Acta*, 59(4):255–266, 2020.

[103] Bernat Esteban, Jordi-Roger Riba, Grau Baquero, Antoni Rius, and Rita Puig. Temperature dependence of density and viscosity of vegetable oils. *Biomass and bioenergy*, 42:164–171, 2012.

[104] O. Lorge, M. Djabourov, and F. Brucy. Crystallisation and gelation of waxy crude oils under flowing conditions. *Revue de l'Institut Français du Pétrole*, 52(2):235–239, 1997.

[105] Christopher J. Dimitriou and Gareth H. McKinley. A comprehensive constitutive law for waxy crude oil: a thixotropic yield stress fluid. *Soft Matter*, 10(35):6619–6644, 2014.

[106] Michela Geri, Ramachandran Venkatesan, Krishnaraj Sambath, and Gareth H McKinley. Thermokinematic memory and the thixotropic elasto-viscoplasticity of waxy crude oils. *Journal of Rheology*, 61(3):427–454, 2017.

[107] Lucie Ducloué, Olivier Pitois, Julie Goyon, Xavier Chateau, and Guillaume Ovarlez. Rheological behaviour of suspensions of bubbles in yield stress fluids. *Journal of Non-Newtonian Fluid Mechanics*, 215:31–39, 2015.

[108] Rafael Mendes, Guillaume Vinay, Guillaume Ovarlez, and Philippe Coussot. Modeling the rheological behavior of waxy crude oils as a function of flow and temperature history. *Journal of Rheology*, 59(3):703–732, 2015.

[109] Maureen Dinkgreve, José Paredes, Morton M Denn, and Daniel Bonn. On different ways of measuring "the" yield stress. *Journal of non-Newtonian fluid mechanics*, 238:233–241, 2016.

[110] Marco De Corato, Brice Saint-Michel, George Makrigiorgios, Yannis Dimakopoulos, John Tsamopoulos, and Valeria Garbin. Oscillations of small bubbles and medium yielding in elastoviscoplastic fluids. *Physical Review Fluids*, 4:073301, 2019.

[111] Moussa Kané, Madeleine Djabourov, and Jean-Luc Volle. Rheology and structure of waxy crude oils in quiescent and under shearing conditions. *Fuel*, 83(11-12):1591–1605, 2004.

[112] Jie Song, Marco Caggioni, Todd M. Squires, James F. Gilchrist, Stuart W. Prescott, and Patrick T. Spicer. Heterogeneity, suspension, and yielding in sparse microfibrous cellulose gels 1. Bubble rheometer studies. *Rheologica Acta*, 58(5):217–229, 2019.

[113] Jie Song, Marco Caggioni, Todd M. Squires, James F. Gilchrist, Stuart W. Prescott, and Patrick T. Spicer. Heterogeneity, suspension, and yielding in sparse microfibrous cellulose gels 2. Strain rate-dependent two-fluid behavior. *Rheologica Acta*, 58(5):231–239, 2019.

[114] Guangnan Meng, Jayson Paulose, David R. Nelson, and Vinothan N. Manoharan. Elastic instability of a crystal growing on a curved surface. *Science*, 343(6171):634–637, 2014.

[115] Nicolas R. Chevalier and Patrick Guenoun. Surface Tension Drives the Orientation of Crystals at the Air-Water Interface. *Journal of Physical Chemistry Letters*, 7(14):2809–2813, 2016.

[116] Supratim Ghosh and Dérick Rousseau. Fat crystals and water-in-oil emulsion stability. *Current Opinion in Colloid and Interface Science*, 16(5):421–431, 2011.

[117] Fiona C. Meldrum and Helmut Cölfen. Controlling mineral morphologies and structures in biological and synthetic systems. *Chemical Reviews*, 108(11):4332–4432, 2008.

[118] Ivan Kuzmenko, Hanna Rapaport, Kristian Kjaer, Jens Als-Nielsen, Isabelle Weissbuch, Meir Lahav, and Leslie Leiserowitz. Design and characterization of crystalline thin film architectures at the air-liquid interface: Simplicity to complexity. *Chemical Reviews*, 101(6):1659–1696, 2001.

[119] Jianfeng Shen, Yongmin He, Jingjie Wu, Caitian Gao, Kunttal Keyshar, Xiang Zhang, Yingchao Yang, Mingxin Ye, Robert Vajtai, Jun Lou, and Pulickel M. Ajayan. Liquid phase exfoliation of two-dimensional materials by directly probing and matching surface tension components. *Nano Letters*, 15(8):5449–5454, 2015.

[120] Souheng Wu. *Polymer Interface and Adhesion.* Routledge, November 1982.

[121] George E. Davis. Scattering of Light by an Air Bubble in Water. *Journal of the Optical Society of America*, 45(7):572, 1955.

[122] Philip L. Marston and Dwight L. Kingsbury. Scattering By a Bubble in Water Near the Critical Angle: Interference Effects. *Journal of the Optical Society of America*, 71(2):192–196, 1981.

[123] W. Patrick Arnott and Philip L. Marston. Optical glory of small freely rising gas bubbles in water: observed and computed cross-polarized backscattering patterns. *Journal of the Optical Society of America A*, 5(4):496, 1988.

[124] S. Arima, S. Ueno, A. Ogawa, and K. Sato. Scanning microbeam small-angle X-ray diffraction study of interfacial heterogeneous crystallization of fat crystals in oil-in-water emulsion droplets. *Langmuir*, 25(17):9777–9784, 2009.

[125] R. Mettin, I. Akhatov, U. Parlitz, C. D. Ohl, and W. Lauterborn. Bjerknes forces between small cavitation bubbles in a strong acoustic field. *Physical Review E - Statistical Physics, Plasmas, Fluids, and Related Interdisciplinary Topics*, 56(3):2924–2931, 1997.

[126] Vincent Poulichet and Valeria Garbin. Ultrafast desorption of colloidal particles from fluid interfaces. *Proceedings of the National Academy of Sciences of the United States of America*, 112(19):5932–5937, 2015.

[127] Timothy G. Leighton, A. J. Walton, and M. J.W. Pickworth. Primary Bjerknes forces. *European Journal of Physics*, 11(1):47–50, 1990.

[128] M. E. Cates, J. Wittmer, J. P. Bouchaud, and P. Claudin. Jamming, force chains and fragile matter. *Physical Review Letters*, 2:1841–1844, 1998.

[129] J. W. Tavacoli, G. Katgert, E. G. Kim, M. E. Cates, and P. S. Clegg. Size limit for particle-stabilized emulsion droplets under gravity. *Physical Review Letters*, 108(26):1–5, 2012.

[130] David A. Edwards, Darsh T. Wasan, and Howard Brenner. *Interfacial transport processes and rheology.* Butterworth-Heinemann series in chemical engineering. Butterworth-Heinemann, Boston ; London, 1991.

[131] Ying Luan, Telli Faez, Erik Gelderblom, Ilya Skachkov, Bart Geers, Ine Lentacker, Ton van der Steen, Michel Versluis, and Nico de Jong. Acoustical Properties of Individual Liposome-Loaded Microbubbles. *Ultrasound in Medicine and Biology*, 38(12):2174–2185, 2012.

[132] Carole Planchette, Elise Lorenceau, and Anne Laure Biance. Surface wave on a particle raft. *Soft Matter*, 8(8):2444–2451, 2012.

[133] Pauline Petit, Anne Laure Biance, Elise Lorenceau, and Carole Planchette. Bending modulus of bidisperse particle rafts: Local and collective contributions. *Physical Review E*, 93(4):1–7, 2016.

[134] Sergey V. Lishchuk. Effective surface dilatational viscosity of highly concentrated particle-laden interfaces. *Physical Review E - Statistical, Nonlinear, and Soft Matter Physics*, 90(5):1–5, 2014.

[135] Sergey V. Lishchuk. Dilatational viscosity of dilute particle-laden fluid interface at different contact angles. *Physical Review E*, 94(6):1–8, 2016.

[136] Jordan S. Lum, David M. Stobbe, Mark A. Borden, and Todd W. Murray. Photoacoustic technique to measure temperature effects on microbubble viscoelastic properties. *Applied Physics Letters*, 112(11):111905, 2018.

[137] Axel Huerre, Marco De Corato, and Valeria Garbin. Dynamic capillary assembly of colloids at interfaces with 10,000g accelerations. *Nature Communications*, 9(1):1–9, 2018.

[138] Akaki Jamburidze, Axel Huerre, Diego Baresch, Vincent Poulichet, Marco De Corato, and Valeria Garbin. Nanoparticle-Coated Microbubbles for Combined Ultrasound Imaging and Drug Delivery. *Langmuir*, 35(31):10087–10096, 2019.

[139] Silke Roovers, Guillaume Lajoinie, Ine De Cock, Toon Brans, Heleen Dewitte, Kevin Braeckmans, Michel Versuis, Stefaan C. De Smedt De Smedt, and Ine Lentacker. Sonoprinting of nanoparticle-loaded microbubbles: Unraveling the multi-timescale mechanism. *Biomaterials*, 217(May):119250, 2019.

[140] Al de Leon, Peiran Wei, Filip Bodera, Dana Wegierak, Madelyn McMillen, David Yan, Christina Hemmingsen, Michael C. Kolios, Emily Pentzer, and Agata A. Exner. Pickering bubbles as dual-modality ultrasound and photoacoustic contrast agents. *ACS Applied Materials & Interfaces*, 12(19):22308–22317, 2020.

[141] Padmaja Natarajan and John E. Johnson. Molecular packing in virus crystals: Geometry, chemistry, and biology. *Journal of Structural Biology*, 121(3):295–305, 1998.

[142] Junaid Raja, Johannes M. Ludwig, Scott N. Gettinger, Kurt A. Schalper, and Hyun S. Kim. Oncolytic virus immunotherapy: future prospects for oncology. *Journal for ImmunoTherapy of Cancer*, 6(1):1–13, 2018.

[143] Robert A. Berkeley, Lynette P. Steele, Aat A. Mulder, Diana J.M. Van Den Wollenberg, Timothy J. Kottke, Jill Thompson, Matthew Coffey, Rob C. Hoeben, Richard G. Vile, Alan Melcher, and Elizabeth J. Ilett. Antibody-neutralized reovirus is effective in oncolytic virotherapy. *Cancer Immunology Research*, 6(10):1161–1173, 2018.

[144] Lawrence A. Crum. Bjerknes forces on bubbles in a stationary sound field. *Journal of the Acoustical Society of America*, 57(6):1363–1370, 1975.

Appendix A

Supporting content for Chapter 4

Supporting Data

Figure 4.5 in the main text illustrates a qualitative trend confirmed by more than ten data sets at $T = 25°\mathrm{C}$. Tracking of bubbles in oleofoams was repeated 2 times as these bubbles hardly dissolve. Tracking of bare bubbles in oil was repeated 2 times as a control experiment. For wax-coated bubbles in oil, 8 repeats were performed.

The results for all bubbles are reported in Table A.1. The bubbles had an initial effective radius R_0. The duration of the experiment for each particular bubble was t_exp; this was not the dissolution time, as it was not always possible to observe a bubble until complete dissolution due to experimental constraints. The effective radius attained at the end of the experiment is $R(t_\mathrm{exp})$. The final radius is zero if the bubble has completely dissolved, and > 0 otherwise.

The theoretical dissolution time for a bare bubble of the same initial radius R_0 can be computed with the classical theory by Epstein and Plesset (1950) as $t_\mathrm{th} = \frac{R_0^2}{3Dk_\mathrm{H}}(\frac{R_0\rho}{2M_\mathrm{w}\sigma} + \frac{1}{R_\mathrm{g}T})$. The gas diffusivity in the liquid, D, the liquid density ρ, the gas-liquid surface tension σ, and the Henry's constant k_H, are evaluated at the reference temperature T. M_w is the molar mass of the gas, and R_g the universal gas constant. The dissolution time corrected for the effect of confinement in the sample enclosure (Duncan and Needham, 2004 [56]) , given by $t^* = \frac{t_\mathrm{th}}{\ln 2}$, is used in the Table to normalise the duration of each experiment, t_exp. The qualitative trend for dissolution times is provided in Table A.1.

Bubble type	R_0 (μm)	t_{exp} (s)	t^* (s)	t_{exp}/t^* (1)
bare	95	4350	4358.1	0.9981
bare	98	3360	4782.9	0.7025
coated	98.21	> 7210	4813.6	> 1.4978
coated	80.76	> 7210	2681.7	> 2.6886
coated	114	> 16020	7519.6	> 2.1304
coated	102.32	3270	5441.7	0.6009
coated	85	11600	3124.9	3.7121
coated	101.5	4090	5312.2	0.7699
coated	110	6980	6757.3	1.0330
coated	107	18750	6220.7	3.0141
oleofoam	106.08	$\gg 16160$	6062.1	$\gg 2.6657$
oleofoam	94.37	$\gg 7240$	4272.2	$\gg 1.6947$

Table A.1 Dissolution times for bare, wax-coated and bubbles in oleofoam. Adapted from [102], which is distributed under the terms of the Creative Commons CC BY 4.0 licence.

Repeat experiments at 74°C were difficult to perform as the bubbles moved out of view and would often get confined at the corners or edges of the enclosure which would affect the dissolution rates. For the oleofoams, the difficulty lay in bubbles coalescing as they became more mobile. These difficulties were not encountered for the experiments performed at 25°C .

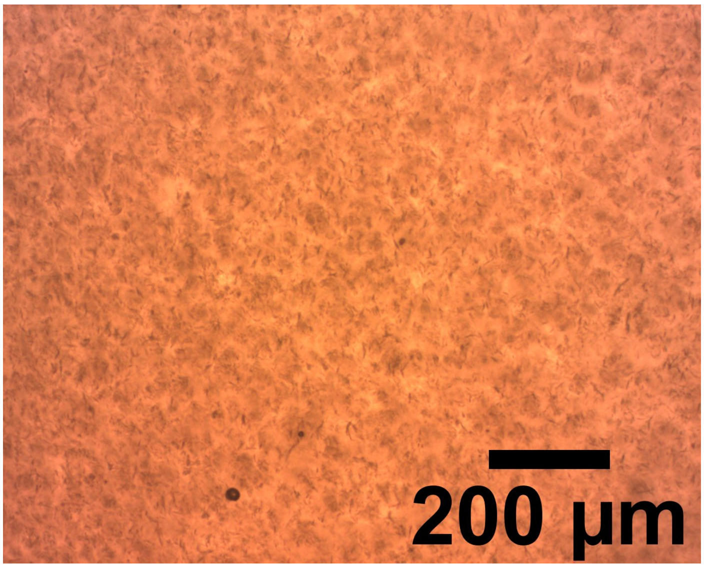

Fig. A.1 There is hardly any bubble introduced into the oleogel samples where vortexing occurs at 750 rpm during preparation. This is supported by this micrograph encompassing an area of 1152 μm ×921.6 μm, where only two bubbles of diameters approximately 21 μm and 6 μm are found near the bottom of the image. Beyond this region, around 10 bubbles at most were found, of similar sizes, for the sample on the slide.

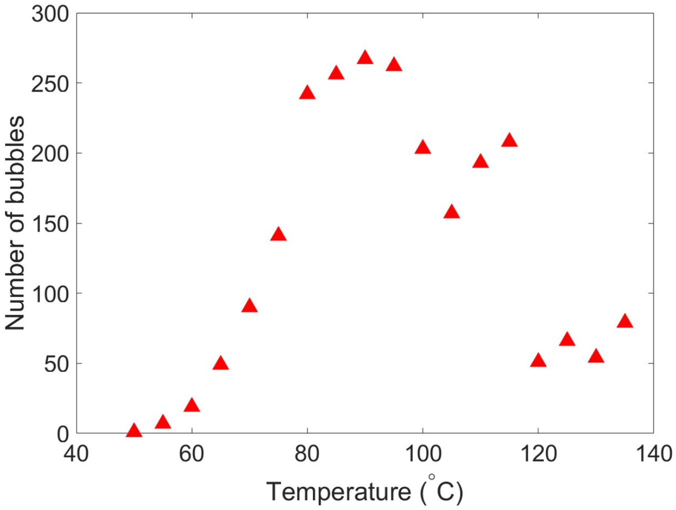

Fig. A.2 Bubble population in oleofoams versus temperature of gel prior to agitation. Numbers of bubbles were counted manually in pictures of the samples taken on the day of preparation. Adapted from [102], which is distributed under the terms of the Creative Commons CC BY 4.0 licence.

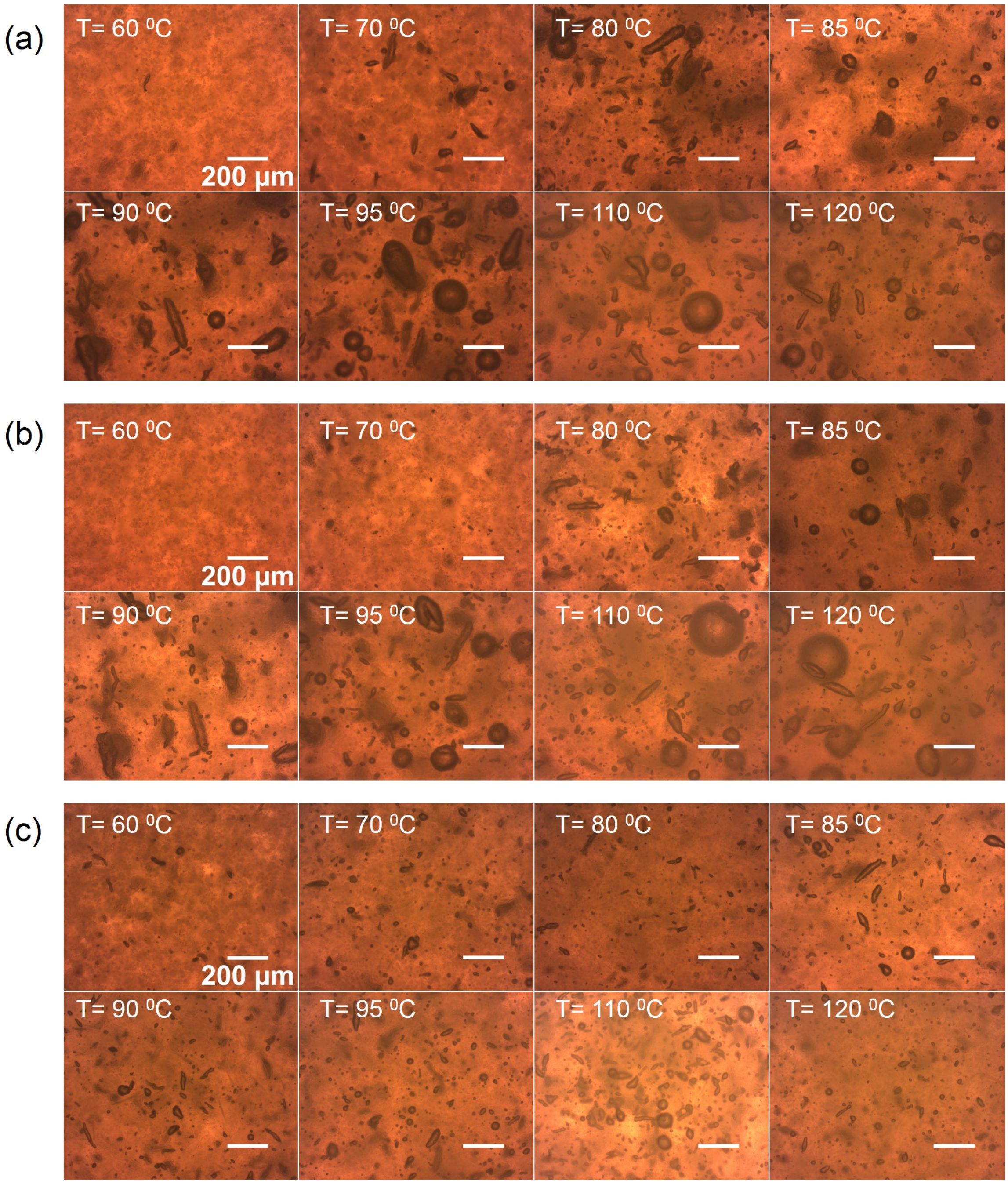
(a)
T= 60 ^{0}C
200 µm
T= 70 ^{0}C
T= 80 ^{0}C
T= 85 ^{0}C
T= 90 ^{0}C
T= 95 ^{0}C
T= 110 ^{0}C
T= 120 ^{0}C
(b)
T= 60 ^{0}C
200 µm
T= 70 ^{0}C
T= 80 ^{0}C
T= 85 ^{0}C
T= 90 ^{0}C
T= 95 ^{0}C
T= 110 ^{0}C
T= 120 ^{0}C
(c)
T= 60 ^{0}C
200 µm
T= 70 ^{0}C
T= 80 ^{0}C
T= 85 ^{0}C
T= 90 ^{0}C
T= 95 ^{0}C
T= 110 ^{0}C
T= 120 ^{0}C

Fig. A.3 Optical micrographs of samples (a) on the day of preparation, (b) 1 week after preparation and (c) 4 months after preparation. The samples were first heated to the temperatures indicated before shaking. Wax concentration was 2.5 % while the mixing time was 2 minutes. The samples were then allowed to cool to room temperature, and stored at room temperature. Adapted from [102], which is distributed under the terms of the Creative Commons CC BY 4.0 licence.

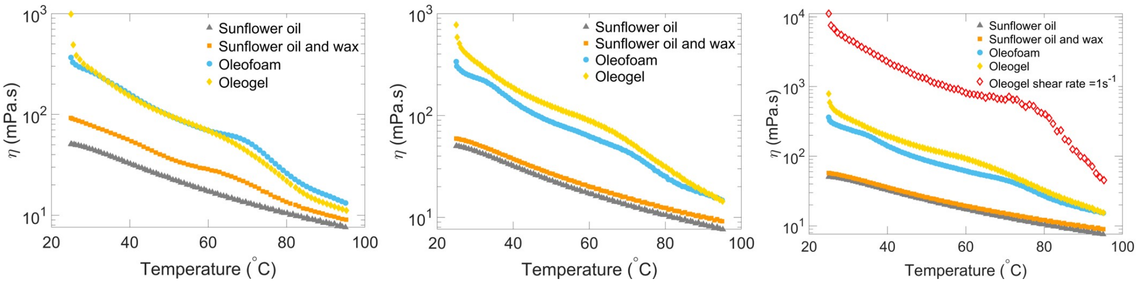

Fig. A.4 Triplicate measurements of viscosity with varying temperature with $\mathrm{d}T/\mathrm{d}t = 10°\mathrm{C/min}$ for sunflower oil (grey triangles), suspension of wax in sunflower oil (orange squares), oleofoam (cyan circles) and oleogel (yellow diamonds). Additionally, in the third panel, the viscosity profile for the oleogel sheared at 1 s^{-1} is also given (open diamonds). First two panels are adapted from [102], which is distributed under the terms of the Creative Commons CC BY 4.0 licence.

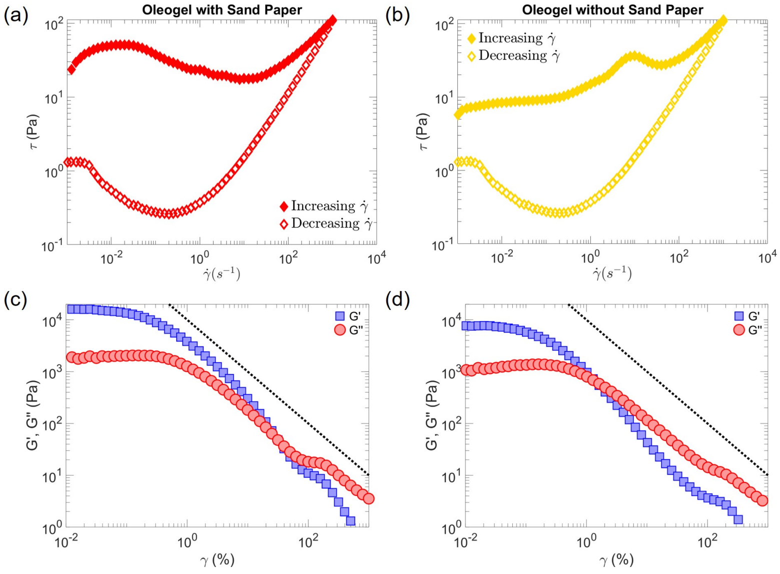

Fig. A.5 Side-by-side comparison of oleogel rheology with sand paper – panels (a) and (c) – and without sand paper – panels (b) and (d). (a,b) Flow curves of oleogel, measured immediately after sample loading, first for increasing shear rates (filled symbols) and then for decreasing rates (open symbols). Panels (c,d) show oscillatory amplitude-sweeps conducted for increasing strain amplitudes, with $f = 1$ Hz, obtained after loading and 500 s of waiting, without any pre-shear step. All experiments done at $T = 25°\mathrm{C}$. Adapted from [102], which is distributed under the terms of the Creative Commons CC BY 4.0 licence.

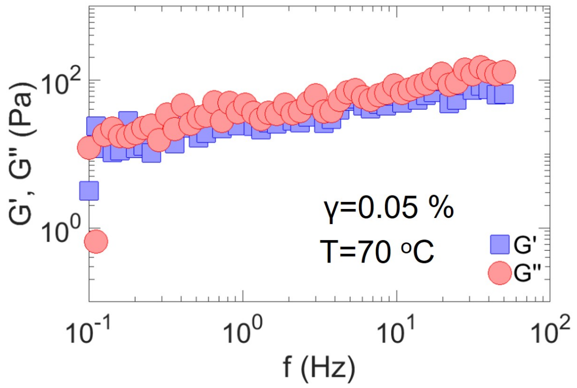

Fig. A.6 Frequency sweep of oleogel at 70°C from $f = 0.1 - 50$ Hz at constant $\gamma = 0.05$ %. Prior to this, the oleogel was heated from $25 - 70$°C at $\mathrm{d}T/\mathrm{d}t = 7$°C/min with constant $f = 1$ Hz and $\gamma = 0.05$ % as described in Figure 4.9(b).

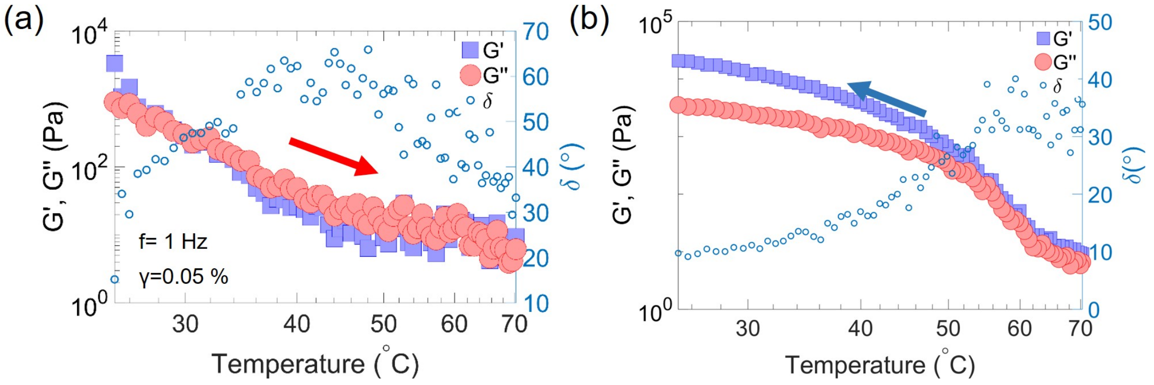

Fig. A.7 Oscillatory rheology of oleogel with varying temperature for (a) heating and (b) cooling between $T = 25 - 70$°C, at a rate of $\mathrm{d}T/\mathrm{d}t = \pm 7$°C/min. The strain and frequencies were held constant at $\gamma = 0.05$ % and $f = 1$ Hz respectively. The raw phase $\delta = \tan^{-1}(G''/G')$ (open circles) is also shown in the two panels.

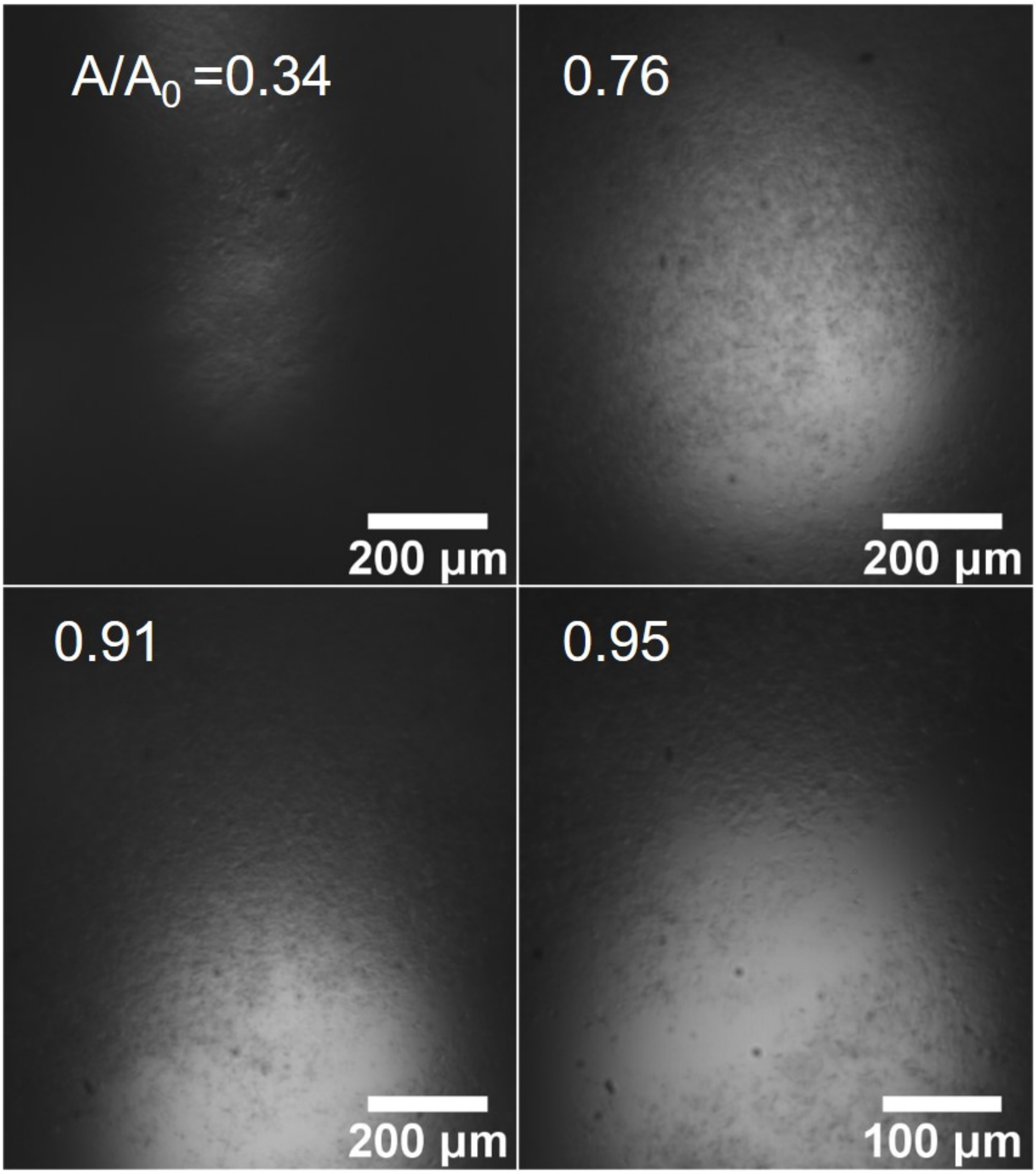

Fig. A.8 Close-up images of the wax-coated oil pendant drop as in Figure 4.11 at different area fractions. For $A/A_0 = 0.34$, the surface crystals are so close and compacted that not enough light is transmitted through the drop and the surface appears dark. As the drop expands, the centre of the drop moves lower with respect to the camera's field of view. This is particularly the case for $A/A_0 = 0.91 - 0.95$. Panel for $A/A_0 = 0.76$ is adapted from [102], which is distributed under the terms of the Creative Commons CC BY 4.0 licence.

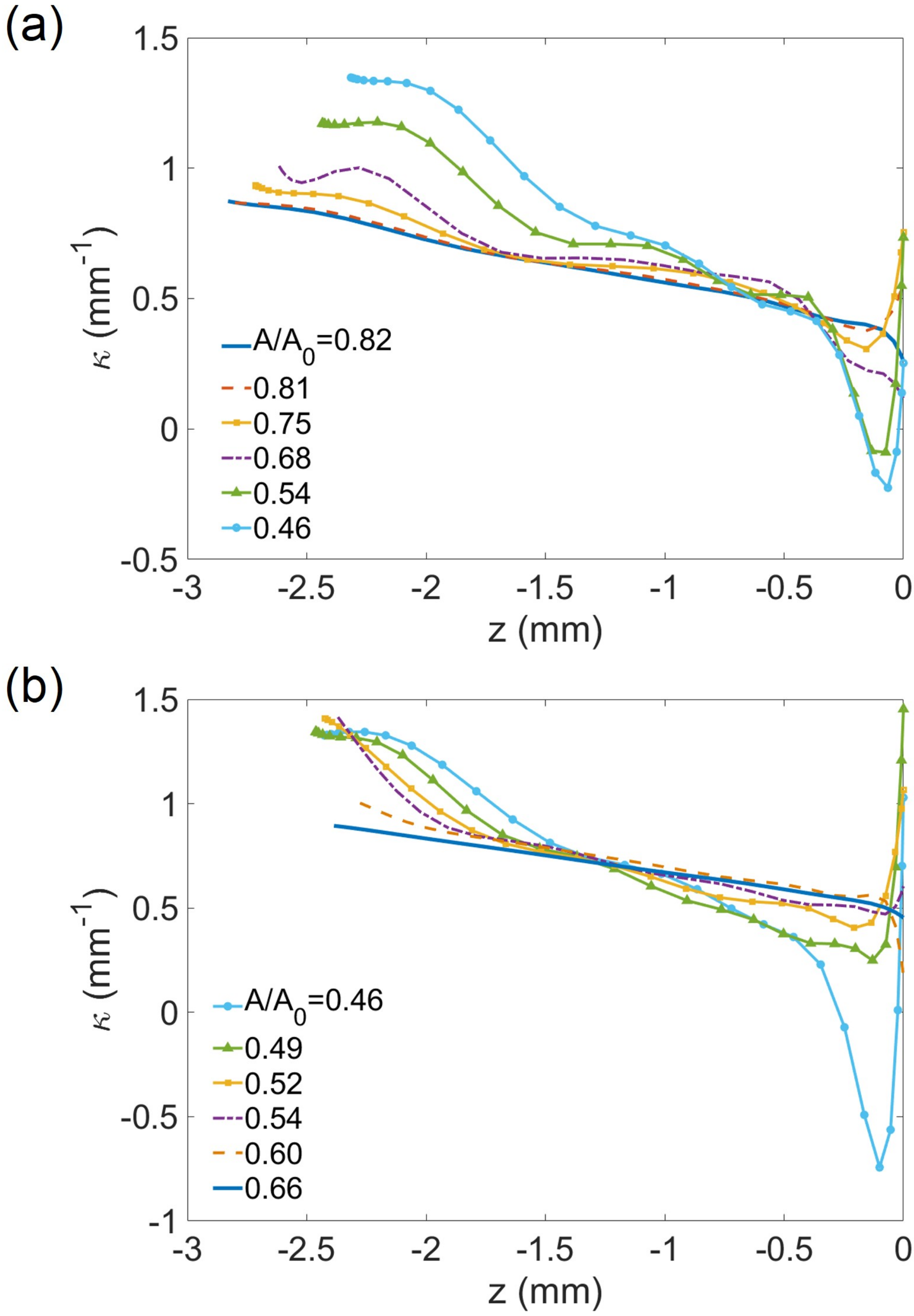

Fig. A.9 Curvature profiles of wax-coated sunflower oil drop for different states, given in terms of area fractions. (a) Curvature profile for drop states during the first compression series; and (b) for the second expansion series. The drop is attached to the needle at $z = 0$ and the z-axis points in the direction opposite to gravity. Adapted from [102], which is distributed under the terms of the Creative Commons CC BY 4.0 licence.

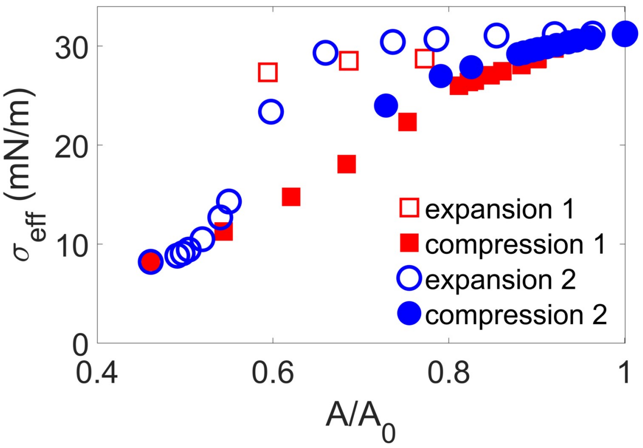

Fig. A.10 Variation of effective surface tension for wax-coated drop, suspended from a 2.11 mm stainless steel needle [same drop as in Figure 4.11] when it is first expanded to spread the wax over the drop, followed by compression and again expansion.

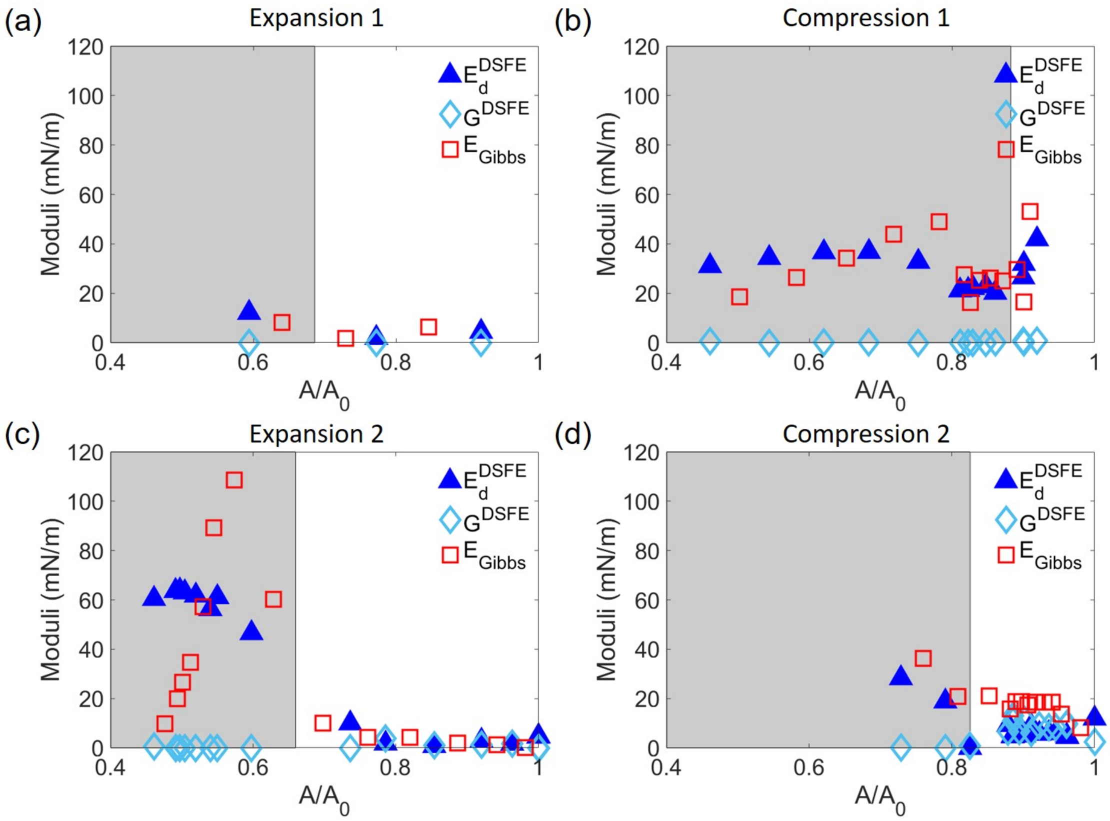

Fig. A.11 The estimates on E_d^{DSFE} (filled blue triangles), G_{2D} (open cyan diamonds) and E_{Gibbs} (open red squares) for (a) expansion, (b) compression, (c) second expansion and (d) second compression. These correspond to the drop suspended from the 2.11 mm stainless steel needle and considered in Figure 4.11.

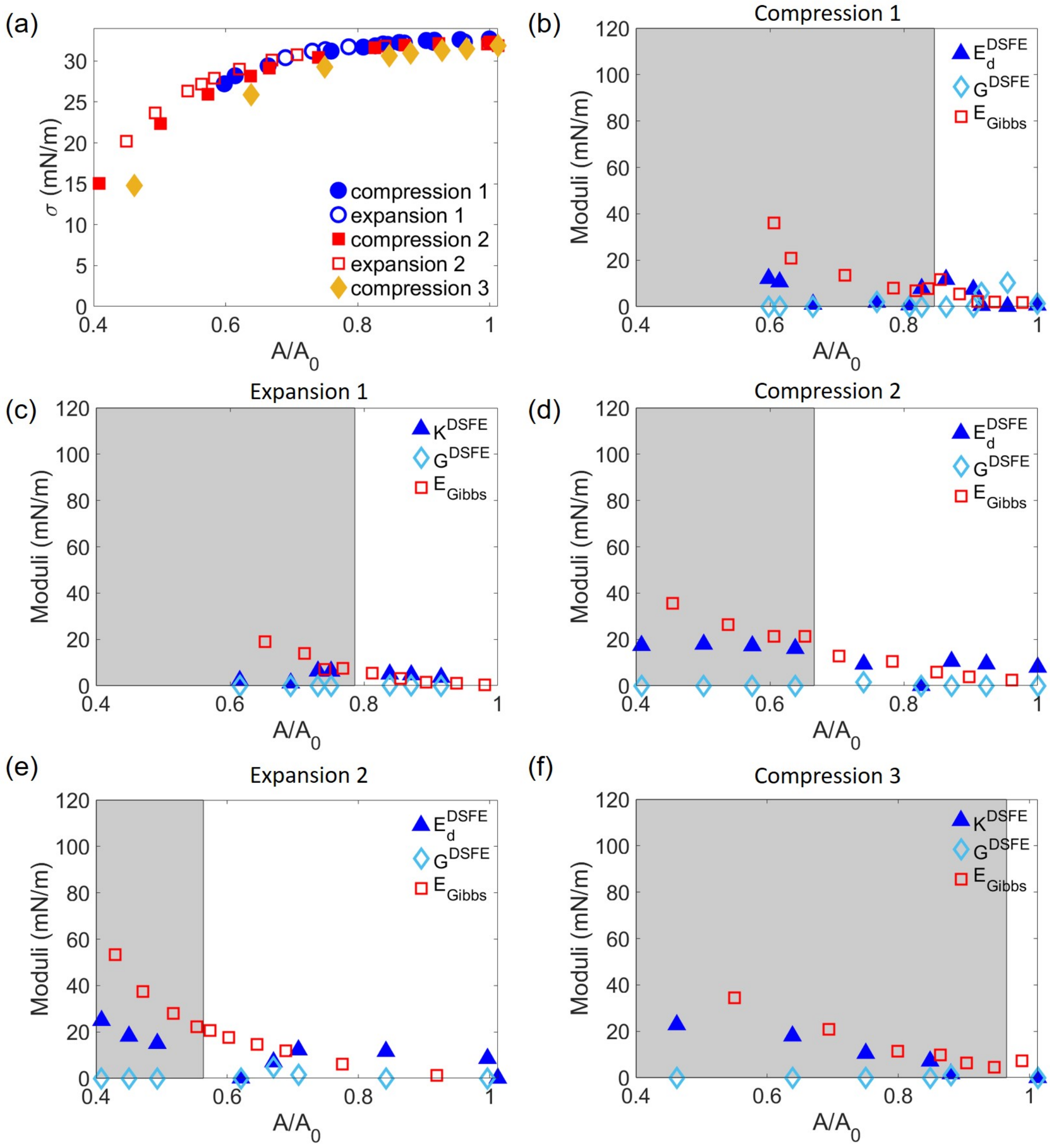

Fig. A.12 **Determination of interfacial compression and shear moduli for wax-coated drop suspended from a PTFE needle.** The drop underwent two cycles of compression and expansion. (a) Variation of effective surface tension for each compression (filled symbols) and expansion (open symbols). The estimates on E_d^{DSFE} (filled blue triangles), G_{2D} (open cyan diamonds) and E_{Gibbs} (open red squares) for (b) first compression followed by (c) first expansion, then (d) second compression, (e) second expansion, and finally (f) third compression.

Appendix B

Supporting content for Chapter 5

Table B.1 The various geometrical elements, for the bubble states $i = 1$ and 2, calculated using image analysis.

State 1	State 2
$l_{11} = 170.56\ \mu\text{m}$	$l_{21} = 132.08\ \mu\text{m}$
$l_{12} = 369.20\ \mu\text{m}$	$l_{22} = 387.92\ \mu\text{m}$
$A_{11} = 2.5451 \times 10^4\ \mu\text{m}^2$	$A_{21} = 2.1666 \times 10^4\ \mu\text{m}^2$
	$A_{22} = 3.4176 \times 10^3\ \mu\text{m}^2$
	$l_{23} = (l_{11} + l_{12}) - (l_{21} + l_{22}) = -19.76\ \mu\text{m}$

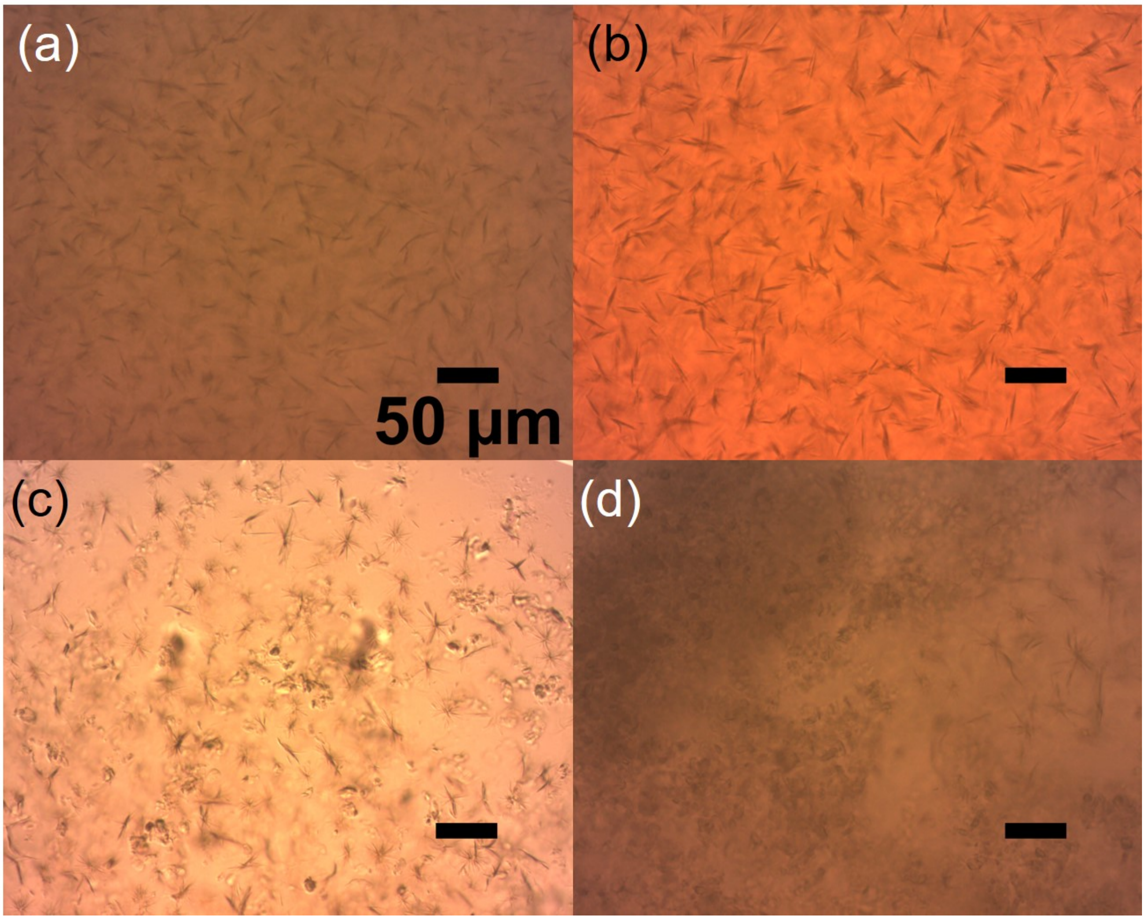

Fig. B.1 **Micrographs of different oleogels prepared without application of shear during crystallisation.** (a) U-oleogel with fast cooling rate $y = -23.5°\text{C/min}$ has mainly needle-shaped and star-shaped crystals. The same is true for (b) another oleogel prepared using the temperature-controlled stage with uniform tempering and fast cooling at $y = -9°\text{C/min}$. (c) Rheometer-prepared oleogel RO-0 with $y = -9.16°\text{C/min}$ having almost equal distribution of star-shaped and platelet-like crystals. (d) As a control experiment, an unagitated oleogel U-oleogel prepared by partially placing the sample within the temperature-controlled region. This led to dominantly platelet-like crystals with few star-shaped crystals in the non-uniformly tempered region. These experiments suggest that platelet-like crystals mainly appear when there is non-uniform tempering.

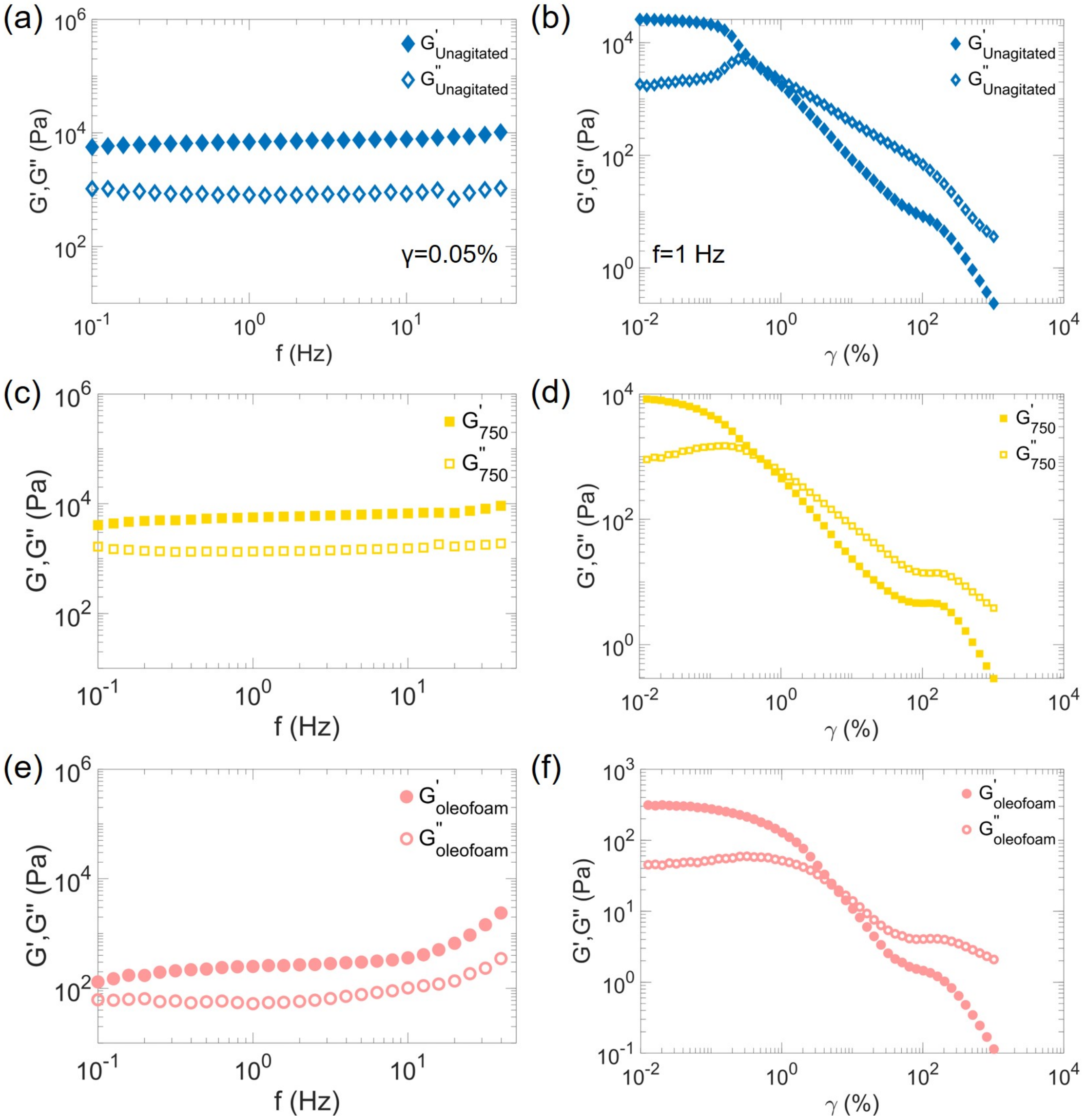

Fig. B.2 **Oscillatory frequency and amplitude sweeps** for (a-b) U-oleogel (blue diamonds), (c-d) oleogel750 (yellow squares) and (e-f) oleofoam (pink circles). Frequency sweep tests were conducted at a constant $\gamma = 0.05$ %; while amplitude sweeps were for a constant $f = 1$ Hz at $T = 25$°C. Filled symbols for G' and open symbols for G''.

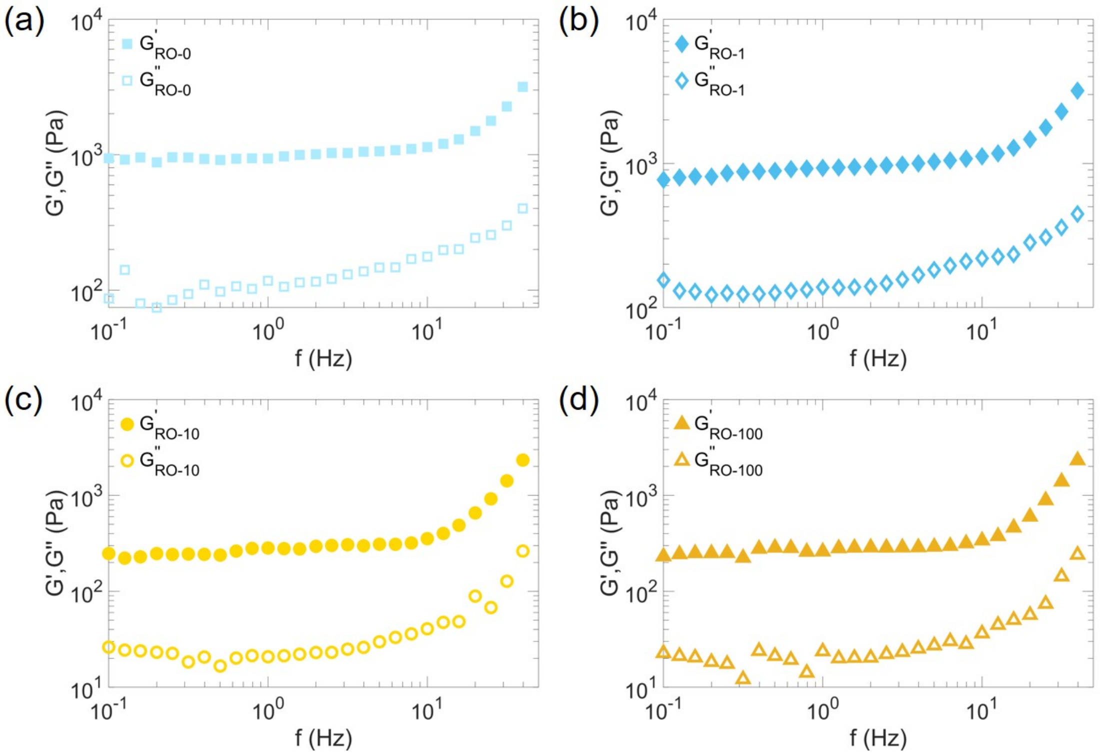

Fig. B.3 **Oscillatory frequency sweeps for rheometer-prepared oleogels.** (a) RO-0, (b) RO-1, (c) RO-10 and (d) RO-100. The strain amplitude was held at $\gamma = 0.05$ % and $T = 25$°C. Filled symbols are for G' and open symbols for G''.

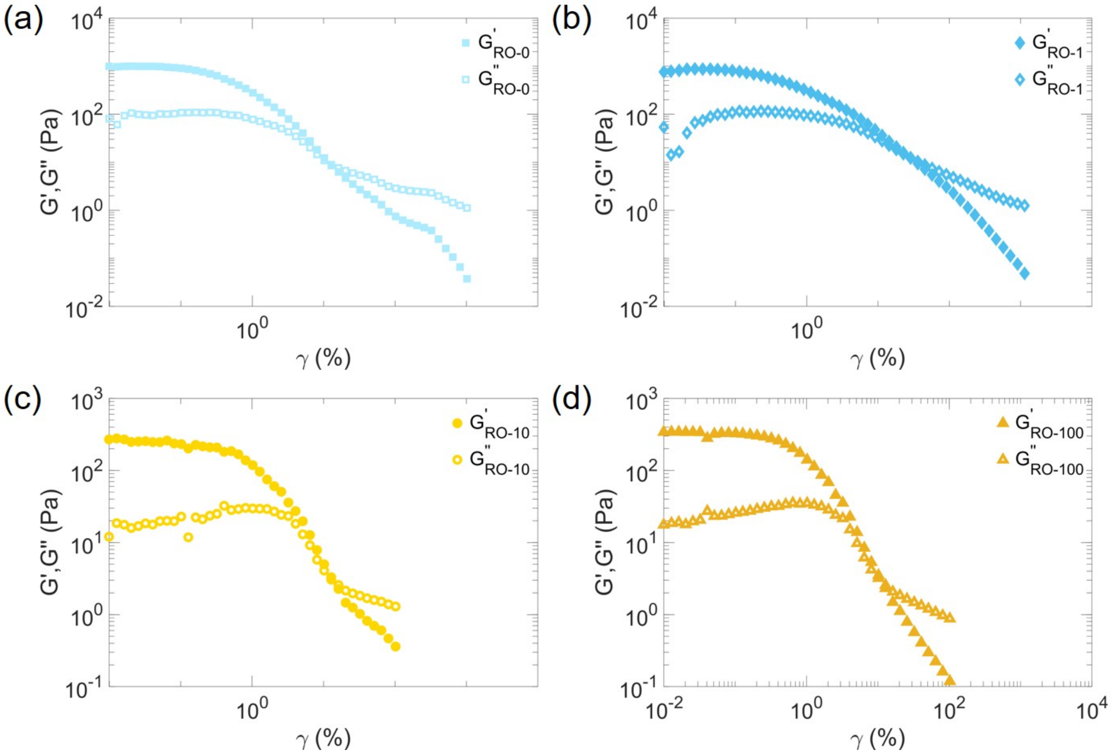

Fig. B.4 **Oscillatory amplitude sweeps for rheometer-prepared oleogels.** (a) RO-0, (b) RO-1, (c) RO-10 and (d) RO-100. The frequency was held at $f = 1$ Hz and $T = 25°$C. Filled symbols are for G' and open symbols for G''.

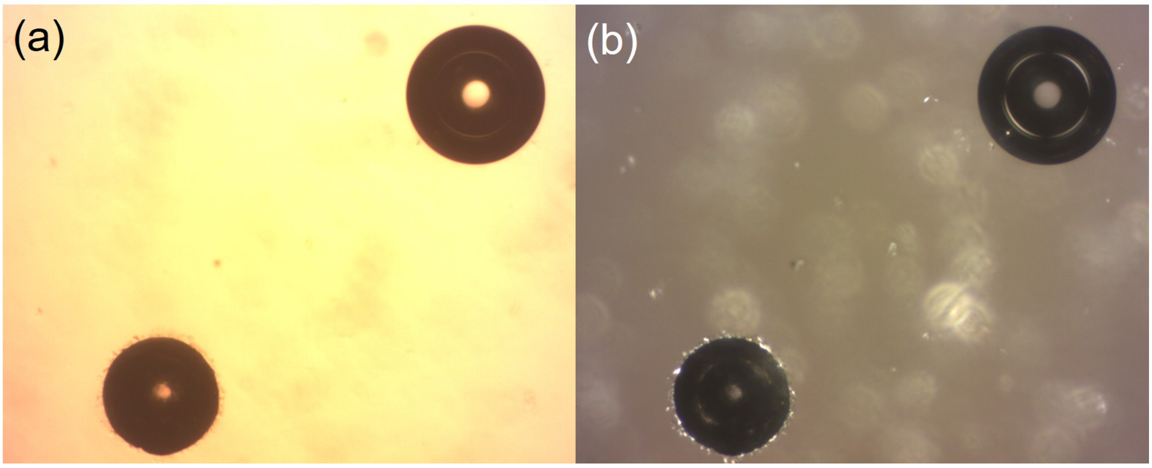

Fig. B.5 Distinguishing between bare and wax-coated bubbles (a) without and (b) with cross-polarisers. The bubble in the top right corner is a bare one. Also bright central regions, attributed to optical effects, are seen in both bubbles. However, these effects are circular for the bare bubble.

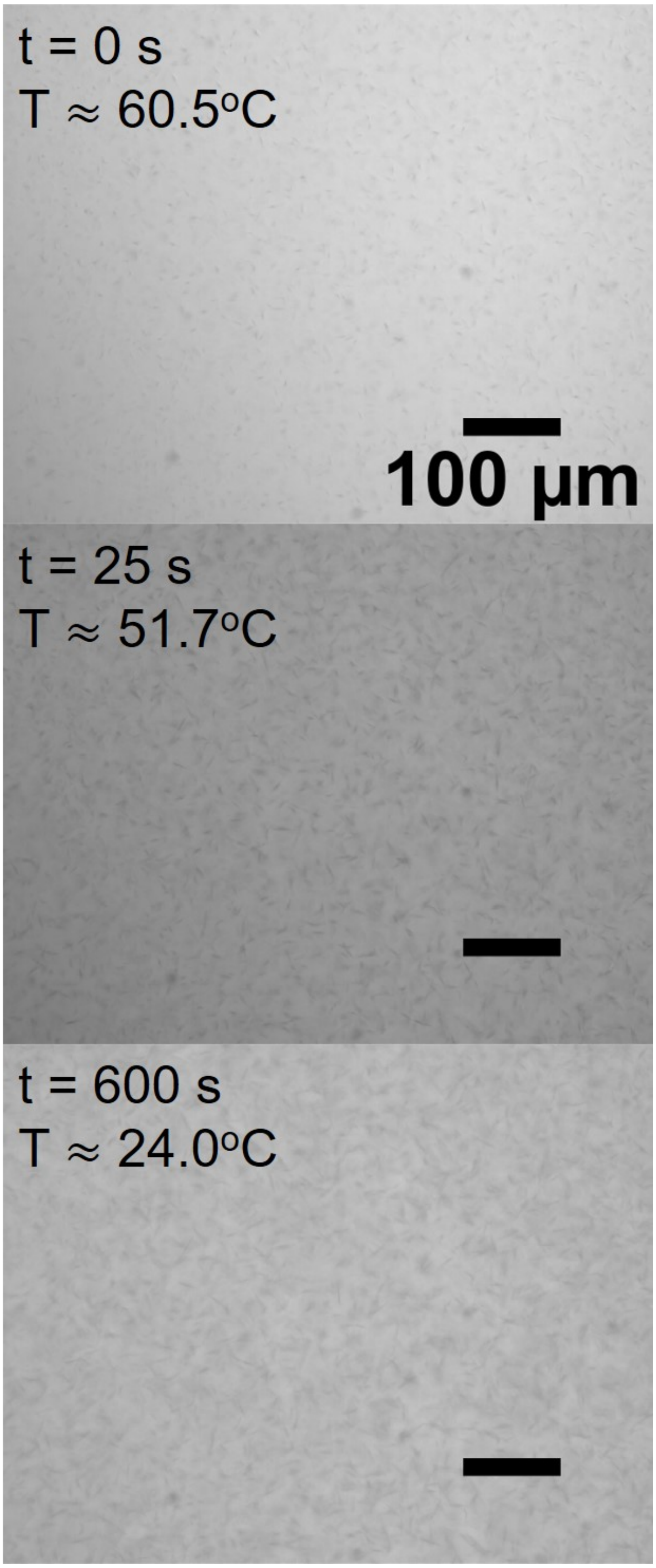
t = 0 s
T ≈ 60.5°C
100 µm
t = 25 s
T ≈ 51.7°C
t = 600 s
T ≈ 24.0°C

Fig. B.6 **Crystal growth during cooling.** Micrographs of crystals during first noticeable appearance at $t = 0$ s then after $t = 25$ s and $t = 600$ s.

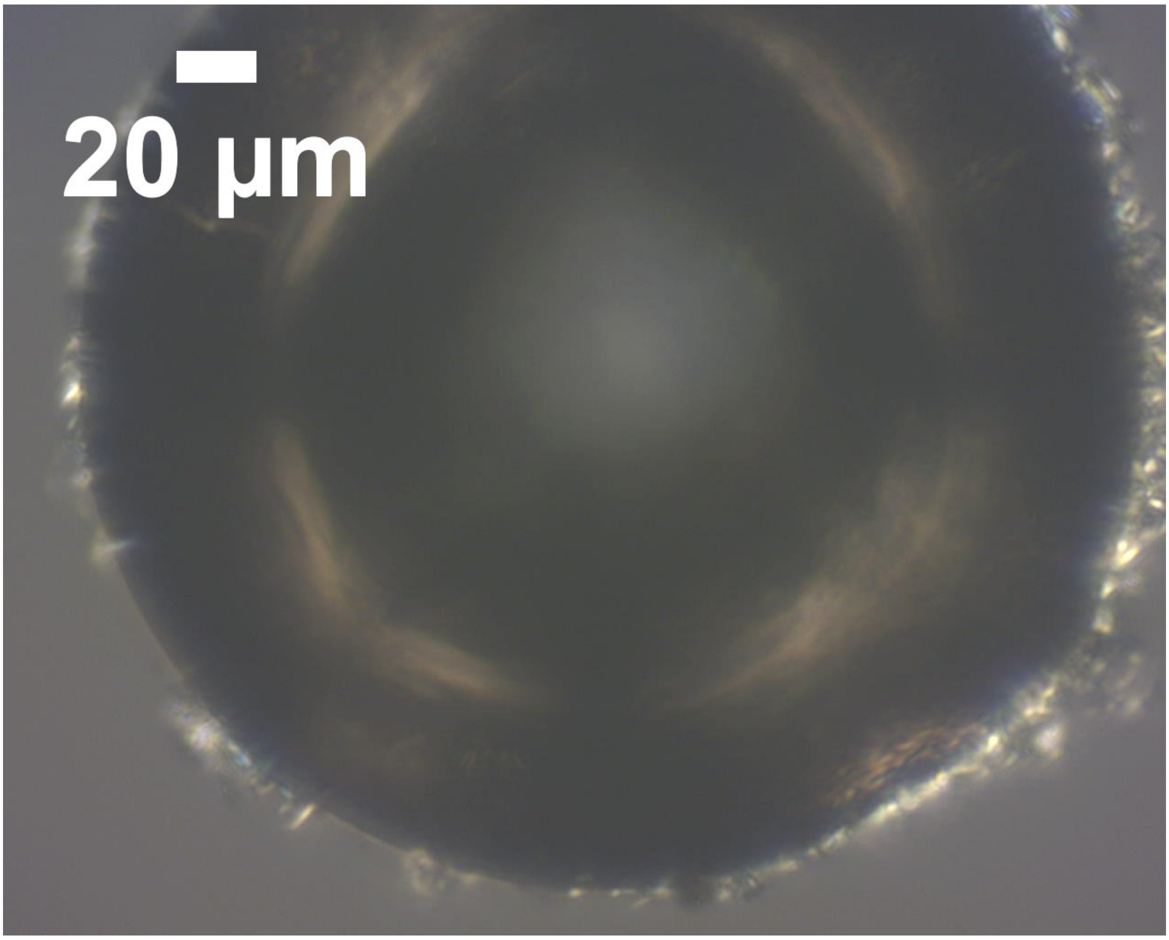

Fig. B.7 A close up of a wax-coated bubble resuspended in oil, viewed with cross-polarisers.

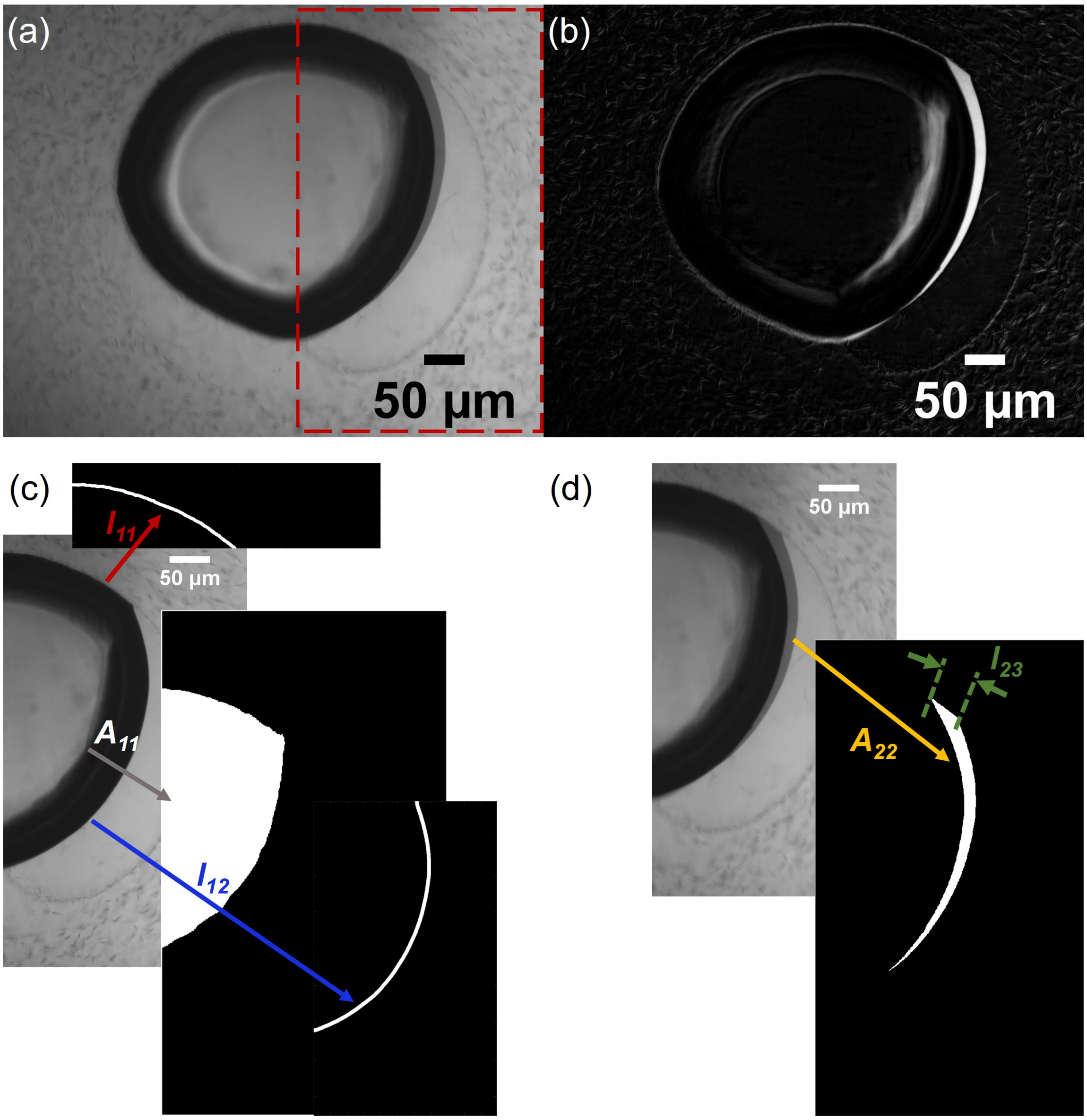

Fig. B.8 Image processing to determine geometrical variables used in equation (5.4). (a) An image stack using median pixel values from parent images. The highlighted region is the region of interest (ROI) as all changes between the two states are expected to be confined here. (b) Another image stack of the same, but with standard deviation of the pixel values. (c) Isolating and measuring the arc and area elements of state 1, within the ROI. (d) Determining the swept area A_{22} and arc l_{23} as the bubble contracts from state 1 to 2.

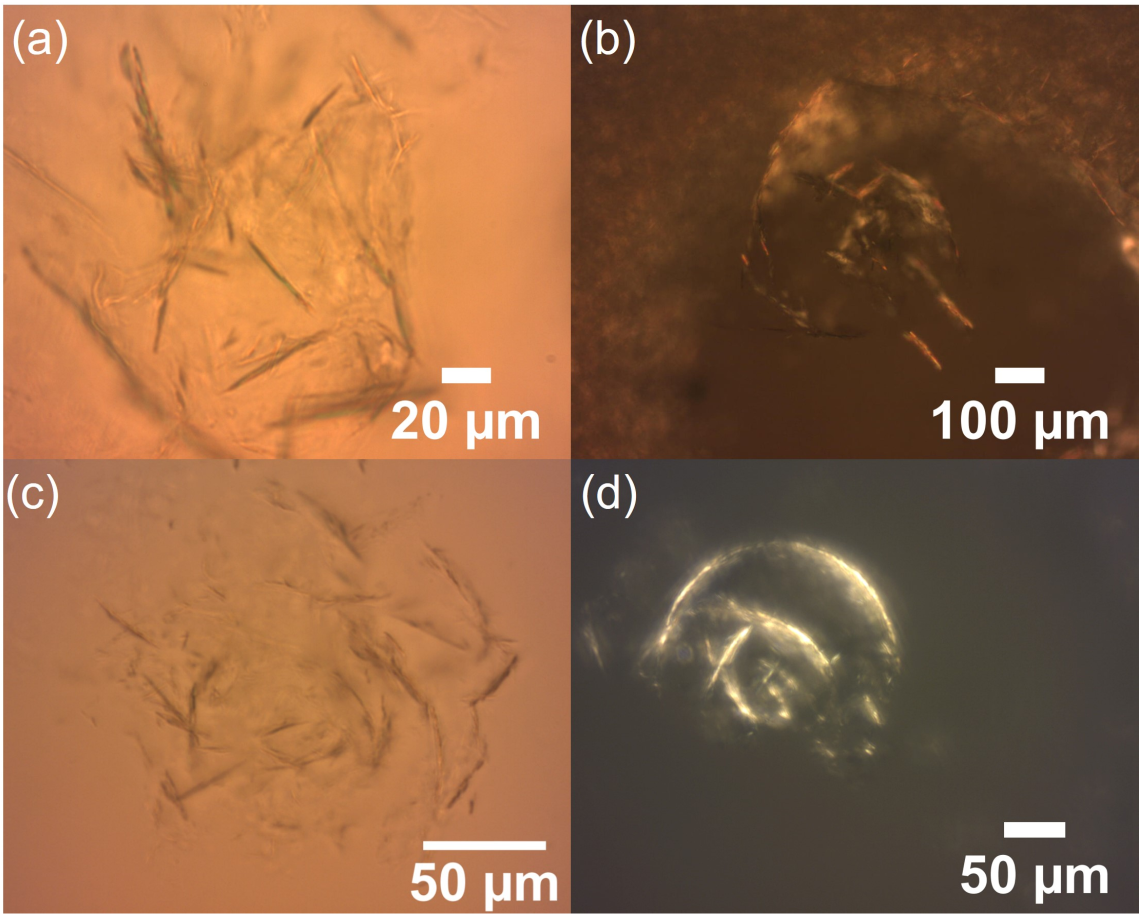

Fig. B.9 **Micrographs of delaminated wax-layers left behind from dissolved wax-coated bubbles.** Remnant interfacial layer of wax-coated bubble (a) prepared in the temperature-controlled stage using the preparation protocol for the U-oleogel, that is without agitation. (b) A similarly prepared bubble, observed using cross-polarisers. Remnant layers of wax-coated bubbles that were extracted from oleofoams and resuspended in oil: (c) observed without cross-polarisers, and (d) a different layer observed with cross-polarisers.

Appendix C

Supporting content for Chapter 6

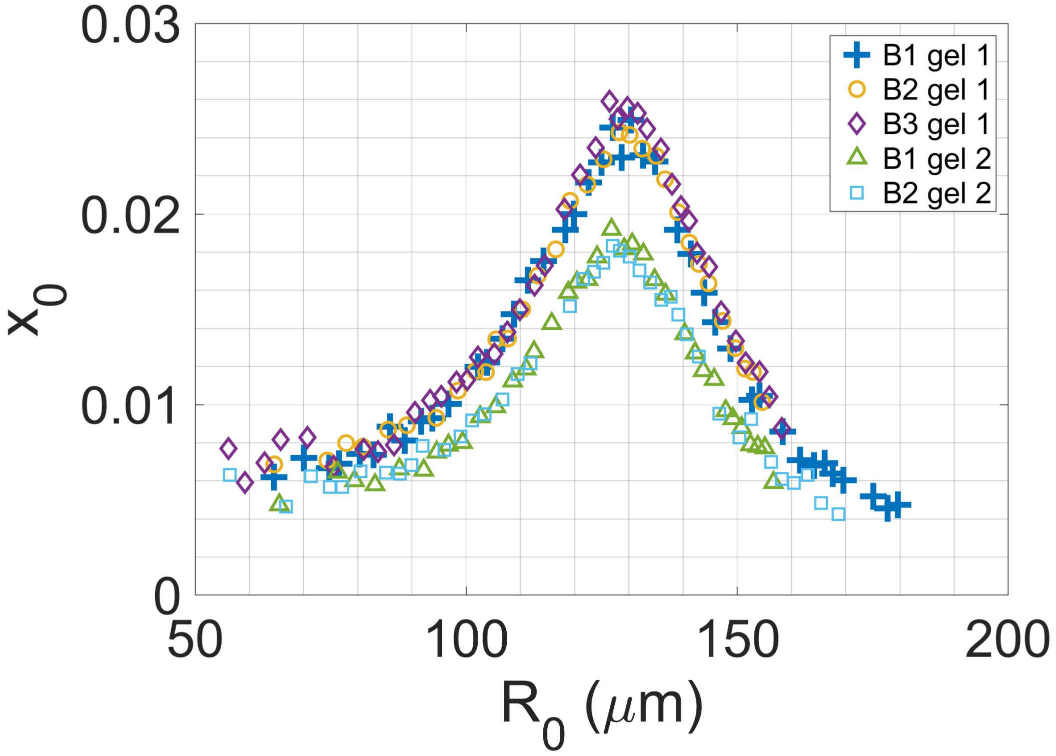

Fig. C.1 **Radius-sweep experiments using two different gels.** The amplification was fixed at $A = 40$ %. For gel 1, with bubbles B1 (blue plus), B2 (orange circles) and B3 (violet diamonds), $R_{\text{res}} = 128.4 \pm 2.0$ μm with $x_0 = 0.025$. For gel 2, with bubbles B1 (green triangles), and B2 (cyan squares), $R_{\text{res}} = 126.9 \pm 0.1$ μm with $x_0 = 0.019$.

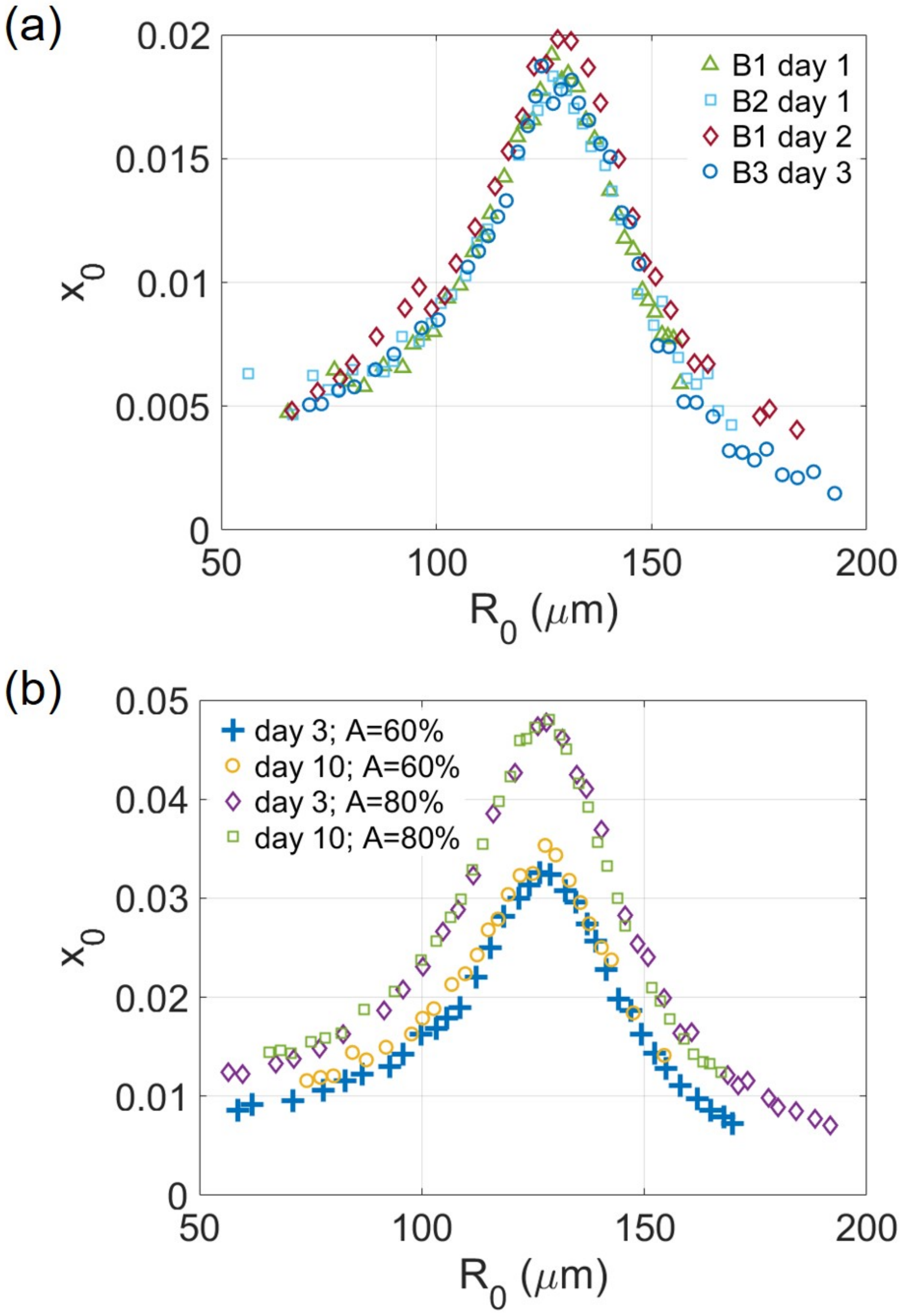

Fig. C.2 Radius-sweep experiments illustrate that the same gel can be used for several days if stored properly. (a) Bubbles oscillated with $A = 40$ %, one day after the gel is prepared: B1 (green triangles), B2 (cyan squares); on day 2 (magenta diamonds); and day 3 (blue circles). (b) Bubbles oscillated in the same gel at $A = 60$ % on day 3 (blue plus) and day 10 (yellow circles); also bubbles oscillated at $A = 80$ % on day 3 (violet diamonds) and day 10 (green squares).

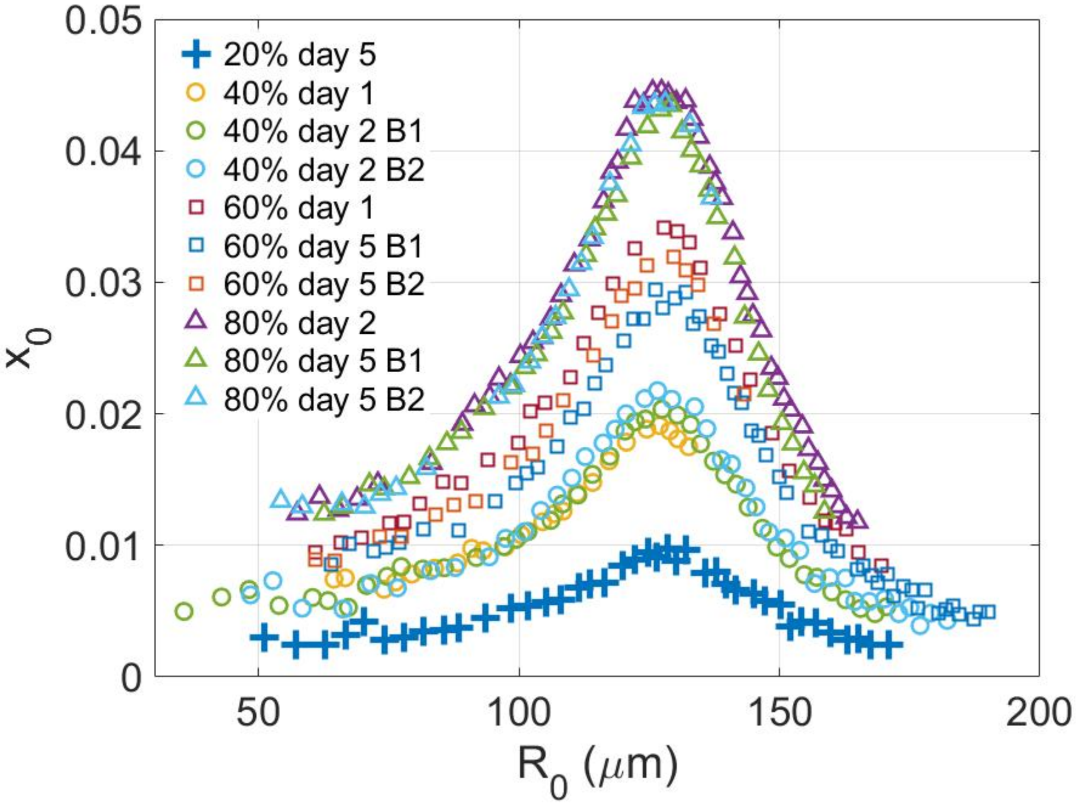

Fig. C.3 Map of excursions of different bubbles, oscillated within the same gel, at different amplifier gain values and on different days. The days are indicated since the preparation of the gel, with day 1 being 24 hours after gel preparation, and so forth.

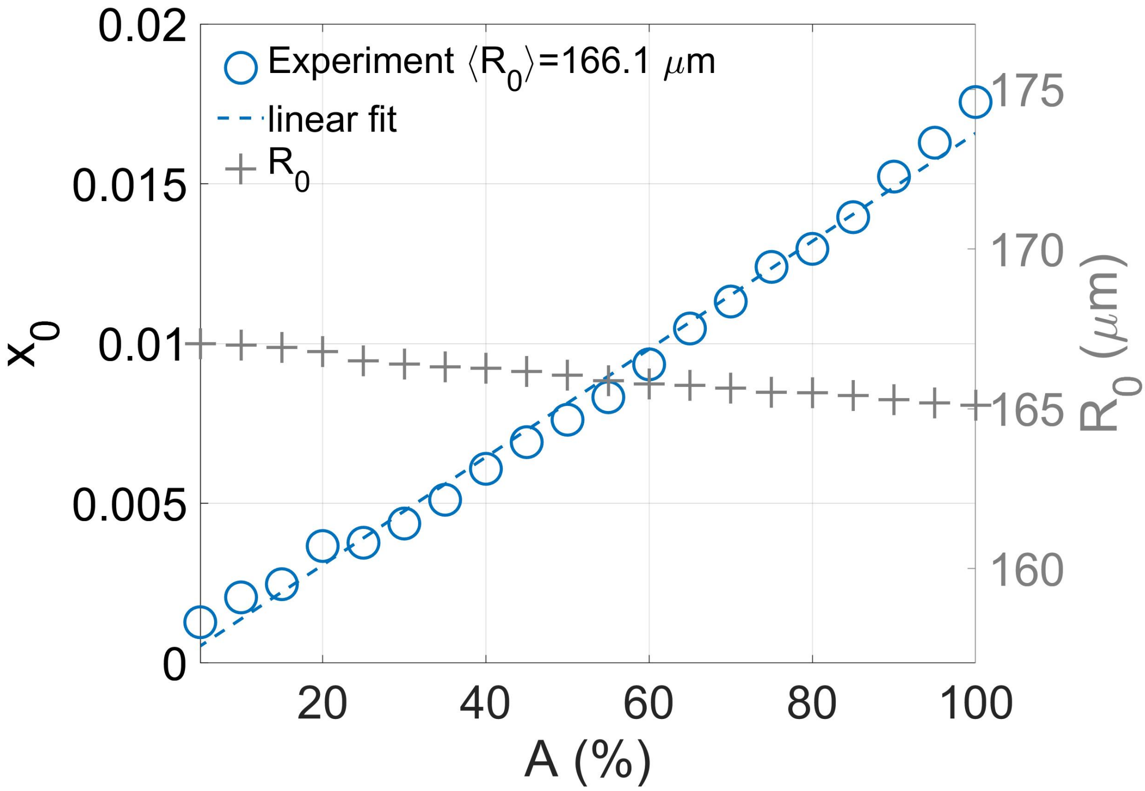

Fig. C.4 Excursion versus increasing amplification (open circles) for a bare bubble with initial radius $R_0 = 167$ μm when $A = 5$ % and final radius $R_0 = 165.1$ μm when $A = 100$ %. The time averaged bubble radius may be considered as $\langle R_0 \rangle = 166.1$ μm, while the corresponding initial radius before each run is shown by the plus symbols (right y-axis). There is a time interval of $\Delta t \approx 30$ s between each run, and to carry out the whole set of runs it took about 7 minutes. The linear fit to the data is shown by the dashed line.

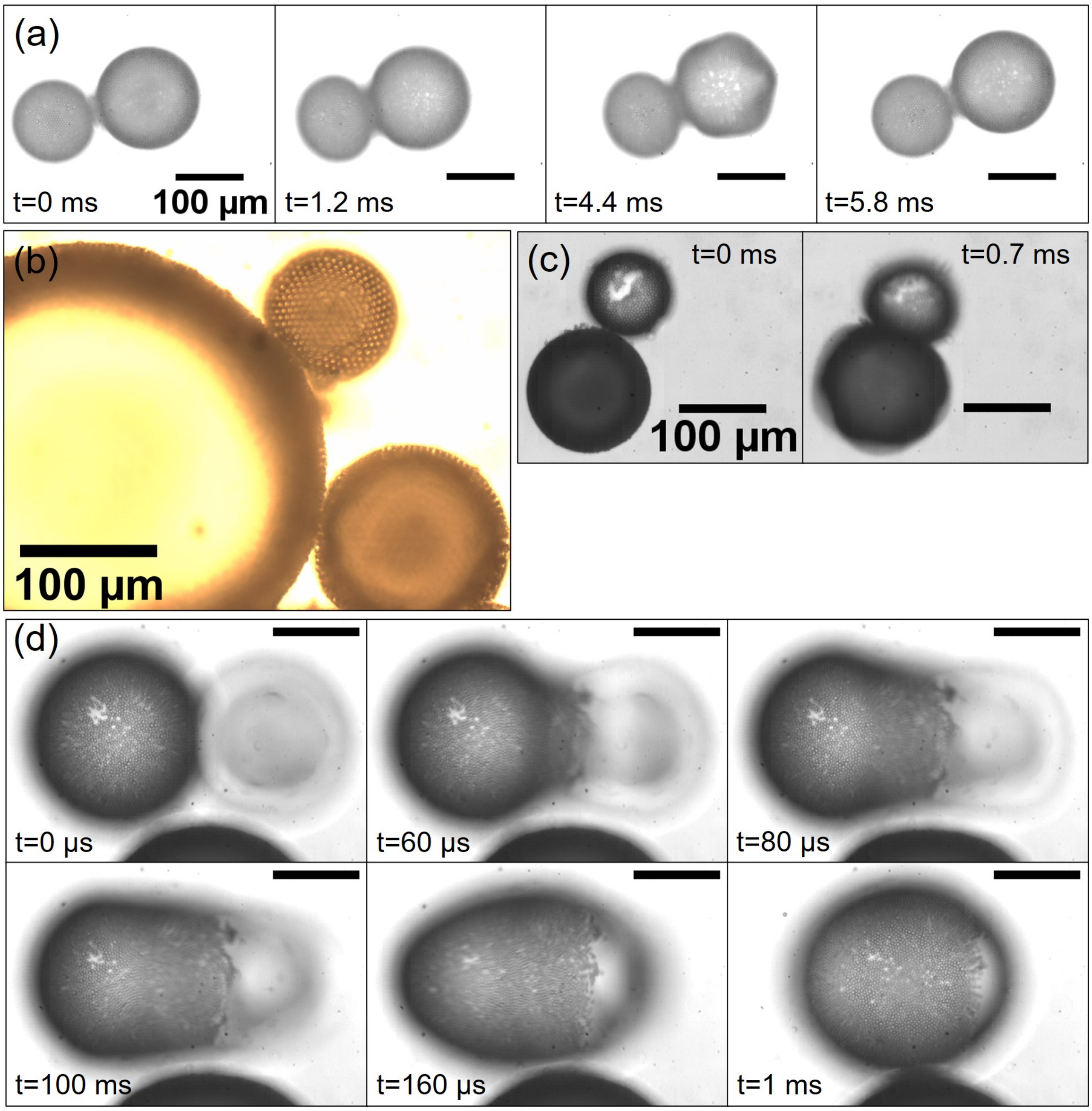

Fig. C.5 **Colloidal armour resisting bubble coalescence.** (a) Two bubbles in contact oscillated at $f = 39$ kHz, with 200 cycles. As the bubbles oscillated, with the larger oscillating stronger, they pressed against each other (possibly due to secondary Bjerknes forces [144]) and then relaxed. There was no coalescence. (b) Micrograph focusing on the contour of three coated bubbles in contact under static conditions. The particle layers appear to intervene between the bubbles. (c) A pair fully coated and partially coated bubbles, in contact and oscillated with $f = 40$ kHz and 100 cycles. No coalescence was observed. (d) High-speed image sequence of a coated bubble in contact with a bare bubble (right) and the subsequent coalescence, without the influence of ultrasound, observed at a frame rate of 50,000 frames per second. All with the same particle size, $a = 2.5$ μm.

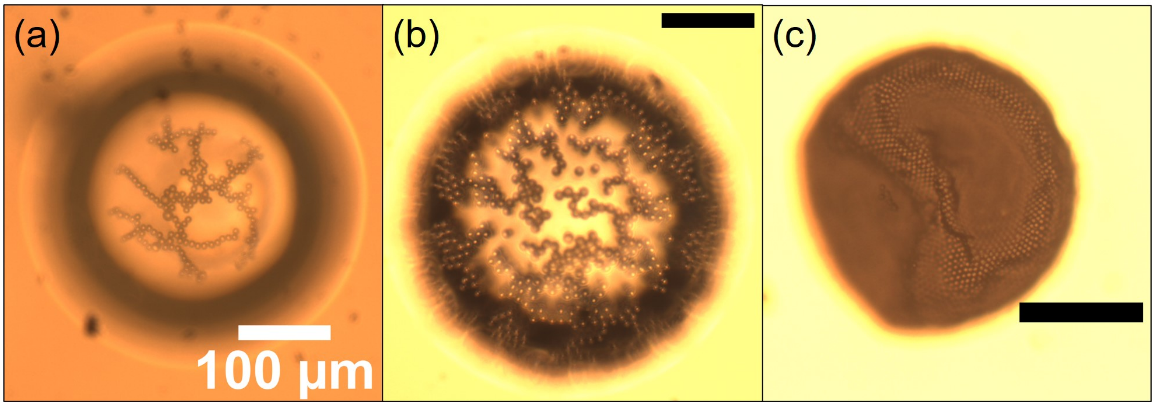

Fig. C.6 **Effect of surface coverage on interfacial structure.** All colloidal particles had size $a = 2.5$ μm, and the bubbles were viewed from the bottom using an inverted microscope. The plane of focus then laid at the bottom of the bubbles. (a,b) At very low coverage, the particles exhibited long range ordering, rather than simply aggregating due to gravity. (c) At very high coverage, a bubble attained a buckled shape.

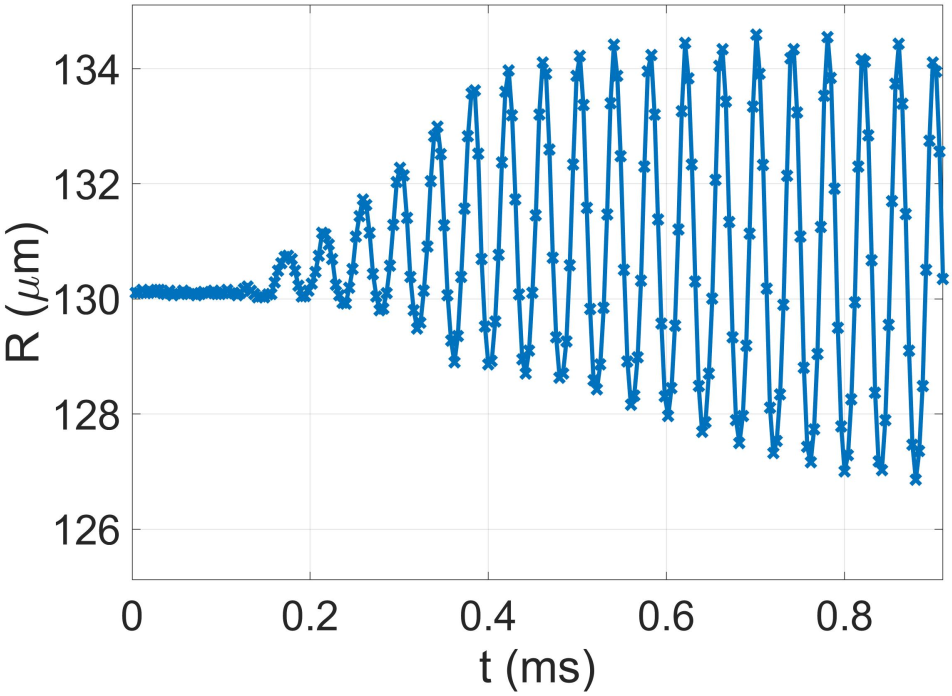

Fig. C.7 A bubble of with $R_0 = 130.11$ μm coated with $a = 1.2$ μm colloids was oscillated with a 20 cycle acoustic pulse at $f = 25$ kHz and $A = 80\%$. The oscillations exhibit expansion-only behaviour.

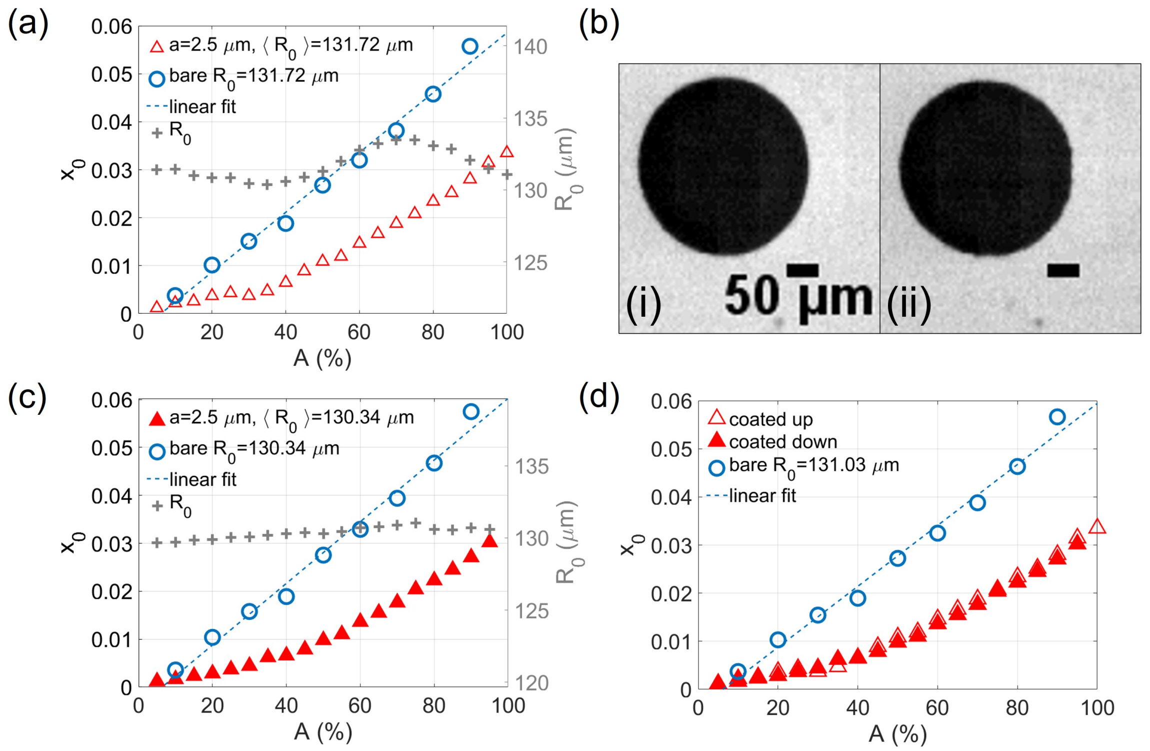

Fig. C.8 **Shape change during bubble oscillations.** (a) Excursions of a coated bubble with increasing gain. The non-monotonic variation in R_0 during the experiment (grey plus symbols, right y-axis) is a result of the bubble changing shape. The shape changes slightly between $A = 10 - 100\%$, with the initial (i) and final (ii) shapes appearing similar in (b). (c) Same bubble as in (a) with gain going down. (d) Comparing excursions in (a) and (c) show that despite shape change, the excursions overlap.

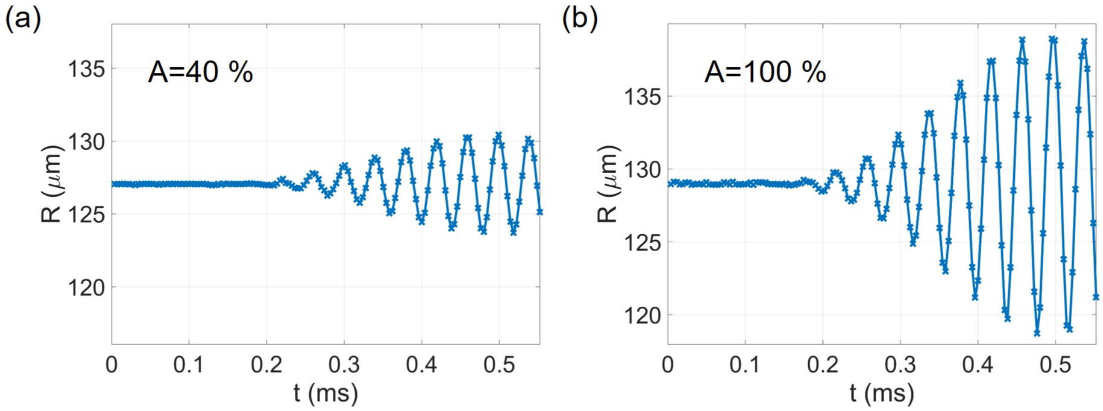

Fig. C.9 At reduced particle surface coverage, the bubble oscillations about the mean radius R_0 become symmetrical. This is the same bubble as the one in Figure 6.11(f) with radius-time curves shown for (a) $A = 40\%$ and (b) $A = 100\%$.

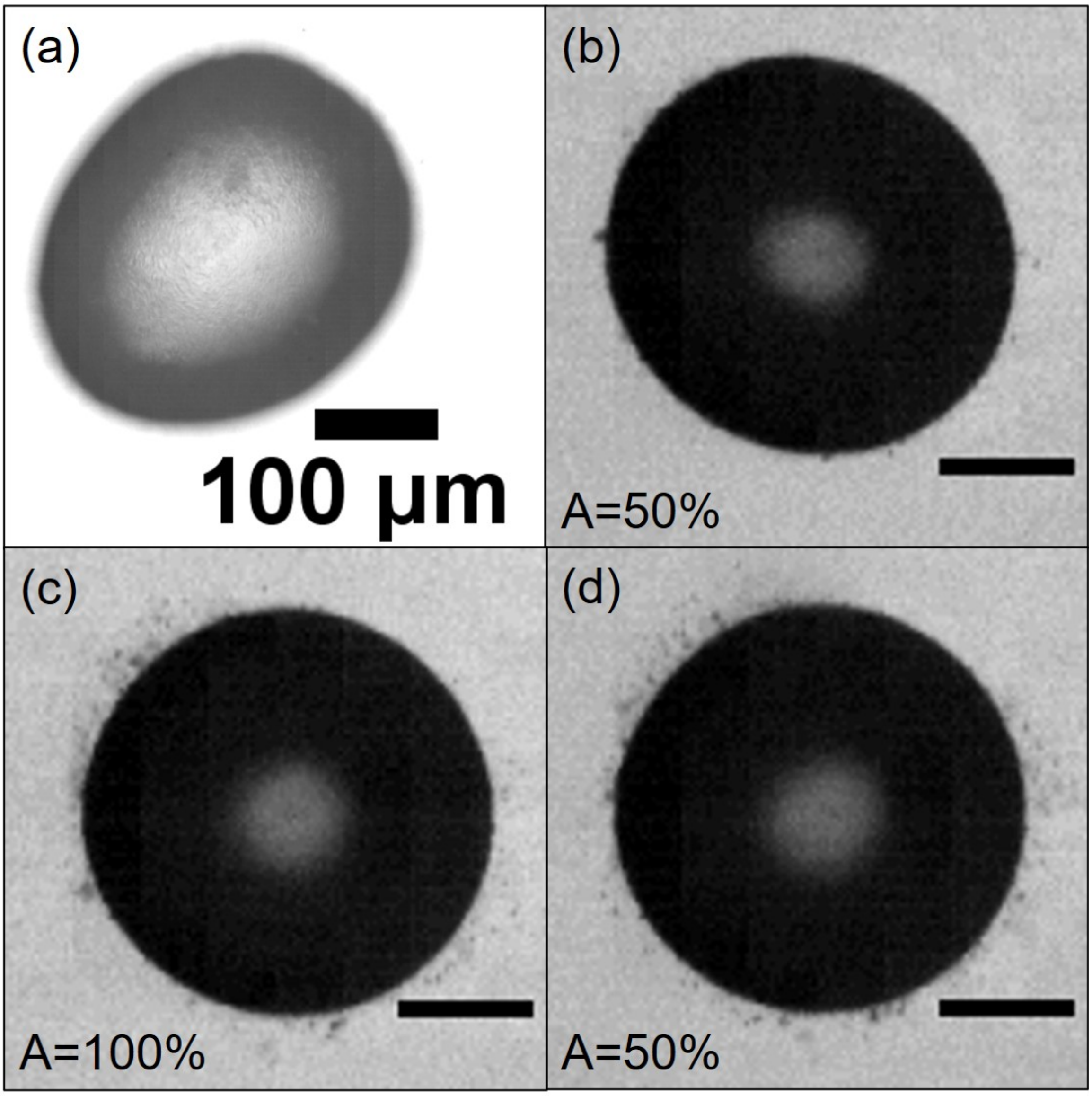

Fig. C.10 **Bubbles coated with colloids of size $a = 0.25\ \mu$m.** (a) A typical coated bubble having a non-spherical shape, suggestive of high surface coverage. (b) Another bubble, after having undergone pressure-sweep with increasing amplitude up to $A \leq 50\%$. (c) The same bubble as in (b) just after oscillations at $A = 100\%$, then (d) for pressure-sweep with decreasing amplitude $A \geq 50\%$. There is successive desorption of particles with the bubble becoming more spherical.

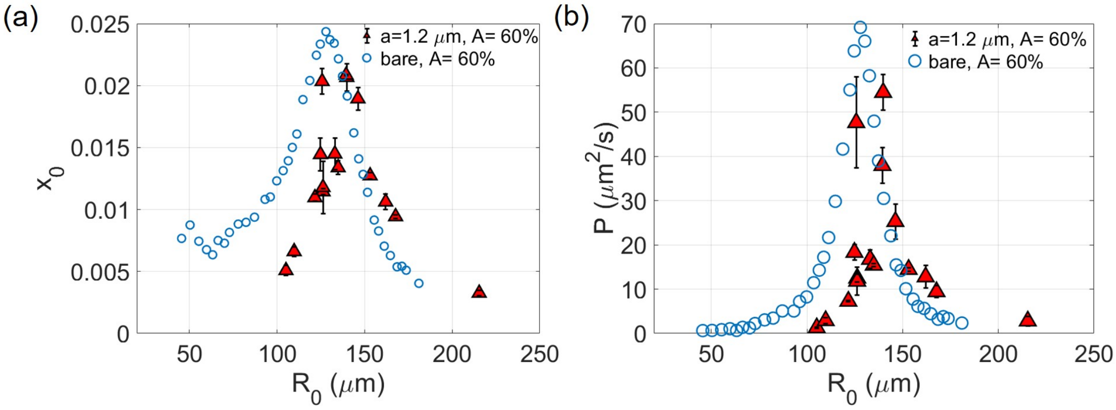

Fig. C.11 **Radius-sweep experiments for coated bubbles, with particle size $\boldsymbol{a = 1.2\ \mu}$m.** (a) Comparison of bare and coated bubble responses for varying R_0 at fixed $A = 60\%$. (b) The same data recast in terms of the power spectrum. The respective resonance radii were found to be $R_{\text{res}}^{\text{coated}} = 139.8\ \mu$m and $R_{\text{res}}^{\text{bare}} = 127.9\ \mu$m.